Evolutionary Stages of Submarine Volcanism in the Cape Verdean Archipelago

DISSERTATION

zur Erlangung des Doktorgrades

an der Mathematisch-Naturwissenschaftlichen Fakultät

der Christian-Albrechts-Universität zu Kiel

vorgelegt von

Tom Kwasnitschka

Kiel, 2012

Referent :.....Prof. Dr. Colin Devey

Koreferent: .....PD Dr. Thor Hansteen

Tag der mündlichen Prüfung: 14.12.2012

Zum Druck genehmigt: .....

Der Dekan

Hiermit erkläre ich, dass ich die vorliegende Doktorarbeit selbständig und ohne Zuhilfenahme unerlaubter Hilfsmittel erstellt habe. Weder diese noch eine ähnliche Arbeit wurde an einer anderen Abteilung oder Hochschule im Rahmen eines Prüfungsverfahrens vorgelegt, veröffentlicht oder zur Veröffentlichung vorgelegt. Ferner versichere ich, dass die Arbeit unter Einhaltung der Regeln guter wissenschaftlicher Praxis der Deutschen Forschungsgemeinschaft entstanden ist.

Kiel, 18.11.2012

Tom Kwasnitschka

Abstract

During most of their development, volcanic ocean islands are hidden beneath the sea, either as seamounts that have not or not yet reached the surface, or as guyots that have been eroded and subsided. The Cape Verdean Archipelago offers the unique opportunity to study the development of seamounts under the condition of a quasi stationary oceanic plate over a continuous magmatic source in the upper mantle, meaning that the volcanoes do not automatically subside with increasing crustal age and they are not carried away from their magmatic source due to plate motion. As a result, no linear island chain forms and new volcanoes develop in the direct vicinity of old ones.

This thesis studies the evolutionary stages of Cape Verdean seamounts based on their morphology using multi beam swath bathymetry of RRS CHARLES DARWIN cruise 168 and R/V METEOR cruises 63/2, 79/3 and 80/3. Rock samples from dredging during R/V POSEIDON cruise 320/2 as well as dredging and ROV deployment during and R/V METEOR cruises M79/3 and M80/3 complement this bathymetric data.

Eleven seamounts were studied with respect to their geometry of volcanic lineaments, distribution of satellite cones along the flanks, size of their volcanic shield, tectonic features, mass wasting events and the presence and shape of summit plateaus including wave cut surfaces. Two seamounts were described for the first time: Sodade Seamount is a young pillow volcano in the western projection of the northern island chain, whereas Tavares Seamount may form the continuation of the southern chain. The distribution and various stages of development of submarine volcanoes reveal that the progression of volcanic activity on the western ends of the island chains is discontinuous. The summits of Nola Seamounts, actually a cluster of two intergrown seamounts, were eroded by exposure above sea level during glacial low stands, arguing for an extended period of inactivity. Yet they are surrounded by morphologically young or recently active volcanoes and seamounts to the west, south and east. Brava Island and the Ilhéus Secos on the western end of the southern chain are in an erosional stage, yet both Cadamosto Seamount to the south and Fogo Island to the east show recent activity, while Tavares Seamount to the west is likely to have been inactive for an extended period.

Maio Seamount forms a solitary extinct edifice stuck in an early stage of seamount development. Maio Rise and Boavista seamount developed on island flanks and are heavily affected by mass wasting, possibly due to their inclined basement. Cabo Verde and Senghor Seamounts are large solitary edifices to the east of the archipelago. Cabo Verde is more affected by mass wasting, whereas Senghor shows a large degree of vertical tectonics possibly connected with central subsidence of a caldera system. It features a flat summit plateau rising as a Somma-type edifice on top of the volcanic shield to 94m bsl. Both Nola East (58m bsl) and Nola West (35m bsl) have more residual summit relief than Senghor, arguing for a shorter period of exposure. All wave cut surfaces are attributed to glacial sea level low stands up to -122m during the past 640 ka. Due to the

lack of age dates for these plateaus and missing bathymetric coverage of the shelf between Maio and Boavista it is not possible to correlate their vertical position or temporally constrain their formation more precisely.

Detailed studies of incipient volcanic activity were conducted within the Charles Darwin volcanic field (CDVF) of solitary and compound cones on the western flank of Santo Antão. Two structures featuring large crater like central depressions were surveyed. Tambor cone is composed of dense, highly fragmented volcaniclastics showing signs of thermal and viscous granulation. Two types of deposits were discriminated based on grain size distributions visible on video and imagery recorded during ROV surveys, with maximum clast sizes in the pebble and block range, respectively. The two deposit types alternate across four units that can only tentatively be correlated due to laterally highly varying deposit thickness attributed to a pulsing, debris jet like eruption style. Tangential antithetic joints along the crater wall and a collapse scar on the eastern sector suggest subsidence of the crater floor.

Kolà crater shows a negative relief cut into a group of small cones and a step-wise morphology of the inner crater walls. The lower portion is formed by steep cliffs of a lava flow penetrated by the eruption. Volcanic deposits are highly fragmented. Juvenile components include pebble sized sub-spherical dense lava clasts with concentric alignments of crystals and quenched rims. Fragments of lava country rock likely originate from the basal lava flow. Coarse crystalline gabbro blocks are extremely well rounded, likely due to abrasion upon fluidization in the vent during the eruption. Laterally discontinuous and mutually capping beds of these components suggest a highly effective lateral transport mechanism. Four units that can be correlated well around the crater due to significant changes in lithology. Morphology and deposits described at Kolá suggest analogies to subaerial diatremes.

The detailed study of the Tambor and Kolá volcanoes was made possible by the development of a remote sensing technique based on the photogrammetric reconstruction of outcrop geometries including full color photo mosaicking from high definition video sequences recorded by the ROV Kiel 6000 on site. The models were corrected and georeferenced to a vehicle track synthesized from a Doppler velocity log (DVL) and ultra short baseline (USBL) positioning system in combination with orientation and pressure sensors on the vehicle. This workflow not only improved the qualitative study of deposits based on 3D models of outcrops, but also facilitated the quantitative measurement of bedding and joint orientations as well as the distribution of grain size fractions visible in the source video. This approach provides a new level of productivity in robotic deep sea exploration.

Zusammenfassung

Ozeaninseln verbringen den überwiegenden Teil ihres Lebenszyklus unter Wasser, entweder als Seeberge die nicht oder noch nicht die Wasseroberfläche durchbrochen haben, oder als Guyots die erodiert wurden und wieder absanken. Der Kapverdische Archipel bietet die einzigartige Gelegenheit, die Entwicklung von Seebergen unter den Rahmenbedingungen einer quasi stationären ozeanischen Platte über einer kontinuierlichen magmatischen Quelle im oberen Mantel zu studieren. Hier versinken die Vulkane nicht automatisch mit fortschreitendem Krustenalter und werden nicht durch die Plattenbewegungen von ihrer magmatischen Quelle entkoppelt. Folglich bildet sich keine lineare Inselkette, und neue Vulkane bilden sich in unmittelbarer Nachbarschaft der alten.

Diese Arbeit beschäftigt sich mit den Entwicklungsstadien kapverdischer Seeberge auf Grundlage ihrer Morphologie, und stützt sich dabei auf Fächerecholotdaten der RRS CHARLES DARWIN reise 168 sowie der R/V Meteor Reisen 63/2, 79/3 und 80/3. Die bathymetrischen Datensätze werden durch Gesteinsproben vervollständigt, die während der R/V POSEIDON Reise 320/2 durch dredgen sowie mittels ROV-Einsatz während der R/V METEOR 79/3 und 80/3 Reisen gewonnen wurden.

Elf Seeberge wurden hinsichtlich ihrer Geometrie vulkanischer Lineamente, der Verteilung peripherer Flankenkegel, der Größe ihres vulkanischen Schildes, tektonischer Strukturen, Rutschungen sowie des Vorhandenseins bzw. der Größe ihrer Gipfelplateaus und Erosionsterrassen untersucht. Zwei Seeberge wurden erstmalig beschrieben: Sodade Seamount ist ein junger Pillowvulkan in der westlichen Verlängerung der nördlichen Inselkette, während Tavares Seamount vermutlich die Verlängerung der südlichen Inselkette bildet. Die Verteilung und die unterschiedlichen Entwicklungsstadien der submarinen Vulkane zeigen Diskontinuitäten in der westwärts fortschreitenden vulkanischen Aktivität der beiden Inselketten auf. Die Gipfel der Nola Seamounts, welche in Wahrheit aus einem Paar miteinander verschmolzener Seeberge bestehen, wurden während glazialer Niedrigwasserstände über den Meeresspiegel gehoben und erodiert, was für eine längere Phase vulkanischer Inaktivität spricht. Dennoch sind sie von morphologisch jungen und rezent aktiven Vulkanen im Westen, Süden und Osten umgeben. Die Insel Brava und die Ilhéus Secos am Westende der Südkette befinden sich im Erosionsstadium, obwohl Cadamosto Seamount im Süden und die Insel Fogo im Osten rezente Aktivität zeigen. Tavares Seamount im Westen hingegen ist vermutlich schon seit längerer Zeit inaktiv.

Maio Seamount bildet ein vereinzelt stehendes Vulkangebäude und ist bereits in einem frühen Entwicklungsstadium erloschen. Maio Rise und Boavista Seamount entstanden auf Inselflanken und sind stark von Flankenrutschungen betroffen, womöglich als Folge des geneigten Untergrundes. Cabo Verde und Senghor Seamount bilden große, allein stehende Vulkangebäude im Osten des Archipels. Cabo Verde ist stärker von Flankenrutschungen betroffen, wohingegen Senghor ein hohes Maß an Vertikaltektonik aufweist, was vermutlich eine Folge zentraler Senkungsprozesse eines Kalderasystems ist.

Er weist ein flaches Gipfelplateau auf, welches sich als Somma-Typ Vulkan vom Scheitel des vulkanischen Schildes bis in eine Wassertiefe von 94m erhebt. Mit 58m bzw. 35m an ihrer flachsten Stelle weisen die Gipfel von Nola East und Nola West ein stärkeres Restrelief als Senghor auf, was für eine kürzere Verweildauer an der Wasseroberfläche spricht. Sämtliche Brandungserosionsflächen werden mit glazialen Tiefständen des Meeresspiegels in Verbindung gebracht, welcher innerhalb der letzen 640 ka mehrmals auf bis zu -122m absank. Aufgrund fehlender Altersdaten für diese Plattformen und ebenfalls fehlender bathymetrischer Karten des Schelfs zwischen Maio und Boavista ist es unmöglich, die vertikale Position der Plateaus oder ihre zeitliche Abfolge genauer zu korrelieren.

Im Charles Darwin Vulkanfeld (CDVF), einer Gruppe einzelner bzw. verbundener Kegel auf der Westflanke von Santo Antão wurden detaillierte Studien zum Beginn der vulkanischen Aktivität eines neuen Seebergs angestellt. Zwei Strukturen die beide große, kraterartige Senken aufweisen, wurden genauer studiert. Der Kegel Tambor besteht aus dichten, hochgradig fragmentierten Vulkaniklastika die Merkmale thermischer und viskoser Granulation aufweisen. Zwei Ablagerungstypen wurden aufgrund ihrer im Videobild der ROV-Untersuchung sichtbaren Korngrößenverteilung unterschieden. Ihre maximale Klastengröße erstreckt sich bis zu Kieseln bzw. Blöcken. Die beiden Ablagerungstypen können nur ansatzweise korreliert werden, da die Schichtmächtigkeiten vermutlich aufgrund eines pulsierenden, debris-jet artigen Eruptionsverhaltens lateral stark schwanken. Tangential-antithetische Klüfte entlang der Kraterwand sowie eine Flankenrutschung der östlichen Kraterwand sind Anzeichen für Senkungsereignisse des Kraterbodens.

Der Kolá Krater zeigt ein negatives Relief und hat sich in eine Gruppe kleinerer Kegel hineingegraben. Seine Kraterwände fallen in Schollentreppen ab. In ihrem unteren Teil bilden sie senkrechte Wände, da ein dicker Lavastrom von der Eruption durchschlagen wurde. Die vulkanischen Ablagerungen sind hochgradig fragmentiert. Zu den juvenilen Komponenten zählen sehr gut gerundete, dichte Lavakiesel die eine konzentrische Einregelung ihrer Minerale sowie abgeschreckte Ränder aufweisen. Fragmente beigemengter Lavabrocken stammen vermutlich von den Lavaströmen der unteren Kraterwand. Grobkristalline, gut gerundete Gabbroblöcke wurden wahrscheinlich während der Eruption im Schlot fluidisiert und dort abgeschliffen. Lateral auskeilende, sich gegenseitig unterbrechende Ablagerungen dieser Komponenten sprechen für einen hocheffektiven lateralen Transportmechanismus. Vier Einheiten können aufgrund ihrer charakteristischen Lithologie leicht entlang des Kraters verfolgt werden. Morphologie und Ablagerungen von Kolá legen den Vergleich mit Diatremen an Land nahe.

Die detaillierten Studien von Tambor und Kolá wurden durch die Entwicklung einer neuartigen Fernerkundungsmethode ermöglicht. Diese stützt sich auf die photogrammetrische Rekonstruktion der Aufschlussgeometrie einschließlich eines Fotomosaiks auf Grundlage der hochauflösenden Videoaufnahmen des ROV Kiel 6000 vor Ort. Die so gewonnenen Modelle wurden georeferenziert und entzerrt anhand eines Bewegungs-

pfades des Roboters, der zuvor aus dem Signal eines Doppler-Geschwindigkeitsmessers (DVL) und eines USBL-Positionierungssystems in Verbindung mit Raumlage- und Tiefensensoren synthetisiert wurde. Diese Arbeitsmethode verbessert nicht nur qualitative Studien der Ablagerungen auf Grundlage von 3D-Modellen der Aufschlüsse, sondern erlaubt auch die quantitative Auswertung der Raumlage von Schüttungshorizonten und Klüftung und der Korngrößenanalyse im Video sichtbarer Fraktionen. Somit hebt dieser Ansatz die Produktivität robotischer Tiefseeforschung auf eine neue Ebene.

Contents

1 Introduction

1.1 The Life Cycle of Ocean Islands

Archipelagos of volcanic islands in the open ocean are among the most obvious manifestations of oceanic intraplate magmatic activity [*Wilson*, 1963]. Many of them form the surface expression of underlying plumes of hot mantle which give rise to magmatism above their tip [*Morgan*, 1971; *Duncan and Richards*, 1991]. As the oceanic plate moves across the plume, the process of island formation is continuously reset and the already formed edifices are carried away from their magmatic source, left prone to erosion [*McDougall and Duncan*, 1980; *Clouard and Bonneville*, 2005]. Yet, as the oceanic crust is covered by water, the volcanoes do not start out as islands, but spend much of their evolution submerged as so-called seamounts, and end beneath the waves as flat-topped guyots [*Menard and Ladd*, 1963]. This has a number of implications, affecting the style of eruptive activity forming the edifices, their transition to subaerial stages, erosion through wave energy especially in the very early and late stages of an island, mass wasting of entire sectors of the edifice along slipping planes formed by the prevolcanic marine sediments underneath the shield, and weathering of volcanic rocks through contact with seawater [*Kokelaar and Durant*, 1983; *Smoot*, 1985; *Batiza*, 1989; *Day et al.*, 1999; *Davis and Clague*, 2006; *Barker et al.*, 2009; *Quartau et al.*, 2010]. The controlling factors of submarine volcanic fragmentation and emplacement are a) hydrostatic pressure at which the eruptions take place, b) chemical composition, especially volatile content of magma, c) bathymetry of the extrusive environment, d) eruptive rate and e) dynamics of magma-water interaction [*Schmidt and Schmincke*, 2000].

The archetypal description of the life cycle of volcanic islands follows the example of the Hawaii-Emperor seamount chain [*Wilson*, 1963; *Morgan*, 1971]. The fast moving Pacific Plate passes across a mantle plume in the center of the Pacific Ocean, creating a track of discrete islands free of influence by surrounding features [*Ballmer et al.*, 2011]. This led to the description of seven stages of ocean island formation [*Clague and Dalrymple*, 1987; *Carracedo*, 1999; *Ramalho*, 2011]:

1. During the pre-shield stage, a number of feeder dykes intrude into the prevolcanic marine sediment resulting in elevated seafloor topography and next leading to isolated volcanic edifices on the sea floor. As this stage generally occurs at great water depth, effusive eruption styles dominate that primarily form alkalic sheet flows and pillow mounds. To some degree explosive activity may occur as the edifice grows to shallower water depth. The pillow mounds become subject to sill intrusions while radial dyke systems begin to define the core of the edifice. As the volcano grows, lateral instabilities of the oversteepened pillow and hyaloclastite slopes lead to collapse events that maintain a steep relief of the growing edifice.
2. An increase in rate and volume of eruptions leads to the shield stage in which the volcano constructs its main edifice by layer upon layer of lava sheets, changing to

a tholeiitic composition. Ever shallowing its peak, and depending on volatile content, the vesicularity increases and explosive eruptive styles play a bigger role, leading to summit calderas but also to satellite scoria cones on the volcano flanks [*Gee et al.*, 2001]. The slopes begin to ease while the crust beneath the edifice subsides under the load of the volcano [*Watts et al.*, 1997]. As the volcano breaks the sea surface, the eruptive style changes over surtseyan to strombolian and Hawaiian after the vent is permanently sealed from, or stays above the influence, of ocean water [*Kokelaar and Durant*, 1983; *Clague and Dixon*, 2000].

3. The subaerial stage is characterized by further buildup of the volcanic shield enhanced by the extended range of lava flows under subaerial conditions and through lava tubes. Intrusions of dykes along fissures and rift systems destabilize the edifice. As the underlying prevolcanic sedimentary basement forms a plane of weakness [*Walker*, 1992], the combination of increasing weight of the edifice, destabilization along rifts [*Gee et al.*, 2001] and the presence of such slipping planes may lead to large-scale slope failures [*Carracedo*, 1999].
4. Drastic decrease of magma supply marks the beginning of the capping stage, as magma compositions once more change to low silica alkali basalts and consequently become more explosive, resulting in irregular morphology of cones and craters on top of the edifice [*Clague and Dixon*, 2000]. At the same time, the increased viscosity of lavas leads to an increased steepness of the morphology along rift zones [*Orton*, 1996].
5. The erosional stage is characterized by a general seizure of volcanic activity while subsidence, erosion and marine abrasion at sea level segment the morphology. Where marine environments are favorable, coastal reef complexes develop.
6. The post-erosional or rejuvenated stage is a comparatively short period of reactivated volcanic activity, during which only small volumes of alkalic lavas from mostly monogenetic edifices such as cinder cones and tuff rings are produced.
7. From this point onwards, the constructional phase of the ocean island is finished and erosion and subsidence diminish the edifice back to sea level as the volcano is driven away from its magmatic source [*Menard and Ladd*, 1963]. A flat top forms from the abraded summit and marginal reef complexes, fringed by steep underwater morphology and erosional debris fans. As the island further subsides, ultimately due to cooling of the oceanic plate, it drowns completely and forms a flat top guyot.

The quasi-linear geometry formed by the motion of the oceanic plate over a hotspot in the Hawaiian example that inspired the above scheme is not universal. The most important factors leading to contrasting development are differing geodynamical settings leading to different melting rates and different chemical composition of magmas [*Ramalho*, 2011]. The islands of the Eastern Tropical Atlantic are, in many ways, such an opposite end member to the Hawaiian example [*Carracedo*, 1999].

The motion of the African Plate is not as linear and considerably more complex as in the Pacific region [*DeMets et al.*, 1990; *Pollitz*, 1991; *Gripp and Gordon*, 2002; *Geldmacher*

et al., 2005]. As a consequence, the islands grow older, their life span exceeding Hawaiian Islands up to an order of magnitude [*Carracedo*, 1999; *Schmincke*, 2005]. Lower magma supply rates and degrees of partial melting prevent the development of a tholeiitic shield, compositions become more evolved and discrimination of a shield building stage becomes less clear [*Carracedo*, 1999]. In addition, the eruptive style is different and pyroclastic deposits of strombolian to plinian subaerial eruptions dominate over effusive Hawaiian eruptions [*Schmincke*, 2005], producing smaller and steeper edifices. These in turn are less stable and more prone to erosion including large scale mass wasting [*Schmincke*, 2005]. The more complicated magmatic evolution over a longer time span may also lead to several consecutive rejuvenated phases [*Geldmacher et al.*, 2001]. As climatic and chemical conditions in the Eastern Tropical Atlantic merely allow the development of cryptic warm water coral reefs [*Spalding et al.*, 2001] and subsidence due to cooling of the oceanic crust is already in an advanced stage, flat top guyots do not represent constructional phases of reef building upon subsidence but erosional features upon the abrasion of the subaerial edifice to sea level prior to drowning [*Quartau et al.*, 2010].

The archipelagos off West Africa (Madeira, Selvagen, Canaries and Cape Verde) each underwent slightly different histories, even though they share many of their overall geodynamical settings, situated on Mesozoic crust and fed by plumes. Some of these plumes are likely affected by the vicinity of the African Plate through processes such as edge driven convection [*Geldmacher et al.*, 2005], leading to a more discontinuous hot spot track. The Selvagen and Canary volcanic provinces can be traced back along discontinuous arcane hot spot tracks to initial activity in southern Iberia about 70Ma ago [*Geldmacher et al.*, 2005]. A parallel track is formed by the Madeira hotspot to the northwest. Both tracks are attributed to the motion of the African Plate over a plume system, and are in agreement with the direction of the Tristan / Walvis / St. Helena hotspot tracks that lie much further away from the proposed Eulerian rotation pole of the African Plate at 56°N, 45°W [*Geldmacher et al.*, 2005].

However, De Mets et al. [1990] and Pollitz [1991] showed that around 6Ma bp. the location of the pole shifted to 19°N, 16°W. This had important implications for the development of the Cape Verdean archipelago as it came into immediate vicinity of the rotational pole (Figure 1-1). Since the oldest rocks of the archipelago (on Sal Island) date back to 25.6Ma [*Torres et al.*, 2002; *Holm et al.*, 2006], the archipelago was constrained to a small geographic area for at least one third of its lifetime. This circumstance makes the Cape Verdes particularly interesting for the study of ocean island evolution as it can be regarded to stay quasi-stationary, forming an opposite end member to the Hawaiian example.

1.2 The Cape Verdean Archipelago

The Cape Verde Islands lie some 500-800km of the West African coast between 15°N and 17°N (Figure 1-1). They form the culmination of the Cape Verde Rise, a morphological high extending across almost 10° of latitude. Rising more than 2000m above the depth assumed for oceanic crust [*Stein and Stein*, 1992] at the respective Mesozoic age

between 120-140Ma [*Williams et al.*, 1990; *Müller et al.*, 2008], they form the largest bathymetrical anomaly of any ocean basin [*Crough*, 1982; *McNutt*, 1988; *Monnereau and Cazenave*, 1990; *Sleep*, 1990]. They are the product of hot spot volcanism associated with magmatic activity forming the Cape Verde Islands [*McNutt*, 1988; *Sleep*, 1990], and likely developed during the early Miocene as inferred by the stratigraphic record from IODP cores [*Faugeres et al.*, 1986].

The archipelago consists of ten islands arranged in a horse-shoe shape opening towards the west (Figure 1-2). Two chains of islands may be discriminated based on their common lower edifice of merged shields: The northern chain consisting of São Nicolau, Santa Lucia, and Sao Vicente terminates with Santo Antão in the northwest. Sal, Boa Vista, Maio, Santiago, Fogo and Brava form the southern chain.

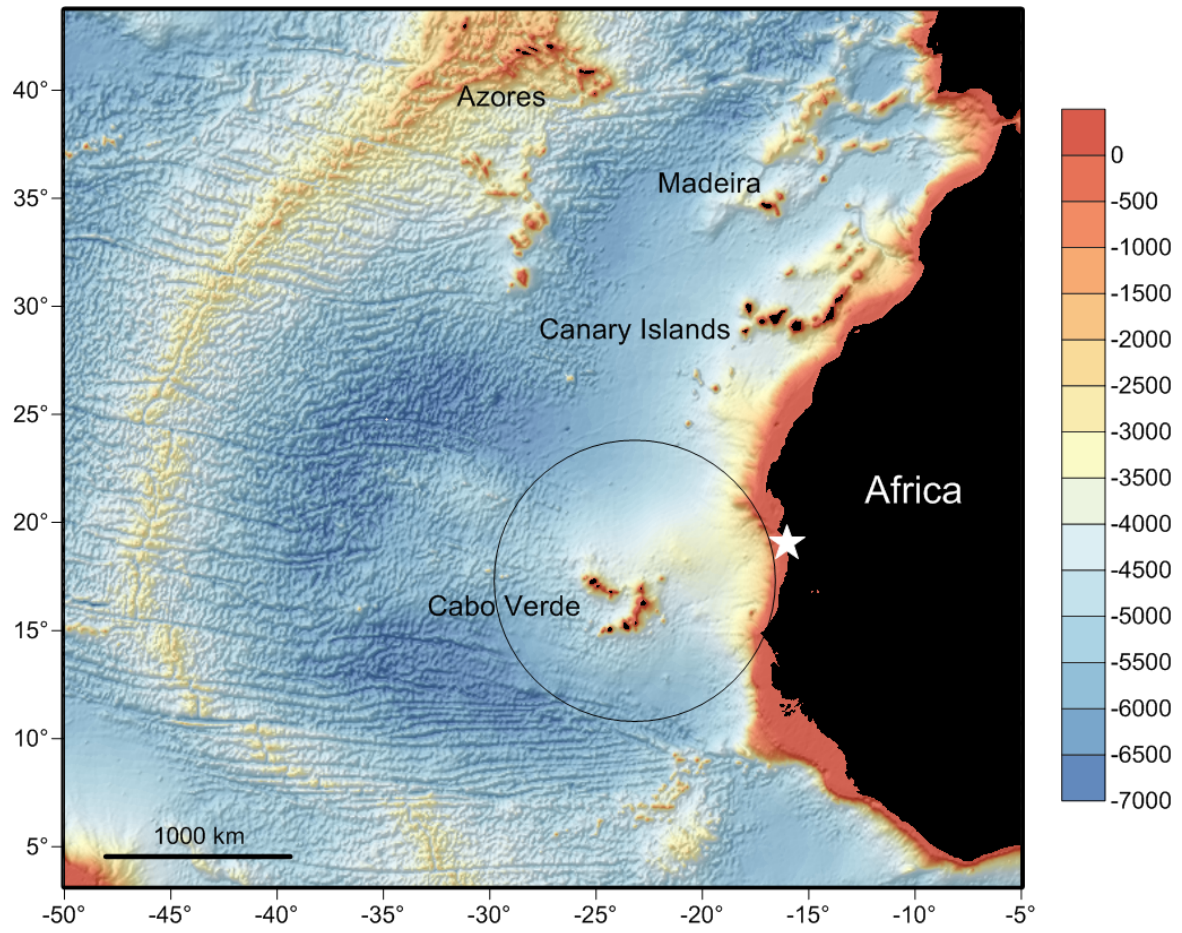

Figure 1-1 *Bathymetric map of the eastern Tropical Atlantic Ocean showing the location of major island chains. White asterisk marks the position of the rotational pole for the time interval 6Ma – present [*Pollitz, *1991]. Black circle shows the maximum extent of a synthetic swell root calculated for the Cape Verde Rise (modified from Ramalho, [2011]).*

The origin and pathways of Cape Verde melts still form a subject of dispute. Trace element and isotope signatures indicate a heterogeneous mantle source [*Gerlach et al.*, 1988; *Jørgensen and Holm*, 2002; *Doucelance et al.*, 2003; *Plesner et al.*, 2003; *Holm et al.*, 2006; 2008; *Barker et al.*, 2012] that may also influence the geographic distribution of magmatic activity. The northern chain including Sal is dominated by a HIMU / DMM signature whereas Fogo, Santiago and Maio are characterized by an EM1 and HIMU signa-

ture. Hildner et al. [2012] showed that this trend is discontinuous to the west as Brava has a HIMU / DMM signature similar to the northern chain. A peculiarity of the Cape Verdes are the occurrences of carbonatites in the volcanic core complexes as well as extrusive volcanics of rejuvenated stages [*Hoernle et al.*, 2002; *Doucelance et al.*, 2003; *Holm et al.*, 2006; *Ancochea et al.*, 2010; *Madeira et al.*, 2010].

Roughly in agreement to the geochemical trends, the islands show a weak age progression from east to west. Especially the ages of the southern chain highly overlap [*Holm et al.*, 2008; *Ramalho et al.*, 2010a], with volcanic activity ranging between 25.6 Ma on Sal to the only contemporary activity of the archipelago on Fogo [*Torres et al.*, 1995], while the northern chain spans from 6Ma on Sao Nicolau to 0.09Ma on Santo Antão [*Plesner et al.*, 2003]. Frequent volcanotectonic activity has been reported from Fogo and offshore to the west of both Santo Antão and Brava [*Heleno da Silva et al.*, 1999; *Grevemeyer et al.*, 2009].

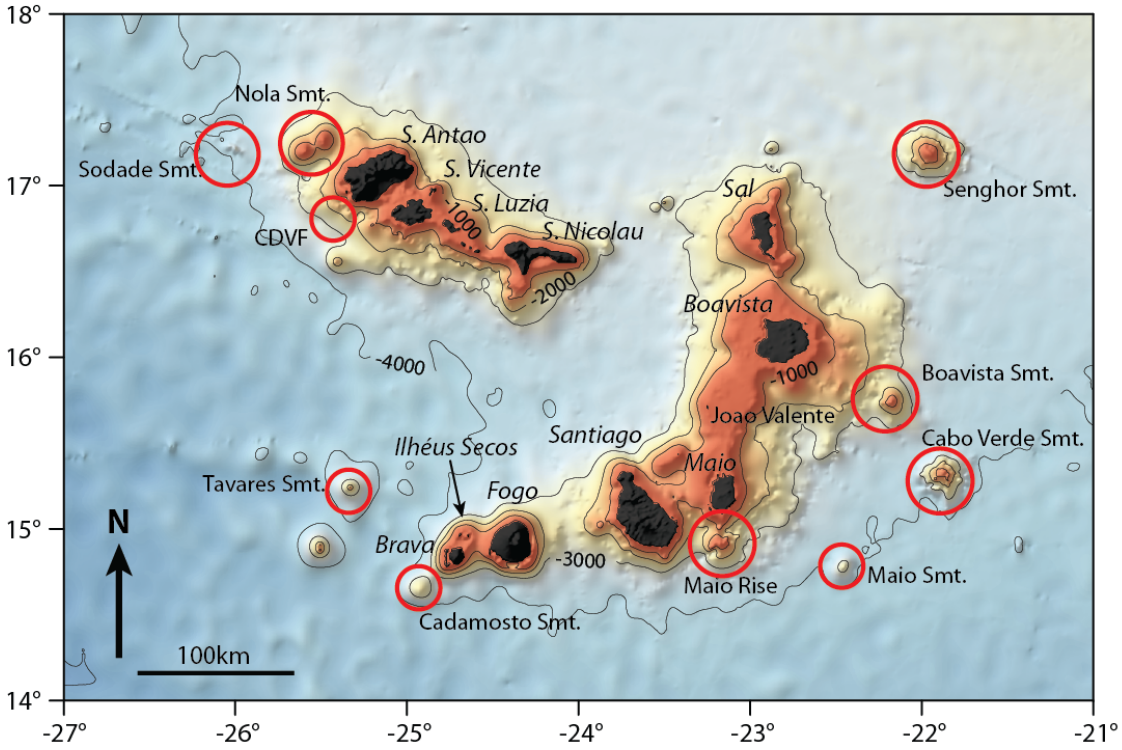

Figure 1-2 *GMRT map of the Cape Verdean Archipelago. Red circles mark the newly mapped seamounts described in this study.*

The parallel westward age progression of the two island chains becomes evident in the island topographies. Sal, Boa Vista, and Maio are eroded almost down to sea level and only former volcanic necks form residual highs. Sao Nicolau, Santa Luzia and Sao Vicente and Brava also show the effect of substantial erosion deep into the island core but still have substantial relief [*Ancochea et al.*, 2010]. The islands of Santiago and Santo Antão are deeply incised by erosion [*Mitchell-Thomé*, 1972] but still show the general geometry of the shield stage. Fogo is an active stratovolcano with steep flanks, its morphology only interrupted by a large collapse scarp to the east [*Day et al.*, 1999].

Beneath sea level, the two island chains form a continuous morphology since the shields of the islands, with the exception of Fogo and Brava, have merged. Especially the older islands from Sal to Maio have developed large shelves that attest a long phase of erosion [*Quartau et al.*, 2010]. The Ilhéus Secos north of Brava are likely formed by remnants of a former island of which only residual morphologies rise above sea level. In between Maio and Boavista, the large Joao Valente Shoals rise to just 14m beneath sea level and obviously represent a former island in its drowned stage [*Ramalho*, 2011]. Most islands have a history of vertical tectonics involving multiple stages of subsidence and uplift throughout their development [*Ramalho et al.*, 2010a]. These are a consequence of magmatic intrusions at the crustal level, accounting for vertical displacements of up to 350m as well as Quaternary regional uplift by 100m due to expansion of the Cape Verde Rise [*Ramalho et al.*, 2010b].

The islands are surrounded by seamounts and smaller volcanic edifices that outnumber the subaerial edifices and extend the range of volcanic activity in the archipelago [*Masson et al.*, 2008]. Senghor, Cabo Verde and Maio Seamounts flank the archipelago to the east. Boavista Seamount and Maio Rise formed on the lower eastern slopes of the respective islands of the same name. Cadamosto Seamount sits on the southern flank of Brava. It not only shows signs of recent volcanotectonic activity [*Grevemeyer et al.*, 2009] but also extends the HIMU / DMM signature of the northern chain and Brava [*Barker et al.*, 2012; *Hildner et al.*, 2012]. Nola Seamount sits on the northwestern flank of Santo Antão, extending the range of the compound edifice of the northern chain. On the southern flank of the island, a field of small solitary and compound cones named the Charles Darwin Volcanic Field (CDVF, [*Hansteen*, 2010]) may represent a case of incipient seamount formation.

As part of the research described here, two previously unknown seamounts were described for the first time. Tavares seamount west of Brava is under the influence of heavy sedimentation from the basin in between the island chains and its developmental stage cannot be clearly addressed, although it shows signs of tectonic overprinting. Sodade Seamount, a young pillow volcano surrounded by peripheral cones, lies on the western projection of the northern island chain [*Barker et al.*, 2012].

So far there has only been a limited amount of research conducted on the Cape Verdean seamounts, in part since they had not been comprehensively mapped until recently. [*Masson et al.*, 2008] conducted a study of the submarine island flanks of the northern chain including the lower part of Nola Seamount. They found two large debris fans on the western flank of Santo Antão, attributed to the Tope de Coroa landslide scar and the adjacent Tarrafal scar. The southwestern flanks of Sao Vicente [*Ancochea et al.*, 2010] and northern and southeastern flanks of Sao Nicolau are also marked by older mass-wasting morphologies. No pronounced signs of mass wasting were identified on Nola seamount. A concurrent study of the southern chain between Brava to Santiago identified the submarine parts of the Monte Amarelo landslide scar on the eastern Flank of Fogo, concluding that it is likely due to a single catastrophic failure event [*Le Bas et al.*, 2007]. Cadamosto seamount had been mapped and interpreted as part of a study on its

recent seismic activity [*Grevemeyer et al.*, 2009]. Based on dredge samples recovered during RRS CHARLES DARWIN cruise 85 in 1985, Cadamosto was recently characterized by Barker et al. [2012] as a phonolitic edifice with a trace element signature similar to the northern chain. A number of biological [*Hanel et al.*, 2010] and biogeochemical studies [*Wang et al.*, 2011] were conducted on Senghor Seamount based on data that also formed the basis of this study.

1.3 Data

The basis of this study is formed by data from a number of research cruises to the Cape Verdes between 2004 and 2010. R/V METEOR cruise 62/3 in 2004 was dedicated to the deployment of ocean bottom seismomenters and the mapping of the lower flanks of the Fogo-Brava complex using an Atlas Hydrosweep, 59 beam swath echo sounder [*Grevemeyer et al.*, 2009]. During RRS CHARLES DARWIN cruise 168 following in 2005, a number of gaps left by M63/2 were filled. The main focus of the cruise was the mapping of the flanks of the northern chain using a Kongsberg EM12 echo sounder [*Masson et al.*, 2008]. The expedition discovered a field of young volcanic cones southwest of Santo Antão and gave its name to the Charles Darwin Volcanic Field (CDVF).

Also in 2005, R/V POSEIDON cruise 320/2 mapped the summit areas of Senghor Seamount using an Elac Seabeam 1050 mobile swath echo sounder down to 1500m, but although the data was used for preparation of further mapping, it was not included in the maps of this study. In 2009, R/V METEOR cruise 79/3 mapped Senghor, Boavista and Cabo Verde Seamounts as well as the CDVF using a Kongsberg EM 120 echo sounder of 191 beams. The same equipment was used during R/V METEOR cruise 80/3 in 2010 to map remaining parts of Senghor, Boavista and Caboverde seamounts in addition to Maio Seamount, Maio Rise, Cadamosto, Tavares, as well as Nola and Sodade Seamounts including most transits.

In addition to multibeam echo sounding, ground truthing by dredging and ROV deployment yielded valuable insights. During P320/2, Senghor Seamount was dredged but only highly altered lava blocks and thick manganese crusts were recovered that did not form a basis for geochemical analyses. The deployment of a tethered camera provided qualitative impressions of the sedimentary cover on the flat summit of Senghor. On M79/3 a Sub-Atlantic Mohawk class ROV was deployed once each to the summit region of Senghor Seamount and along its upper flanks to 700m depth, providing visual clues on the terrain, erosional features and biology [*Christiansen*, 2010]. Dredge samples recovered from Senghor, Boavista and Cabo Verde Seamount were in a similar stage of preservation as the previously recovered P320/2 samples and were of questionable value for further analytical work, whereas samples dredged at CDVF yielded fresh lava, dense and vesicular volcaniclastic deposits and fragments of country rock. During cruise M80/3, the GEOMAR working class ROV Kiel 6000 was deployed on 13 transects between 4000m and 600m depth that provided visual coverage and rock samples of Senghor, Cabo Verde, Cadamosto, CDVF, Nola and Sodade Seamounts. Whereas the quality of samples from Senghor did not yield improvements on the existing suite, localized ROV samples from the remaining Seamounts showed a good stage of preservation and were

complemented through dredge hauls at the respective sites, also including Boavista and Maio Seamounts as well as Maio Rise.

The visual data recovered by the ROV and camera deployments during P320/2 and M79/3 was of limited quality as the deployments had a strong experimental character. This situation was improved during M80/3 through the deployment of ROV Kiel 6000 that not only yielded rock samples, but also relatively stable-quality film and still imagery of highly complex volcanic structures. Volcanic core complexes were exposed along the caldera walls of Cabo Verde and Cadamosto Seamounts that consist of sequences of sheet lavas and volcaniclastic deposits crossed by dyke swarms. Several dives at CDVF revealed complex and highly variable morphologies ranging from cones to crater-like depressions. The suite of dredge samples recovered during M79/3 could be tentatively correlated to volcaniclastic deposits of marked characteristics that were encountered on ROV transects. Steep vertical outcrops yielded insights to the structure of the cones and craters that could not have been gained through acoustic sounding or downward-looking probes such as OFOS [*Wright et al.*, 2002]. But despite the large surveying efforts, the visual information provided by ROV video and photos remained highly qualitative and biased by its two dimensional nature so that only qualitative clues could be gained and the interpretation of features obviously fell behind the true nature of the complex outcrops surveyed.

1.4 Structure of this Study

Based on this data set, this thesis is organized as a series of three stand-alone research articles (Chapters 2-4) that are either published, in revision or in preparation. Their overall aim is to describe submarine volcanic activity on the Cape Verdes on several scales. The methods chosen focus on the morphology and physical volcanology of the study objects and deliberately do not involve geochemical characterization of the rocks or detailed studies of magmatic processes. Macroscopic descriptions of deposits were only included where they provided constraints to physical processes of eruption dynamics or documented varying states of preservation that provide the most general clues on the age of volcanism. Since chapters 2-4 are written in the form of self-consistent publications, repetition particularly of aspects mentioned in Chapter 1 cannot be avoided.

Chapter 2 presents a comparative study of Cape Verdean submarine volcanic edifices, i.e. seamounts in various stages of development and association with neighboring islands, including incipient clusters of cones. The study draws upon multi beam echo sounder data, supported by the description of samples from dredges and ROV dives. The incorporation of local peculiarities on seamount development but especially comparison to varying sea level during the ice ages allows estimates on the timing of late erosional stages and compilation of a tentative age progression.

The remainder of the thesis is dedicated to the detailed study of incipient volcanism encountered at CDVF on the basis of data collected by ROV Kiel 6000 (i.e. visual information), refined cross sections derived from the vehicle track geometry and rock sam-

ples. Chapter 3 describes the development of a processing workflow that allowed the reconstruction of outcrop geometry and the rock face on a scale of centimeters, based on photogrammetric reconstructions derived from the high definition video sequences recorded on site by the ROV. This workflow not only offers advanced means to visualize and communicate the data but also allows quantified measurements to be derived from georeferenced, virtual outcrops including orientation and grain size measurements.

Chapter 4 reports on the application of these techniques on two crater like structures of the CDVF, highlighting their morphological characteristics, geometry of outcrops, internal correlation of their stratigraphy, bedding and joint orientation as well as grain size distribution in the visible range. The study further reveals the limitations of the method proposed in chapter 3. Chapter 5 presents a summary of the results of the previous three chapters in a larger context, and provides an outlook to the further application of virtual fieldwork in the deep sea based on photogrammetry.

References

Ancochea, E., M. J. Huertas, F. Hernán, and J. L. Brändle (2010), Volcanic evolution of São Vicente, Cape Verde Islands: The Praia Grande landslide, *J Volcanol Geoth Res*, *198*(1), 143–157, doi:10.1016/j.jvolgeores.2010.08.016.

Ballmer, M. D., G. Ito, J. van Hunen, and P. J. Tackley (2011), Spatial and temporal variability in Hawaiian hotspot volcanism induced by small-scale convection, *Nature Geosci*, *4*(7), 457–460, doi:10.1029/2003JB002949.

Barker, A. K., P. M. Holm, D. W. Peate, and J. A. Baker (2009), Geochemical Stratigraphy of Submarine Lavas (35 Ma) from the Flamengos Valley, Santiago, Southern Cape Verde Islands, *J Petrol*, *50*(1), 169–193, doi:10.1093/petrology/egn081.

Barker, A. K., V. R. Troll, R. M. Ellam, and T. H. Hansteen (2012), Magmatic evolution of the Cadamosto Seamount, Cape Verde: beyond the spatial extent of EM1, *Contributions To Mineralogy And Petrology*, (163), 949–965.

Batiza, R. (1989), Geological and petrologic evolution of seamounts near the EPR based on submersible and camera study, *Marine Geophysical Researches*, *11*(3), 169–236, doi:10.1007/BF00340203.

Carracedo, J. C. (1999), Growth, structure, instability and collapse of Canarian volcanoes and comparisons with Hawaiian volcanoes, *J Volcanol Geoth Res*, *94*(1), 1–19.

Christiansen, B. (2010), Short Cruise Report Meteor M 79/3, *Universität Hamburg*, 1–12.

Clague, D. A., and G. B. Dalrymple (1987), The Hawaiian-Emperor volcanic chain. Part I. Geologic evolution, *Volcanism in Hawaii*, *1*, 5–54.

Clague, D. A., and J. E. Dixon (2000), Extrinsic controls on the evolution of Hawaiian ocean island volcanoes, *Geochem Geophy Geosy*, *1*(4), 1–9, doi:10.1029/1999GC000023.

Clouard, V., and A. Bonneville (2005), Ages of Seamounts, Islands, and Plateaus on the Pacific Plate, in *Plates, Plumes, And Paradigms*, vol. 388, edited by G. Foulger, J. H. Natland, D. C. Presmall, and D. L. Anderson, pp. 71–90, Geological Society of America.

Crough, S. T. (1982), Geoid Height Anomalies Over the Cape Verde Rise, *Marine Geophysical Researches*, *5*(3), 263–271.

Davis, A. S., and D. A. Clague (2006), Volcaniclastic deposits from the North Arch volcanic field, Hawaii: explosive fragmentation of alkalic lava at abyssal depths, *B Volcanol*, *68*(3), 294–307, doi:10.1007/s00445-005-0008-7.

Day, S., S. I. N. Heleno da Silva, and J. F. B. D. Fonseca (1999), A past giant lateral collapse and present-day flank instability of Fogo, Cape Verde Islands, *J Volcanol Geoth Res*, *94*(1-4), 191–218.

DeMets, C., R. G. Gordon, D. F. Argus, and S. Stein (1990), Current plate motions, *Geophysical Journal International*, *101*(2), 425–478, doi:10.1111/j.1365-246X.1990.tb06579.x.

Doucelance, R., S. Escrig, M. Moreira, C. M. Gariepy, and M. Kurz (2003), Pb-Sr-He isotope and trace element geochemistry of the Cape Verde Archipelago, *Geochim Cosmochim Ac*, *67*(19), 3717–3733, doi:10.1016/S0016-7037(03)00161-3.

Duncan, R. A., and M. A. Richards (1991), Hotspots, mantle plumes, flood basalts, and true polar wander, *Reviews in Geophysics*, (1), 31–50.

Faugeres, J. C., P. Legigan, N. Maillet, and C. Latouche (1986), 18. Pelagic, Turbiditic, and Contouritic Sequential Deposits on the Cape Verde Plateau (Leg 108, Site 659, Northwest Africa): Sediment Record During Neogene Time, in *Proceedings of the Ocean Drilling Program: Scientific results*, vol. 108, edited by W. Ruddiman and M. Sarnthein, p. 311.

Gee, M. J. R., D. G. Masson, A. B. Watts, and N. C. Mitchell (2001), Offshore continuation of volcanic rift zones, El Hierro, Canary Islands, *J Volcanol Geoth Res*, *105*(1-2), 107–119.

Geldmacher, J., K. Hoernle, P. Bogaard, S. Duggen, and R. Werner (2005), New 40 Ar/ 39 Ar age and geochemical data from seamounts in the Canary and Madeira volcanic provinces: Support for the mantle plume hypothesis, *Earth and Planetary Science Letters*, *237*(1), 85–101.

Geldmacher, J., K. Hoernle, P. van den Bogaard, G. Zankl, and D. Garbe-Schönberg (2001), Earlier history of the ≥70-Ma-old Canary hotspot based on the temporal and geochemical evolution of the Selvagen Archipelago and neighboring seamounts in the eastern North Atlantic, *J Volcanol Geoth Res*, *111*(1-4), 55–87, doi:10.1016/S0377-0273(01)00220-7.

Gerlach, D. C., R. A. Cliff, G. R. Davies, M. Norry, and N. Hodgson (1988), Magma Sources of the Cape-Verdes Archipelago - Isotopic and Trace-Element Constraints, *Geochim Cosmochim Ac*, *52*(12), 2979–2992.

Grevemeyer, I., G. Helffrich, B. Faria, G. Booth Rea, M. Schnabel, and W. Weinrebe (2009), Seismic activity at Cadamosto seamount near Fogo Island, Cape Verdes—formation of a new ocean island? *Geophys J Int*, *180*(2), 552–558.

Gripp, A. E., and R. G. Gordon (2002), Young tracks of hotspots and current plate velocities, *Geophys J Int*, *150*(2), 321–361.

Hanel, R., H. C. John, O. Meyer-Klaeden, and U. Piatkowski (2010), Larval fish abundance, composition and distribution at Senghor Seamount (Cape Verde Islands), *Journal of Plankton Research*, *32*(11), 1541–1556, doi:10.1093/plankt/fbq076.

Hansteen, T. (2010), Meteor M80-3 Short Cruise Report, *Universität Hamburg*, 1–9.

Heleno da Silva, S. I. N., S. Day, and J. F. B. D. Fonseca (1999), Fogo Volcano, Cape Verde Islands: seismicity-derived constraints on the mechanism of the 1995 eruption, *J Volcanol Geoth Res*, *94*(1-4), 219–231.

Hildner, E., A. Klügel, and T. H. Hansteen (2012), Barometry of lavas from the 1951 eruption of Fogo, Cape Verde Islands: Implications for historic and prehistoric magma plumbing systems, *Journal of Volcanology and Geothermal ….*

Hoernle, K., G. Tilton, M. J. Le Bas, S. Duggen, and D. Garbe-Schonberg (2002), Geochemistry of oceanic carbonatites compared with continental carbonatites: mantle recycling of oceanic crustal carbonate, *Contributions To Mineralogy And Petrology*, *142*(5), 520–542.

Holm, P. M., J. R. Wilson, B. P. Christensen, L. Hansen, S. L. Hansen, K. M. Hein, A. K. Mortensen, R. Pedersen, S. Plesner, and M. K. Runge (2006), Sampling the cape verde mantle plume: Evolution of melt compositions on Santo Antao, Cape Verde Islands, *J Petrol*, *47*(1), 145–189.

Holm, P. M., T. Grandvuinet, J. Friis, J. R. Wilson, A. K. Barker, and S. Plesner (2008), An 40Ar-39Ar study of the Cape Verde hot spot: Temporal evolution in a semistationary plate environment, *Journal of Geophysical Research*, *113*(B8), B08201.

Jørgensen, J. Ø., and P. M. Holm (2002), Temporal variation and carbonatite contamination in primitive ocean island volcanics from Sao Vicente, Cape Verde Islands, *Chemical Geology*, *192*(3), 249–267.

Kokelaar, P., and G. P. Durant (1983), The Submarine Eruption and Erosion of Surtla (Surtsey), Iceland, *J Volcanol Geoth Res*, *19*(3-4), 239–246.

Le Bas, T. P., D. Masson, R. Holtom, and I. Grevemeyer (2007), Slope failures of the flanks of the southern Cape Verde Islands, *Submarine Mass Movements and Their Consequences*, 337–345.

Madeira, J., J. Mata, C. Mourão, A. Brum da Silveira, S. Martins, R. Ramalho, and D. L. Hoffmann (2010), Volcano-stratigraphic and structural evolution of Brava Island (Cape Verde) based on 40Ar/39Ar, U–Th and field constraints, *J Volcanol Geoth Res*, *196*(3-4), 219–235, doi:10.1016/j.jvolgeores.2010.07.010.

Masson, D. G., T. P. Le Bas, I. Grevemeyer and W. Weinrebe (2008), Flank collapse and large-scale landsliding in the Cape Verde Islands, off West Africa, *Geochem Geophy Geosy*, *9*, Q07015, doi:10.1029/2008GC001983.

McDougall, I., and R. A. Duncan (1980), Linear volcanic chains — recording plate motions? *Tectonophysics*, *63*(1-4), 275–295, doi:10.1016/0040-1951(80)90117-1.

McNutt, M. (1988), Thermal and mechanical properties of the Cape Verde Rise, *Journal of Geophysical Research*, *93*(B4), 2784–2794.

Menard, H. W., and H. S. Ladd (1963), Oceanic islands, seamounts, guyots and atolls, *The sea*, *3*, 365–385.

Mitchell-Thomé, R. C. (1972), Outline of the geology of the Cape Verde Archipelago, *Geologische Rundschau*, *61*(3), 1087–1109.

Monnereau, M., and A. Cazenave (1990), Depth and geoid anomalies over oceanic hotspot swells: A global survey, *Journal of Geophysical Research*, *95*(B10), 15429–15–438.

Morgan, W. J. (1971), Convection Plumes in the Lower Mantle, *Nature*, *230*(5288), 42–43, doi:10.1038/230042a0.

Müller, R. D., M. Sdrolias, C. Gaina, and W. R. Roest (2008), Age, spreading rates, and spreading asymmetry of the world's ocean crust, *Geochem Geophy Geosy*, *9*(4), Q04006.

Orton, G. J. (1996), Volcanic environments, in *Sedimentary Environments; Processes, Lithofacies and Stratigraphy*, edited by H. Reading, pp. 485–567, Blackwell Science, Oxford, UK.

Plesner, S., P. M. Holm, and J. R. Wilson (2003), 40Ar-39Ar geochronology of Santo Antão, Cape Verde Islands, *J Volcanol Geoth Res*, *120*(1-2), 103–121.

Pollitz, F. F. (1991), Two-stage model of African absolute motion during the last 30 million years, *Tectonophysics*, *194*(1), 91–106.

Quartau, R., A. S. Trenhaile, N. C. Mitchell, and F. Tempera (2010), Development of volcanic insular shelves: Insights from observations and modelling of Faial Island in the Azores Archipelago, *Marine Geology*, *275*(1), 66–83.

Ramalho, R. (2011), *Building the Cape Verde Islands*, Springer, Heidelberg.

Ramalho, R. S., G. Helffrich, M. Cosca, D. Vance, D. Hoffmann, and D. N. Schmidt (2010a), Vertical movements of ocean island volcanoes: Insights from a stationary plate environment, *Marine Geology*, *275*(1-4), 84–95, doi:10.1016/j.margeo.2010.04.009.

Ramalho, R., G. Helffrich, M. Cosca, D. Vance, D. Hoffmann, and D. N. Schmidt (2010b), Episodic swell growth inferred from variable uplift of the Cape Verde hotspot islands, *Nature Geosci*, *3*(11), 774–777, doi:10.1038/ngeo982.

Schmidt, R., and H.-U. Schmincke (2000), Seamounts and island building, in *Encyclopedia of Volcanoes*, edited by H. Sigurdsson, B. F. Houghton, M. McNutt, H. Rymer, and J. Stix, pp. 383–402, Academic Press.

Schmincke, H.-U. (2005), *Volcanism*, Springer.

Sleep, N. H. (1990), Hotspots and mantle plumes: Some phenomenology, *Journal of Geophysical Research*, *95*(B5), 6715–6736.

Smoot, N. C. (1985), Guyot and seamount morphology and tectonics of the Hawaiian—Emperor elbow by multi-beam sonar, *Marine Geology*, *64*(3-4), 203–215, doi:10.1016/0025-3227(85)90105-7.

Spalding, M. D., C. Ravilious, and E. P. Green (2001), *World Atlas of Coral Reefs*, University of California Press.

Stein, C. A., and S. Stein (1992), A model for the global variation in oceanic depth and heat flow with lithospheric age, *Nature*, *359*(6391), 123–129.

Torres, P. C., J. Madeira, L. C. Silva, A. Brum da Silveira, A. Serralheiro, and A. Mota Gomes (1995), Carta geologica das erupciones historiicas da Ilha do Fogo:revisao e actualizacao,

Torres, P. C., L. C. Silva, A. Serralheiro, and C. Tassinari (2002), Geochronological framework with the K/Ar method of the main volcano-stratigraphic sequences of Sal island-Cape Verde, *Garcia de Orta*, *18*(1-2), 9–13.

Walker, G. P. L. (1992), "Coherent intrusion complexes" in large basaltic volcanoes — a new structural model, *J Volcanol Geoth Res*, *50*(1-2), 41–54, doi:10.1016/0377-0273(92)90036-D.

Wang, X., F. Peine, A. Schmidt, and H. C. Schröder (2011), Concept of biogenic ferromanganese crust formation: coccoliths as bio-seeds in crusts from Central Atlantic Ocean (Senghor Seamount/Cape Verde), *Natural Product Communications*, *11*(0), 1–10.

Watts, A. B., C. Peirce, J. Collier, and R. Dalwood (1997), A seismic study of lithospheric flexure in the vicinity of Tenerife, Canary Islands, *Earth and Planetary Science Letters*, (146), 431–447.

Williams, C. A., I. A. Hill, R. Young, and R. S. White (1990), Fracture zones across the Cape Verde Rise, NE Atlantic, *Journal of the Geological Society*, *147*(5), 851–857, doi:10.1144/gsjgs.147.5.0851.

Wilson, J. T. (1963), Continental Drift, *Sci Am*, *208*(4), 86–103, doi:10.1038/scientificamerican0463-86.

Wright, I. C., P. Stoffers, M. Hannington, C. E. J. de Ronde, P. Herzig, I. E. M. Smith, and P. R. L. Browne (2002), Towed-camera investigations of shallow–intermediate water-depth submarine stratovolcanoes of the southern Kermadec arc, New Zealand, *Marine Geology*, *185*(3-4), 207–218, doi:10.1016/S0025-3227(01)00285-7.

2 Age Progression and Evolutionary Stages of Seamounts in the Cape Verde Archipelago

Tom Kwasnitschka*, Thor H. Hansteen, Colin W. Devey

GEOMAR Helmholtz Centre for Ocean Research Kiel
Wischhofstr. 1-3, 24148 Kiel
*tkwasnitschka@geomar.de

(This article has not yet been submitted for publication. Please note that it contains its own reference list.)

Abstract

The origin of the Cape Verde Archipelago is related to a mantle plume located close to the rotational pole of the African Plate, which is reflected by a weak east-west age progression of the islands' shield stages. The apparently near-stationary Cape Verde Plume creates a unique setting for the study of intraplate volcanism, not only through the islands themselves but also through peripheral seamounts. We present a comparative morphologic study of 11 seamount edifices around the Cape Verde Islands. The easternmost structures represented by the Senghor, Boa Vista, Cabo Verde and Maio Seamounts are morphologically old and partly eroded edifices, suggesting that the seamounts follow the general pattern of westward younging. The distribution of volcanic centers, volcanic rift zones as well as mass wasting processes allow us to place the seamount edifices within a general seven-phase classification scheme of ocean island evolution. Two previously unknown seamounts, Sodade and Tavares Seamounts, are described for the first time, while a third, Maio Rise, was identified to be a separate edifice rather than a platform of Maio Island. Morphological evidence suggests that recent volcanic activity in the northwestern part of the archipelago extends to Sodade Seamount in the far west, and thus does not terminate at the Nola Seamounts. Nola itself was found to be a compound of two separate volcanic edifices. Wave cut terraces of Senghor, Nola East and Nola West seamounts suggest repeated subaerial stages. The age and distribution of Cape Verdean seamounts confirms the concept of an eastward age progression but also offers new insights to the geographic and temporal development of magmatic activity throughout the archipelago.

2.1 Introduction

The most evident morphological expression of oceanic intraplate volcanism are seamounts and, as larger edifices, ocean islands. Subject to the relative motion and aging of the oceanic plate on which they are located, the life cycle of ocean islands is governed by the interplay of volcanic activity and erosion. Hot Spots often form, in geographical terms, a controlled source driving submarine volcanism on a moving plate resulting in an age progression of edifices as demonstrated by e.g. the Hawaii-Emperor chain of islands and seamounts [*Morgan*, 1971; *Clague and Dalrymple*, 1987]. In the case of the archipelagos of the Atlantic Ocean, though, comparatively slower rates of plate motion have led to more complicated age progression scenarios [*Carracedo*, 1999; *Geldmacher et al.*, 2001; *Schmincke*, 2005]. Archipelagos such as the Canary Islands and the Cape Verdes form clusters of very different morphological stages in direct vicinity to each other. Another important difference of Atlantic ocean islands compared to those in the Pacific is the age span of their shield stage (up to 30Ma., [*Geldmacher et al.*, 2005]) which is an order of magnitude greater than the age of the oldest Hawaiian island Kauai (6Ma, [*Carracedo*, 1999]) For these archipelagos, the following stages of ocean island life cycle may be characterized:

1. During the pre-shield stage, feeder dykes intrude the prevolcanic seafloor sediment causing uplift and the creation of effusive sheet flows and pillow mounds. Lateral instabilities of the over-steepened pillow and hyaloclastite slopes lead to collapse events that maintain a steep relief of the growing edifice.
2. An increase in rate and volume of eruptions initiates the *shield stage* characterized by a large basaltic shield. Rising to shallower water depths, and depending on volatile content, the vesicularity increases and explosive eruptive styles lead to summit calderas but also to satellite scoria cones on the volcano flanks.
3. As the volcano breaks the sea surface, the eruptive style changes over surtseyan to strombolian after the vent is permanently sealed from ocean water. The *subaerial stage* is characterized by pyroclastic deposits alternating with lava flows resulting in a steep composite edifice destabilized by intrusion of dykes along fissures and rift systems. In combination with increasing weight of the edifice, this may lead to large-scale slope failures [*Carracedo*, 1999].
4. Drastic decrease of magma supply marks the beginning of the *capping stage*, resulting in an irregular morphology of monogenetic cones and craters on top of the edifice.
5. The *erosional stage* is characterized by a general seizure of volcanic activity while subsidence, erosion and marine abrasion segment the morphology. Extensive shelves may form offshore by deposition of erosional debris.
6. The *post-erosional* stage is a comparatively short period of reactivated volcanic activity, although the small volumes magma produce mostly monogenetic edifices such as cinder cones while lava flows follow already deeply incised valleys. There may actually be several such phases on a single volcano.

7. From this point onwards, the constructional phase of the ocean island is finished and erosion and subsidence diminish the edifice back to sea level forming a flat top. Eventually the edifice sinks back beneath the waves, entering the *guyot stage*.

The Cape Verdean archipelago shows good examples of this type of volcano evolution, as most stages are represented, especially taking into account the number of seamounts and large submarine volcanic edifices equaling the number of major islands. Below we present a comparative morphological study of Cape Verdean seamounts, categorizing the edifices in analogy to the above scheme.

2.2 Regional Setting

Situated between 15°N and 17°N, 450-800km off the West African coast, the Cape Verdean archipelago is the culmination of the largest morphological high of any ocean basin, the Cape Verde Rise [*Lancelot et al.*, 1978; *Sleep*, 1990], which is attributed to a deep-seated mantle plume [*McNutt*, 1988; *Holm et al.*, 2006]. At the same time, the Cape Verdes lie in the vicinity of the rotational pole of the African Plate [*Pollitz*, 1991]. Therefore none of the islands may have experienced a shift away from their magmatic source more than a few hundred kilometers if any [*Burke and Wilson*, 1972; *Morgan*, 1983], manifested in a weak and highly overlapping age progression [*Holm et al.*, 2008]. Trace element and isotope signatures indicate a heterogeneous mantle source [*Davies*, 1988; *Gerlach et al.*, 1988; *Jørgensen and Holm*, 2002; *Doucelance et al.*, 2003; *Plesner et al.*, 2003; *Holm et al.*, 2006; *Mata et al.*, 2006; *Holm et al.*, 2008; *Barker et al.*, 2012] that may also influence the geographic distribution of magmatic activity. The oldest known rocks of the archipelago are exposed on the islands of Sal and Maio at 25.6 and 16Ma, respectively [*Holm et al.*, 2006]. The islands lie on Mesozoic oceanic crust 120Ma to 140Ma old, as indicated by Mesozoic sea floor spreading magnetic anomalies M0-M16 [*Müller et al.*, 2008] and nearby IODP sites [*Lancelot et al.*, 1978; *Faugeres et al.*, 1986]. Whether crustal fractures influenced the geometry of the archipelago is not clear [*Williams et al.*, 1990]. However, outcrops of pre-island MORB-type oceanic crust on Maio Island strongly suggest that vertical tectonics played a role in the formation of the archipelago [*Mitchell et al.*, 1983].

Two chains of islands developed westward giving the archipelago its “horse shoe” geometry (Figure 2-1). The northern chain comprising São Nicolau, Santa Lucia, São Vicente ends with Santo Antão in the northwest, with its latest reported activity at 0.09Ma [*Plesner et al.*, 2003]. The southern chain is formed by Sal, Boa Vista, Maio, Santiago, Fogo and Brava, where Fogo shows the only contemporary volcanic activity on any of the islands, erupting on average every 20 years in recorded time [*Torres et al.*, 1995]. However, frequent volcano-tectonic earthquakes are recorded offshore to the west of both Santo Antão and Brava islands [*Grevemeyer et al.*, 2009], testifying to current activity. The parallel westward age progression of these chains becomes evident in the island topographies. Sal, Boa Vista and Maio are eroded almost down to sea level and only former volcanic necks form residual highs.

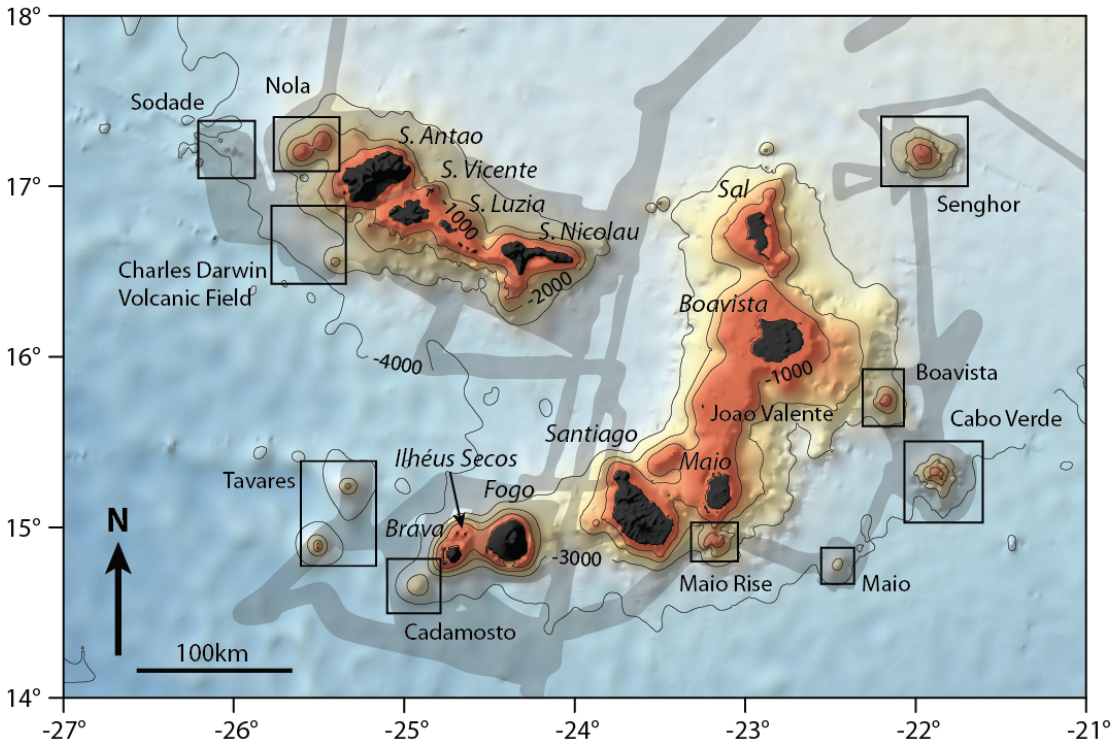

Figure 2-1 *GMRT map of the Cape Verdean archipelago including the multi beam bathymetry data available for this study (shaded grey). Boxes mark the extent of the maps of individual seamounts. Islands are marked black.*

São Nicolau, Santa Luzia and São Vicente also show the effect of substantial erosion deep into the island core but still have substantial relief (Ancochea et al., 2010). The islands of Santiago and Santo Antão are deeply incised by erosion (e.g. Mitchell-Thomé, 1972) but the general geometry of the shield stage still is evident. Fogo is an active stratovolcano with steep flanks, its morphology only interrupted by a large collapse scarp to the east. The island of Brava west of Fogo, which already entered the posterosional stage, is an exception to this trend. Just north of Brava, the Iléus Secos form the remains of an eroded island of which only residual morphologies still rise above sea level.

Beneath sea level, the two island chains show an interconnection among their volcanic edifices forming a common shelf, the only exception being Fogo and Brava. This shelf is particularly broad and shallow between the most eroded islands from Maio to Sal, attesting to their posterosional development stage. The João Valente Shoals rise to only 14 m beneath the waves and likely constitute a drowned island in its guyot stage.

The perimeter of the two island chains is lined by a number of seamounts displaying an equally varied spectrum of edifice sizes and erosional stages as the islands themselves. Not all of these seamounts can be directly related to one of the island chains, however (Figure 2-1). Senghor, Cabo Verde and Maio seamounts are clearly detached from the compound edifice of the southern chain and reside solitarily on the Cape Verde Rise. Boavista Seamount and Maio Rise are located on the flank of the southern chain. Cadamosto Seamount shows a morphological link to Brava although the platform around Fogo and Brava has not yet merged to a compound edifice. Similarly, Nola Sea-

mount and the Charles Darwin Volcanic Field are located on the flank of Santo Antão, the former along the axis of the northern chain, the latter perpendicular to it. Both chains have a western projection down the slope of the Cape Verde Rise, in the form of solitary, less conspicuous edifices, both of which are described here for the first time. Sodade Seamount continues the northern chain westward, lying just south of the island chain axis, while Tavares Seamount continues the clockwise arc of the southern chain whose direction of propagation thus aligns with that of the northern chain. This total of 11 seamounts forms the subject of this study.

2.3 Previous Work

Previous studies of Cape Verdean Seamounts and submarine morphology focused on the island slopes of the northern chain and the southwestern chain segment, where a number of slope failure events were identified and the extent of their submarine deposits was mapped [*Masson et al.*, 2008]. According to this study, the dominant submarine features are landslide scars which may feature erosional channels in their upper part, partly attributed to the onset of volcanic activity triggered by the failure event, the proximal and distal deposits of debris flows including large-scale sediment waves and contour parallel sagging features. The predominant undisturbed features are volcanic satellite cones on the upper slope of islands.

In contrast to the islands, no absolute ages have yet been obtained for any of the submarine edifices of the Cape Verdes, and thus only very rough relative ages have been inferred from morphology and their geographic position relative to dated islands. Initial dredge sampling of Cape Verde seamounts was undertaken on RRS CHARLES DARWIN cruise 85 [*Hill*, 1985]. So far, particular attention has been paid to Cadamosto Seamount, which not only shows the most vigorous seismic activity of the whole archipelago [*Grevemeyer et al.*, 2009] but is largely composed of phonolitic rocks in contrast to the mafic volcanism dominating the islands [*Barker et al.*, 2012]. As part of integrated biological, biogeochemical and geological studies (P320/2, [*Hanel et al.*, 2010], M79/3, [*Wang et al.*, 2011]) we performed reconnaissance sampling of Senghor, Boavista, Cabo Verde and Cadamosto seamounts as well as throughout the CDVF. Detailed sampling using ROV dives and dredging was performed during R/V METEOR cruise 80/3 in 2010 [*Hansteen*, 2010]. The three former seamounts yielded greatly altered rocks which generally confirmed our hypothesis on their comparatively old ages, while fresh glassy samples from Cadamosto, CDVF and Sodade confirmed relatively recent activity.

2.4 Data Acquisition and Processing

The data presented here is primarily based on multibeam swath bathymetry and backscatter data gathered over the last ten years. During RRS CHARLES DARWIN cruise 168, the slope and foothill of the northern chain were surveyed using a Kongsberg EM12 echo sounder [*Masson et al.*, 2008]. The same cruise added coverage to a data set of the southern chain between Santiago and Brava surveyed in 2004 during R/V METEOR cruise 62/3 using an Atlas Hydrosweep, 59 beam swath echo sounder. Also during the CD168 cruise, the field of young volcanic edifices southwest of Santo Antão was discov-

ered that gave its name to the Charles Darwin Volcanic Field (CDVF). R/V POSEIDON cruise 320/2 mapped the summit areas of Senghor Seamount using an Elac Seabeam 1050 mobile echo sounder down to 1500m depth, but although the data was used for preparation of further mapping, it was not included in the maps of this study. R/V METEOR cruise 79/3 mapped Senghor, Boavista and Cabo Verde Seamounts as well as the CDVF using a Kongsberg EM 120 echo sounder of 191 beams. The same equipment was used during R/V METEOR cruise 80/3 to map remaining parts of Senghor, Boavista and Caboverde seamounts in addition to Maio Seamount, Maio Rise, Cadamosto, Tavares as well as Nola and Sodade seamounts including most transits. On M79/3 a Sub-Atlantic Mohawk class ROV was deployed to the summit region of Senghor Seamount and along its upper flanks to 700m depth, providing visual clues on the terrain, erosional features and biology. M80/3 carried the Schilling working class ROV Kiel 6000 used to transect edifices between 4000m and 600m depth providing visual coverage and rock samples of Senghor, Cabo Verde, Maio Rise, Cadamosto, CDVF and Nola Seamounts.

The Kongsberg echo sounder data were received as raw .all files and processed using QPS Fledermaus v.7.3.2. The data of the M63/2 cruise were received as a pre-edited grid of 100m x 100m resolution [*Grevemeyer et al.*, 2009] and merged with overlapping data sets. Since the great depth span of several edifices led to highly varying native resolution of the swath bathymetry data, the portions deeper than 3000m were gridded to a 100m x 100m grid resolution, the interval between 3000m and 1000m at 50m x 50m or 25m x 15m based on data density, whereas shallow mountaintops of Nola and Senghor seamounts allowed even for 10m x 10m resolution. Upon extensive post processing, CDVF was gridded to 20m x 20m resolution, despite its great depth. Different grids where stacked and merged using Global Mapper v.13 and plotted in Surfer v.10. Backscatter of M79/3 and M80/3 data was processed using QPS FMGT and merged with existing maps of the M62/3 and CD168 cruises.

2.5 Rationale for Bathymetric Interpretation

The maps were visually interpreted and annotated. The symbology aims to clarify common features to facilitate comparison (Figure 2). As many features of the bathymetric charts are subject to interpretation, we refrained from quantitative assessment of e.g. the volume of landslides or the number and geometric distribution of volcanic centers and focused on a qualitative description and comparison of features. Below follows an explanation of the editing effort.

The extent of the volcanic edifices was measured from bathymetric profiles. A dashed line indicates the perimeter of the edifice as the first upward departure from the relief (i.e. change of slope) of the surrounding ocean floor. Especially in cases where the volcano rests on an island flank, the geometry departs from a circular shape and the true extent of the edifice is ambiguous due to sediment cover up- and downslope as well as erosional channels on the sides of the edifice.

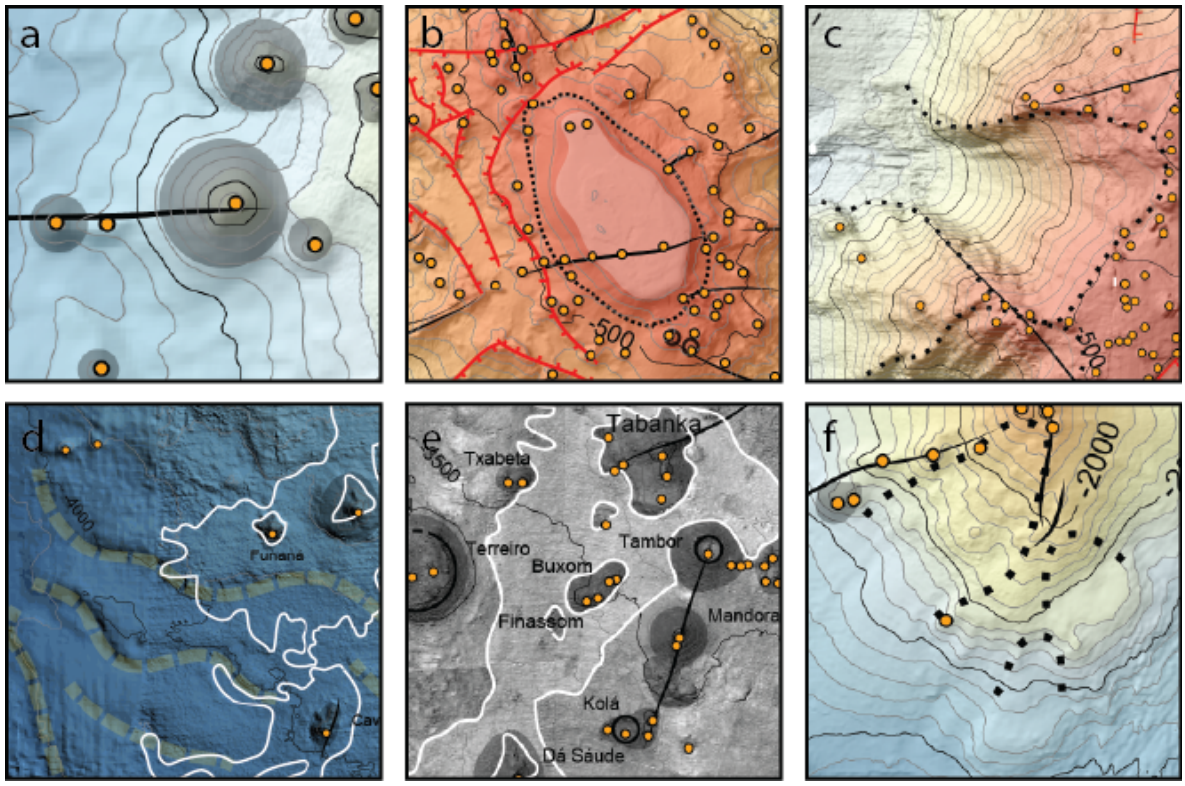

Figure 4-2 *Samples of the symbology used on interpretive maps. a) solitary cones (grey) and smaller volcanic vents (yellow) linked by a volcanic lineament (black); b) the flat summit plateau (white) of Senghor Seamount including the erosional apron (densely dotted) and the surrounding fault systems (red); c) a mass wasting scar on Boavista Seamount (sparsely dotted); d) sediment waves (yellow) and volcanic flows (white) at CDVF; e) the backscatter image of young volcanics at CDVF as well as ring shaped cones (black); f) three slumps on the southern sector of Cadamosto Seamount (sparsely dotted).*

Eruptive centers on each edifice were marked if they show a clear morphological expression, even if they did not produce cones of significant volume or were merely preserved as residual complexes such as former volcanic necks whose lavas are more resistant to erosion.

Solitary volcanic cones were marked in cases of undisturbed satellite cones downslope from the intermediate flanks of major edifices, which have a significant volume relative to their surroundings [*Gee et al.*, 2001]. If they maintained a visibly circular cone shape, they were marked with circles, whereas clusters of compound cones were outlined along their assumed irregular maximum extent. Several cones show circular wall structures with a large crater-like central depression reminiscent of subaerial tuff rings. Regardless of their possible formation processes these structures were marked as ring type cones as they are clearly morphologically distinct from adjacent classical cones.

Dyke remnants and volcanic lineaments were marked based on the presence of volcanic ridges which clearly stand above the surrounding slope terrain or, in their lower extension, line erosional channels. As dykes propagate through the country rock and may only form discontinuous surficial expressions, lineaments were either drawn as solid or broken lines. Chains of cones, ideally even showing aligned ridges of their own were linked if they follow a direct projection of clearly visible up-slope ridges of the

main volcanic edifice. The difficulty, especially in areas of the seamount foothill, lies in the discrimination of volcanic lineaments and erosional channels as the radial symmetry of dykes often coincides with the downslope gradient followed by erosive forces. Therefore, we only marked the most prominent ridges in the range of seamount foothills.

Faults were marked in places where subsidence and/or lateral displacement seemed to have produced offsets in the terrain surface with a clear height contrast, i.e. in cases where the direction of faulting could be inferred. If the faults involved movement of part of the flank downhill, they are addressed as a slump.

Landslide scars mark major slope failure events like debris avalanches that significantly altered the volume and appearance of the volcanic edifice. Since the resolution of the multibeam data does not always resolve the extent of the debris flow fan downslope, only the negative relief changes resulting from the failure were mapped along the headwall and lateral cliffs including those created downslope by erosion through debris flows. This includes slumps of seamount slopes [*Moore et al.*, 1989]. In contrast to slope failure scars left by debris avalanches, the rock bodies in slumps are still in place and have not experienced significant horizontal displacement.

Sediment waves are not only generated on the island flanks [*Masson et al.*, 2008] but also on the foothill of seamounts. Small slumps of < 10km lateral extent were included in this category as it is often unclear whether these seafloor features represent constructive or destructive processes.

Backscatter (i.e., returned signal intensity) from multibeam data provides valuable additional information on the degree of compaction of the sea floor [*Le Bas et al.*, 2007]. Areas of high backscatter correspond to either bare rock, surfaces coated by precipitates or coarse gravel whereas low backscatter areas mark softer sediment, which often corresponds to marine background sedimentation. The quality of such backscatter may vary with the distance from the swath center and the angle of incidence on a submarine slope. Particularly, surfaces of high backscatter on eastern seamounts are often coated by manganese crusts [*Wang et al.*, 2011], as ground truthing by ROV and dredge samples proved. Therefore the only features discriminated by backscatter were young lava flows at CDVF and Sodade, where they clearly contrasted with adjacent marine background sedimentation.

2.6 Description of Seamounts

Eleven seamounts and incipient volcanoes were chosen from the available data set. For clarification, they are not discussed in geographical order but by their development stage to which we aligned them based on their morphological characteristics (see below).

2.6.1 Charles Darwin Volcanic Field

The CDVF is situated on the southwestern slope of Santo Antão, at depths between 4000m and 3000m. The field consists of thirteen major single or compound volcanic cones (Figure 2-3), which have been named after ensemble setups of traditional Cape Verdean music. They are surrounded by a number of smaller cones that are partly buried particularly upslope of the field by two overlapping deposits of mass wasting events associated with the subaerial Tope de Coroa and Tarrafal landslide scars. To the east, CDVF is lined by a channel dug by turbidity currents mobilized following the main slope failure events [*Masson et al.*, 2008]. The observation that the entire field is crossed by sediment waves and small-scale slumping structures suggests that the cones themselves postdate the main failure events. To the northeast of CDVF, following the 4000m contour, a morphologically older cone has been buried on its upslope flank by presumably debris flow deposits forming a terrace. Its downslope sector has a hummocky irregular surface contrasting with the surrounding smooth contours. Towards the east, two faults attest to subsidence of the terrain. The larger, semi-circular fault may be interpreted as a slump, exposing a headwall of 20m height that may result from destabilization of the adjacent cone by sediment loading.

Taking into account the distribution of smaller upslope cones, many of which were previously interpreted as blocks belonging to the debris flow [*Masson et al.*, 2008], many cones of CDVF align along lineaments pointing towards the western summit area of Santo Antão. Just above the main field, the lineaments fork into two components. A SSW-oriented branch aligns the Tambor, Mandora and Kolá volcanoes, possibly extending towards the Cavaquinho cone downslope. A weaker parallel component points along a ridge towards Koladera. A second, SW-oriented branch includes the Tabanka group of cones, possibly the Txabeta volcano and the Batuku compound cone. A parallel line is formed by linking Funaná, Dá Sáude and Kolá, but this connection is not well developed.

Most of the volcanoes have a circular cone-shaped geometry, whereas Tambor, Kolà and Terreiro have clear circular depressions. Tambor and Terreiro have constructive morphologies relative to the surrounding terrain, the latter covered by the morphologically younger Kumpánia and Profeta cones. Kolá, on the contrary, is a morphological depression within a group of older, smaller cones (Kolá A-C), which were eroded by the excavation of the crater. The Tabanka group reveals a succession of eruptive activity as well, as the eruption centers Kommandanti di Terreiro, Raninha de Agasalho, Corneta and Rei di Agasalho overlie each other.

All structures are covered by a 50-150cm thick layer of pale brown to white foraminfer ooze as verified during ROV dives. Among the Batuku group, no samples were recovered from Terreiro due to the lack of outcrops and a thick layer of ooze. Kumpania yielded samples of mafic spatter and coarse-grained plutonite fragments but also manganese coated, carbonate cemented volcaniclastic breccia.

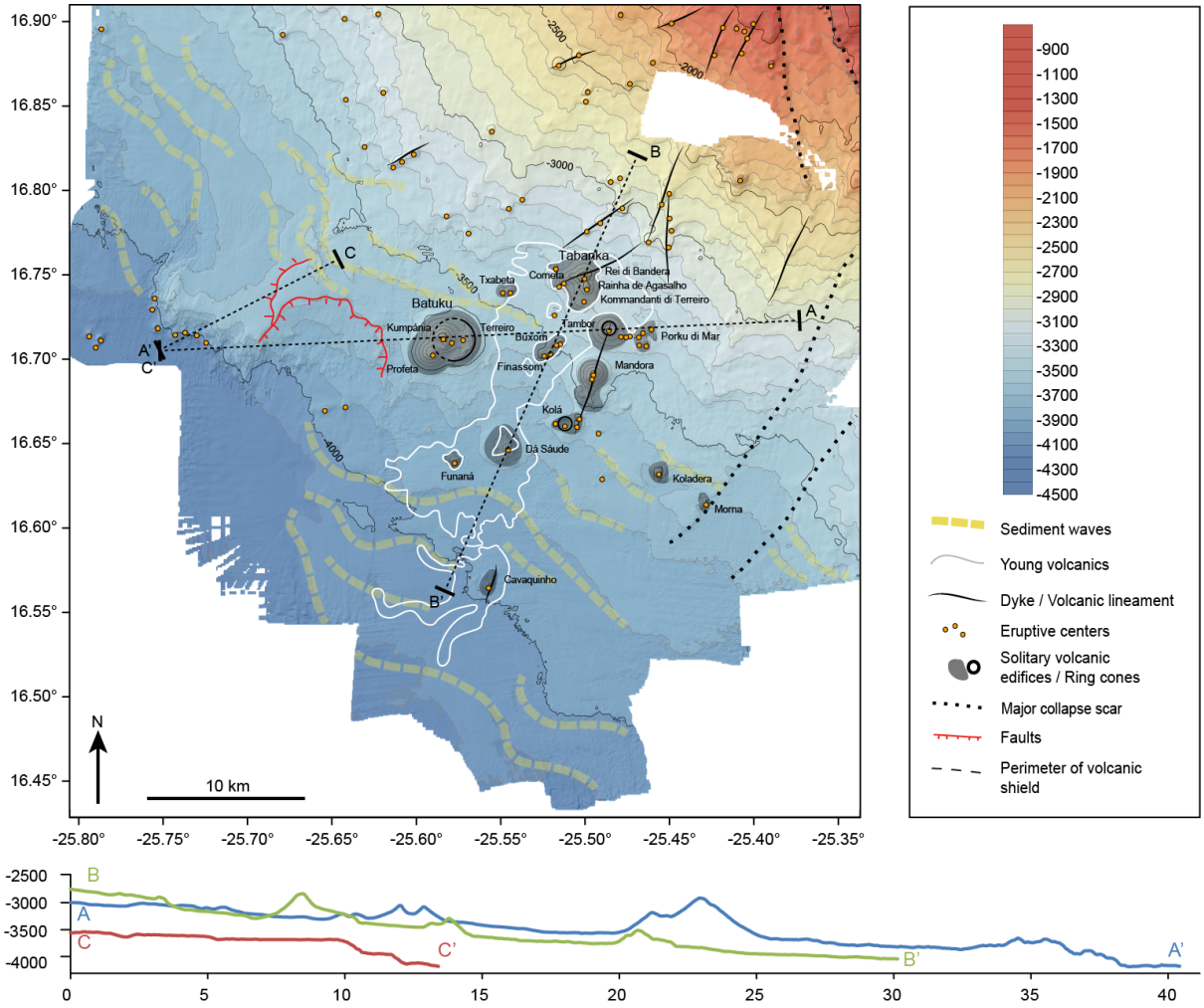

Figure 2-3 *Structural interpretation of the CDVF and 2x height exaggerated sections.*

Microvesicular, fresh (partly glassy) and nearly aphyric lava and angular volcaniclastic breccia were recovered from Corneta and Rei di Bandera, which display a state of preservation similar to the Batuku group. Dredge samples of Kommandanti di Terreiro included vesicular phonolitic lava with glassy crusts. Tambor is also covered by ooze, but its inner crater shows a young morphology of steep cliffs exposing alternating sequences of dense clasts of lava containing plutonic fragments. Kolá has an even more complicated inner crater facies of highly fragmented layers of juvenile pebbles mixed with coarse crystalline gabbro blocks and lava country rock, affected by various signs of highly energetic lateral transport such as rounding by abrasion. The detailed description of Tambor and Kolá is the subject of a separate study presented in Chapter 4 [*Kwasnitschka et al.*, in prep.]. Koladera is a large cone edifice that suffered collapse of its entire western flank leaving an 80m high headwall of volcaniclastic sediment exposed. The mafic pillow lava fragments recovered from the base are up to 50 vol.% vesicular and contain 15 vol.% plutonic fragments. Much of the upper sequence consists of scoriaceous agglutinates or carbonate-cemented moderately vesicular scoria. Analysis of joints exposed at edifices of the CDVF reflects local volcanotectonic processes.

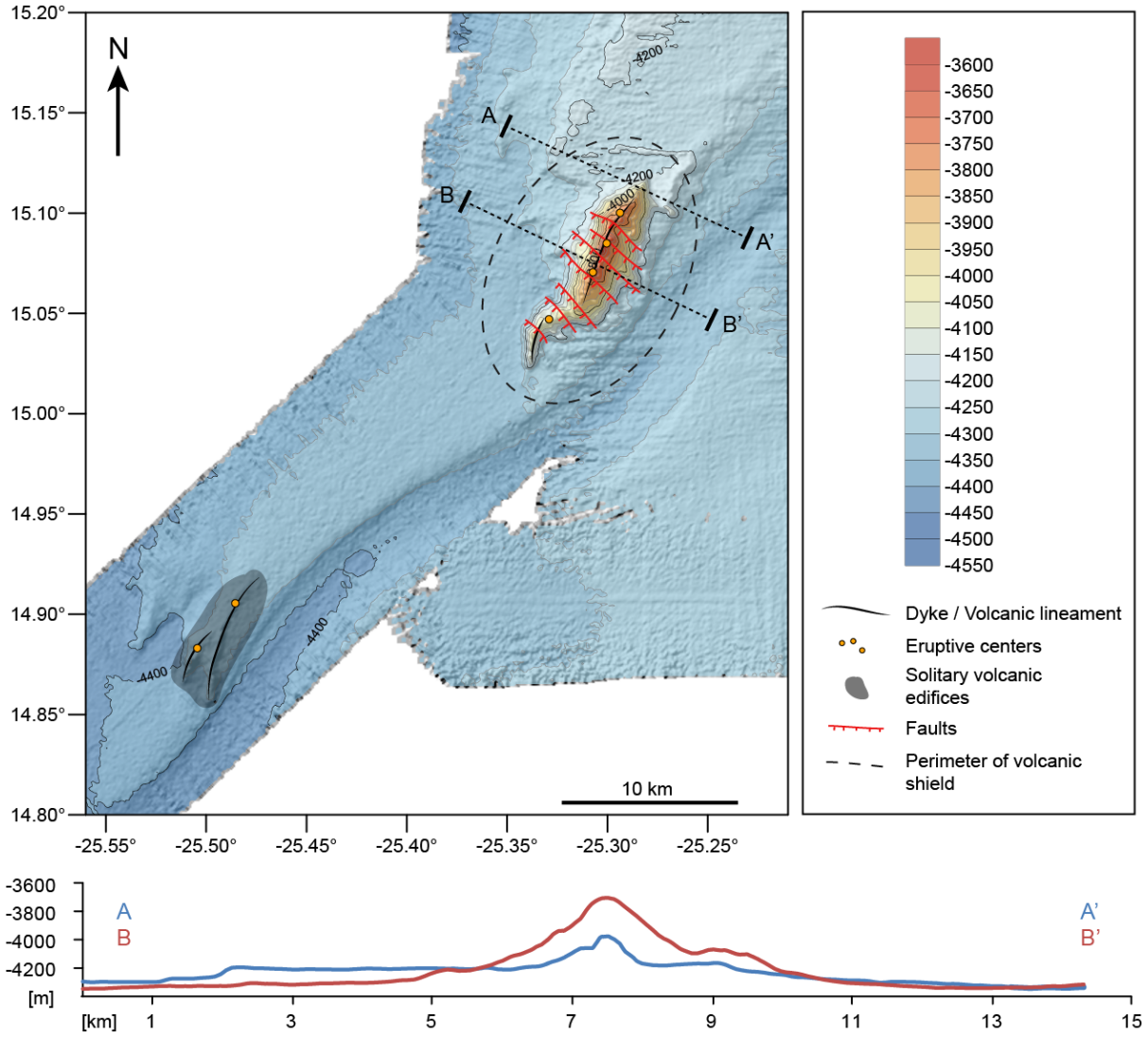

Figure 2-4 *Structural map of Tavares Seamount including 2x vertically exaggerated profiles.*

The central part of the CDVF between Tabanka, Batuku and Mandora is covered by a very high backscatter deposit with sharp boundaries and lobate downhill flow patterns (Figures 2-2e & 2-3). ROV dive 059 revealed that this signal correlates with a hummocky field of lava flows. The observation that the lavas drape over the terrain of sediment waves supports the idea that CDVF postdates the slope failure events of western Santo Antão and may be of relatively recent age. As they also surround the highest parts of the Tabanka group, they must, at least in part, originate here, although it may be possible that the Dá Saude and Cavaquinho volcanoes gave rise to their own lava flow fields that slightly overlap on the backscatter.

2.6.2 Tavares Seamount

Informed by undulations of the GMRT base map of the area, which also contains gravity data through its Gebco V2 components [*Smith and Sandwell*, 1997; *Jena et al.*, 2012], two gravity anomalies were mapped on a transit during cruise M80/3. The northern target called Tavares Seamount (after Eugénio Tavares, poet of Brava Island) is a narrow ridge of 12km length, 3km width and 500m height. It is situated at the tip of a 7km wide and at

least 25km long plateau with pronounced edges reminiscent of sheet flows (Figure 2-4). Tavares is segmented by a sequence of southeasterly striking faults that shifted the southern ridge segment by 1200m towards NE, possibly due to regional crustal stress [*e.g., Ali et al.*, 2003]. The low ridge occurring 26 km to the southeast does not have a pronounced morphology and appears to be either a short lava flow or a fissure eruption, with its altimetry footprint possibly due to subsurface intrusions. Both objects are affected by heavy sedimentation from the basin between the northern and southern chain, as a flow channel along their eastern flanks documents. Both show no signs of peripheral volcanic activity or a connection to nearby volcanic complexes. Multibeam backscatter merely reflects the comparatively steep relief of Tavares on an otherwise flat sedimentary plain.

2.6.3 Sodade Seamount

Sodade Seamount was discovered during cruise M80/3 while investigating an undulation on the GMRT map we attributed to a gravity anomaly (Figure 2-5). It is situated some 40 km northwest of Nola, on a morphological high rising 200m above the surrounding seafloor and outlined by the 4000m depth contour. In combination with a number of solitary cones in between them, this small rise may be seen as a weak morphological link to Nola. Sodade has an oval shape oriented NNW-SSE with a maximum diameter of 15km at a height of 1100 m above the seafloor. Volcanic lineaments follow two directions (E-W and N-S) crossing through the main edifice and upon which are situated a great number of satellite cones within a radius of 5km of the summit, lining the entire perimeter except the northwestern sector, the direction in which the morphological high ceases. Most of these satellite cones are compound cones, whereas four of them have large central depressions analogue to Tambor and Kolá in the CDVF. A fifth “crater” exists 10km west of the summit but does not show substantial relief above the surrounding seafloor. West of Sodade, the sea floor subsides stepwise in a series of south facing scarps striking E-W towards the summit. A number of volcanic cones to the west suggest that these faults served as pathways for magmatism.

The main edifice of Sodade above a depth of 3500m shows a steep morphology with a number of arcane, spinal shaped ridges leading to the top. The southern flank shows a large slump while the northern and eastern flanks contain small channels, which may attest to subordinate slope failure events. No debris fans are visible beneath these flanks. The mountain is surrounded by a field of high backscatter that forms lobate downhill flow structures towards the western lower flank. Analogous to CDVF, this area is interpreted as covered by young volcanic deposits with a thin cover of marine background sediment.

An ROV transect of the western flank showed that Sodade forms a single giant pillow mound reaching all the way up to its crest. Sheet flows were not observed. Samples yielded glassy basanitic and nephelinitic pillow fragments with vesicles between 1mm and 4mm size. Manganese crusts cover some of the northeastern peripheral cones.

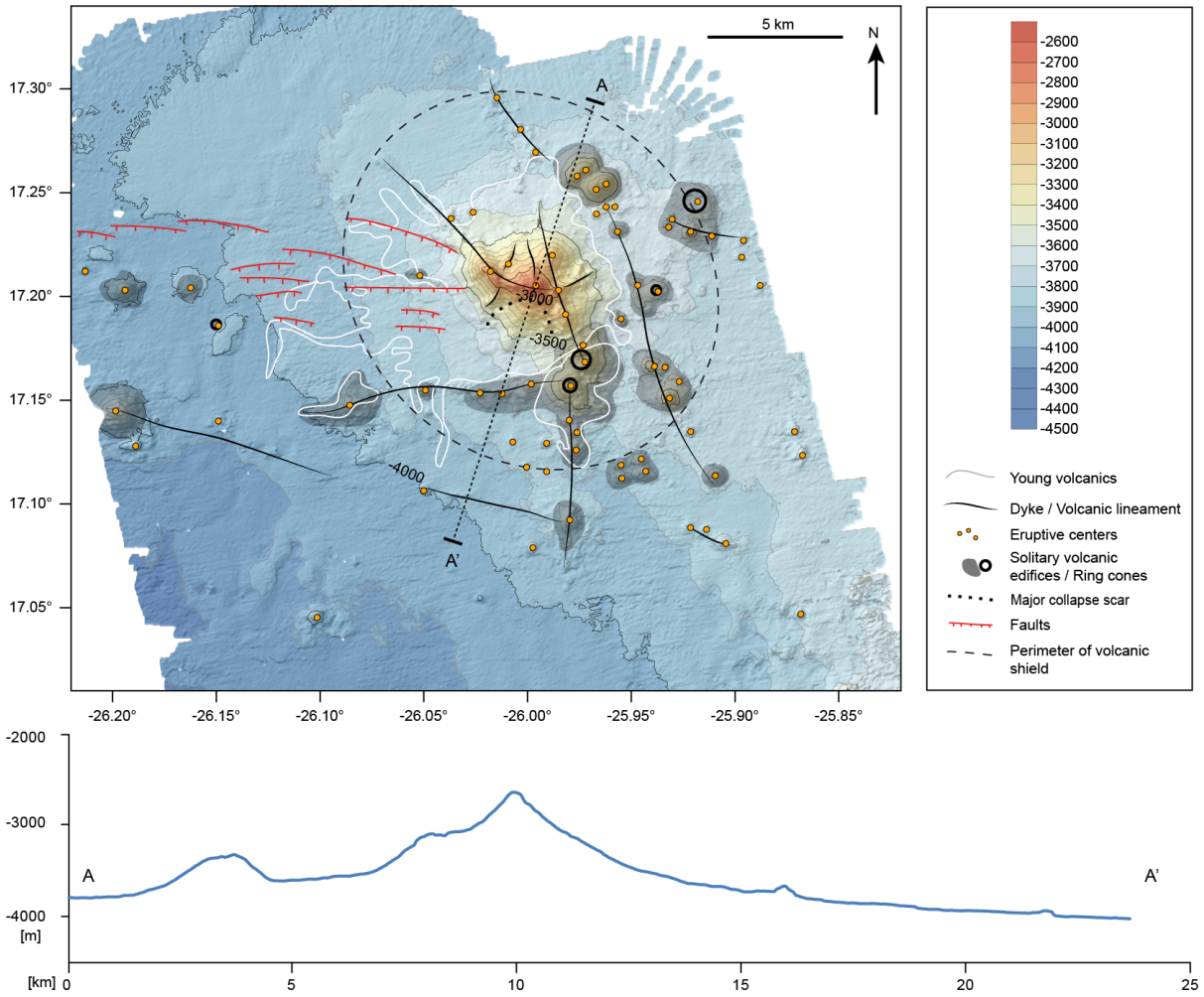

Figure 2-5 *Structural map of Sodade Seamount including 2x exaggerated cross section.*

2.6.4 Cadamosto Seamount

Cadamosto Seamount forms the western end of the morphological high of the southern chain rising above the 4000m depth contour (Figure 2-6). This contour also marks the extent of the lower Cadamosto shield, which elliptical shape connects it to Brava. Apart from the main edifice rising 2500m above the seafloor with a basal diameter of about 30km, the most striking feature is a large field of composite cones 7km in diameter situated on the saddle between Cadamosto and Brava. Volcanic lineaments throughout this field but also on the flank of Brava likely link both edifices. Cadamosto itself is segmented by a number of lineaments, which project onto the lower flanks as satellite cones (i.e., flank eruption centers). The flanks are incised by a number of slope failures. A debris avalanche on the northern flank left a broad depositional fan.

It is likely that the western flank experienced mass wasting as it shows, in contrast to the eastern flank, a number of smaller channels and gullies in its upper part between two volcanic ridges whereas the lower two thirds are very smooth and devoid of cones although there is no apparent debris fan.

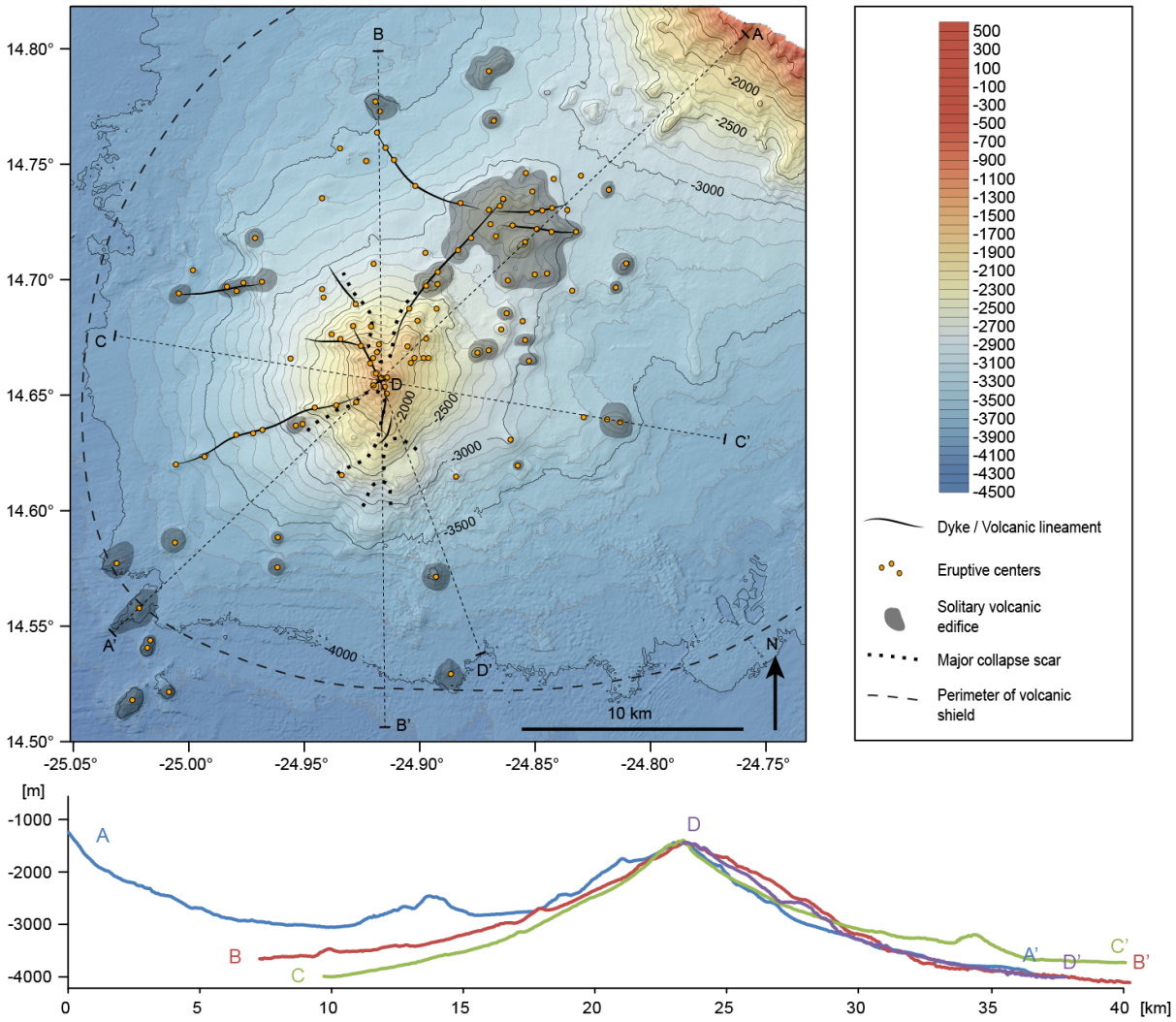

Figure 2-6 *Structural map of Cadamosto Seamount including 2x exaggerated cross sections.*

The southwestern sector is considerably more rugged and likely affected by slumping. A debris fan stretches from the lower scarp of the slump around the 2500m depth contour down to the 3600m contour. Two clearly visible slumps occurred on the southern sector, with well exposed headwalls and their talus bodies deformed to flats on the slope. The summit region is comprised of a complicated cluster of several eruption centers forming cones and caldera structures several hundred meters wide and up to 60m deep. Although they could not be resolved well using swath bathymetry, two ROV dives revealed a complex internal structure of sheet flows intercalated with dykes. The summit is dominated by apparently young pahoehoe lava flows of basaltic and phonolitic composition. Samples from the inner crater walls show signs of hydrothermal alteration. Fresh samples of typically phonolitic lava flows are black and glassy with patchy alteration and are nearly aphyric. Dredge samples of the cone field between Cadamosto and Brava are also phonolitic but are phyric (<10 vol%) containing feldspar, foides, clinopyroxene, amphibole and sphene.

2.6.5 Maio Seamount

Maio Seamount has the simplest structure of all Cape Verde seamounts and, together with Senghor, it is the most remote regarding its distance to the two island chains and the absence of smaller edifices linking it to them (Figure 2-7). Situated 90km southeast of Maio Island, it rises from otherwise undisturbed seafloor showing negligible elevation of its surrounding terrain and is devoid of any peripheral volcanic centers. Its basal diameter is 20km; it rises as a circular cone 2100m above the 4000m isobath. Small channels less than 500m wide uniformly line its flanks running straight down the slope gradient to the foothill. Lines of high backscatter at their bottom end in small patches at the lower end, likely representing erosional fans.

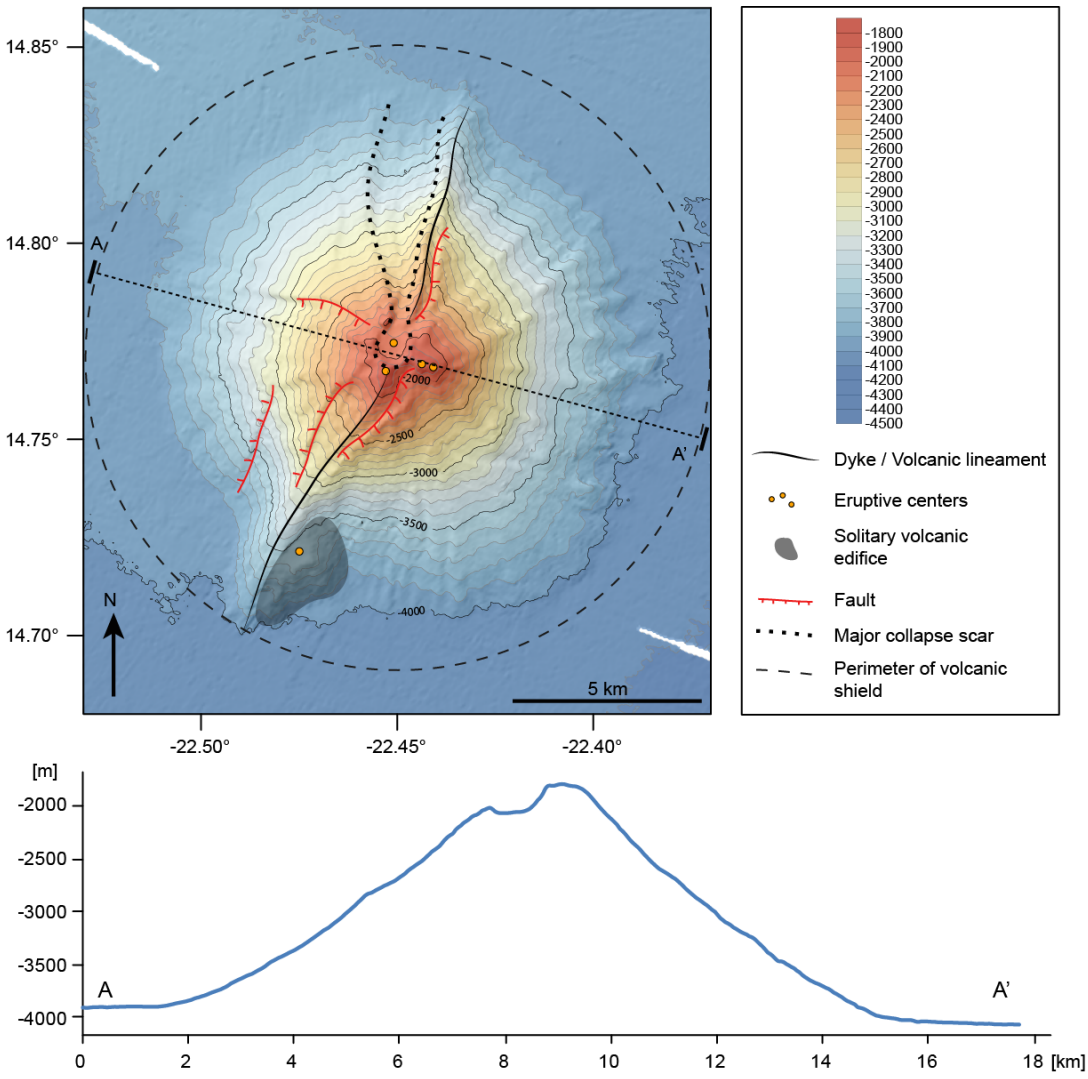

Figure 2-7 *Structural map of Maio Seamount including a 2x exaggerated cross section.*

The only striking feature is a prominent volcanic ridge bisecting Maio Seamount from NNE to SSW, interrupted by a 1000m wide summit caldera, which opens towards a narrow landslide scar lining the western edge of the ridge. The flanks show several signs of subsidence along faults facing downslope. These are, with one exception on the western flank, adjacent or parallel to the ridge. Four volcanic centers were mapped on the summit including the caldera. A fifth may lie on the southern foothill of the ridge, where the

latter is flanked to the east by a small plateau that may either have been formed by a volcanic cone or by slumping of the parental edifice. Dredges across the summit yielded thick crusts of manganese oxides but only a marginal, strongly altered volcanic rock sample, providing evidence for a comparatively old age.

2.6.6 Cabo Verde Seamount

Cabo Verde is a large solitary seamount 150km east of Maio Island. Its only morphological connection to neighboring edifices is by a 100km wide seafloor elevation of 50m towards a more prominent sea floor bulge off Boavista Seamount, 35km to the northwest (Figure 2-8). At a basal diameter of 35km outlined by the 3900m contour, it rises 3390m to its peak at 511m water depth. Its shape is slightly star shaped due to the presence of three major directions of volcanic lineaments, two of which radiate from the summit towards NW and NNE while a third lineament passes through the volcano striking NNW-SSE. At a radius of 9km from the summit, or roughly between 3500m and 2000m water depth, numerous satellite edifices line its flanks and concentrate along radial lineaments expressed as ridges. Above the 1000m depth contour, clusters of small eruption centers mark a summit plateau of 5km diameter and a relief of 280m. Some of the major lineaments may protrude into the summit area as indicated by chains of small cones aligned to their axis.

The most striking morphological feature of Cabo Verde Seamount is a pair of long and deep landslide scars aligned to the NNW-SSE striking lineament. The southern scar reaches all the way into the central summit area, terminating in a semi-circular caldera of 1.2km diameter and 220m depth. The opposite scar leading down the northern flank features a number of smaller channels incising its headwall. Another, less deep but equally voluminous landslide scar cuts into the northern flank. A fault running down the volcano flank parallel to the NNW scar indicates that it is in the process of broadening as its western rim seems to have slumped into the trench of the scar. The western and eastern flanks are lined by slope-parallel faults, which cannot be attributed to a preferred direction of failure. These flanks are also lined with erosional channels corresponding to high backscatter areas exposing smaller radial ridges, yet they are subordinate in volume to the large events. At the eastern foothill between 3800m and 4000m depth, a succession of sediment waves formed within a narrow segment. We attribute these to turbidites of one or more mass wasting events upslope.

An ROV dive inside the southern scar into the summit caldera yielded insights to the volcanic core complex, exposing sheet flows, pyroclastic and hydroclastic rocks cut by dykes. Rock samples of the southern collapse scar comprise basanitic and tephritic lavas and hyaloclastites of varying grades of alteration and a coating of manganese crust up to several centimeters thick. Rounded vesicles are mostly filled by zeolites or carbonate cement. A dredge from the center of the seamount yielded fragments of pillow lavas, slightly rounded boulders, and a polymict volcaniclastic breccia. Rocks are dominantly of basaltic composition, partly with fresh olivine. Dredges from the northeast flank contained highly vesicular and strongly altered basaltic breccia attributed to cinder cone deposits.

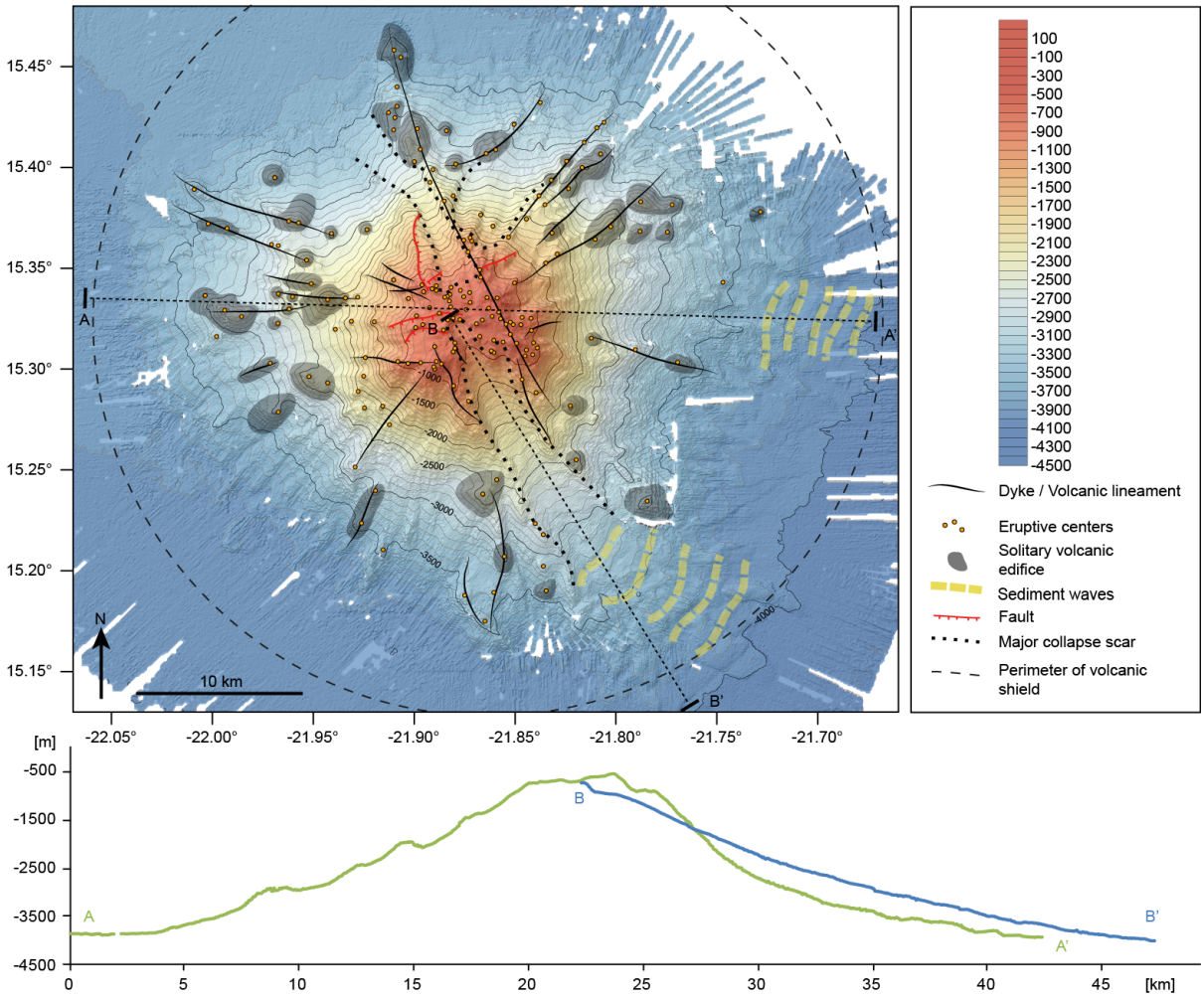

Figure 2-8 *Structural map of Cabo Verde Seamount including 2x exaggerated cross sections.*

2.6.7 Boavista Seamount

Boavista Seamount lies 65km to the southeast of the island of the same name, at the foot of the longest continuous slope of any Cape Verdean island. As a result, deep erosional channels cut into the gentle slope of 2° which likely existed before the construction of the seamount edifice. The edifice has a maximum basal diameter of 24km and rises from its foothill at 3000m to 400m depth where it forms an extensive double plateau separated by a saddle of low relief (Figure 2-9). A large number of smaller volcanic vents creating a hummocky relief concentrate in two areas at its northern and southern ends, which are elevated by 50m and connected by the saddle of comparatively smooth terrain. Two volcanic lineaments run tangentially along the northern and southern flanks, lined by volcanic centers on the summit. The volcano is strongly incised by four giant flank collapse scars. As a consequence, only in the southeastern, unaffected flank a number of satellite edifices remained between depths of 1500m and 3000m.

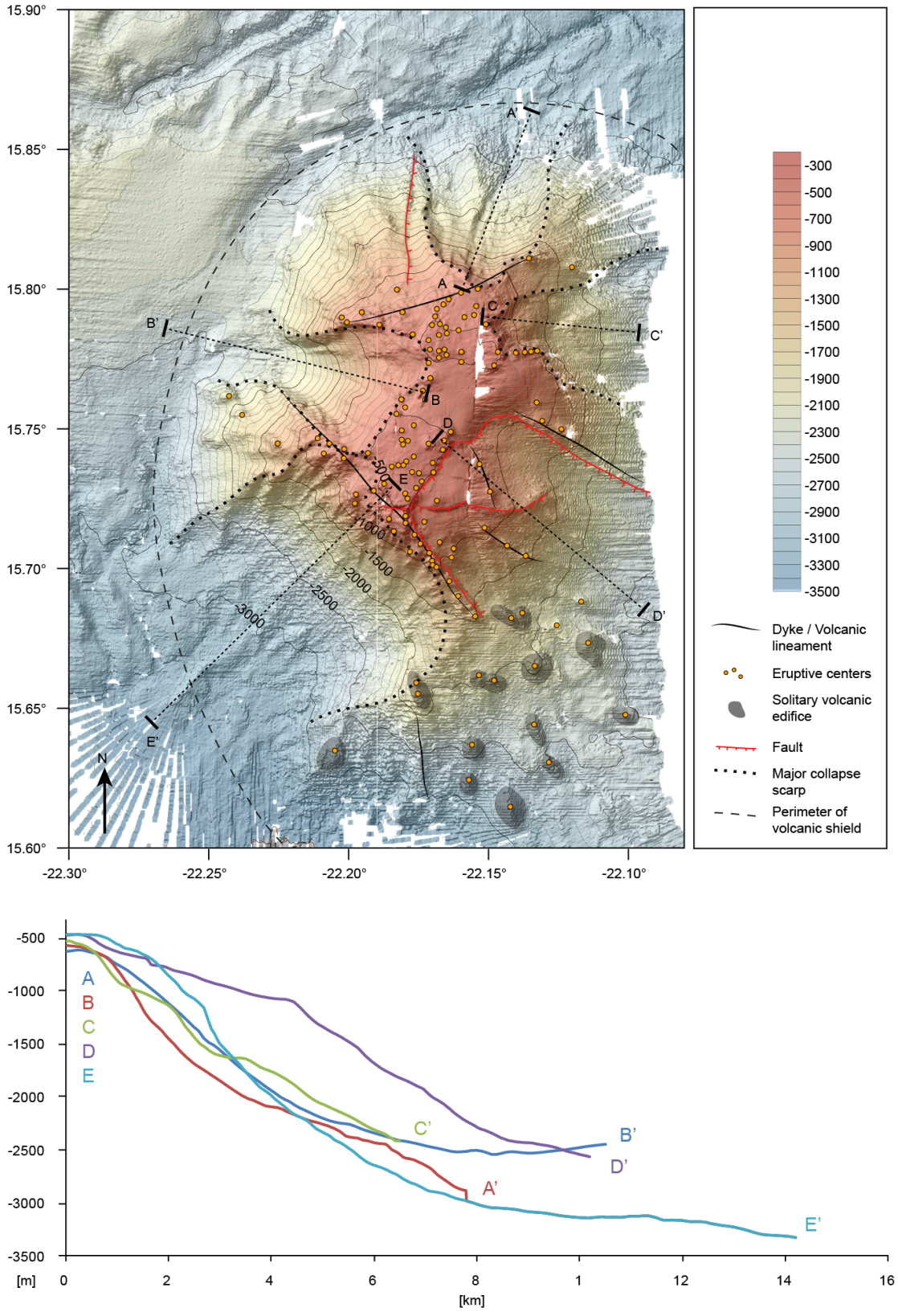

Figure 2-9 *Structural map of Boavista Seamount including 2x exaggerated cross sections.*

The largest, southwestern landslide scar has been completely cleared and its erosional debris removed into the open deep-sea basin. It is likely the oldest failure event as its headwall is most deeply incised by smaller channels and gullies. A large scar to the west is funneled by two ridges into an outlet half its upper diameter, so that a number of larg-

er blocks remained at its foot and the sedimentary fan ran uphill onto the eastern flank of Boavista, leveling the former erosive channels to form a smooth terrain. Around the northern perimeter of the seamount, a possibly pre-existent channel from upslope Boavista Island now channels the debris runoff around the seamount. A collapse scar featuring a steep headwall affects the northern flank, although a large volume of slumped material still rests at its foothill. A failure of the northeastern flank shows even less amount of mobilization, with a large debris fan within the lower scar while the respective segment of the summit plateau merely slumped producing a steep scarp at its lower front. The southeastern flank was mobilized as well but remained intact, as merely a number of arcane downslope faults signal its instability.

To the southeast, Boavista seamount or the slope of Boavista Island finds an extension through a plateau which flanks are incised by gullies. This plateau is oriented in the direction of Cabo Verde Seamount but was only poorly surveyed.

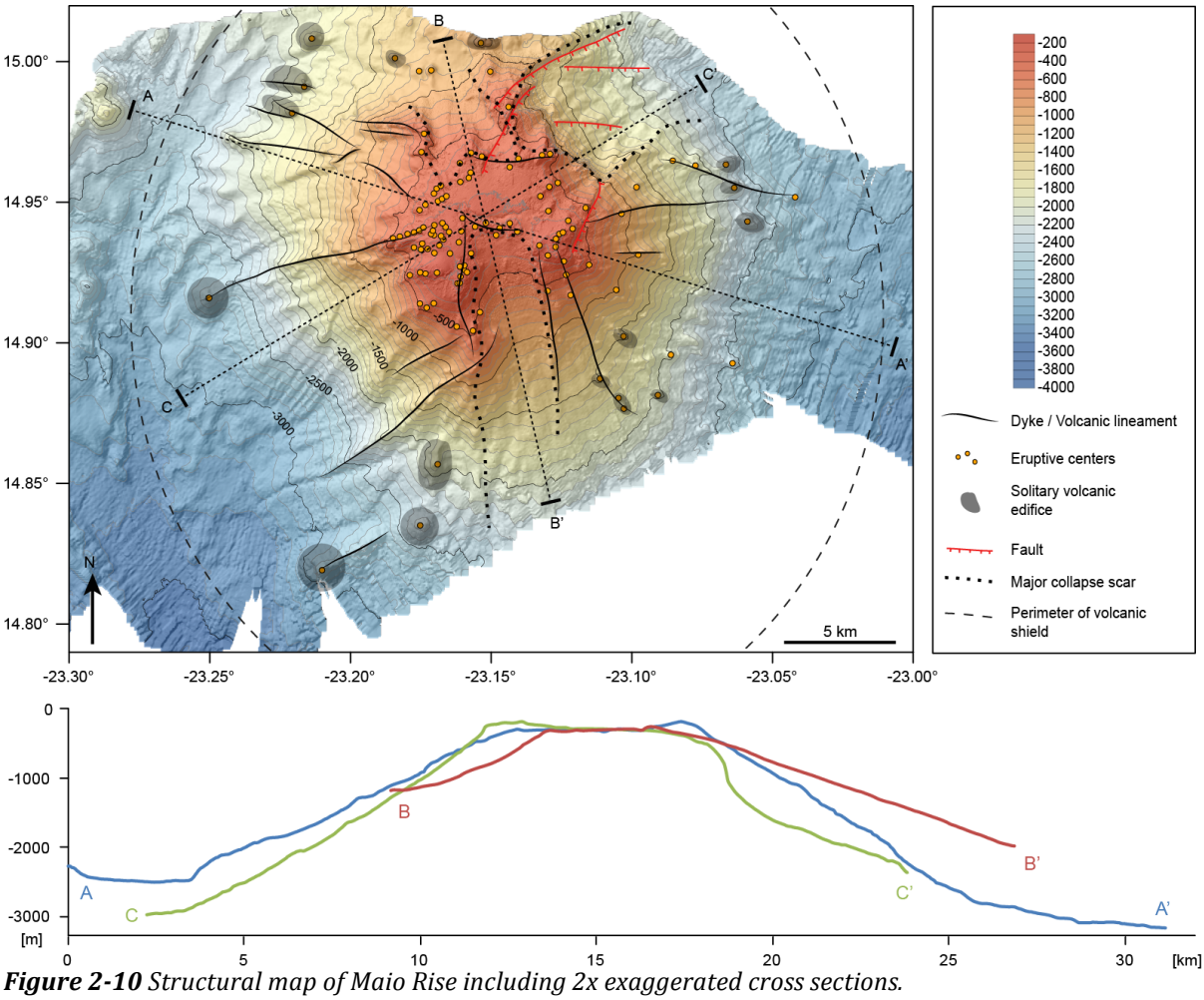

Figure 2-10 *Structural map of Maio Rise including 2x exaggerated cross sections.*

2.6.8 Maio Rise

Similar to Boavista Seamount, Maio Rise also resides on the flank of an island, although on a much steeper slope so that the edifices almost meet at the summit level of the seamount (Figure 2-10). Likewise, a deeply incised erosional channel lines the western perimeter of the seamount. Maio Rise has a basal diameter of 24km and rises from 3000m

depth to just 300m beneath sea level. On a summit plateau 6km in diameter, hummocky terrain constructed by a great number of small volcanic centers line a central plain of smooth terrain and very low backscatter, which likely is covered by soft sediment. From the plateau, radial volcanic lineaments run as volcanic ridges down the seamount in many directions.

The volcano flanks have suffered varying degrees of erosion and thus only few satellite edifices can be found, again between 3000m and 1500m depth. Three major collapse scars dominate the relief. Maio Island deflected the northern debris avalanche through the westward channel. A scar on the southern flank reaches up onto the summit plateau. Its lower slope is lined by small gullies. The northeastern sector of Maio Rise has also failed, exposing a steep headwall. Several downslope dipping (i.e. SE oriented) faults indicate slumping within the scar talus but also instability of the summit area and southeastern flank of the seamount. Dredge samples yielded moderately to heavily altered basalt fragments with a manganese crust of 5mm thickness as well as volcaniclastic breccia of basanitic clasts with carbonate filled vesicles.

2.6.9 Senghor Seamount

Senghor Seamount marks the northeastern limit of volcanic activity in the Cape Verde archipelago, some 100km northeast of Sal. It is also the object that received the most extensive multibeam echo sounder coverage. At 3400m bsl, its foothill lies about 500m higher on the Cape Verde Rise than that of the western Seamounts and islands and it rises to a depth of just 93m bsl (Figure 2-11). Volcanic lineaments radiate from the summit in all directions adding to the circular geometry of the volcano. Merely the summit area has an oval shape oriented NNW-SSE. A particularly well-developed lineament striking WSW-ENE can be traced across the summit. From the foothill up to 1500m bsl a large number of well developed circular and compound satellite cones can be found in any sector. Towards the summit around 500m depth, a large number of smaller volcanic centers have developed a hummocky relief although large portions of the northeastern upper slope have smooth featureless stretches. The summit itself forms a large flat top plateau with very little relief intercalated with low backscatter patches identified as carbonate sand on ROV dives during cruise M79/3 [*Christiansen*, 2010]. Towards the edges, steep slopes end in sedimentary talus fans covering large portions of the hummocky volcanic intermediate plateau.

Senghor lacks large-scale mass wasting scars but features the most extensive and complicated tectonic system of any of the Cape Verdean seamounts. A network of faults concentrates in the western and northern sectors between depths of 500m and 1000m. At this height, the entire western flank has subsided to form a graben which forks at its northern end into an eastward branch around the northern slope sector and complex horst and graben sequence in the northwestern sector. A well-exposed debris avalanche fan marks the collapse of the outer graben wall on the western flank. The circumstance that the seamount might be affected by deep-rooted tectonic activity is indicated by an eastward dipping fault at the foothill in the southern sector.

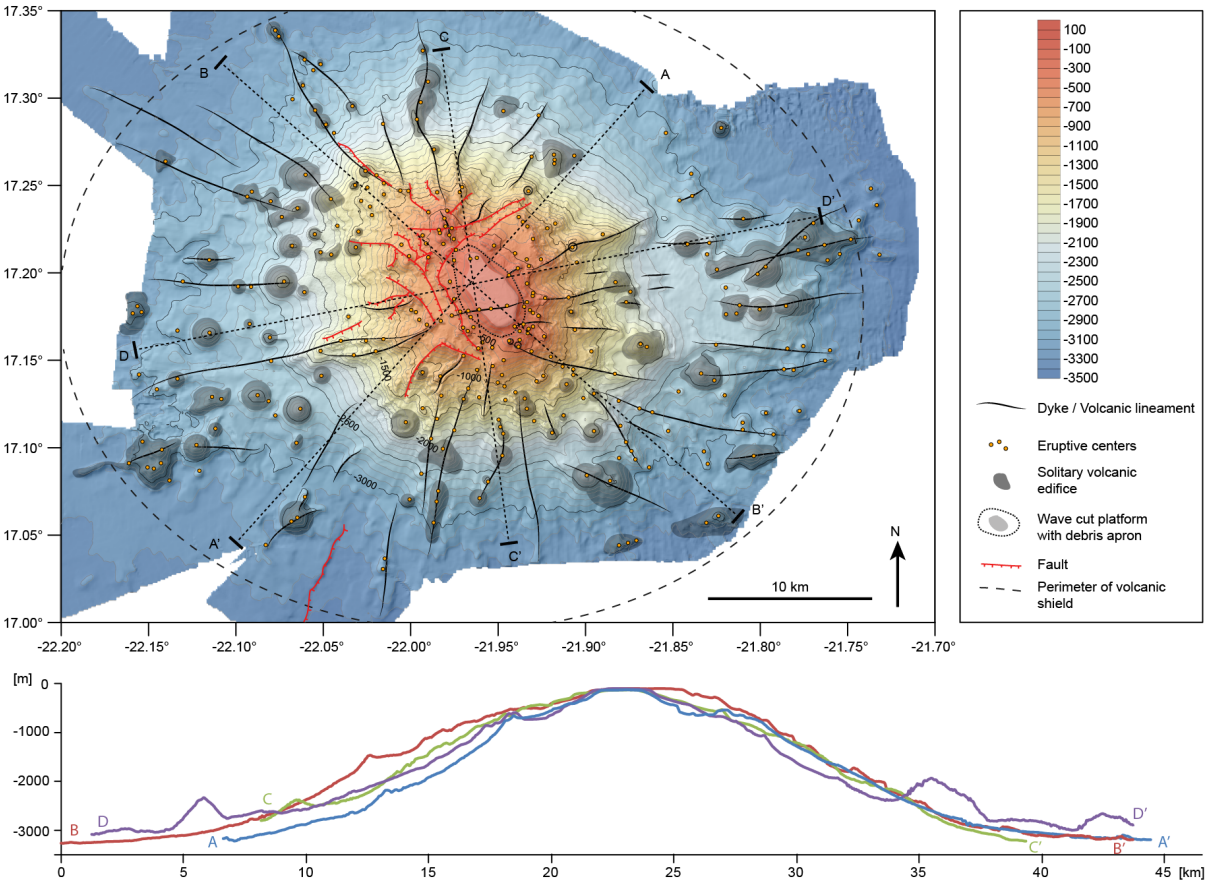

Figure 2-11 *Structural map of Senghor Seamount with 2x exaggerated cross sections.*

Samples obtained from dredges and ROV contain highly altered volcaniclastic material, uniformly coated with manganese crusts of up to 9cm thickness. ROV video coverage of the lower slopes confirmed the ubiquitous layer of manganese on all hard substrate, including the flanks of volcanic cones, which explains the poor recovery by dredging from such a sealed surface.

2.6.10 Nola Seamounts

In the absence of detailed maps of the upper slope, Nola is described in the literature [*Masson et al.*, 2008] as a single seamount with a twin peak. A closer look reveals that in fact it represents two seamounts of almost identical genesis, which have merged to form a common base but are still separated by a saddle at a depth of 1200m while individual shield geometries can be identified down to at least 2000m depth (Figure 2-12). A distance of 13km separates their summits. We therefore address them as the Seamounts Nola East and Nola West.

Their summits project down onto the 2500m and 3000m contour of the western slope of Santo Antão, respectively, and their common base is necessarily elliptical at a maximum diameter of 40km. They both show equally well-developed volcanic lineaments in any direction in the form of ridges and satellite cones between 3500m and 1500m depth. In the southern sector of Nola East, it is impossible to distinguish between cones originating from the plumbing system of Santo Antão and those of the Nola seamounts. Although some lineaments can be projected from the island towards the seamounts, there is no clear morphological suggestion of a link between the three plumbing

systems. At a depth around 500m, both seamounts display a number of small volume volcanic centers creating a complex relief. Nola East features a system of two or three intercalated ring structures. Both summits are formed by elliptical plateaus, which reach as shallow as 35m bsl. They feature dark patches of backscatter analogous to those seen at Senghor but also steep residual morphologies interpreted as volcanic necks which are particularly prominent at Nola East and apparently lie on dominant lineaments across the summit of Nola West. Both plateaus have steep flanks and talus fans, which grade into shield plateaus around 500m depth.

The northern flank of Nola East features a scar of a debris avalanche cutting off the shelf with the respective deposit fan spread from 1500m down to 3500m depth. Half of the western shelf of Nola East collapsed onto the saddle between the seamounts. The eastern flank of Nola East features a large collapse scar, which internally is segmented by a number of channels. Beneath 1000m down to 3200m, a debris flow deposit is deflected northward between the slopes of the seamount and the island into a deep channel running onto the western plain. Three northward-dipping faults run down the eastern slope of Nola West.

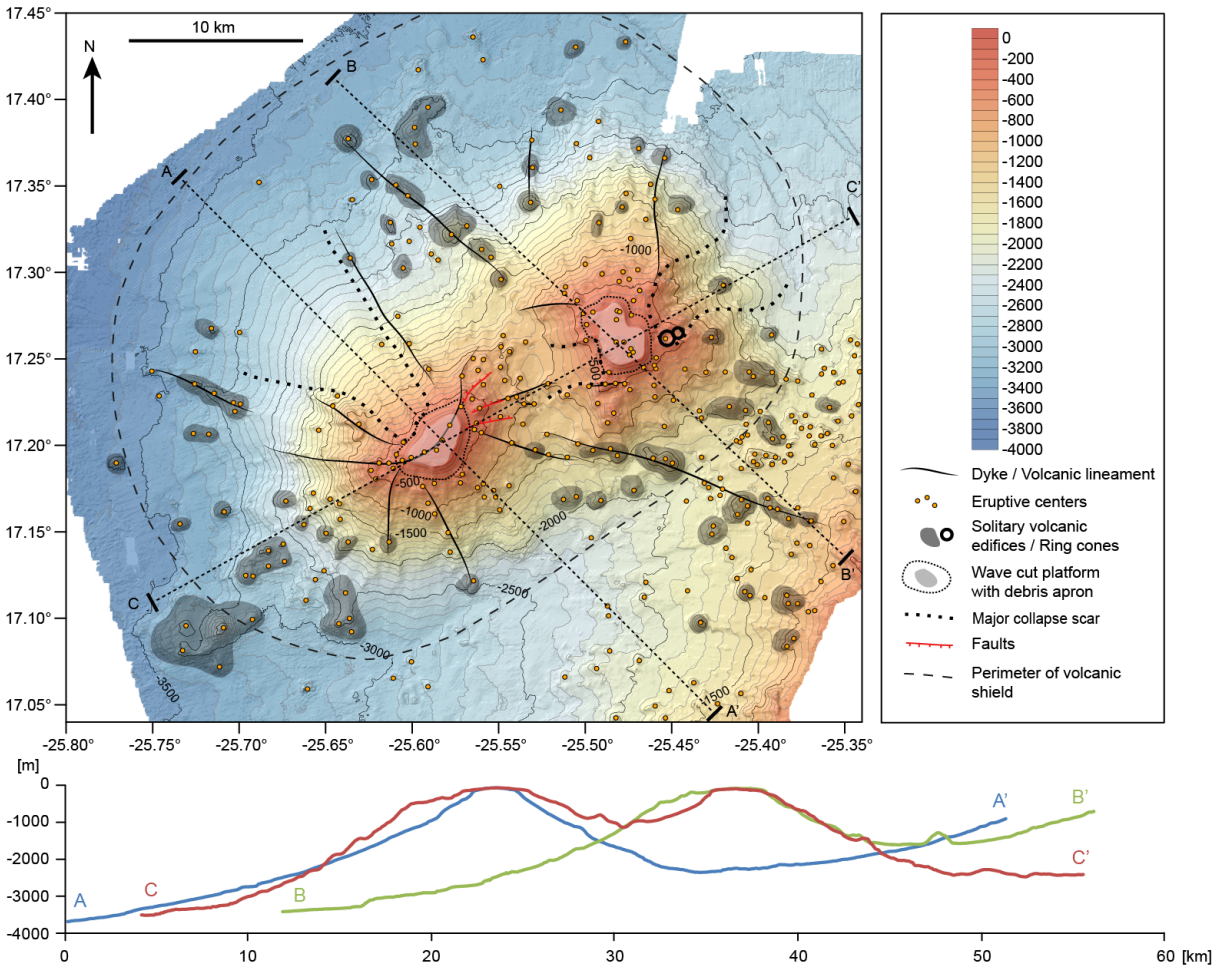

Figure 2-12 *Structural map of Nola Seamounts including 2x exaggerated cross sections.*

ROV and dredge samples of peripheral cones on the southwestern lower flank yielded altered basanitic pillow fragments, carbonate cemented volcaniclastics and scoria fragments. The upper slope of Nola East yielded basanitic and ankaramitic, vesicular lava

fragments with a millimeter thick manganese crust coating. Nola West has occurrences of basanite lavas and pyroxenitic cumulates coated by manganese crusts.

2.7 Regional Influences on Cape Verdean Seamount Evolution

The age distribution of Cape Verdean Seamounts inferred from preservation of samples, developmental stages and geographic position complicates the picture of a westward progression of volcanism, as it can only be maintained on a first order. At a closer look, there are discontinuities and activity seems to jump back and forth within the two island chains.

The seamounts and younger islands of the Northern and Southern Chains are roughly equally spaced. In the western Northern Chain, the Nola Seamounts and CDVF off Santo Antão, and Sodade Seamount off the Nolas, are separated by 40km each. In the Southern Chain, new volcanoes are slightly closer, as roughly 30km separate Maio Rise from Maio Island, Brava and the Ilhéus Secos from Fogo and Cadamosto Seamount from Brava.

In the Northern Chain, Sodade Seamount, CDVF and Santo Antão (with its 0.17 Ma old Tope de Coroa Somma-volcano, [*Plesner et al.*, 2003]) show recent activity, documented below sea level by fresh rock samples and a young morphology. A seismic network recently installed on Santo Antão recorded volcanic tremor at Sodade Seamont and CDVF [*Bruno Faria*, pers. comm. 2012]. In contrast, the flat plateaus of the Nola Seamounts signal a longer period of quiescence amidst active volcanic centers. In the Southern Chain, Fogo and Cadamosto Seamount have shown contemporary volcanoseismic or even eruptive activity [*Grevemeyer et al.*, 2009; *Hildner et al.*, 2012], whereas Brava and the Iléus Secos in between are in an erosional or even posterosional stage. Tavares Seamount, comparatively young judging by its location to the west even of Cadamosto, does not show signs of recent activity but is heavily segmented by faults. Unfortunately, no such clues can be derived from the eastern seamounts, as they all are considerably older and there is no recent activity. Their temporal succession is all the more important as they are further apart and lie opposite to the westward progression of magmatic activity.

Inferring an age progression based on geographic position and state of preservation works well for the western extensions of the two island chains, Nola, Sodade, Cadamosto and, to some degree, Tavares, but the location of the easternmost seamounts Maio, Maio Rise, Boavista, Cabo Verde and Senghor, remains challenging in geodynamical respect. The age progression of the eastern islands from Sal to Maio is still not resolved in detail [*Holm et al.*, 2008], and the large seamounts of the northeast must be incorporated in any future age model.

On the other hand, the distribution of seamounts may add to a larger picture in a broader geodynamical concept. Ramalho [2011] modeled the volume and extent of the buoyant swell root underneath the Cape Verde Rise, assuming its deepest parts close to the island of Sal thinning outwards in an approximately radial fashion (Figure 2-13). Comparing the positions of the seamounts to this swell root, they lie on circles of equal

root thickness, which is also true for the presently active younger systems to the west. Ramalho further inferred that the swell root developed from the center outward over time.

We suggest that, depleted by magmatic production, an ever-outward thickening restitic reservoir develops under the archipelago. This reservoir may form a barrier for further volcanic activity and motivate its outward propagation away from the initial plume head location. Although, in this view, the location of the (initially formed) eastern islands and seamounts suggests a roughly even sectorial distribution of edifices, the later focusing of two main westward trends cannot be explained by this hypothesis alone. Furthermore, the mantle source shows discrete trace element and isotope signals, with a HIMU and DMM source beneath the northern chain and an EM1-HIMU component feeding the southern chain. Recent studies show that the southern chain trend is discontinuous since rocks on Brava and Cadamosto show an EM1-like signature [*Hildner et al.*, 2011; *Barker et al.*, 2012] similar to the northern chain, which is of younger age than the central southern chain [*Holm et al.*, 2008]. Barker et al. [2012] conclude that this may indicate a temporal succession of the source components. This in turn fits the concept of an outward propagation of magmatic activity over time, reflected in a change in geochemistry.

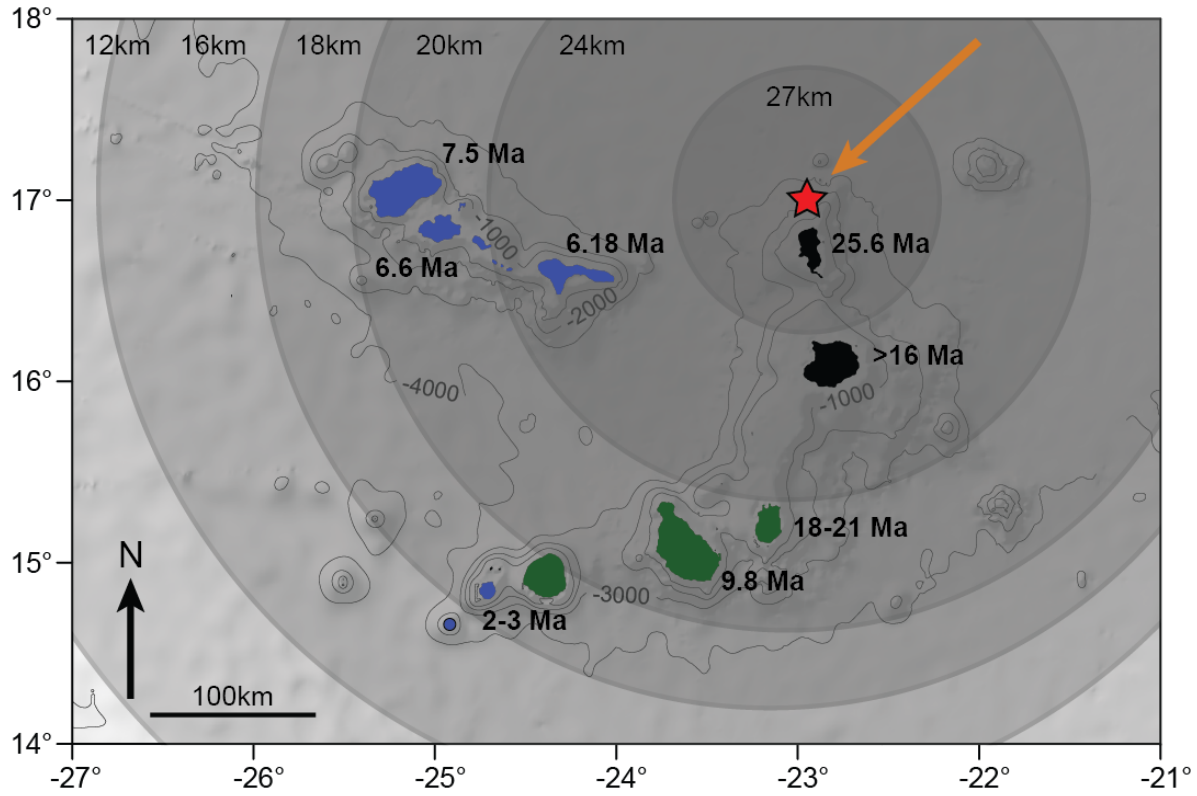

Figure 2-13 *Swell root of the Cape Verde Rise as modeled by Ramalho [2011] (grey circles with thicknesses given at top) around the currently assumed position of the plume head (red asterisk). The orange arrow marks the net direction of the plume head wander calculated by Holm [2008] after [*Pollitz*, 1991;* O'Connor and le Roex*, 1992;* Müller et al.*, 1997;* Geldmacher et al.*, 2001]. The islands and Cadamosto Seamount are colored according to their HIMU-DMM (blue) and EM1-HIMU (green) components (see text). Uncertain islands are left black.*

2.8 Comparison of Local Volcanic Features

Regardless of their absolute ages, the above description of the Cape Verdean seamounts shows that they share common characteristics that may be used to discriminate stages of development in a common life cycle or detect local factors that give rise to an individual development.

2.8.1 Distribution of Volcanic Lineaments

The distribution of individual vents forming a large submarine volcanic edifice is influenced by the presence of planes of weakness. Depending on the development stage of the volcano, these may develop different patterns and have multiple causes. At the same time, erosive forces alter the appearance of the seamounts and the discussion of eruptive centers can only be conducted on those still in place. This in particular means that no quantitative estimates can be made on their spatial distribution. In this study, volcanic lineaments have been identified that can be divided into three different subcategories, based on influences that gain importance during consecutive stages of development:

1. **Influence of pre-existing seafloor structures.** Regional influence by the crustal structure of the underlying seabed or the presence of nearby larger edifices may result in the alignment of lineaments to such preferred direction. This becomes apparent particularly in smaller, i.e. generally younger edifices that lack a well developed, high volume plumbing system and which local stress field is not influenced by a heavy volcanic edifice. In such cases, a clear radial pattern is not developed.
   An example of such a system is Sodade Seamount, where the central edifice already shows a radial alignment but the regional system of dykes and faults in the oceanic crust still dominates the geometry of peripheral edifices. The strong tectonic overprint of Tavares across its main axis may indicate that regional faulting of the underlying oceanic crust rather than internal failure of the edifice affects it.

2. **Influence of nearby edifices.** Islands can have a strong if not determining effect on the location and morphology of nearby edifices by modifying the stress field. On the scale of the entire archipelago, new seamounts occur in the vicinity of older ones, often on the lower flanks of existing island.
   These edifices are likely strongly affected by unilateral slipping created by the inclined slopes of preceding edifices on which they rest resulting in subsidence of the edifice and volume increase due to the emplacement of intrusions [*Walter and Troll*, 2003]. This may be observed in oblique lineaments of Boavista seamount and Maio Rise. The subsidence of older edifices west of CDVF may also be attributed to such influences.

3. **Mature edifices.** In most oceans, seamounts in their shield stage and beyond feature a starfish-like structure of radial ridges called volcanic rift zones [VRZs, *Vogt et al.*, 1984]. In the Cape Verdes, this pattern is generally not as pronounced but best observed on large solitary edifices that show an advanced degree of erosion but are less deformed by collateral mass wasting scars, such as Senghor, Cabo Verde and Nola West.

Satellite cones between 1km and 5km diameter form along the outward projections of VRZs on the lower flanks of the main shield. They are observed at Senghor, Cabo Verde, Boavista, Maio Rise and the Nola seamounts, where they all occur at depths between 3500m and 1500m or at distances greater than 5km from the summit.

2.8.2 Distribution of Central Eruption Centers

Towards the summit, the density of volcanic centers increases as their volume decreases. The concentration of vents between 1000m depth and 500m depth is either due to their formation late in the development of the volcano, their preservation unaffected by large scale mass wasting on the flanks or their development as cones unlike large intercalated deposits comprising the main shield. Nevertheless, a considerable sampling bias must be assumed.

2.8.3 Mass Wasting Scars

As the edifices mature, they become prone to mass wasting due to subsidence of the edifice, over-steepening of the volcano flanks and outward lateral pressure by intrusive bodies [*Day et al.*, 1999]. The measure of destruction of a volcanic edifice cannot directly be used as a gauge for its relative age as local conditions such as inhomogeneity of the prevolcanic basement may speed up its decay. Comparable situations are given for Maio Rise and Boavista seamount as they both are deeply incised by collapse scars and both are situated on an inclined surface. Both do not show a favored direction of slip with respect to the inclination. Even upslope failures are present in both cases, possibly due to over-steepening of the flank due to erosion by turbidity currents from the main island. The combination of an inclined slipping plane and erosion of the foothill may be postulated for Boavista, Maio Rise as well as for Nola East.

Cabo Verde, Senghor and Maio Seamounts are situated on flat undisturbed oceanic basement, judging from the surrounding sea floor. All three show a varying degree of mass wasting contained along or in between volcanic lineaments which are most pronounced in these edifices. Likewise, smaller seamounts also show a focusing effect of lineaments on flank instability, as is the case on the northern and western flanks of Cadamosto and the southern flank of Sodade.

2.8.4 Posterosional and Rejuvenated Activity

Mass wasting events are not the only effect of volcanotectonic activity. Fault systems have been detected on a number of edifices (Cabo Verde, Boavista, Maio Rise, Nola West) but most prominently on Senghor. Although Senghor does not have large land slide scars, it features a complicated structure of ring-like grabens that may even extend into the northeastern sector, judging by the slope of its upper flank which indicates subsidence, i.e. formation of a caldera structure. In this context, the flat-topped summit plateau may represent a rejuvenated Somma-type intra-caldera growth stage. The presence of this plateau prevents further insights, but we suggest that the entire central part of Senghor experienced considerable subsidence due to deflation of an underlying magmatic

reservoir. No equivalent signs of subsidence can be claimed for the other edifices. The caldera of Cabo Verde is likely a phenomenon of erosion as it forms the headwall of a landslide scar. The low backscatter flat central plateau of Maio Rise may be interpreted as a depression filled by volcanic sediment although no tectonic clues support this view, apart from the presence of hummocky terrain composed of volcanic edifices around the plateau.

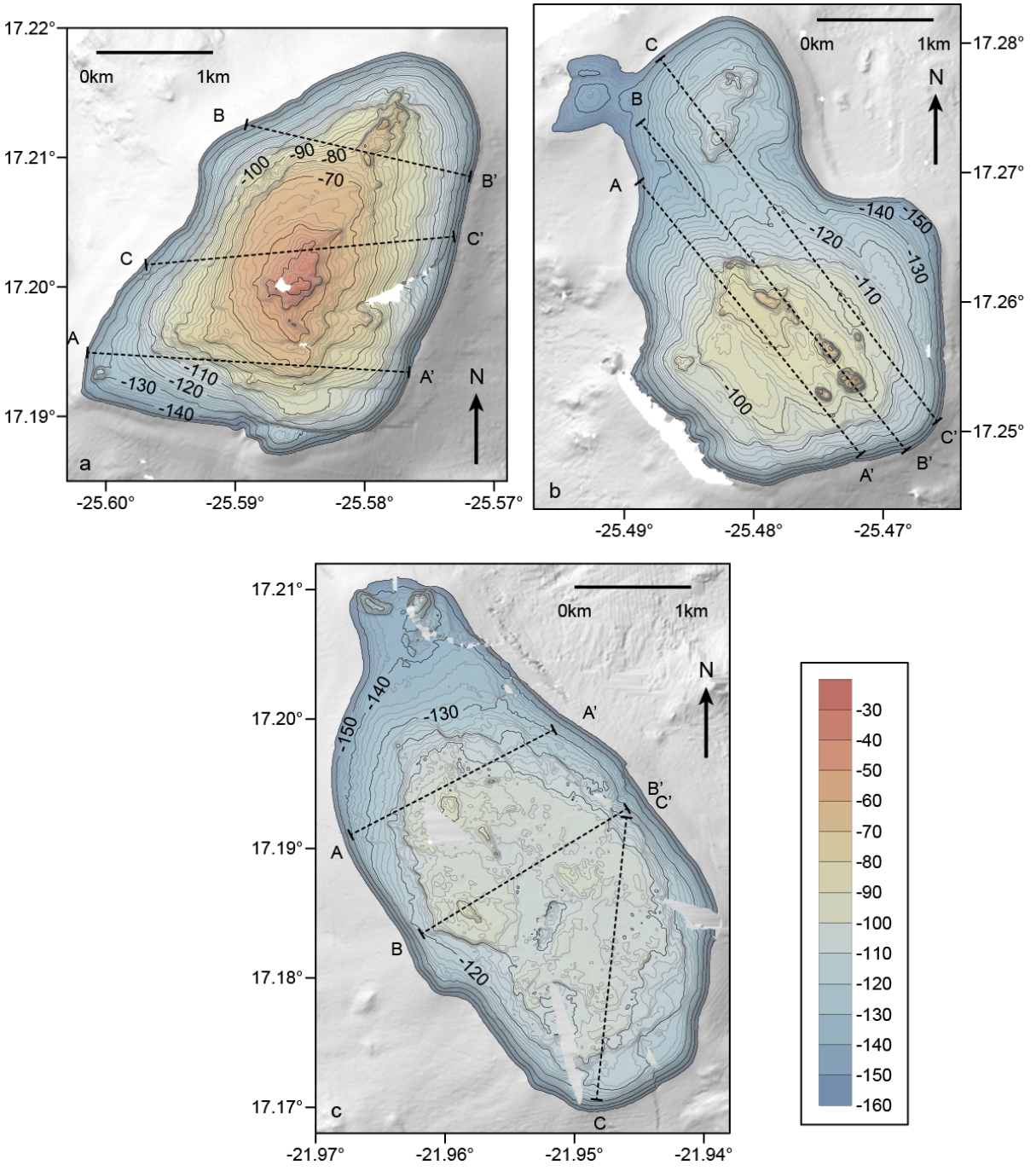

Figure 2-14 *Bathymetrical maps of the summit plateaus of a) Nola West b) Nola East and c) Senghor Seamounts. Depth contours were drawn down to 160m, below which only a shaded relief is shown. Marked cross sections refer to Figure 2-15.*

2.8.5 Morphologies of Subaerial Erosion

A number of seamounts have flat tops or summit plateaus (Figure 2-14). The shallow plateaus of the Nola and Senghor Seamounts show all morphological characteristics of a guyot. Boavista, Maio Rise and Cabo Verde seamounts also have summit plateaus, yet these are considerably deeper (between 300 m and 500 m bsl) and, apart from a central patch of smooth sediment cover, form a hummocky terrain of small compound cones. Such deeper plateaus can also be found on Senghor, although strongly affected by faulting, and at both Nola seamounts, where they are smaller due to the overall steeper slope of the edifices resulting in mass wasting.

Senghor and the Nola seamounts appear to share similar features of their summit plateaus. For the purposes of comparison, the edge of the summit plateau was defined at -160m for all three seamounts, which is where the slope becomes ubiquitously steep. The relief across an area of 7.9 km² to about 40 m. Similar estimates for Nola West and Nola East give ratios of 6.6 km² to 100 m and 6.7 km² to 65 m. A closer look reveals that the plateau at Senghor is much further eroded. Although they have a comparable amount of undulation in their relief, a domed edifice tops the plateau on Nola West while Nola East still shows a number of residual volcanic necks.

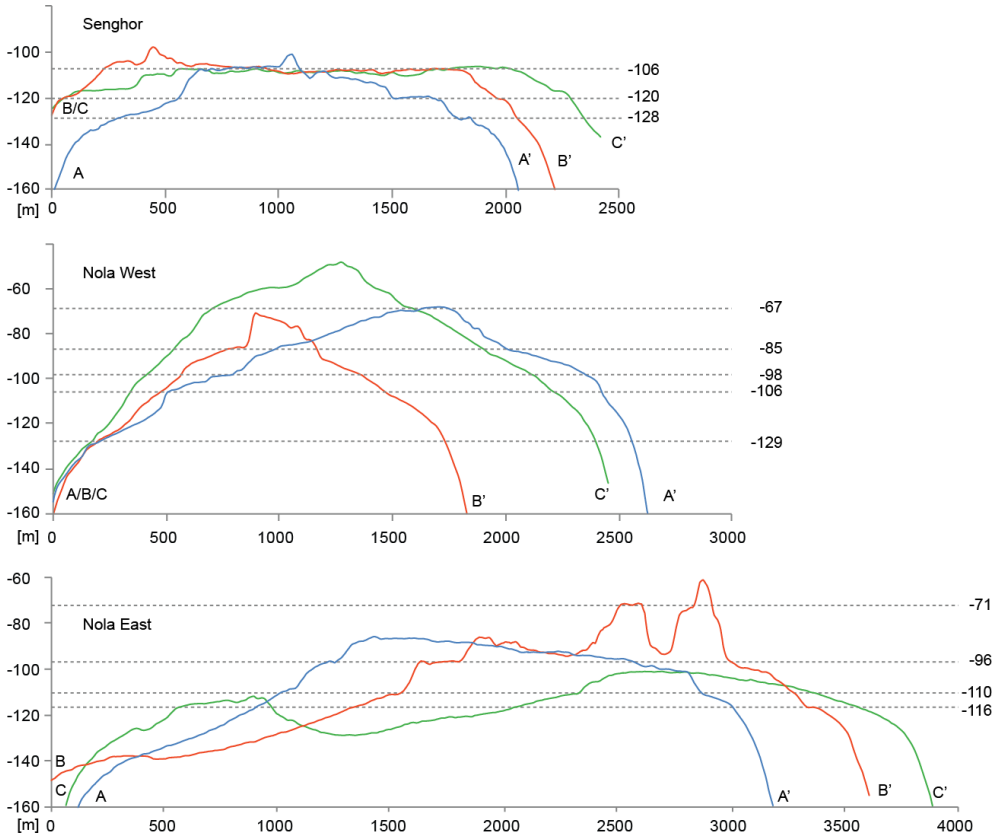

Figure 2-15 *Stacked cross-sections of the plateaus imaged in Figure 2-14, at a 10x vertical exaggeration. Dashed lines and numbers to their right indicate the vertical position of wave cut surfaces.*

The summits of the Nola Seamounts and Senghor show several wave cut surfaces between 71m and 129m depth, which do not readily align vertically (Figure 2-15). Senghor shows terraces at depths of 106m, 120m and 128m, whereas they are found at 67m,

85m, 98m, 106m and 129m depth on Nola West and 71m, 96m, 110m and 116m depth on Nola East. Assuming that these mark events of sea level low stands, the sea level curve of Miller et al. [2005] provides some temporal constraints. Within the last 10 Ma, the maximum low stand never exceeded 122m, but such low stands occurred at 20ka, 30ka, 440ka and 640ka. Thus, it is plausible to attribute the lower terraces of Senghor to erosion during ice age low stands. Possible events causing shallower terraces in between these events are much more difficult to constrain, as the sea level cycled past these tide marks much more often. Beyond varying sea level, the structure of the seamount tops adds to the complication, since erosion may advance more rapidly along horizons of weakness such as volcaniclastic layers or breccia followed by sheet flows. Finally, subsidence of the edifice may play a role, particularly as the comparatively less consolidated summit regions are involved. In this respect, the vast shallow platforms of the Maio-Boavista basement may provide constraints as they may show much less vertical movement due to their great age, especially compared to Nola. The rates of vertical motion have already been constrained on the islands [*Ramalho et al.*, 2010], found to be overprinted by Quaternary uplift of the entire archipelago by 100m due to inflation of the Cape Verde Rise. It may be due to this uplift that Senghor, although a very old feature judging by the westward propagation of volcanic activity, developed a flat top but has drowned to considerable depth again. Unfortunately there are no high-resolution multi beam charts of these shoals available to date. As they cover a much larger area compared to the small flat tops of the seamounts, the rate of erosion needs to be taken into account, and the presence of plateaus shallower than 100m depth by themselves offer no basis for a correlation.

2.9 Evolutionary Stages of Cape Verdean Seamounts

The comparison of seamount morphologies alone should not lead to the assumption that evolutionary stages of volcano growth directly correlate to relative ages in every case. Additional means to infer an age progression for the seamounts based on the available evidence comes by comparing the preservation of their surface through dredge samples and ROV surveys, and by extrapolating the age progression of the island chains to neighboring submarine edifices.

Incipient volcanic activity of a number of morphologically unlinked cones, as seen at CDVF, marks the first signs of a new seamount in its pre-shield phase. Magmatic activity is still diffuse and no main plumbing system has developed yet. The small cone south of Tavares, falls into the same stage, while at Tavares and Sodade the formation of a major plumbing system has lead to a pillow edifice with steep cliffs. Many peripheral cones around Sodade, their manganese coating attesting a moderate age, document that the main, potentially younger pillow volcano is just one of several centers of initial volcanism in this area.

Cadamosto marks an early shield stage, where the edifice rises steadily from a growing shield, while a system of increasingly explosive edifices forms cones and calderas in the summit region. VRZs begin to dominate the relief and a significant volume of its flanks has already collapsed in mass wasting events. As volcanic activity continues, the

seamount may grow into a new island. Maio seamount may have halted its development at a similar stage since it has a summit caldera. Volcanic rift zones are prominent but did not lead to collapse of its flanks. Dredge samples did not hint to any recent activity.

Cabo Verde Seamount has a fully developed subaquatic shield, but as its summit plateau is still at considerable depth and its hummocky terrain shows no signs of wave cut surfaces, indicating it never reached a subaerial stage. Either the magma production rate drastically decreased at the end of the shield stage or it entered a post erosional stage some time later, creating the summit morphology. In any event, it appears to have been exposed to mass wasting for a long time, and, like the other major eastern seamounts, shows no signs of recent activity. Maio Rise and Boavista Seamount appear to have halted at a similar stage. Both developed a hummocky summit plateau, although these, in contrast to Cabo Verde, accumulated substantial sedimentary cover. This may be due to their vicinity to islands, in which case the sediments are most likely calcareous, but whether these sediments are an indication for further volcanic activity beyond the submerged shield stage needs to be addressed by further studies involving sampling. Mass wasting is slowly diminishing both edifices to a skeletal shape.

The only eastern seamount with evidence of a subaerial stage is Senghor. The fact that it did not establish itself as an island is due to the circumstance that its shield is not substantially larger than, e.g., that of Cabo Verde. But in contrast, Senghor experienced a strong rejuvenated stage that resulted in an edifice on top of the summit plateau that broke the surface and fell dry at least briefly, and likely several times during sea level low stands of the ice ages. It cannot be assessed whether the summit edifice was affected by tectonics of the upper shield and experienced subsidence. The two Nola seamounts show a summit morphology rather similar to Senghor, although they are not as voluminous and their upper shield is consequently not as large. Both wave cut plateaus show residual topographies of up to 40m height (Nola East). The fact that the relief at Senghor is much lower than at summits of the Nola seamounts suggests either an older age, which is likely due to its position within the archipelago, or a core complex which is less resistant to wave erosion [*Vogt and Smoot*, 1984]. In any event, it appears that the Nola Seamounts have not experienced activity of their summit vents for a considerable amount of time.

2.10 Conclusion

We have presented a first comprehensive morphological interpretation of Cape Verdean Seamounts and incipient submarine volcanic edifices, based on multibeam bathymetry data, macroscopic description of dredge samples and seafloor observations by ROV. The state of preservation of seamounts generally matches the westward age progression of volcanism along two island chains. The westward extent of the Northern and Southern Chains could be expanded by the previously unknown Sodade and Tavares Seamounts. Our findings on relative ages of seamounts combined with their geographic position and reports on recent volcanic or volcanoseismic activity reveal that within a radius of 100km on each end of the Northern and Southern Chains, volcanism is discontinuous and does not follow the previously assumed clear westward trend. This discovery fits

recent observations on a heterogenous mantle source and its possible explanation through the geometry of the swell root undertheath the Cape Verde Rise.

Pleistocene erosional activity can be demonstrated for the summits of Nola and Senghor, which feature abrasion surfaces corresponding to the sea level low stands of glacial maxima of the last ice ages. This implies that the Nola Seamounts are indeed a younger feature of the northwestern Cape Verdes but have not experienced a recent phase of activity, unlike surrounding volcanoes and seamounts. The solitary location of Senghor Seamount, on the other hand, prevents further clues from the wave cut surfaces, although it is the only seamounts showing definite signs of a rejuvenated phase of volcanic activity.

Lacking a geochemical characterization and radiometric age dates especially for the eastern seamounts, their absolute age progression and magmatic source cannot be addressed, subject to further analysis of the samples recovered. Signs of recent volcanic activity at the CDVF document the discontinued, episodic occurrence of volcanism in the Cape Verdes, and may be interpreted as the beginning of a new seamount on the flank of an existing island similar to Maio Rise, Cadamosto, Boavista Seamounts.

References

Ali, M. Y., A. B. Watts, and I. Hill (2003), A seismic reflection profile study of lithospheric flexure in the vicinity of the Cape Verde Islands, J Geophys Res-Sol Ea, 108(B5), 2239, doi:10.1029/2002JB002155.

Barker, A. K., V. R. Troll, R. M. Ellam, and T. H. Hansteen (2012), Magmatic evolution of the Cadamosto Seamount, Cape Verde: beyond the spatial extent of EM1, *Contributions To Mineralogy And Petrology*, (163), 949–965.

Burke, K., and J. T. Wilson (1972), Is the African Plate Stationary? *Nature*, *239*(5372), 387–390, doi:10.1038/239387b0.

Carracedo, J. C. (1999), Growth, structure, instability and collapse of Canarian volcanoes and comparisons with Hawaiian volcanoes, *J Volcanol Geoth Res*, *94*(1), 1–19.

Christiansen, B. (2010), Short Cruise Report Meteor M 79/3, *Universität Hamburg*, 1–12.

Clague, D. A., and G. B. Dalrymple (1987), The Hawaiian-Emperor volcanic chain. Part I. Geologic evolution, *Volcanism in Hawaii*, *1*, 5–54.

Davies, G. F. (1988), Ocean bathymetry and mantle convection 1. Large-scale flow and hotspots, *Journal of Geophysical Research*, *93*(B9), 10467–10–480.

Day, S., S. I. N. Heleno da Silva, and J. F. B. D. Fonseca (1999), A past giant lateral collapse and present-day flank instability of Fogo, Cape Verde Islands, *J Volcanol Geoth Res*, *94*(1-4), 191–218.

Doucelance, R., S. Escrig, M. Moreira, C. M. Gariepy, and M. Kurz (2003), Pb-Sr-He isotope and trace element geochemistry of the Cape Verde Archipelago, *Geochim Cosmochim Ac*, *67*(19), 3717–3733, doi:10.1016/S0016-7037(03)00161-3.

Faugeres, J. C., P. Legigan, N. Maillet, and C. Latouche (1986), 18. Pelagic, Turbiditic, and Contouritic Sequential Deposits on the Cape Verde Plateau (Leg 108, Site 659, Northwest Africa): Sediment Record During Neogene Time, in *Proceedings of the Ocean Drilling Program: Scientific results*, vol. 108, edited by W. Ruddiman and M. Sarnthein, p. 311.

Gee, M. J. R., D. G. Masson, A. B. Watts, and N. C. Mitchell (2001), Offshore continuation of volcanic rift zones, El Hierro, Canary Islands, *J Volcanol Geoth Res*, *105*(1-2), 107–119.

Geldmacher, J., K. Hoernle, P. Bogaard, S. Duggen, and R. Werner (2005), New 40 Ar/ 39 Ar age and geochemical data from seamounts in the Canary and Madeira volcanic provinces: Support for the mantle plume hypothesis, *Earth and Planetary Science Letters*, *237*(1), 85–101.

Geldmacher, J., K. Hoernle, P. van den Bogaard, G. Zankl, and D. Garbe-Schönberg (2001), Earlier history of the ≥70-Ma-old Canary hotspot based on the temporal and geochemical evolution of the Selvagen Archipelago and neighboring seamounts in the eastern North Atlantic, *J Volcanol Geoth Res*, *111*(1-4), 55–87, doi:10.1016/S0377-0273(01)00220-7.

Gerlach, D. C., R. A. Cliff, G. R. Davies, M. Norry, and N. Hodgson (1988), Magma Sources of the Cape-Verdes Archipelago - Isotopic and Trace-Element Constraints, *Geochim Cosmochim Ac*, *52*(12), 2979–2992.

Grevemeyer, I., G. Helffrich, B. Faria, G. Booth Rea, M. Schnabel, and W. Weinrebe (2009), Seismic activity at Cadamosto seamount near Fogo Island, Cape Verdes—formation of a new ocean island? *Geophys J Int*, *180*(2), 552–558.

Hanel, R., H. C. John, O. Meyer-Klaeden, and U. Piatkowski (2010), Larval fish abundance, composition and distribution at Senghor Seamount (Cape Verde Islands), *Journal of Plankton Research*, *32*(11), 1541–1556, doi:10.1093/plankt/fbq076.

Hansteen, T. (2010), Meteor M80-3 Short Cruise Report, *Universität Hamburg*, 1–9.

Hildner, E., A. Klügel, and F. Hauff (2011), Magma storage and ascent during the 1995 eruption of Fogo, Cape Verde Archipelago, *Contributions To Mineralogy And Petrology*, *162*(4), 751–772, doi:10.1007/s00410-011-0623-6.

Hildner, E., A. Klügel, and T. H. Hansteen (2012), Barometry of lavas from the 1951 eruption of Fogo, Cape Verde Islands: Implications for historic and prehistoric magma plumbing systems, *Journal of Volcanology and Geothermal …*.

Hill, I. (1985), *Geophysical studies of the Cape Verde archipelago*, University of Leicester.

Holm, P. M., J. R. Wilson, B. P. Christensen, L. Hansen, S. L. Hansen, K. M. Hein, A. K. Mortensen, R. Pedersen, S. Plesner, and M. K. Runge (2006), Sampling the cape verde mantle plume: Evolution of melt compositions on Santo Antao, Cape Verde Islands, *J Petrol*, *47*(1), 145–189.

Holm, P. M., T. Grandvuinet, J. Friis, J. R. Wilson, A. K. Barker, and S. Plesner (2008), An 40Ar-39Ar study of the Cape Verde hot spot: Temporal evolution in a semistationary plate environment, *Journal of Geophysical Research*, *113*(B8), B08201.

Jason Morgan, W. (1983), Hotspot tracks and the early rifting of the Atlantic, *Tectonophysics*, *94*(1), 123–139.

Jena, B., P. J. Kurian, D. Swain, A. Tyagi, and R. Ravindra (2012), Prediction of bathymetry from satellite altimeter based gravity in the Arabian Sea: Mapping of two unnamed deep seamounts, *International Journal of Applied Earth Observation and Geoinformation*, *16*, 1–4.

Jørgensen, J. Ø., and P. M. Holm (2002), Temporal variation and carbonatite contamination in primitive ocean island volcanics from Sao Vicente, Cape Verde Islands, *Chemical Geology*, *192*(3), 249–267.

Lancelot, Y. et al. (1978), Site 368: Cape Verde Rise, in *Initial Rep. Deep Sea Drill. Proj.*, vol. 41, edited by Y. Lancelot et al., pp. 223–326, US Government Printing Office.

Le Bas, T. P., D. Masson, R. Holtom, and I. Grevemeyer (2007), Slope failures of the flanks of the southern Cape Verde Islands, *Submarine Mass Movements and Their Consequences*, 337–345.

Masson, D. G., T. P. Le Bas, I. Grevemeyer and W. Weinrebe (2008), Flank collapse and large-scale landsliding in the Cape Verde Islands, off West Africa, *Geochem Geophy Geosy*, *9*, Q07015, doi:10.1029/2008GC001983.

Mata, J., M. Moreira, R. Doucelance, and L. C. Silva (2006), Noble gases isotopic signatures from Cape Verde oceanic carbonatites, *Geophysical Research Abstracts*, *8*, 07462.

McNutt, M. (1988), Thermal and mechanical properties of the Cape Verde Rise, *Journal of Geophysical Research*, *93*(B4), 2784–2794.

Miller, K. G., M. A. Kominz, J. V. Browning, J. D. Wright, G. S. Mountain, M. E. Katz, P. J. Sugarman, B. S. Cramer, N. Christie-Blick, and S. F. Pekar (2005), The Phanerozoic record of global sea-level change, *Science*, *310*(5752), 1293–1298, doi:10.1126/science.1116412.

Mitchell, J. G., M. J. Le Bas, J. Zielonka, and H. Furnes (1983), On dating the magmatism of Maio, Cape Verde Islands, *Earth and Planetary Science Letters*, *64*(1), 61–76.

Moore, J. G., D. A. Clague, R. T. Holcomb, P. W. Lipman, W. R. Normark, and M. E. Torresan (1989), Prodigious submarine landslides on the Hawaiian Ridge, *Journal of Geophysical Research*, *94*(B12), 17465, doi:10.1029/JB094iB12p17465.

Morgan, W. J. (1971), Convection Plumes in the Lower Mantle, *Nature*, *230*(5288), 42–43, doi:10.1038/230042a0.

Müller, R. D., M. Sdrolias, C. Gaina, and W. R. Roest (2008), Age, spreading rates, and spreading asymmetry of the world's ocean crust, *Geochem Geophy Geosy*, *9*(4), Q04006.

Müller, R. D., W. R. Roest, J. Y. Royer, L. M. Gahagan, and J. G. Sclater (1997), Digital Isochrones of the World's Ocean Floor, *Journal of Geophysical Research*, *102*, 3211–3214, doi:10.1029/96JB01781.

O'Connor, J. M., and A. P. le Roex (1992), South Atlantic hot spot-plume systems: 1. Distribution of volcanism in time and space, *Earth and Planetary Science Letters*, *113*(3), 343–364, doi:10.1016/0012-821X(92)90138-L.

Plesner, S., P. M. Holm, and J. R. Wilson (2003), 40Ar-39Ar geochronology of Santo Antão, Cape Verde Islands, *J Volcanol Geoth Res*, *120*(1-2), 103–121.

Pollitz, F. F. (1991), Two-stage model of African absolute motion during the last 30 million years, *Tectonophysics*, *194*(1), 91–106.

Ramalho, R. (2011), *Building the Cape Verde Islands*, Springer, Heidelberg.

Ramalho, R. S., G. Helffrich, M. Cosca, D. Vance, D. Hoffmann, and D. N. Schmidt (2010), Vertical movements of ocean island volcanoes: Insights from a stationary plate environment, *Marine Geology*, *275*(1-4), 84–95, doi:10.1016/j.margeo.2010.04.009.

Schmincke, H.-U. (2005), *Volcanism*, Springer.

Sleep, N. H. (1990), Hotspots and mantle plumes: Some phenomenology, *Journal of Geophysical Research*, *95*(B5), 6715–6736.

Smith, W. H., and D. T. Sandwell (1997), Global Sea Floor Topography from Satellite Altimetry and Ship Depth Soundings, *Science*, *277*(5334), 1956–1962, doi:10.1126/science.277.5334.1956.

Torres, P. C., J. Madeira, L. C. Silva, A. Brum da Silveira, A. Serralheiro, and A. Mota Gomes (1995), Carta geologica das erupciones historiicas da Ilha do Fogo:revisao e actualizacao,

Vogt, P. R., and N. C. Smoot (1984), The Geisha Guyots: Multibeam bathymetry and morphometric interpretation, *Journal of Geophysical Research*, *89*(B13), 11085–11,107, doi:10.1029/JB089iB13p11085.

Walter, T. R., and V. R. Troll (2003), Experiments on rift zone evolution in unstable volcanic edifices, J Volcanol Geoth Res, 127(1-2), 107–120, doi:10.1016/S0377-0273(03)00181-1.

Wang, X., F. Peine, A. Schmidt, and H. C. Schröder (2011), Concept of biogenic ferromanganese crust formation: coccoliths as bio-seeds in crusts from Central Atlantic Ocean (Senghor Seamount/Cape Verde), *Natural Product Communications*, *11*(0), 1–10.

Williams, C. A., I. A. Hill, R. Young, and R. S. White (1990), Fracture zones across the Cape Verde Rise, NE Atlantic, *Journal of the Geological Society*, *147*(5), 851–857, doi:10.1144/gsjgs.147.5.0851.

3 Doing Fieldwork on the Seafloor: Photogrammetric Techniques to yield 3D Visual Models from ROV Video

Tom Kwasnitschka[1], Thor H. Hansteen[2], Colin W. Devey[3], and Steffen Kutterolf[4]

GEOMAR Helmholtz Centre for Ocean Research Kiel
Wischhofstr. 1-3, 24148 Kiel, Germany
[1]tkwasnitschka@geomar.de, phone: +49 431 600-2136, fax: +49 431 600-2924 (Corr. Author)
[2]thansteen@geomar.de
[3]cdevey@geomar.de
[4]skutterolf@geomar.de

(This article has been accepted for publication in Computers & Geosciences (Ref. No. CAGEO3053) but has been reformatted since the final typeset has not yet been carried out. Please note that it contains its own reference list.)

Abstract

Remotely Operated Vehicles (ROVs) have proven to be highly effective in recovering well localized samples and observations from the seafloor. In the course of ROV deployments, however, huge amounts of video and photographic data are gathered which present tremendous potential for data mining. We present a new workflow based on industrial software to derive fundamental field geology information such as quantitative stratigraphy and tectonic structures from ROV-based photo and video material. We demonstrate proof of principle tests for this workflow on video data collected during dives with the ROV Kiel6000 on a new hot spot volcanic field that was recently identified southwest of the island of Santo Antão in the Cape Verdes. Our workflow allows us to derive three-dimensional models of outcrops facilitating quantitative measurements of joint orientation, bedding structure, grain size comparison and photo mosaicking within a georeferenced framework. The compiled data facilitate volcanological and tectonic interpretations from hand specimen to outcrop scales based on the quantified optical data. The demonstrated procedure is readily replicable and opens up possibilities for post-cruise "virtual fieldwork" on the seafloor.

3.1 **Introduction**

The scientific use of Remotely Operated Vehicles (ROVs) has traditionally concentrated on making visual observations, installing equipment precisely on the seafloor and the recovery of physical samples. While the samples can later be localized with high precision, the sampling decision is often based upon very limited visual information relayed through video cameras. Without comprehensive prior surveys of the study area on scales at which the ROV operates afterwards, researchers cannot be sure to be observing or sampling in the scientifically most relevant places.

During the R/V METEOR 80/3 cruise to the Cape Verdes, we encountered a complex submarine cone field, called the Charles Darwin Volcanic Field (CDVF), located at a depth of 3500m off the Island of Santo Antão. Based on a ship-based bathymetric map gridded at 25m resolution (Figure 3-1) and on a scattered set of dredge samples, we identified targets for the detailed surveying of several structures using the ROV Kiel6000 vehicle. It quickly became clear that the observational protocols usually used during ROV operations were failing to capture much geological information (especially on the relationships between rock structures in 3D), which could greatly help interpretation of the samples post-cruise. This motivated the development of the photogrammetric mapping workflow described below, as available acoustic survey methods and video coverage did not allow adequate interpretation of the bedding structures and series of deposits which we observed. The detailed geological interpretation and resulting development of new concepts on eruptive mechanisms in the deep sea is the subject of Chapter 4 [*Kwasnitschka et al.,* in prep.].

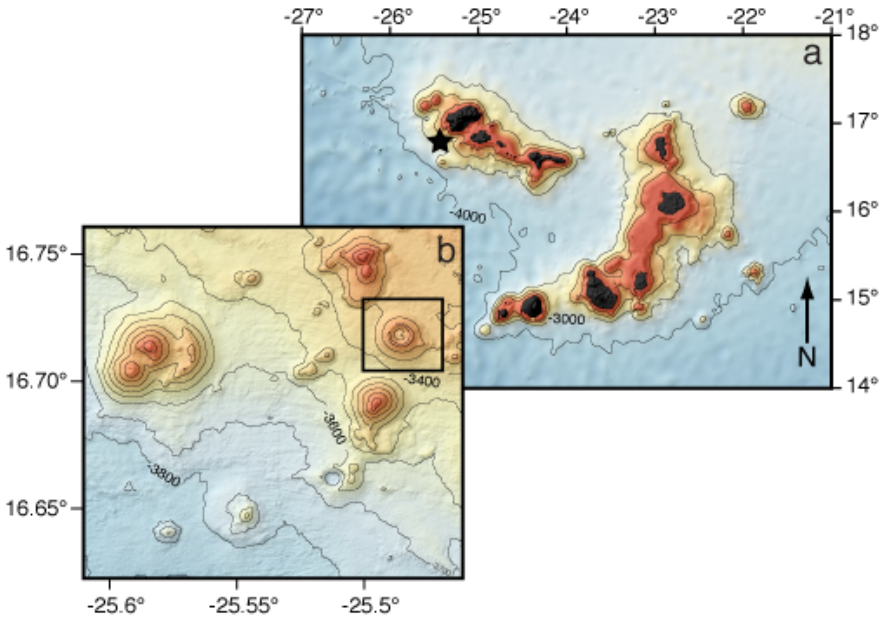

Figure 3-1 *Location of the working area. a) Asterisk marks the location of CDVF on the southwestern slope of the Island of Santo Antão. b) Box marks the working area of ROV dive 059 at Tambor Cone, part of the central group of CDVF (compare Figure 3-4 for close up view).*

Our aim was to design a workflow that would allow examination of the outcrops indirectly after the dive, based on a three-dimensional digital model [*e.g., Kreylos et al.,* 2006]. This model should be accurate enough to allow quantitative measurements matching the precision of terrestrial surveys. At the same time, the representation of geological features should be realistic and unobstructed by effects of the water in order to allow the development of discussable qualitative field impressions. The procedure should be stable, repeatable and reasonably fast while easy to use, allowing a first evaluation of new data while still at sea. The workflow should be open, follow industry standards, and offer interfaces to further third party data treatment procedures. We directed our attention towards existing industry-proven components that would allow integration on a user level and be widely available to other users without specialized programming knowledge (although a familiarity with the features of the software we used (which can be acquired from the software documentation and HowTo video tutorials) is assumed here).

3.2 Previous Work

Photogrammetry has previously been successfully applied to a variety of marine scientific disciplines, an overview of which is given by Johnson-Roberson et al. [2010]. Our own work was inspired by recent applications in the field of aerial archeology [*Verhoeven*, 2011] with which we share the same general requirements of georeferenced visualization of terrain features on multiple scales. At the same time, photogrammetric methods have been developed to derive structural geology data from outcrops in time-critical situations such as tunneling and quarrying [*Gaich*, 2001]. Our own previous use of such packages [*Kwasnitschka*, 2008] also informed the development of the current project.

The underwater application of photogrammetric techniques poses considerable problems since all camera equipment needs to be housed in some form of water-tight (and, in our case, pressure-resistant) housing. The air-glass-water interface introduced by this camera housing acts as an additional optical element - in the case of pressure housings, the optical geometry will also change in a possibly non-linear manner as its multiple components deform under load. Various approaches have been taken to address these issues [*Beall et al.*, 2010; *Sedlazeck and Koch*, 2011]. Previous authors have investigated the optical aberrations induced by the air-water interface [*Sedlazeck*, 2009] providing critical constraints for positional reconstruction in the absence of reliable external navigation data.

Using established subaerial calibration methods, it is also possible to achieve locally well-defined reconstructions by using rigid stereoscopic camera rigs [*Johnson-Roberson et al.*, 2010] or monoscopic approaches [*Pizarro and Eustice*, 2009] and aligning clusters of such local models using vehicle navigation data. Much of the previous work has been made using images from Autonomous Underwater Vehicles (AUVs) rather than ROVs since they are generally able to cover larger areas due to their deployment scheme [*Yoerger et al.*, 2007]. For our scientific purposes, though, AUV have two major drawbacks: (a) they do not allow an immediate reaction to new discoveries and so often have

objects of interest at the edges of images and (b) they generally view scenes from above, not the visualization angle most suited to seafloor geological interpretation, where dip angles are mostly low and so features of interest are best viewed by looking horizontally onto vertical walls.

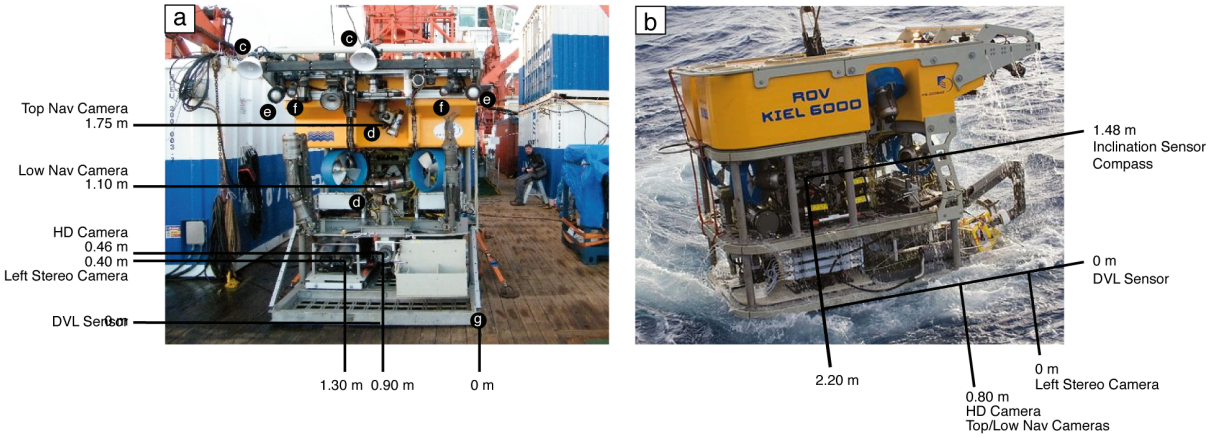

Figure 3-2 *Cameras, positional sensors and lighting of ROV Kiel6000 seen from a) front and b) right views. Relevant lighting equipment is labeled as c) Flash guns for the stereo system (OE11-242), d) Halogen lamps (Deep Multi-SeaLite) e) HMI lamps (SeaArc 2), f) HID lamps (SeaArc 5000). The stereo camera rig was mounted on a retractable sled and is shown in retracted position, while during operation the lenses were positioned over the front edge of the vehicle. The DVL and orientation sensors are obstructed. Approximate positions of the cameras and sensors are given relative to g) lower front port corner of vehicle. Photos courtesy H. Huusmann and N. Augustin.*

3.3 Hardware

The ROV KIEL 6000 is a 6000m-rated work class ROV built by Schilling Robotics, Inc.. Seven thrusters allow precise positioning; an automatic station-keep mode is available for stationary operation. The lighting is centered to the front within a cone of approximately 100°, featuring a total of 990 Watt. Table 3-1 and Figure 3-2 give an overview of the standard camera equipment available on the vehicle. In addition to this, an experimental stereo camera rig consisting of two Ocean Imaging Systems camera housings with Nikon D80 cameras and 20 mm optics was tested during the test deployments described here. The cameras were mounted parallel at a separation of 20 cm between the optical axes. All housings are equipped with flat glass ports. Only the stereo rig was successfully calibrated for optical aberrations since the other cameras, mechanically and electrically fully integrated into the vehicle itself, were unavailable for such a procedure.

The underwater navigation system installed on the vehicle consists of three elements. An RDI Workhorse Navigator 1200 Doppler Velocity Logger (DVL) provides three-dimensional differential motion tracking at sub-centimeter resolution. Absolute position determination is supported by a Posidonia 6000 Ultra Short Baseline Logger (USBL) pinger installed on the vehicle and used in combination with a USBL antenna mounted on the surface vessel (in this case R/V METEOR). A compass (Precision Navigation TCM2-50) provides information on the vehicle heading. Depth and altitude readings were provided by a Seabird Electronics FastCat SBE 49 CTD sensor, the DVL and by a Paroscientific Digiquartz pressure sensor. Orientation data of the vehicle (heading, pitch

and roll) were received from a Crossbow VG700CA orientation sensor. Pan and tilt values of the navigation cameras were logged from the Schilling rotary actuators.

Table 3-1 *Relevant camera equipment installed on ROV Kiel6000. (Only HD and stereo cameras were used for reconstruction.)*

	Brand	Recording format	FoV	Type of mount	Operation mode
Navigation Cameras	Kongsberg OE14-366 MKII	PAL	63°	pan/tilt, logged	continuous
HD Cameras	Kongsberg OE14-500	HDV, 1080i	50°	tilt, unlogged	on demand
Rear Navigation Camera	Oktopus 6000	PAL	75°	fixed	not recorded
Stereo Camera	Ocean Imaging Systems	10.2MP RAW	57°	fixed	4 sec interval on demand
Still Camera	Kongsberg OE14-208	5MP JPEG	62°	pan/tilt, logged	on demand

3.4 Data

The outcrops which we used to test the 3D reconstruction workflow are situated on the Charles Darwin Seamounts. They display abundant units with clearly visible bedding structures cut by several generations of joints. Our test data was acquired on ROV dive 059 during Meteor cruise 80/3 which led across the northwestern flank of a volcanic crater showing the morphological characteristics of a tuff ring (Figure 3-3). The ring rises about 200 m above the surrounding terrain and its central depression measures 1 km across featuring steep inner walls dropping step wise between 20 m and 50 m at angles between 35° and 90°. The structure is composed of loose to strongly compacted volcaniclastics and lava flows, featuring a sparse to locally moderate population of vagile and sessile epibenthic fauna.

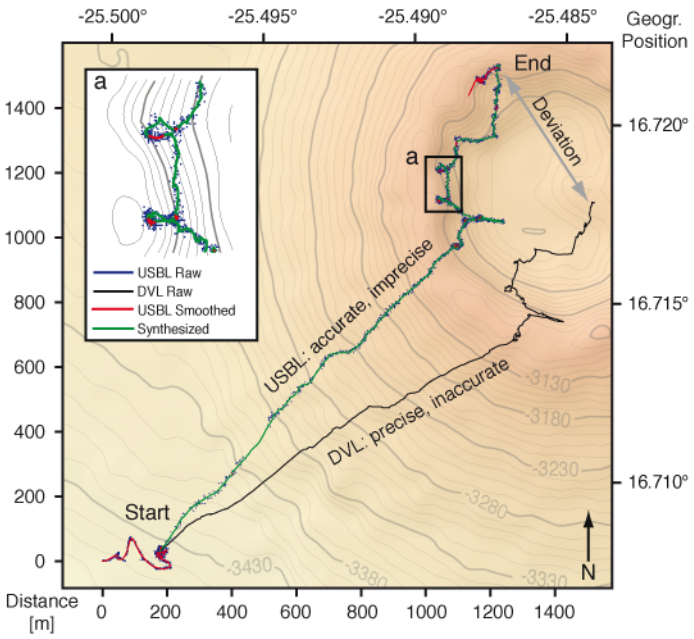

Figure 3-3 *(previous page) The vehicle track of dive 059 used for alignment of the reconstructed geometry data consists of the merged DVL bottom velocity and USBL data substituted by just the smoothed USBL data where DVL data was unavailable (a). The grey arrow marks the accumulated offset (458m) between the raw USBL and uncorrected DVL signal by the end of the dive.*

The sample film clip (059-47) was recorded during a descent of the vehicle 28 m down a cliff of 65° inclination with sedimentary talus at the foot of the cliff marking the transition to the crater floor. Using the ROV´s onboard sonar, a roughly constant distance of 2.5 m to the wall could be maintained. Consequently, the width of the model ranges between 3.8 m and 8.5 m. The duration of the sequence is just over two minutes, resulting in a set of 125 source images after pre-processing. All but the last 7 images (where the image quality deteriorated with increasing distance to the wall) could be included in the reconstruction. This yielded a model of 200 000 polygons and a texture of 8192x8192 pixels, corresponding to an estimated geometrical resolution of 15 cm and a local maximum textural resolution of 2 cm. The textures of the uppermost and lowermost 25 % of the model in particular show signs of color absorption into bluish hues due to a slightly increased object distance. Since there was little variation in the horizontal viewing angle, some laterally facing portions, especially features facing right, remained occluded from the camera and could not be textured.

3.5 Data Pre-Processing

The individual streams of video and still imagery were synchronized in Adobe Premiere and merged into a master stream for reference. At this point it became clear that we would not be able to use the data from the experimental stereo camera system as it showed synchronization faults and had collected data only sporadically during the dive. Pre-selected video sequences covering outcrops were reformatted using Adobe After Effects. Elements obstructing the view such as visible parts of the vehicle and non-static objects were masked out from the video (as they are not part of the static seafloor which we wanted to reconstruct and so would have led to erroneous results during automated 3D reconstruction). No noise reduction filters were applied as we found that the resulting loss of detail caused reconstruction gaps on uniform surfaces. The clips were exported at a rate of one frame per second as still sequences with the mask embedded as an alpha channel. The complete workflow is illustrated in Figure 3-4.

The USBL (absolute position with relatively large errors) and DVL (relative position with smaller errors) navigational data underwent extensive correction as it formed the only frame of reference to which the quality of reconstructed models could be gauged. Using a semi-automatic Matlab routine, we generated a hybrid vehicle path, stabilizing the two data sources with respect to each other (Figure 3-3): The x and y components of both signals were filtered for system-inherent outliers, after which the short-wavelength component of the DVL was copied onto the long-wavelength component of the USBL signal. We take this to be a best-practice approach with the given data quality, with the drawback that, in passages where the DVL failed, the precision of the accepted position is diminished to an average of the USBL position and can only serve for rough georeferencing but not for quality control. Likewise, the vertical component of the DVL signal

was corrected for drift effects and failed passages using a merged version of the CTD and Digiquartz pressure sensors.

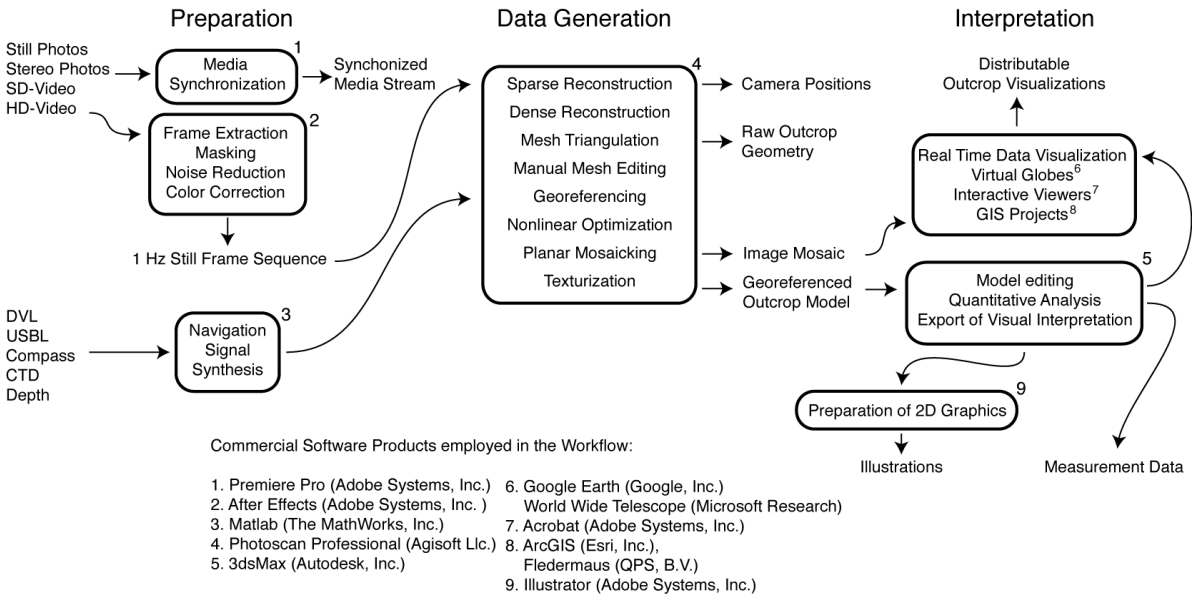

Figure 3-4 *Workflow scheme developed during this study employs a number of commercial software products which are linked using their own data interfaces as well as custom import and export scripts for quantitative interpretation.*

3.6 Photogrammetric Reconstruction

A number of different processing approaches can be grouped under the term photogrammetry, employing heterogeneous image clusters, a single camera or stereo pairs. In order to mathematically reverse the projection of a camera and reconstruct three-dimensional information from two-dimensional images, the algorithms require the extrinsic camera parameters (essentially, camera position relative to the object) and intrinsic camera parameters (a description of the optical path of light through the lens onto the sensor). A truly accurate reconstruction can only be achieved if there is precise information on the intrinsic parameters and some minimal external information in the form of camera position and orientation or reference points on the object in order to establish absolute scale, orientation and position within a world coordinate system.

After tests using a variety of motion tracking packages (PFtrack5.0, Boujou; [*Condell et al.*, 2006]), open source and free bundle adjustment software (Bundler, Microsoft Photosynth; [*Triggs et al.*, 2000; *Snavely et al.*, 2010]), we now rely on Agisoft Photoscan Professional, a commercial suite for aerial photogrammetry. This software offers an integrated workflow including a core of sturdy reconstruction and georeferencing tools along with sufficient means to pre-process the input images and edit the finished models for further export. Verhoeven [2011] gives a detailed overview of the software functionality and the basic process of (1) model triangulation from image features matched across a cluster of overlapping images into (2) a sparse estimate of the scene geometry from which (3) a dense model is derived, followed by (4) surface modeling, and (5) texture generation (Figure 3-4). The range of features has since been expanded for georeferencing based on landmarks visible on the model for which coordinates have been de-

termined by GPS. Since a high-resolution, georeferenced AUV map was unavailable, we registered our models to the camera poses (i.e. position and orientation) derived from the ROV motion record. The software first tries to georeference by a best-fit, rigid seven-parameter transformation. In a second step, the reconstructed geometry and camera poses are subjected to a nonlinear optimization process to the ROV vehicle track. For all poses, the degree of misfit is reported, along with RMSE values.

Afterwards, the photographic texture can be exported as an orthophoto mosaic after re-projecting the images from the camera poses back across the model surface. Various texture blending rules can be chosen to treat overlapping areas. The most instructive results can be acquired by always choosing the brightest available pixel from the set of overlapping pixels, which could be projected onto a given surface coordinate. This somewhat suppresses the effects of light absorption through the water and brightness falloff towards the outer parts of the cone of illumination. In the case of strongly varying object distances, more visually pleasing results can be achieved by forming an average of overlapping pixels. A mathematically correct treatment of this problem appears to be difficult as the distance of the objects to the light sources and the camera varies strongly compared to a case of flat sea bottom and a monotonous vehicle track, where such corrections have been successfully demonstrated [*Sedlazeck et al.*, 2009; *Johnson-Roberson et al.*, 2010].

The models can be exported to a variety of formats and geographic reference frames. The full-resolution model is exported in the Autodesk .3ds format containing the textured model and the camera positions to be used for further interpretation. The orthophoto mosaic is derived at a resolution of 5cm per pixel, which matches the average resolution of the input material. For immediate visualization purposes, the model resolution is diminished to 20 000 polygons, and the texture is downscaled from 8192x8192 pixel to 2048x2048 pixel to be compatible to real time viewing applications. Another .3ds version is saved, along with a georeferenced Collada model with a KML link, and a U3D file contained in a PDF.

3.7 Model Interpretation

The goal of our project was to derive quantitative data of geological structures beyond mere size and distance measurements. To achieve this, we edit the models in Autodesk 3dsMax, which counts among the standard tools of the CGI industry. One major drawback of the software is that geographic references are lost while scale and orientation are maintained. The 3D scenes build upon a cartesian coordinate system in meters but cannot deal with geographic positions due to limitations in computational precision facing large numbers [*Mach et al.*, 2007]. A workaround is to define a reference point at the center of the working area and to arrange all data relative to that point.

To derive quantitative geological information from the model, we follow the same basic route [*Jones et al.*, 2008]: (1) Create an Autodesk 3dsMax helper object, (2) align and scale it to match the geological feature to be measured, (3) read the respective

property of the helper object. The additional benefit is a direct visualization of the measurements, which can later be refined to produce a visually informative illustration.

To measure the orientation of planar structures such as faults, joints or bedding planes, a planar Autodesk "section object" is placed on the model. The orientation of this "section object" is then adjusted until its intersection with the modeled seafloor matches that of the geological structure (Figure 3-5). The more surface relief there is on the model, the more accurate the measurement is. This procedure is not only an easy graphical way to determine the orientation of a planar geological structure; it also has some distinct advantages over, for example, using a compass in the field. Firstly it allows the orientation of features with ill-defined boundaries (such as banks of coarse gravel) to be accurately determined. Secondly it increases the sampling area for the orientation measurement, providing a more representative "average strike and dip" than a point measurement.

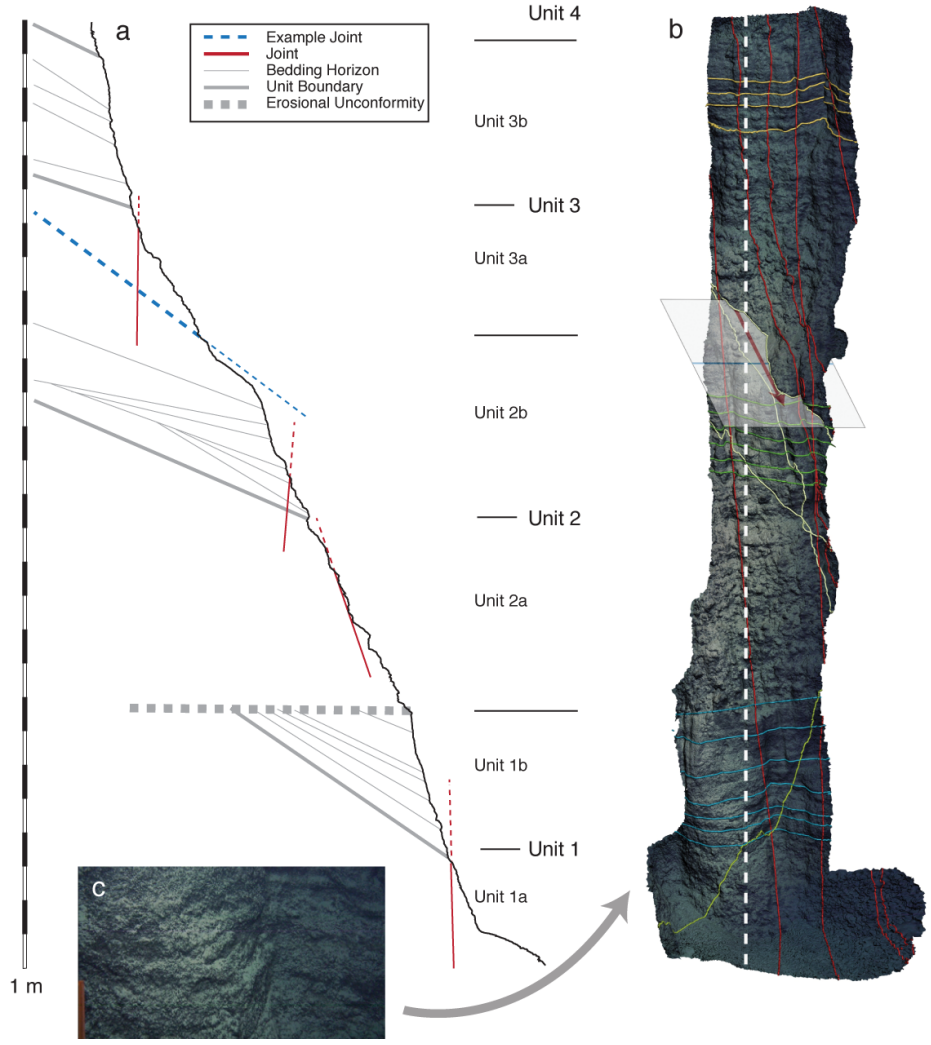

Figure 3-5 *a) Vertical profile, geometric features and stratigraphic units of outcrop 059-47 derived from b) the outcrop model. Lateral and vertical extent match in dimensions. The white dashed line marks the location of the profile. Linears on the model mark the intersection of the rock face and the joints and bedding planes. Note the white semitransparent example joint plane with indicators for strike (line) and dip (arrow) directions. c) shows a frame of the original video sequence at its approximate position in the outcrop (grey arrow).*

On a larger scale, a "master section" can be used to vertically slice the orientated "section objects" along with the outcrop model, to provide a proportionally accurate geological profile through the outcrop which can be directly imported into vector drawing programs (Figure 3-5a).

A grain size estimate can be derived from the models by creating appropriate spheres, ellipses or boxes around the clasts to be measured, and reading the size of the object along the respective axes of interest. Working with a multitude of individual measurements, objects can be batch renamed and assembled into groups while the arrangement of these groups into visibility layers allows order to be maintained. As the textural resolution is higher than the geometrical resolution, clasts can also be measured based on the texture alone, allowing work down to the centimeter scale.

Thanks to the powerful scripting interface of 3dsMax, we developed a suite of import and export scripts for camera poses, grain size data and orientation measurements converted to geologic notation, and to visualize statistical parameters of the reconstruction step. This feature also opens endless possibilities for future, case-sensitive data mining routines as well as further optimization of the models themselves. The scripts are available from the leader author on request.

3.8 Visualization

Next to the quantitative evaluation of the models, another main goal of our project is the enhancement of qualitative analysis by means of appropriate data visualization. Particularly ROV visual data is generally only made available to users in the geologically irrelevant temporal dimension (time stamped rather than georeferenced) meaning that much of the information it contains is difficult to access retrospectively. We wanted to use the 3D models to transpose the ROV visual data set into a geographical frame of reference and so provide access to the video information via its position.

Once more, 3dsMax serves as a powerful editor to prepare the models for use in real time visualization software. But in addition it is also a visualization tool in its own right. Several outcrop models can be loaded at once, and upon re-establishing their relative positions, the correlation of geologic features between adjacent outcrops is as natural as in the field on land. The software allows appropriate visualization geometry to be constructed to illustrate the findings. Camera objects represent the poses in the scene. Since these originate from a film sequence and the ROV followed a track, the path of the ROV across the outcrop can be animated and navigated using a time line.

The pre-processed ROV track record can be visually compared against the reconstructed ROV path, along with digital elevation models of the local bathymetry, still and video footage, and any other 2D or 3D content that can be referenced within the scene's coordinate system [*Kwasnitschka*, 2008]. Thus, this is the only software applied in our study allowing the simultaneous visualization of all our data sets in four dimensions. At the same time, it is the only fully featured application able to actively manipulate the

models in order to create new data products. We use a number of other visualization platforms that mostly allow the passive interaction with the data:

A birds-eye view computer animation of the reconstructed scene is rendered by 3dsMax and added to the original Adobe Premiere video composition allowing the comparison of the video material to a four dimensional, animated map.

Various applications focus on the geospatial aspect of our data, first and foremost an ArcGIS project including the bathymetric map, the ROV track, the photo mosaics of the reconstructed outcrops, event marks such as sample locations and the final geologic map layers. Some limited control over the temporal coordinates of data is available, too.

The bathymetric post processing and visualization software Fledermaus is capable of displaying most of the GIS layers within a four dimensional space. The simulation is based around a bathymetrical height field and the animated ROV track. The mode of visualization is passive as the software is designed primarily for the dissemination of bathymetry data, which has to be pre-processed. A major drawback to date is the restriction of import interfaces to support merely untextured models or monochrome point clouds providing a relatively inferior representation of the outcrop reconstruction effort.

Virtual Globes such as Google Earth and World Wide Telescope digest distribution formats (photo mosaics, .3ds and Collada models using accompanying KML files) directly exported from Photoscan. By the nature of the applications, navigation on a scale of meters is challenging.

An even easier way to examine the unedited reconstructions with low-level tools is the U3D format contained in PDF format, which allows passive interaction with the model through Adobe Acrobat or Reader on any operating system. Quantitative measurements of sizes, angles and even orientation can be made.

KML samples of the data discussed in this article can be downloaded as online supplements.

3.9 Consideration of Errors

In the absence of hard constraints on size and orientation of seafloor features provided by artificial gauges (e.g. parallel laser beams), evaluation of errors in the reconstructed geometry had to rely on indirect methods and assessment calculations in which we vary influences of imperfect navigation and optical distortion.

We assume the positional uncertainty within the navigational data to exceed the drift of the geometrical reconstruction. We infer this from a comparison of the reconstructed orientation data with the orientation data derived from the on-board sensors (certified to be accurate within one degree). The in-situ optical distortion parameters could not be constrained rigorously. Nevertheless, examining the contribution of different parameters to the overall result can elucidate the robustness of the reconstruction method. In

all of the cases outlined below, nonlinear optimization was omitted in order to reveal the differences between acoustic navigation and optical measurements.

For dive 059, with a total distance traveled of 3354 m at an average of 0.076 m/s during 12.2 h (Figure 3-3), the expected drift of the DVL sensor based on manufacturer´s specification lies at +-95 m. Nevertheless, we found that, relative to USBL fixes (which have lower precision (quoted by the manufacturer as 1% of the operational water depth) but should not be subject to time-dependent drift) our instrument deviated by 458 m (24% of the true distance between start and end points) even after cleaning of the DVL record to remove obviously erroneous episodes (e.g., apparent movement of vehicle above its maximum velocity or movement when the video showed the vehicle was stationary). The USBL on R/V METEOR had been calibrated at depths comparable to our deployment relative to a fixed seafloor beacon on a preceding cruise and been shown to have positional RMS error values of 13.7 m (x), 13.3 m (y) and 6.5 m (z) relative to ship's axis.

Table 3-2 *Top to bottom: Pose deviation of the best reconstruction attempt compared to effects of improper filtering, timing, capture interval, missing calibration aligned to the first pose (1) and the attempt to fit the uncalibrated model to the track record (2). Values are averages or root mean square errors of the entire series with respect to the telemetry data.*

	Orientation Differences (Average in °)			**Positional Differences (RMSE in m)**			
	pitch	roll	heading	err x	err y	err z	net
proper	3.2	0.0	2.0	0.10	0.06	0.08	0.14
USBL smooth	-22.3	13.9	50.9	0.24	0.63	0.23	0.71
USBL -3 sec.	-24.5	14.0	57.1	0.17	0.63	0.23	0.69
six sec. early	1.2	-0.9	1.8	0.23	0.21	0.38	0.49
six sec. late	4.7	-0.4	3.8	0.24	0.17	0.27	0.40
0.5 Hz interval	3.1	-0.2	2.3	0.10	0.06	0.09	0.14
missing calib. (1)	20.0	2.9	1.0	0.54	1.41	2.10	2.58
missing calib. (2)	1.9	-4.4	10.7	0.55	0.24	0.51	0.79

In our example model, the overall, timestamp corrected positional offset of the reconstruction against the track is 0.143 m as laid out in Table 3-2. Figure 3-6 shows a graphical representation of such offsets based on motion tracks and illustrates that, despite considerable uncertainties in the overall positioning, the local fit among acoustical navigation and optical derivation of camera poses can be very good. The concentration of positional misfit (Figure 3-6a) around turning points throughout the sequence suggests that high frequency movement has been suppressed during the track synthesis or that the DVL sensor occasionally exaggerated the amount of vehicle motion in cases of fast movement. Meanwhile, the resulting differences in camera orientation stay below 0.1°. The overall accuracy of the reconstruction can be further constrained by a comparison of the camera orientation data to the original track, which yields a cumulative average deviation of 5.2° (Figure 3-6c, Table 3-2).

A vital prerequisite for successful georeferencing is the availability of the high frequency DVL signal. Referencing the data only on the long wavelength component of the USBL signal increases the positional misalignment and suggests a temporal misalignment of 3 seconds between ROV track and reconstructed track towards a new positional alignment optimum resulting in an ever increasing orientation imprecision (Table 3-2). In order to illustrate the importance of correct timing, we compare the alignment at minus six seconds to the alignment at plus six seconds, resulting in comparable deviations in orientation but leading to a considerable degradation in positional accuracy. It should be noted though that the degree of misalignment also depends on the length and complexity of the tracks to be fitted. It is advisable to work with as large a model as possible in order to suppress local disturbances.

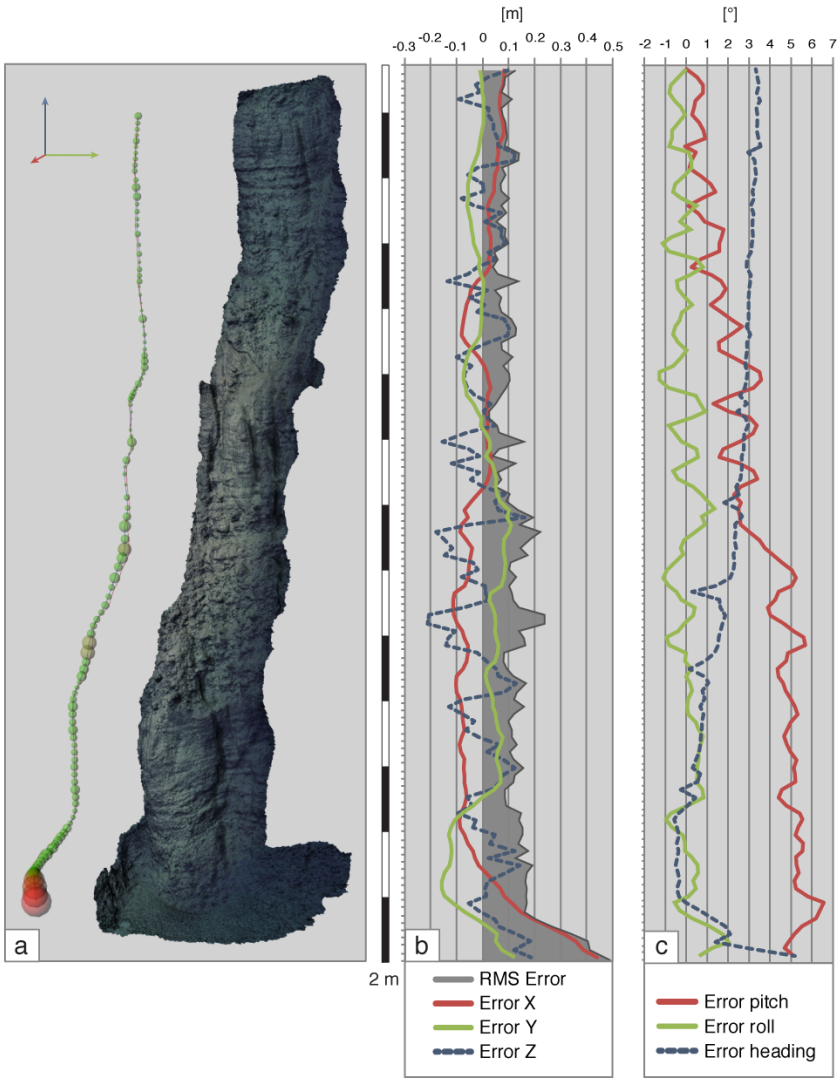

Figure 3-6 *Visualization of the deviation of reconstruction values against the navigational data. a) Spatial deviation along the track path is plotted as a color-coded spherical marker with the radius of the resulting error around the assumed position. b) Spatial deviation of the individual axes along the track including the resulting error vector. c) Orientation deviation along the three axes.*

The temporal resolution required is governed by the amount of overlap between the images and thus by the speed of the ROV over ground. We achieve good results for a one-second interval at vehicle speeds around 0.25-0.5 m/s, although a two or three-

second interval often still provides sufficient information. To investigate effects of varying data coverage on reconstruction quality and to define a minimum shooting interval, we attempted reconstruction from a subset of photographs chosen at ever-increasing intervals. For our setup, we find a sampling frequency of 0.5 Hz (one image every 2 seconds) or higher to be sufficient. The models created at one and two-second sampling intervals are essentially identical in their extent, resolution and orientation (Table 3-2). Longer intervals create coverage gaps that cause the reconstruction to halt. Since the algorithm does not look for unlinked clusters beyond the first one it finds, the remaining images must be identified and a reconstruction may be attempted in a new project. Such unlinked snippets of the entire outcrop must then be individually georeferenced, introducing additional errors.

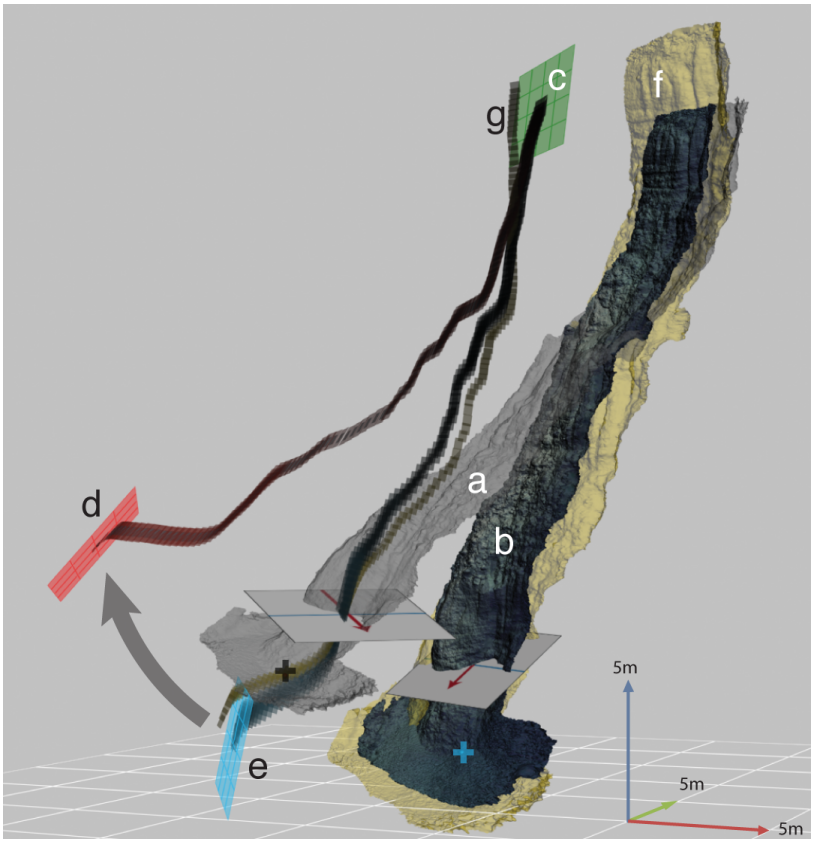

Figure 3-7 *Warping effects due to missing lens distortion parameters (a) superimposed on the correct reconstruction (b). Both models have been aligned at the first camera pose (c), where deviations in the model geometry and position are already apparent. The largest dislocation (gray arrow) in position and camera angle is found between the last images, (d) showing the warped path and (e) the correct path, deviating 29° in pitch, 8° in roll and 1.8° in heading. Crosses mark the location of a corresponding feature referenced in the text. Measurements of a corresponding bedding plane (white planes) indicate a strong deviation in strike (67°, lines) and dip (12°, arrows). The light transparent model (f) and camera planes (g) illustrate the model, which has been aligned to the track coordinates, resulting in positioning and also scaling errors. The white grid represents the true horizontal plane.*

To illustrate the effect of an erroneous camera calibration we removed the calibration data for the nonlinear lens distortion parameters K1-K3 [*Brown*, 1966]. This resulted in a warping of the scene along the x-axis expressed by a propagating deviation of the camera tilt, the location of the point of view and a corresponding warping of the model around the x-axis and vertical stretching. Instead of using the usual rigid alignment to

the known vehicle track, we superimposed the initial (i.e. the topmost) camera poses of the "correct" (i.e. with camera calibration) and warped reconstructions to observe the propagation of drift throughout the model. Deviations developed as given in Table 3-2 resulting in an offset of 7.6 m in position (-4.6 m in x, 5.1 m in y and -3.2 m in z) for a feature at the bottom of the model. The largest offset is experienced for any orientation measurements of faults and bedding planes towards the lower end of the model, which are effectively rendered useless as illustrated in Figure 3-7. Once the usual rigid body alignment to the vehicle track was carried out, the misfit was distributed throughout the model but should still be regarded as unacceptable (Table 3-2). Moreover, a strong deviation in scale becomes apparent. This experiment underlines the vital importance of proper calibration of intrinsic camera parameters.

3.10 Lessons Learned

Having developed a workflow based on already existing data, we present here a number of observations and best practice rules to be applied during data acquisition, which, with minimal additional effort when preparing and carrying out a ROV dive, can greatly improve the quality and quantity of subsequent reconstructions.

First and foremost, the quality of reconstructed models depends critically on the quality of the camera technology used to acquire the data. Using a high-resolution sensor with a low noise level is the critical factor, as poor image quality significantly contributes to erroneous matching of images. The optical system should be as simple as possible, utilizing a lens with a very wide depth of focus or fixed focus balanced with a small relative aperture.

Although an optically corrected "dome port" window for the camera pressure housing is ideal, a minimal requirement is that corrections can be made for optical aberrations due to the air/glass/water interface, requiring in-situ calibration of the camera image using appropriate test objects (e.g., a checkerboard).

While the wish to invest in multifunctional deep-diving camera equipment to satisfy a range of user requirements is understandable, it should be realized that the use of zoom optics during photogrammetry is highly detrimental and can only be accommodated if focal length can be logged accurately, and the concomitant changes in optical aberration calculated, for every picture taken. Additionally the reconstruction software must be able to incorporate these data into its model-generation process; otherwise zoom will be interpreted as motion closer to the object, rendering track alignment impossible.

Photogrammetry is a computationally very intensive process. Our project was processed on a workstation equipped with a twin Intel Xeon Processor, 12 GB RAM and one ATI Crossfire 4800 Series graphics card (which is used with the GPU features of Photoscan), which matched our HD video source in required performance. A crucial bottleneck was the amount of RAM available. With this hardware, a 200 000 polygon reconstruction based on one-second samples of two minutes of HD video required just over four hours to process. The camera should be held orthogonal to the objects, angles larg-

er than 45° may lead to a failure in reconstruction or to inaccuracies. Rapid movements (which lead either to blurring of the images or inaccuracies in the vehicle´s position and attitude determinations, possibly as a result of timing errors) should be avoided. An ideal platform for photogrammetric survey in the deep sea would move on a continuous gridded track ("mowing the lawn"). Tracks should cross each other frequently or ideally run parallel with considerable overlap.

Finally, it should be noted that our selection of software to pre-process and interpret the data is to be regarded as preliminary. Originating from the entertainment industry, many programs are barely able to cope with the amount of data generated at sea. The long duration of ROV dives requires workarounds in video editing, and 3D animation packages also require a rescaling of geographic coordinates and time (e.g. minutes expressed as seconds to fit a limited timeline).

3.11 Conclusion

We present a review of available software and a practical workflow to virtually replicate morphological, geological and biological features of the seafloor accurately enough to conduct scientific studies. Our aim was to create synthetic model visualizations of the seafloor to provide more geologically useful and quantitative information than individual video frames. Although we recognize that technical improvements can be made in order to further substantiate and calibrate the interpretations inferred from our surveying method, we have demonstrated that a georeferenced reconstruction of the features imaged during a video transect is (a) possible and (b) yields quantitative geological information not otherwise accessible. The example presented shows the potential of quantitative geoscientific measurements and fieldwork on the deep ocean floor provided there is sufficient coverage by adequate surveying. Similar benefits can be expected for biological habitat mapping as well as for a wide variety of industrial seabed monitoring applications. At the same time, our method is capable of processing archived data meeting minimal standards in order to re-evaluate remote targets or to monitor changes at sites of high temporal variability such as hydrothermal vents. In addition, the method provides a means to re-cast ROV video data in a geographical rather than a time-line reference frame.

Acknowledgements

We would like to thank the Captain and crew of R/V METEOR for their excellent assistance at sea, and the crew of ROV Kiel6000 for their support during the development of such a specific application, and for clarifying many engineering details. T. Kwasnitschka would like to thank Anne Jordt for an introduction to underwater photogrammetry and many valuable comments. This work was carried out within the Jeddah Transect project (www.jeddah-transect.org).

References

Beall, C., B. J. Lawrence, V. S. Ila, and F. Dellaert (2010), 3D reconstruction of underwater structures, *IEEE Robotics and Automation Society (RAS)*.

Brown, D. C. (1966), Decentering Distortion of Lenses, *Photometric Engineering*, *32*(3), 444–462.

Condell, J., G. Moore, and J. Moore (2006), Software and Methods for Motion Capture and Tracking in Animation,

Gaich, A. (2001), Geotechnische Datenerfassung unterstützt durch ein 3D Computer Vision System.

Johnson-Roberson, M., O. Pizarro, S. B. Williams, and I. Mahon (2010), Generation and visualization of large-scale three-dimensional reconstructions from underwater robotic surveys, *J. Field Robotics*, *27*(1), 21–51.

Jones, A., N. Cantin, R. Berkelmans, and B. Sinclair (2008), A 3D modeling method to calculate the surface areas of coral branches, *Coral Reefs*, *27*, 521–526, doi:10.1007/s00338-008-0354-y.

Kreylos, O., G. Bawden, T. Bernardin, M. I. Billen, E. Cowgill, R. Gold, B. Hamann, M. A. Jadamec, L. H. Kellogg, and O. Staadt (2006), Enabling scientific workflows in virtual reality, Proceedings of the 2006 ACM international conference on Virtual reality continuum and its applications, 155–162.

Kwasnitschka, T. (2008), *Stratigraphy of the Old Ilopango Formation, El Salvador, and 3-D visualization of the sedimentary and tectonic structures*. Christian-Albrechts-Universität zu Kiel.

Mach, R., P. Petschek, and S. Ervin (2007), *Visualization of Digital Terrain and Landscape Data*, Springer.

Pizarro, O., and R. M. Eustice (2009), Large area 3-d reconstructions from underwater optical surveys, *Oceanic Engineering*, *34*(2), 150–169.

Sedlazeck (2009), Supporting Underwater Archaeology by 3D Reconstruction from Underwater Images, pp. 1–10, Kiel.

Sedlazeck, A., and R. Koch (2011), Calibration of Housing Parameters for Underwater Stereo-Camera Rigs.

Sedlazeck, A., K. Koser, and R. Koch (2009), 3D reconstruction based on underwater video from ROV Kiel 6000 considering underwater imaging conditions, pp. 1–10, IEEE.

Snavely, N., I. Simon, M. Goesele, R. Szeliski, and S. M. Seitz (2010), Scene reconstruction and visualization from community photo collections, *Proceedings of the IEEE*, *98*(8), 1370–1390.

Triggs, B., P. McLauchlan, R. Hartley, and A. Fitzgibbon (2000), Bundle adjustment—a modern synthesis, *Vision algorithms: theory and practice*, *1883*, 298–372, doi:10.1007/3-540-44480-7_21.

Verhoeven, G. (2011), Taking computer vision aloft–archaeological three-dimensional reconstructions from aerial photographs with photoscan, *Archaeological Prospection*, (18), 67–73.

Yoerger, D., A. Bradley, M. Jakuba, and C. German (2007), Autonomous and remotely operated vehicle technology for hydrothermal vent discovery, exploration, and sampling, *Oceanography*, *20*(1), 152–161.

4 Stratigraphy and Physical Volcanology of Deep-Sea Pyroclastic Deposits at Charles Darwin Volcanic Field, Cape Verdes

Tom Kwasnitschka*, Thor H. Hansteen, Colin W. Devey, Steffen Kutterolf and Armin Freundt

GEOMAR Helmholtz Centre for Ocean Research Kiel
Wischhofstr. 1-3, D-24148 Kiel, Germany
*tkwasnitschka@geomar.de

(This article has not yet been submitted for publication. Please note that it contains its own reference list.)

Abstract

Incipient stages of seamount formation, including two types of explosive volcanism, were identified in a submarine field of volcanic cones and pit craters called Charles Darwin Volcanic Field (CDVF) located at about 3600 m depth on the lower southwestern slope of the Cape Verdean Island of Santo Antão. We examined two of these submarine volcanic edifices (Tambor and Kolá), each featuring a pit crater of 1 km diameter, using photogrammetric reconstructions derived from ROV-based imaging followed by 3D quantification using a novel remote sensing workflow. The measured and calculated parameters of physical volcanology derived from the 3D model enabled quantitative field work in unprecedented detail for deep-sea outcrops.

Tambor cone, which is 2500 m wide and 250 m high, consists of dense monogenetic medium to coarse-grained volcanics that are highly fragmented by thermal and viscous granulation upon contact with seawater. Tangential joints indicate subsidence of the crater floor after primary emplacement. Kolá crater shows a negative relief, with step wise sagging features on the inner flanks as well as a complicated succession of highly fragmented deposits, including spheroidal juvenile lapilli, likely formed by spray granulation. The eruption entrained blocks of gabbroic country rocks, likely abraded by fluidization within the vent, with diameters of up to 20 cm that were laterally transported for hundreds of meters through water. In spite of the great depth, both edifices feature dense but highly fragmented volcanic deposits with an unexpected combination of large clast sizes and wide clast dispersal. This suggests an energetic eruptive environment that may have some similarities with that seen in pyroclastic eruptions on land.

4.1 Introduction

The mechanisms or even existence of volcanic activity that strongly fragments rock or magma in the deep sea have been controversially discussed since the early days of deep-sea volcanology [*Fisher*, 1984; *Head and Wilson*, 2003]. Nevertheless, weakly explosive volcanic products have been reported from mid-ocean ridge settings [*Clague et al.*, 2003a; *Sohn et al.*, 2008; *Helo et al.*, 2011], ocean island settings [*Clague et al.*, 2003a; 2003b; *Schipper et al.*, 2010] and subduction related regimes [*Chadwick et al.*, 2008]. Most of these deposits are fine grained and contain volcanic glass, some of which is described as Limu-o-Pele [*Clague et al.*, 2000], they show wide dispersal of particles (beyond the ballistic range in water) and are deposited across multiple underlying facies, often showing mantle bedding [*Pontbriand et al.*, 2008].

The prime consideration has been that the density of water vapour varies in a strongly non-linear way with pressure in the 1-300 bar region, whereas liquid water is essentially incompressible over this pressure interval. This means that even at moderate water depths, the well-established mechanisms which drive explosive volcanism on land by producing large volumes of steam from relatively small volumes of water during water-magma interaction [*Wohletz*, 1983; *Zimanowski et al.*, 1995; 1997; *Lorenz et al.*, 1999; *Buettner et al.*, 2006] appear problematic. At pressures above the critical point of seawater (407°C, 298.5 bar ≈ 3000 m b.s.l. [*Bischoff and Rosenbauer*, 1985]), there is no density difference between a vapor and a liquid phase. Two different models have, therefore, been developed to provide a mechanism for effective fragmentation at great depth: 1) Processes generally linked to the contact of magma with seawater leading to thermal quench granulation [*Lonsdale and Batiza*, 1980; *Smith and Batiza*, 1989; *Maicher and White*, 2001; *Sonder et al.*, 2011], oscillation of a super-critical fluid film [*Wohletz*, 2003] and steam-driven bubble expansion [*Clague et al.*, 2000; *Maicher et al.*, 2000; *Schipper et al.*, 2010] as well as 2) a magmatic model in which the fragmentation is primarily driven by CO_2-slugs rupturing the magma either in the conduit or at the vent [*Hekinian et al.*, 2000; *Head and Wilson*, 2003; *Clague et al.*, 2003a; *Clague*, 2009].

Not only the fragmentation mechanism but also the processes leading to widespread transport of the particles up to kilometers away from the vent remain obscure [*Head and Wilson*, 2003; *Barreyre et al.*, 2011]. Clague et al. [2009] argued that an equivalent to subaerial eruption columns might be found in plumes of hot water entraining volcaniclasts, rising either due to heat transfer from the volcanic products themselves [*Palmer and Ernst*, 1998] or propelled by a massive release of hydrothermal fluids [*Baker et al.*, 1987; *Cann and Strens*, 1989; *Lupton et al.*, 1999].

Although more and more deep-sea volcaniclastic deposits are discovered, the assessment of eruption and transport mechanisms is hampered by the difficult accessibility of the few known outcrops and limited number of samples lacking broader vertical and horizontal stratigraphic context [e.g. *Schipper et al.*, 2010]. The extent of such deposits is frequently assessed by correlation of backscatter maps with conditions at the few sites surveyed by submersible or ROV [e.g. *Fouquet et al.*, 1998; *Hekinian et al.*, 2000]. Some analogies have been drawn to uplifted and subaerially exposed outcrops of ancient sub-

marine volcanic deposits [*Cashman and Fiske*, 1991; *Mueller and White*, 1992; *Kano*, 2003; *Busby-Spera*, 2005] for which the original water depth, however, can be difficult to constrain. Likewise, shallow submarine eruptions [*Wright et al.*, 2002; *Deardorff et al.*, 2011], especially those producing pumice [*Baker et al.*, 2002; *Allen et al.*, 2008], are no direct equivalent due to the above-mentioned role of water pressure, although some of them represent good examples of submarine survey methods for complex stratigraphies [*Carey and Sigurdsson*, 2007; *Hekinian et al.*, 2008].

Here we present results of a survey of a recently discovered submarine volcanic field formed by incipient seamount volcanism and featuring a great variety of volcaniclastic edifices, situated at a depth of around 3600 m in the Cape Verdean archipelago. The large edifice sizes, the extent of volcaniclastic deposits and the coarse grain sizes encountered within single deposits challenge the working models for underwater particle emplacement developed so far. The deposits crop out in very well exposed cliffs, providing good accessibility to remotely operated vehicles so that a wide spectrum of deep-sea volcanic deposits can be studied within a small area, allowing for comparison between localities. Applying a recently developed photogrammetric reconstruction workflow [*Kwasnitschka et al.*, 2012] we have produced digital models of the surveyed outcrops. On this basis, and aided by samples taken by ROV, we are able to quantify the extent and orientation of beds for single outcrops, leading to a correlation of facies across each edifice. Grain size measurements of coarse clast fractions help confirm the correlation results. Analysis of faults and joints suggests that syneruptive edifice inflation and later subsidence occurred.

4.2 Recent Volcanic Activity at Charles Darwin Volcanic Field

The Cape Verde Archipelago is situated some 600 km from the West African coast, between 15°N and 17°N. The crescent shaped group of 10 major volcanic islands and associated peripheral seamounts form the tip of the Cape Verde Rise, a bathymetric swell associated with mantle plume activity [*McNutt*, 1988; *Holm et al.*, 2006]. The near-stationary nature of this plume relative to the motion of the African Plate has produced a complex age progression in two westward branches of island formation [*Holm et al.*, 2006] (Figure 4-1). Consequently, the most recent subaerial volcanic activity (since 500 ka, [*Plesner et al.*, 2003]) can be found on the islands of Fogo, Brava and Santo Antão, along with various submarine edifices in the northwest and southwest of the archipelago: While Cadamosto Seamount shows strong signs of contemporary activity [*Grevemeyer et al.*, 2010] of the southern branch, a northern equivalent may be identified, together with other seamounts of the northwest, in the Charles Darwin Volcanic Field (CDVF, Figure 4-1).

Located on the lower southern flank 25-40 km off the island of Santo Antão, this group of volcanoes was discovered during RRS Charles Darwin cruise 168. The CDVF lies towards the southern edge of a massive debris avalanche deposit associated with the Tope de Coroa slope failure events, which originated from western Santo Antão and imparts a gentle 2° southwest slope to the surrounding terrain.

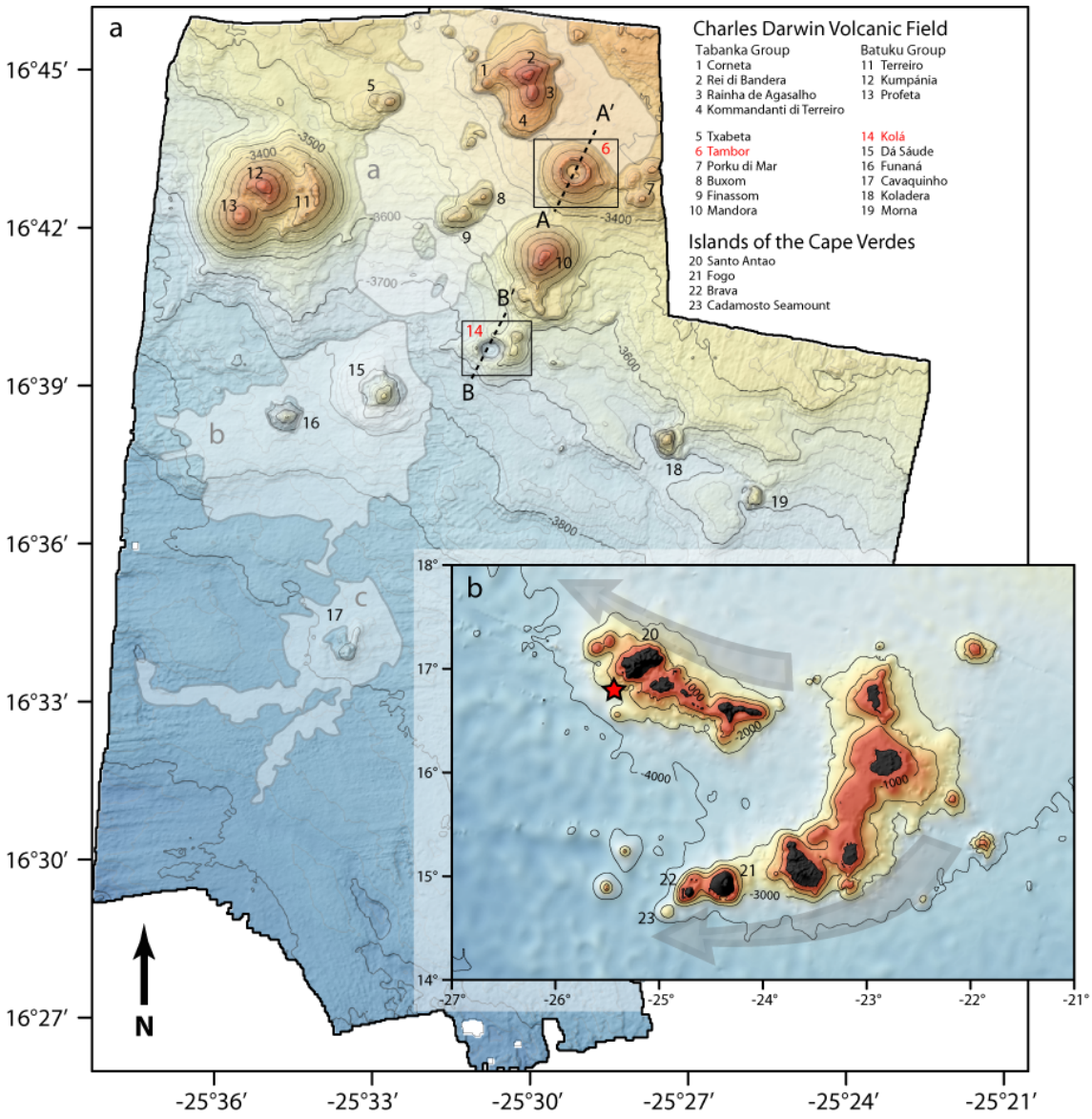

Figure 4-1 *a) Bathymetric map of CDVF off Santo Antão based on data gathered during cruise M80/3. Grey fields and letters mark the extent of the a) Tabanka, b) Dá Saude and c) Cavaquinho volcanic terrains identified from backscatter and verified during ROV dive 059 as lava flows. Black rectangles mark the extent of Figures 4-2 and 4-3. b) GMRT map of the Cape Verdean Archipelago including features mentioned in the text (numbered). Grey arrows show the westward age progression of subaerial volcanic activity. A red asterisk marks the position of the CDVF off Santo Antão. Islands are drawn in black. Dashed lines indicate profiles of Figure 4-4.*

The CDVF postdates this event, which has been dated at > 0.5 Ma [*Masson et al.*, 2008]. A cluster of 10 solitary or compound volcanic cones, 200 m to 700 m high and of base diameters between 1 km and 6 km forms a central cone field, measuring 20 km across. Multibeam backscatter data indicate that a high backscatter field volcanic deposits covers the terrain amidst these cones. These deposits likely originated from the northern (i.e. uppermost on the slope of Santo Antão) Tabanka group of volcanoes since they surround it, extending downslope in between the other cones. Thus the flows are morphologically younger than the surrounding cones. Two similar fields line the Dá Saude and Cavaquinho cones downslope (Figure 4-1).

The majority of these volcanoes are cones and lava domes with no visible crater depressions. The fact that many eruption centers overlap each other is evidence for a range of ages. The morphology of the Tambor and Kolá eruption centers clearly differs from the other edifices by featuring large central depressions of about 1000 m diameter.

4.3 Surveying and Sampling

We re-mapped the CDVF using the Simrad EM 120 multibeam on board R/V METEOR during cruises M79/3 and M80/3 yielding a data set that was slightly oversampled to a resolution of 25 m. These maps were used as the basis for planning ROV dives to investigate the deposits making up the Tambor and Kolá craters. The ship-based echo sounder was unable to reliably map the steep crater walls, so that the true crater wall morphology only became apparent during the ROV dives. As a result, the discovery of the exposures discussed here occurred by accident upon examining the steep inner crater walls.

Tambor was investigated during ROV dive 059 (Figure 4-2, Appendix 1), covering the southwestern outer slope and the northwestern quadrant of the inner crater wall including six vertical transects. The total distance traveled on the seafloor was 3354 m. The recordings of the HD camera, the navigation cameras and the stereo camera rig were used to reconstruct 13 3D-models covering about 1350 m^2 of outcrop face using photogrammetric techniques [*Kwasnitschka et al.*, 2012]. Reconstructions used for quantitative analysis were based on source data retrieved by the HD cameras. A number of outcrops were reconstructed from the lower navigation camera but remained poorly aligned and are used here for illustrative purposes only.

During M80/3, eleven samples were taken on ROV dive 059 using the manipulator and a variety of sediment scoops. Six of these samples were extracted from rock successions exposed in vertical walls (059-1 / 059-7 - 11) whereas five samples (059-2 - 6) were picked from talus on the crater floor. The sample spectrum includes lava fragments, weakly to moderately cemented volcaniclastics facies, compacted silts and a talus mixture composed of foraminifer ooze and volcaniclastics.

At Kolá (Figure 4-3, Appendix 1), ROV dive 071 was carried out entirely within the crater whereas the perimeter remained uninvestigated. The track transected the crater from WSW to ENE, yielding three vertical profiles of each of the two crater rims visited. A lateral distance of 3440 m was covered including transit across the northwestern quadrant of the crater floor. Reconstruction using the upper and lower navigation cameras and the HD video camera yielded 19 photogrammetric models covering 1200 m^2 of outcrop face. For quality reasons only nine models from the HD camera were used for quantitative evaluation. In total 17 rock- and one sediment sample were taken by the ROV, complemented by 9 samples from a dredge haul along the northwestern crater slope, following the ROV dive. All ROV samples except 071-001 - 005 and 071-010 were taken from in situ deposits.

Figure 4-2 *(following page) Bathymetric map of Tambor Cone (Dive ROV 059, red line) with 10 m contours. Insets show an interpolated geological map, the location of the reconstructed rock walls, sample locations (sample 1 on big map!), tectonic interpretation (tangential joints in blue, radial joints in green) and dip direction of bedding.*

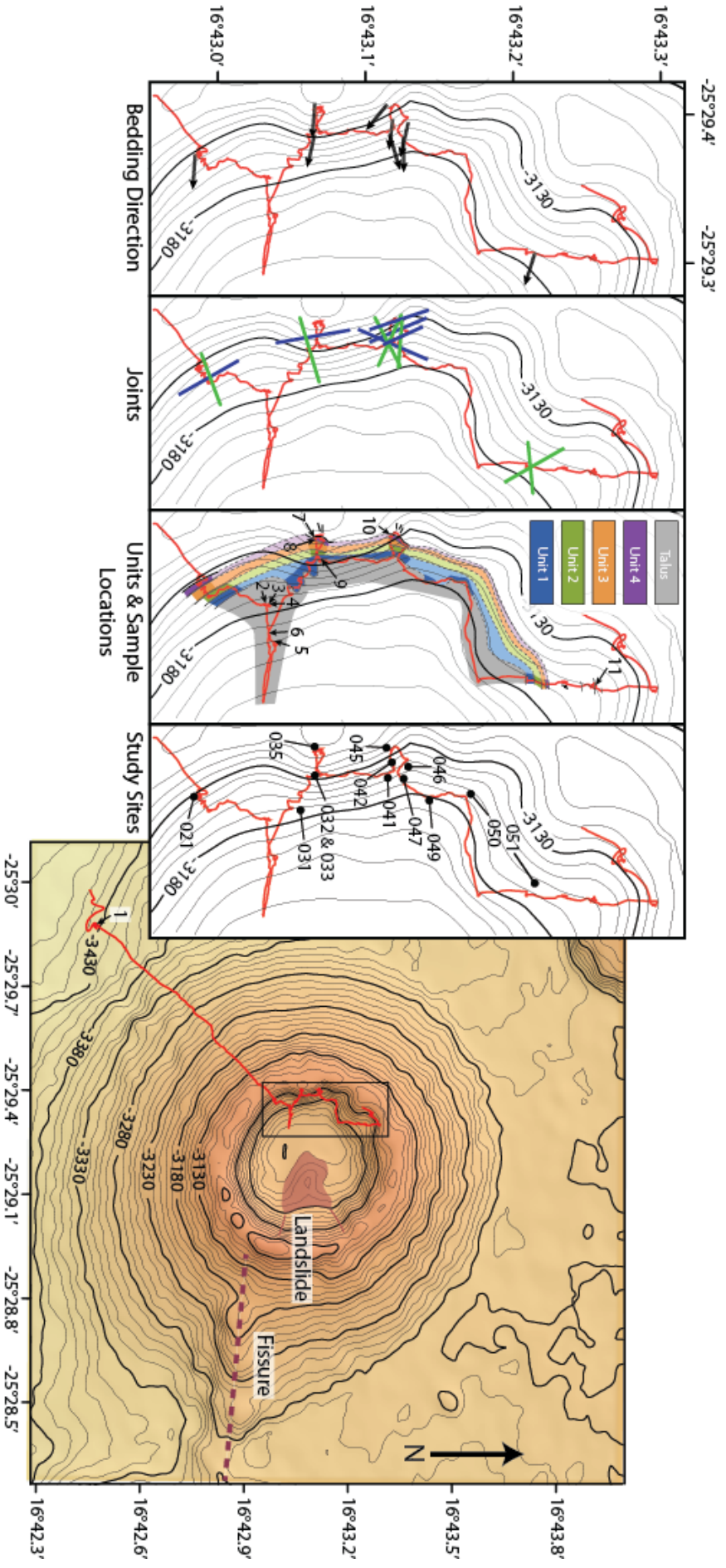
Bedding Direction
Joints
Units & Sample Locations
Study Sites
Unit 1
Unit 2
Unit 3
Unit 4
Talus
Landslide
Fissure
N
-3130
-3180
-3230
-3280
-3330
-3380
-3430
16°43.3'
16°43.2'
16°43.1'
16°43.0'
-25°29.4'
-25°29.3'
16°43.8'
16°43.5'
16°43.2'
16°42.9'
16°42.6'
16°42.3'
-25°30'
-25°29.7'
-25°29.4'
-25°29.1'
-25°28.8'
-25°28.5'

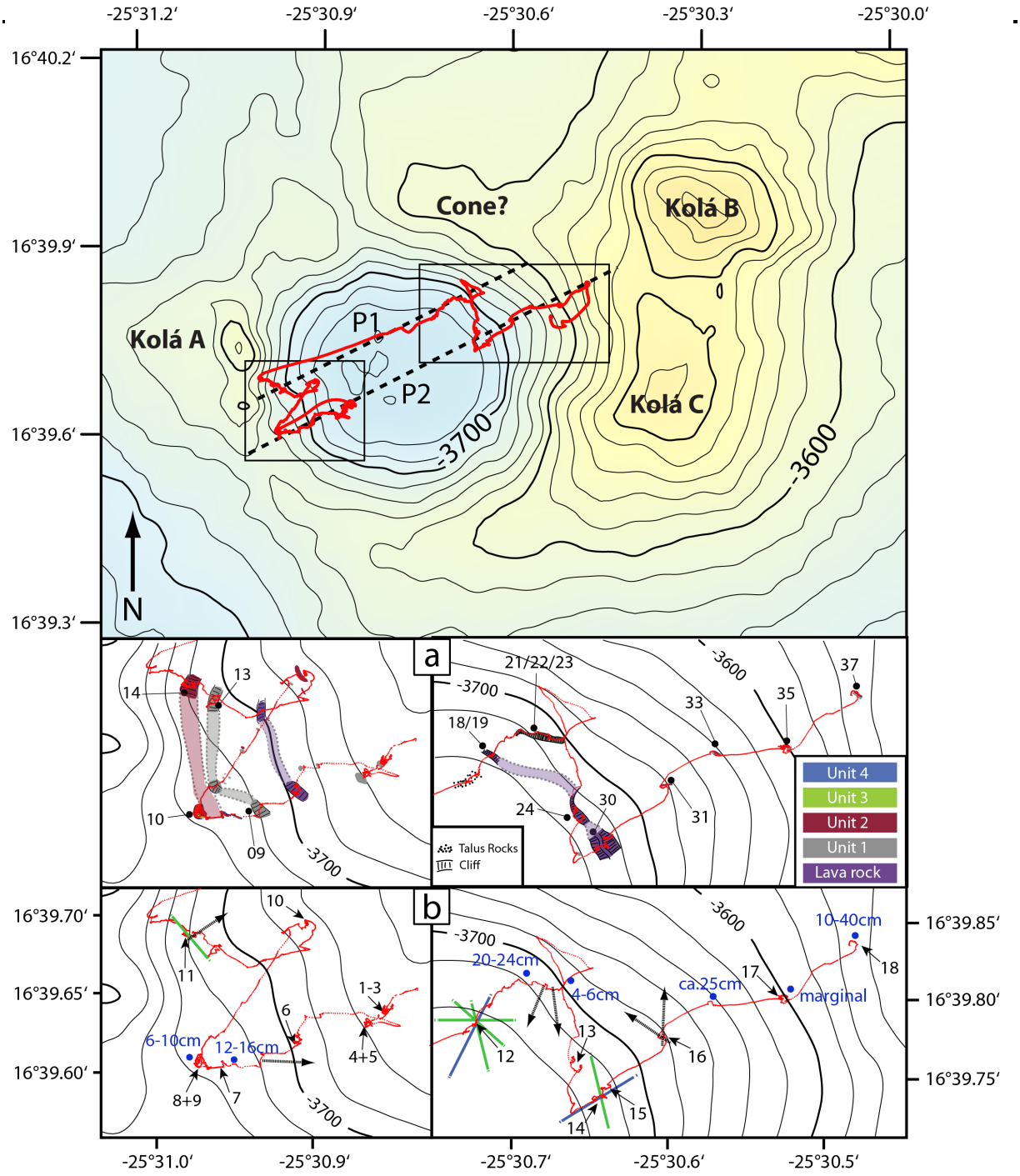

Figure 4-3 *Bathymetric map of Kolá crater, dive track (red) and location of the profiles contained in Appendix 1 (P1, P2, dashed black lines). Inset figures show a) the location of study sites on a geological map, b) the dip direction of bedding (dashed arrows) and the thickness of unit 4 at selected outcrops (blue dots), the sample locations (black arrows) and the strike of radial (blue) and tangential (green) joints across the crater.*

Tambor is a circular cone with a base diameter of 2500 m and 225 m to 250m high, (3060 m bsl.), and has a central depression of 900 m diameter that is 100 m deep. A tongue-shaped morphological high (320 x 200 x 34 m) extends from the foot of the eastern crater wall across the crater floor and may have formed by partial collapse of the eastern inner crater wall (Figure 4-2). On the southeastern outer flank of Tambor, a 200 m wide volcanic ridge extends towards the Porku di Mar cone field 2.8 km to the east.

The crater of Kolá is comparable in size (1000 m diameter, 3600 m – 3760 m depth) to Tambor but morphologically more complex (Figure 4-3). It is situated on a small plateau, within the southern outskirts of a field of smaller cones and lava flows associated with the Mandora cone. Contrary to Tambor cone, the Kolá crater reaches below the level of the surrounding seafloor, i.e. the prevolcanic basement (Figure 4-4). The western, eastern and northeastern crater rim of Kolá cuts through three older volcanic cones (Kolá A, B and C, respectively) that surround the younger Kolá vent site. Due to the morphological complexity of the surrounding cones and the situation on a morphological high, and given the resolution of the bathymetric chart available, it is not possible to determine whether ejected material surrounds the crater and what its thickness and volume would be. The most conservative figure for crater depth is 120 m, not taking into account the height difference to any neighboring volcanic edifice that would increase the depth to up to 270 m. The inner walls are not continuous, but segmented into morphological steps, presumably formed during tectonic subsidence of the crater floor. Each step is covered by an extensive marine sediment blanket such that most outcrops are formed by the steep cliffs.

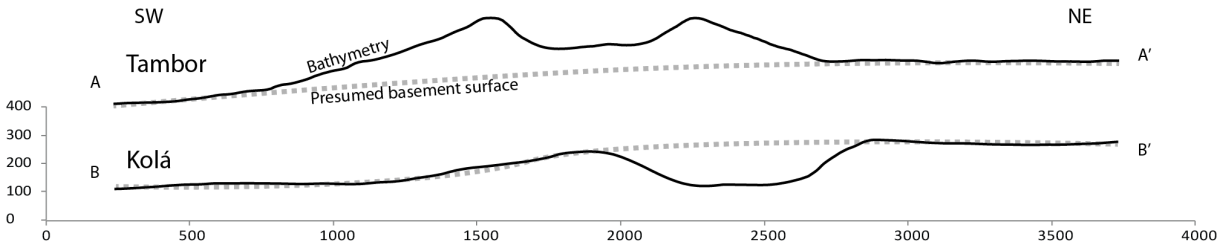

Figure 4-4 *Profiles of the Tambor and Kolà edifices (compare Figure 4-1 for location of the sections) show that Tambor is a constructive edifice while Kolá is a morphologic depression with respect to the presumed pre-eruptive sea floor level. Scale units are in meters.*

4.4 Results for the Tambor Volcanic Cone (Dive ROV 059)

4.4.1 Stratigraphy and Samples

The Tambor stratigraphy was developed on the basis of study sites 046 and 047 that are on top of each other, covering the entire height of the crater wall (Figure 4-2). For all study sites referred to below, profiles of outcrop walls along with stratigraphic correlation diagrams can be found in the electronic supplements to this article and are referred to as a reference. The succession of deposits was subdivided based on the back-weathering relief of the rock face and on visible grain size distribution. Since unit boundaries could not be followed across outcrops, thickness changes of units around the crater perimeter were not quantified.

The evaluation of digital outcrop reconstructions allows the application of quantitative geological and sedimentological methods such as grain size analysis, although the results are, at the moment, not as precise as sieving results. Grain size statistics were gathered using a point counting scheme analogue to Van der Plas and Tobi [1965], applying a square array of 361 points with a point spacing of 10 cm to avoid double count-

ing of large clasts. Image resolution, defocusing, illumination or obstruction by marine sediment set a lower grain size detection limit of -3 ϕ (8 mm, [*Wentworth*, 1922]), the level at which single clasts could still be reliably measured (Figure 4-5) although visual clues could occasionally be gained down to -0 ϕ (1 mm).

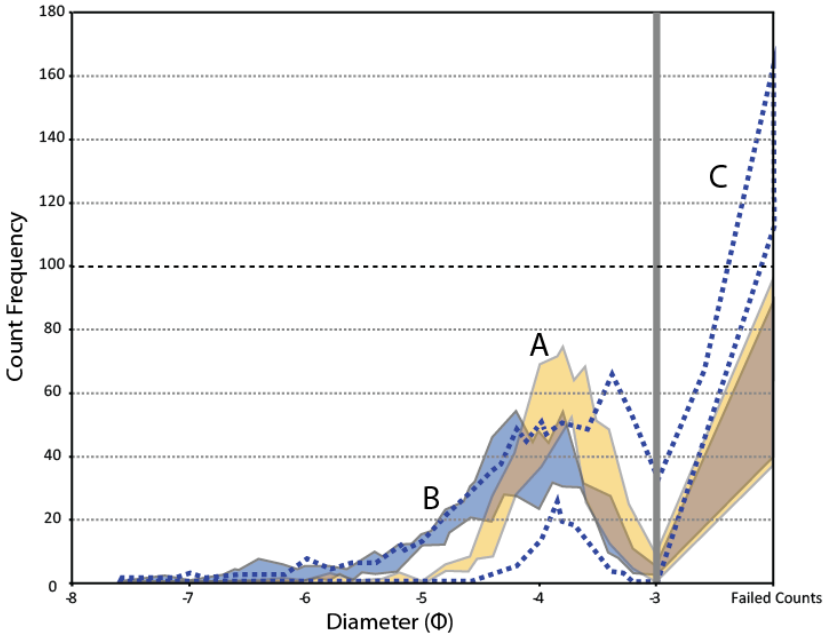

Figure 4-5 *Grain size histogram for Tambor in Phi (ϕ) units. The samples are divided into two groups of different grain size distribution (A and B) and an additional class of measurements for which the number of outliers (>100, dashes) is too high to reliably classify the distribution (C). The cutoff for statistical analysis (grey bar) was defined at -3 ϕ, equaling the effective resolution of the textures.*

Any grid points with components below this threshold were added to the number of counts which failed due to marine sediment cover occluding the deposit, or the above mentioned camera limitations. The amount of failed counts ranges from 9 % to 62 %. Therefore, we cannot discuss sorting based on the complete grain size distribution. [e.g. *Inman*, 1952]. Instead, we used for Tambor a simplified classification scheme of three deposit classes based on the subordinate coarse fractions resolved by our method (Figure 4-5). Class A shows a pronounced unimodal distribution of the grain sizes between -7.5 ϕ and -3 ϕ (128 mm and 8 mm), with a span of medians between -4.1 ϕ and -3.8 ϕ (17 mm and 14 mm diameter), i.e. the majority of clasts in the deposit consist of coarse lapilli, and only very little clasts with sizes over -5 ϕ. Examples for such a deposit are units 047-2,4 and 6 (Figure 4-6 a,b and c). Class B also is unimodal, with a span of medians between of -4.3 ϕ and -4.2 ϕ (20 mm and 18 mm diameter) and a well developed tail up to block sizes of -7 ϕ (12.8 cm diameter), an example of which is unit 047-3 (Figure 4-6a). Where failed counts account for more than several tens of percent, the grain size distribution remains unknown. To fall into either of these classes, we set an arbitrary limit of failed counts at 100, i.e. 27% of possible counts for a sample. Above this number, the grain size distribution remains unknown, forming class C despite that many such samples show an indication towards class A or B.

The crater wall segments studied at Tambor comprise clast-supported volcaniclastic deposits with variations mainly in grain size and degree of compaction. The deposits vary between densely packed and partly cemented lapilli stone and breccia. Clasts are sub-angular to rounded showing irregular textures. Four units were identified, each containing a lower, mostly massive class B layer followed by a stratified class A layer. Particularly the upper A type layers frequently contain lenses that are variably coarser or finer grained than the host layer A and undulating bedding with amplitudes of a few dm at wave lengths of a few meters.

Sites 046/047 and 041 are just 20m apart but there is only one unit boundary (between units 1 and 2) that can definitely be correlated. Above this boundary, layer thicknesses vary greatly between these outcrops suggesting strong lateral changes in bed characteristics.

The lowermost 2.4 m thick subunit (unit 1a) is massive, class C breccia mainly comprising dense and angular clasts. It is poorly exposed and partly buried by the sedimentary talus of the crater bottom (Figure 4-6). The contact with the overlying unit 1b (class A) is sharp and marked by the absence of the coarsest grain size fractions. Unit 1b shows upward fining towards a lapillistone over the first two meters with a constant grain size distribution over the upper three meters. Beds between 20 cm thickness in the lower and 10 cm in the upper part do not show grain size shifts. This subunit drastically increases in thickness in the lower parts of the northern outcrops (site 050). The contact with unit 2a is very sharp and possibly erosive (Figure 4-6a).

Unit 2a consists of a coarse class B, 5.2 m thick breccia. It appears massive and moderately well sorted in its lower half. Stratification of parallel to sub-parallel horizons characterized by variations in maximum grain size develops in the upper half. Unit 2b, a 6.5 m thick class A lapillistone, has a sharp back-weathered boundary with the underlying unit. Its appearance is similar to unit 1b, with pronounced beds of 30 – 40 cm thickness and an upward transition into finer, well-consolidated beds of 10 – 20 cm width each (Figure 4-6b).

The contact with unit 3a is obscured by the intersection of a normal joint plane and poor preservation of adjacent deposits (Figure 4-6b). Unit 3a is a class C breccia of 2 m thickness showing poorly developed inverse grading of the coarsest clasts. Unit 3b is better sorted than 3a. It appears massive and brecciated in its lower 2.5 m, but upwards develops sub-parallel layering. The upper 4 m of Unit 3b consists of well-consolidated class A lapillistone and show a pronounced layering between 5 and 20 cm thickness (Figure 4-6c).

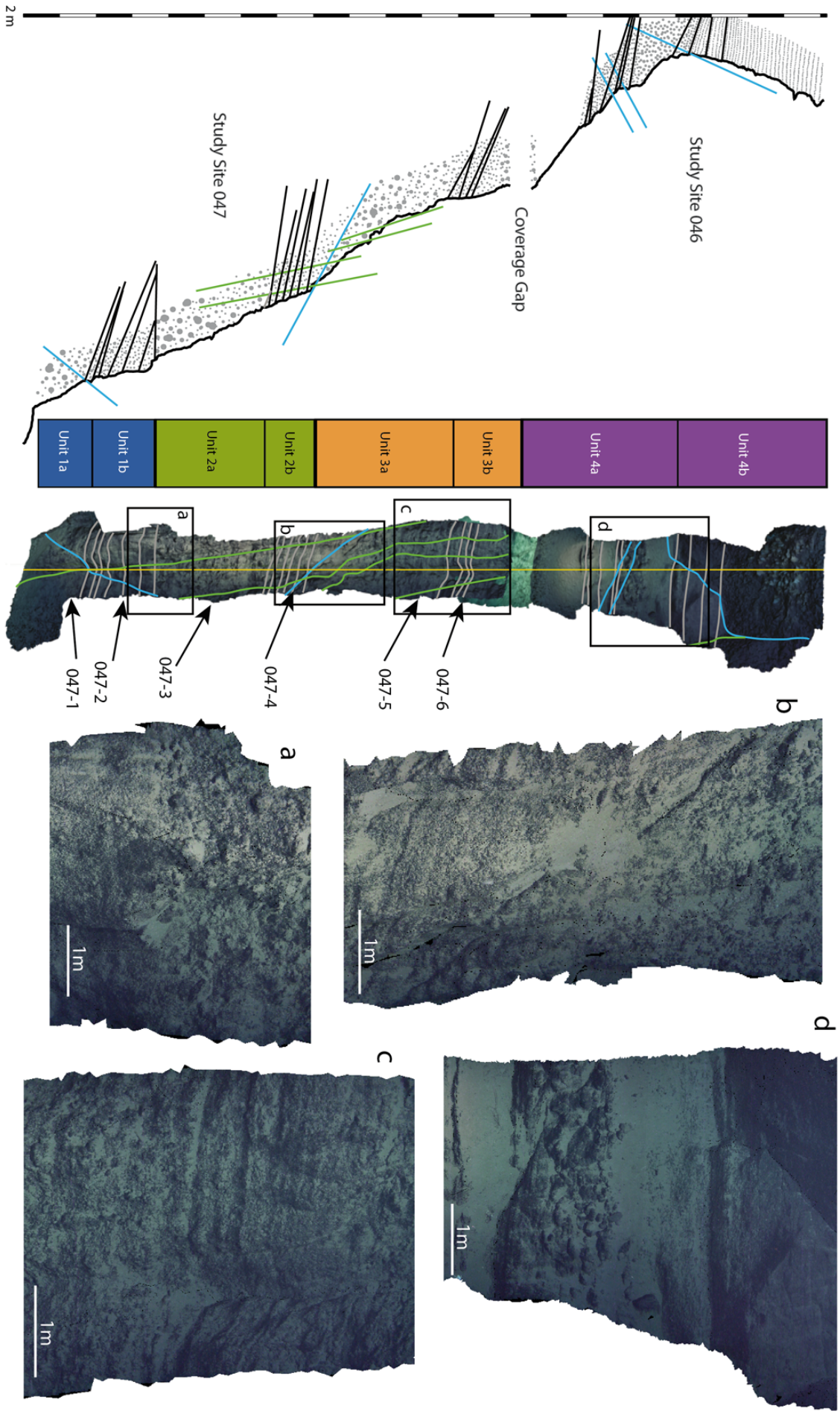
2 m
Study Site 046
Coverage Gap
Study Site 047
Unit 4b
Unit 4a
Unit 3b
Unit 3a
Unit 2b
Unit 2a
Unit 1b
Unit 1a
a
b
c
d
047-1
047-2
047-3
047-4
047-5
047-6
1m

Figure 4-6 *(previous page) Normal Profile for Tambor Crater developed using the models of sites 046 and 047, including a true-scale section derived from the models. Bedding planes are marked black, tangential joints in blue, radial joints in green. The yellow line marks the location of the section. Arrows mark the position of grain size measurements. Inset a) shows the erosional unconformity between units 1b and 2a. b) shows the detachment plane between units 2b and 3a. c) shows the upper part of unit 3b. d) shows the transition between units 4a and 4b.*

Throughout the southern part of the surveyed crater wall, these lower three units are not as readily distinguishable as in the northern outcrops. Sites 021 through 032 show 5 - 10 m thick deposits of well-layered class A breccia, alternating with slightly coarser, massive class B and C deposits, all of which could not be attributed to a specific unit. A large bomb measuring 10 cm across (059-2) was sampled on the sedimentary talus close to the crater wall and may be associated to this sequence since clasts of such size and outer texture are abundant in the lower units. Sample 059-9 (Figure 4-7a) contains lava fragments from the footwall of site 047. Their outer texture is lobate to cauliflower shaped and lined by cracks. The rock contains < 5 %vol. of spheroidal microvesicles up to 0.5 mm size. The ground mass is partly microcrystalline. Plutonic fragments of varying gabbroic compositions account for 10 %vol.

Unit 4a is an 8 m thick class C lapillistone, which shows thin beds around 10 cm thickness. The degree of compaction varies, as single beds are strongly recessive and the entire unit forms a terrace on the slope. Only the upper 1.5 m is massive, less compacted grain sizes are coarser.

A sharp contact separates unit 4a from the 8 m thick unit 4b, a well consolidated or cemented coarse ash tuff (class C, Figure 4-6d). Samples 059-10 and 059-11 came from this deposit (Figure 4-7b). Clasts are angular to sub-rounded in shape and vesicular. No volcanic glass was found. The lava fragments contain up to 5 %vol. of Olivine, Clinopyroxene and Plagioclase phenocrysts as well as accessory mica. The groundmass is fragmented and crevassy but not vesicular. Sub-angular xenolithic lava or gabbroic crustal fragments constitute less than 1 % of the deposits.

The topmost portion of unit 4b consists of well-compacted 5 – 10 cm thick parallel layers exposed in benches of up to 3 m high. This top unit appears to be ubiquitous in the western half of the crater, but thins out by an estimated 50 % towards the northern outcrops. Especially the upper few meters are very well sorted (e.g., samples 059-5 and 059-10). Unit 4b forms overhangs in the crater wall at sites 035, 045, 046 and 051 that form a substrate colonized by a characteristic community of corals, forming a marker horizon. Sample 059-7, which is attributed to this unit, is a coarse, weakly cemented volcaniclastic sandstone, showing a high degree of alteration with authigenic clay minerals filling the pore space between grains.

The top of this unit commonly forms the crest of the inner crater wall. From here, a gentle slope leads to the saddle of the crater. On the crest of outcrops formed by this unit (e.g. 021, 045 and 051), hard grounds with crater-inward dipping lobate flow structures reminiscent of rope lava dominate the relief, but it could not be resolved whether these are lava flows or slumped and solidified volcaniclastics of unit 4. The crest of the crater wall is often covered by a 20 – 50 cm thick carbonate cemented, laminated deposit of brown to yellow fine sand (samples 059-6 / -8) made up of dense lava analogue to the

underlying units. The samples contain fine grain size fractions that are missing in the coarser deposits below, with 60 – 90 vol.% of crystals in carbonate cement, and show mm scale layers that are bioturbated. Such deposits were identified at most outcrops reaching the crest (021, 035 and 045). Apart from these uppermost strata, none of the deposits or their samples contains a significant amount of macroscopic calcareous components that might suggest intermediate phases of marine sedimentation between eruptive phases or extensive reworking much later than the eruption period.

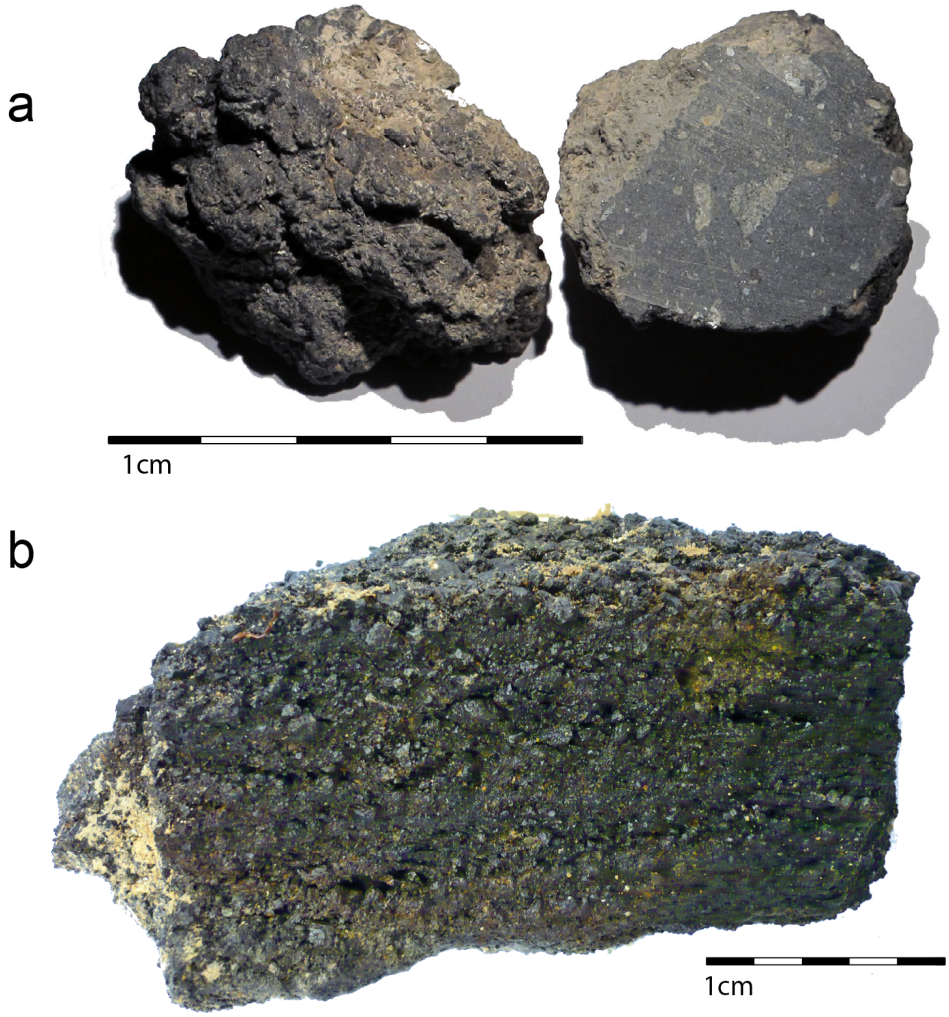

Figure 4-7 *Types of dense lava clasts at Tambor. a) 059-09 is a larger, dense clast with lobate crust containing plutonic xenoliths. b) sample 059-10 shows a sub-parallel horizontal alignment of medium to well sorted angular clasts.*

A thick layer of fine-grained foraminifer ooze covers the crater except the nearly vertical inner crater walls. As all samples within the crater and on its perimeter contained such ooze, we suppose this to be the ubiquitous marine background sediment. The crater bottom is covered by a sedimentary talus of a mixture of ooze and <5 vol.% volcaniclastic debris of sub-centimeter size. Meter sized blocks broken off the crater wall occur sporadically. Two talus samples (059-3 and 059-4) consist of ooze and about 10 vol.% of reworked volcaniclasts up to -4 ϕ (16 mm).

These clasts are sub-angular to rounded and slightly oxidized with a 30 %vol. microphenocryst content of ores, dense, but some contain < 1 vol.% of irregular vesicles.

On the outer perimeter of the cone, a lava field occurs at the location of the previously known high backscatter area [*Masson et al.*, 2008]. Ropy lava forms mounds several tens of meters across. No direct association with Tambor could be determined due to sediment cover of 0.5 – 2 m as determined visually. A sample of this lava (059-1) has a breadcrust surface. A largely altered glass rim of 5 mm surrounds the clast. The microlithic groundmass contains < 5 %vol. of spheroid vesicles up to 2 mm diameter.

4.4.2 Correlation by Grain Size

For the first time on a deep-sea deposit, we carried out grain size measurements on images yielding a data set of 14 measurements for Tambor (Table 4-1). The most complete stratigraphic sequence was identified at outcrop 047. It yielded clear differences in grain size distributions, but these distributions strongly overlap over the resolvable grain size interval. Six consecutive beds alternate between class A and B deposits corresponding to subunits 1a through 3b, a change that is clearly visible in the imagery and reconstructions. Their resolved median size differs about 0.5 ϕ. The visual estimate that the sorting of lapilli stone deposits is better compared to breccias becomes evident through the clast size counts, as poor sorting hindered the counting effort.

The grain size distributions were subjected to a similarity analysis, which, along with field observations of the relative positions of deposits within the outcrops, were used to infer a tentative correlation of outcrops given in Table 4-1.

Table 4-1 *Distribution of visible grain sizes in Phi (ϕ) units, compare Figures 2 and 3 for sample locations. Correlations for Outcrops 41 and 47 are unambiguous. All other correlations are drawn based on relative vertical position within the stratigraphy and strength of correlation factors. Set 035 could not be matched to any other deposit due to its position high up in the sequence, and seems to represent a local coarsening in the upper sections of unit 4. Original data are presented in Appendix 2.*

	Statistics							Correlation		
Sample	**Average**	**St Dev**	**Median**	**Min**	**Max**	**Count**	**Class**	**Unit**	**Corr. Sample**	**Factor**
021	-4,3	0,4	-4,2	-3,2	-5,8	198	C	3b	047-6	0,95
032-1	-4,1	0,5	-3,8	-2,9	-8,8	270	A	1b	047-2	0,96
032-2	-4,6	0,8	-4,3	-3,1	-6,9	272	B	2a?	047-3	0,86
035	-4,4	0,7	-4,2	-2,6	-6,8	296	B	3b/4b?	047-5	0,90
041-1	-3,9	0,3	-3,8	-3,2	-4,8	218	C	1b	047-2	0,98
041-2	-4,6	0,6	-4,3	-3,4	-7,1	233	C	2a	047-3	0,89
042	-3,6	0,3	-3,5	-2,8	-5,0	252	C	4b	visual	none
047-1	-4,7	0,6	-4,4	-3,4	-7,5	245	C	1a	visual	
047-2	-4,0	0,4	-3,9	-2,6	-6,4	329	A	1b	visual	
047-3	-4,8	0,9	-4,2	-3,0	-7,4	287	B	2a	visual	
047-4	-4,0	0,4	-3,9	-2,9	-6,2	289	A	2b	visual	
047-5	-4,8	0,7	-4,4	-3,4	-7,9	249	C	3b	visual	
047-6	-4,2	0,4	-4,1	-3,2	-6,7	275	A	3b	visual	
051-1	-4,4	0,5	-4,3	-3,1	-6,0	321	B	1a	047-1	0,96

4.4.3 Bedding Orientation

The oriented 3D-models derived from the HD-video allow us to measure the orientation of planar beds based on their intersection with the rugged outcrop surface. The depositional structures dip toward the crater at a mean orientation of 23°/096° (dip / dip direction, (Figure 4-8). The variation around this value (root mean square error 8°/014°) is smaller than expected given the location of outcrops along a 75° arc section of the (circular) crater wall. The mean difference in dip direction between the most peripheral sites (051 and 021) is 11° due to peculiarities of the local crater morphology. Based on the sparse amount of data and the coverage of less than 25 % of the crater circumference, no further insights could be gained.

No clear correlation could be identified regarding a change of dip angle depending on stratigraphic height. Its only exception to this uniform dip angle is the sharp contact between units 1b and 2a at site 047. The deviation in orientation and the change in lithology suggest the presence of an erosional unconformity.

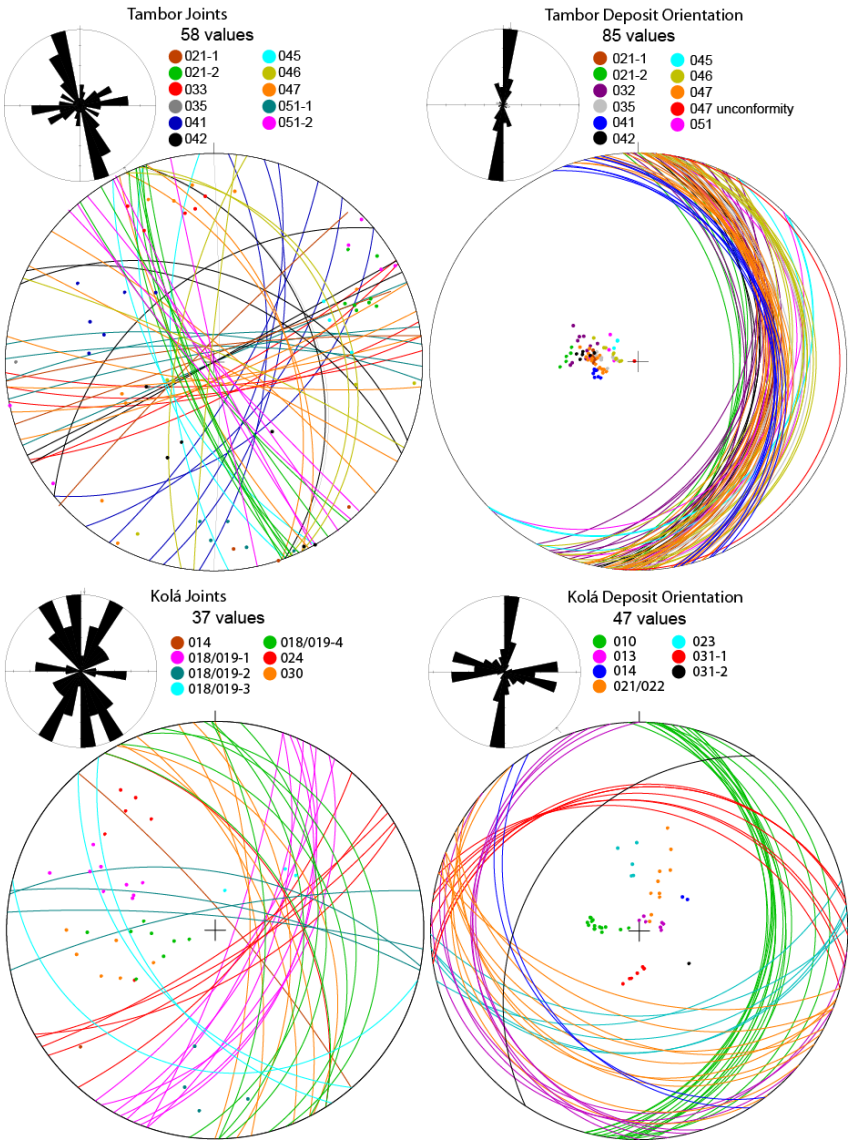

Figure 4-8 *(previous page) Measurements of joints and bedding structures at Tambor and Kolá craters, drawn as cyclographic plots with points representing the individual data points (color). Inset Rose diagrams (black/white) indicate the mean resultant directions of the data set. Original data are presented in Appendix 2.*

4.4.4 Tectonic Features

Two major joint strikes are obvious in the 3d-reconstruction (Figure 4-8). They follow radial and tangential directions around the crater (Figures 4-2 & 4-6). The radial joints dip steeply (80° and above). The majority of tangential joints have steep, outward angles. The average dip of the crater wall is around 65°, for comparison. Since only joints with no measureable amount of displacement could be identified, the establishment of a temporal succession of tectonic trends is not possible.

4.5 Results for Kolá Crater (Dive 071)

4.5.1 Description of Units

The major units at Kolá can be correlated as a result of them forming morphological steps at locally consistent levels on the crater wall, although occurrences on the eastern wall are a bit lower than in the west (Figure 4-3). The bedding character and texture of the four major units vary greatly between outcrops and especially between the eastern and western flank. Nevertheless, the units retain common characteristics relative to each other that allow their correlation.

The crater bottom is covered by foraminifer ooze analogous to Tambor. Towards the western flank Kolá features small mounds and ridges on the scale of a few meters, formed by single boulders or whole undisturbed, meter-sized chunks of deposits of units 1 and 2 (see below). Their arrangement relative to each other is chaotic.

The base of the crater walls is formed by a series of lava flows, following the 3700 m - depth contour. The lava sequence has an outcropping thickness between 8 m and 32 m (Sites 18 & 19). It contains a complex sequence of several–meters-thick, stacked lavas separated by autoclastic breccias. Towards the top 10 m of the sequence, pillows up to 1m in diameter dominate. Lava samples taken by ROV (samples 071-12 through -14) are dark grey, almost aphyric apart from clinopyroxene phenocrysts but contain gabbroic xenoliths. The lava only contains a few percent of partly zeolite filled, elongate vesicles up to 7 mm length.

The contact of the lavas with the overlying volcaniclastic deposits is poorly exposed due to sediment cover. The largest sample subset from these units is formed by 22 samples (dredge and ROV) of clast types that were found in all units. They consist of country rock, coarsely crystalline (1 – 5 mm) greenish gabbros, as well as other less crystalline plutonites.

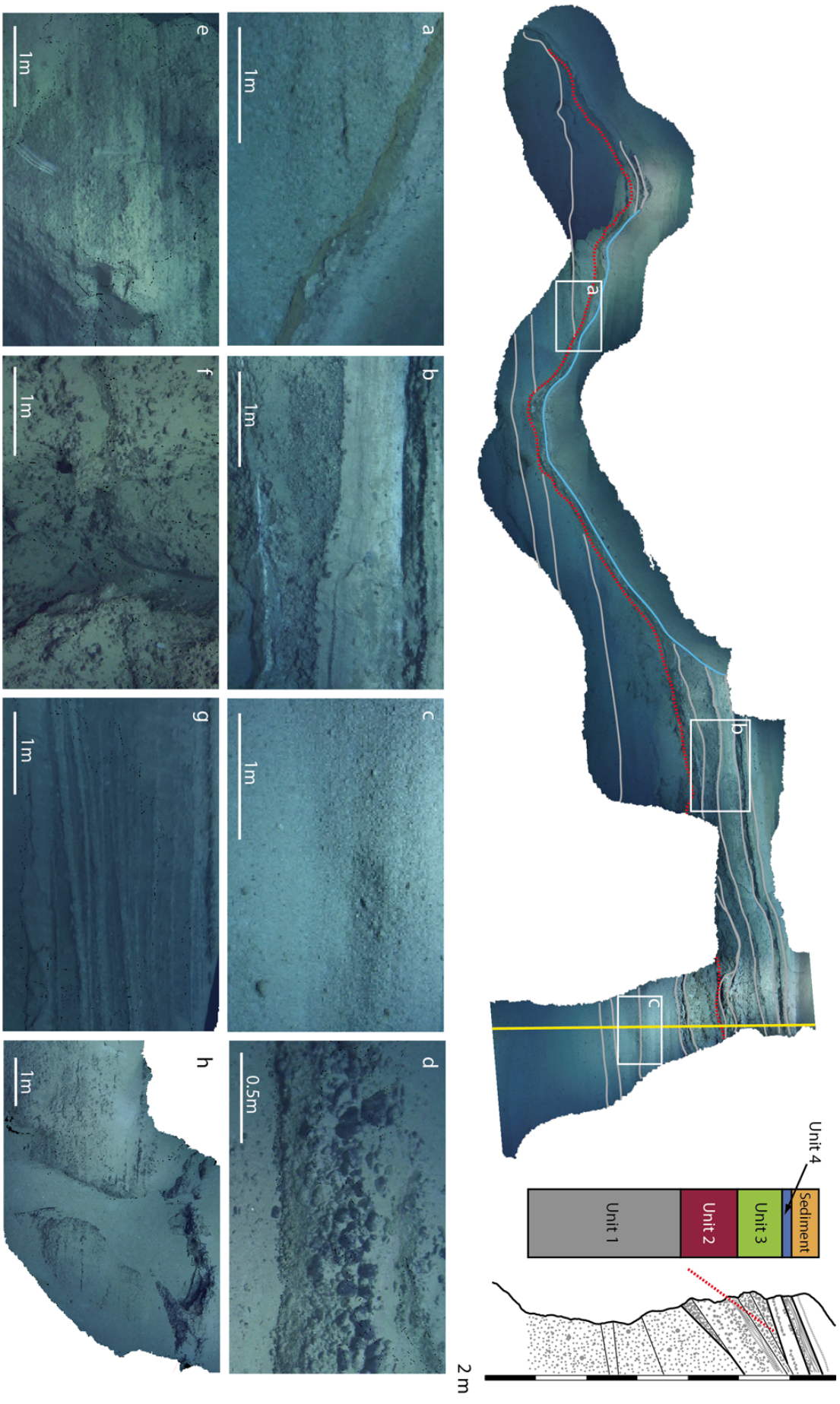
a
b
c
d
e
f
g
h
1m
0.5m
Unit 4
Sediment
Unit 3
Unit 2
Unit 1
2 m

Figure 4-9 *(previous page) Profile and digital model of Site 021/022 which is the most complete series at Kolá crater found in one outcrop. The yellow line marks the location of the profile. Insets are partial views of the reconstructed outcrop models. a) shows the discordant surface at the base of unit 2 (red dashed line) and its reactivated plane (blue line); b) shows the condensed stratigraphy of units 2 - 4; c) shows the massive section of unit 1; d) shows black clasts of unit 4 lying on unit 1 at site 033; e) shows the stratified upper part of unit 1 at site 009; f) shows the massive chaotic main body of unit 3 at site 014; g) shows the intercalated foraminifer ooze and volcanic layers of unit 3 at site 010; h) shows unit 4 lying on a stratified part of unit 1 at site 031.*

A relief-forming voluminous deposit with a thickness of up to 12 m forms the lowermost unit 1 (Figure 4-9a, c, e, h). The lower half (at sites 013, 021 and 023) is a massive deposit with poorly developed stratification and layer thicknesses of several meters. The upper half (site 009) features cm- to dm- thick parallel to sub-parallel layers. The upper stratified portions at sites 009 and 013 (not shown) show a strong degree of erosion into highly articulate trenches, pillars and even arches. Higher up on the eastern slope, unit 1 is continuously exposed on small scarps (sites 031 – 035).

The unit is pale grey and shows small variations in maximum grain size but not in lithology throughout the layers. It contains a varying but very high load of rounded non-juvenile fragments, with their visible sizes ranging between -3 ϕ (8 mm) and -7 ϕ (128 mm).

Unit 2a is a massive, 2 – 12 m thick, poorly sorted conglomerate of black, very well rounded lithic fragments (Figure 4-9f) found only in the western outcrops (sites 010 and 014). It is clearly clast-supported and does not show stratification. A sharp contact separates it from unit 2b, which is much better sorted and shows decimeter thick sub-parallel bedding. These layers are matrix supported and show sharp transitions between beds of different matrix color, sharing the same monolithic well-rounded content as unit 2a.

Unit 2b is a double layer of 1.5 m at site 010, but more complex and thicker at sites 021 and 023. Here, the deposit consists of a complicated series of sub-parallel discontinuous beds. These beds strongly vary in maximum visible grain size, sorting of these fractions, lithology and degree of compaction, and white precipitate is present in many layers.

A 0.3 – 1 m thick bed of brown to ochre compacted clay marks the start of unit 3. It is most conspicuous at sites 021 and 023 where it overlies an erosion surface cut into units 1 and 2 (Figure 4-9a). After the deposition of units 3 and 4, further erosion removed all but a 20 cm thick volcaniclastic layer overlain by 30 cm of foraminifer ooze. On the flanks of the reactivated channel, units 3 and 4 are preserved (Figure 4-9b).

Above unit 2, cross-bedded grey volcaniclastics alternate with layers of foraminifer ooze. The former is well sorted, clast-supported and rounded. Between outcrops, the thickness of volcaniclastic beds varies considerably and can reach up to 2 m. Cm- thick, discontinuous volcaniclastic beds also line the beds of white marine foraminifer ooze. The largest exposure of unit 3 is a formation of discontinuous beds at site 010 (Figure 4-

9g). Just down slope of this unit at site 009-3 there is a much thinner grey, volcaniclastic, thinly bedded layer through 70cm of ooze. One sediment sample (071-09, Figure 4-9) was collected using the ROV scoop, again confirming our interpretation of the marine background sediment. After removal of the formainifers and fines comprising about 80% of the volume through wet sieving, the sample yielded a polymictic suite of sub-angular plutonitcs and lavas (< -4 ϕ or 16 mm, Figure 4-10 a,b) but mostly well rounded, dense lapilli (< -3.5 ϕ or 10 mm, Figure 4-10c,d) containing amphibole needles (< 1 mm) clinopyroxene and phlogopite. Within these lapilli, crystals are concentrically aligned in layers around a nucleus of either a small plutonic fragment, a larger crystal or an unaligned body of the same crystal assemblage.

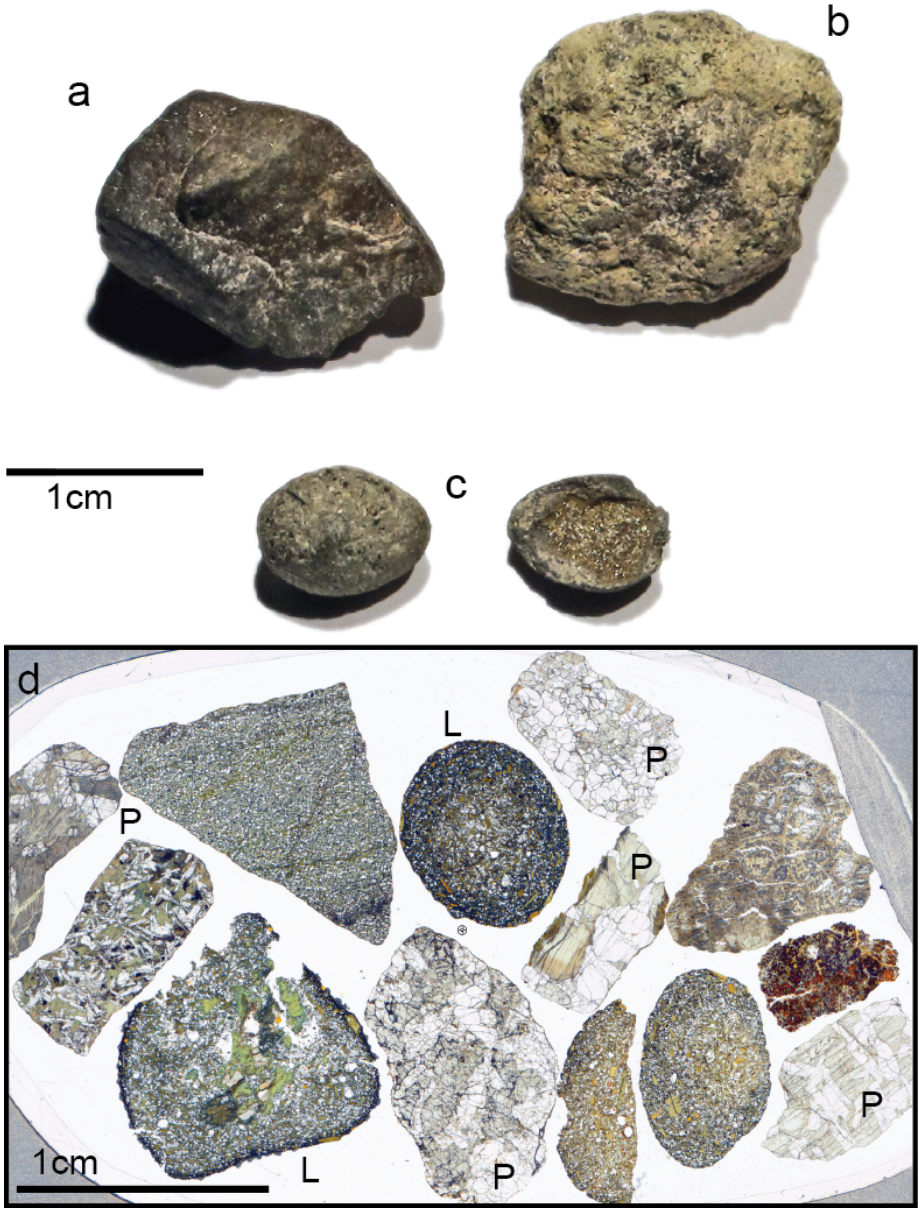

Figure 4-10 *Selected clasts from sample 071-09 showing a) dark angular lava fragments, b) greenish coarse-grained gabbro and c) pale grey, spheroidal lapilli of presumably juvenile magmatic origin. d) shows a micrograph of plutonite fragments (P) and spheroidal lapilli (L) illustrating zonation around a nucleus and quench rims.*

Many such clasts have quenched rims. Two dredge samples (064-4 and -8) contained carbonate cemented lithic sands of lava fragments analogous to sample 071-09. Additionally, they contain free crystals of amphibole, clinopyroxene and accessory plagioclase around 1 mm size. Spheroidal lapilli are smaller in this deposit (< -2 ϕ or 4mm) but contain the same mineralogy. We infer, based on their rounded shape and their high content of well-preserved crystals, that these lapilli belong to the juvenile volcaniclastic component.

Unit 4 is well distinguishable from others: it is pitch-black and monomictic (Figure 4-9b). It shows a highly variable, often-lenticular thickness from 24 cm at site 021 to 6 cm at site 023 (Figure 4-3b), which does not follow a systematic trend. Site 009-3 contains a poorly exposed impact sag structure of 60 cm in diameter, deforming unit 4. Although lateral grain size differences are suspected, the generally small grain sizes < -3 ϕ (8 mm) prevented thorough comparisons. Its lower half shows a fine mm scale layering of well-sorted very coarse sand. Towards the top, larger clasts up to -3 ϕ (8 mm) make up 50 vol.% and beds are present. Sites 033 and 035 contain subangular to rounded clasts between -5 ϕ (32 mm) and -7 ϕ (128 mm), which were likely subject to abrasion and in turn question their correlation to unit 4 (Figure 4-9d). It is topped by about 1 m of marine sediment with a 10 cm lower layer of reworked components of unit 4.

4.5.2 Grain Size Distribution

Five sets of grain size measurements were obtained at Kolá. In comparison to Tambor crater, generally smaller grain sizes, different lithology and varying sediment cover lead to an even larger number of failed counts (Table 4-2), which complicated the grain size measurement. Therefore quantitative correlation, even in generalized terms similar to Tambor, was impossible and factors such as lithology and stratigraphic context were given preference for the correlation outlined below. The difficulties in correlating by grain size fractions also reflect strong changes in the character of deposits throughout the crater. The overall quantity of measurements in relation to the amount of reconstructed surface is smaller than for Tambor, due to the extent of large lava flows at Kolá.

Table 4-2 *Grain sizes determined for deposits at Kolá Crater in ϕ units. The original data is available through Appendix 2.*

Sample	Average	St. Dev.	Median	Min	Max	Count
010	-4.7	0.7	-4.6	-6.9	-3.4	132
014	-4.7	0.8	-4.5	-6.9	-3.3	157
021-1	-3.9	0.4	-3.9	-6.4	-3.0	238
021-2	-4.5	0.7	-4.4	-6.9	-3.4	188
021-3	-4.3	0.5	-4.3	-6.1	-3.5	183
009-1	-4.5	0.5	-4.4	-6.5	-3.8	216

4.5.3 Bedding Orientation

Particularly in the western sector of the crater, the morphology is complicated and comprises steps and small hills with a high amount of erosional features. Therefore, the interpretation of bedding orientation is complex (Figure 4-8). The general dip direction follows the slope of the crater wall at the respective sites, for example, at site 010. Sites 021 and 023 also display the direction of the crater slope at this location, whereas the spread in dip angle reflects the interplay of erosion and deposition on steep slopes. Site 031 lies on the upper eastern slope where a deposit of unit 1 is cut at an angle of 45° by an erosional contact with unit 4. A number of smaller outcrops higher up the eastern wall (031 – 037) were not interpreted as their small extent posed uncertainties in georeferencing and scaling.

4.5.4 Tectonics

The measurements of joints are strongly biased by outcrop coverage through photogrammetry, which favored the eastern lava outcrops over the less covered deposits of the western flank. Most of the joint sets are represented by sites 018 and 019 (Figure 4-8). Like at Tambor, there is a radial and a tangential component. The radial component changes from sites 018 / 019 to site 024 around a focal point slightly to the south of the crater center. Site 030 does not show a radial component; only the tangential one is well developed. The tangential joints dip steeply outward (i.e., antithetic), whereas the radial ones are close to vertical.

The scarps on the upper eastern wall (031 – 037) result from faults produced by the sagging of the flank at displacements of 0.5 – 2 m each. Their fresh relief on the steep slope suggests a comparatively recent age relative to the overall edifice.

4.6 Discussion

4.6.1 Interpretation of the Tambor Edifice

There are no sheet lava flows at Tambor. Two kinds of highly fragmented volcaniclastic deposits were identified, both of which have dense clasts. It is therefore unlikely that volume expansion due to volatile exsolution played a major role in the fragmentation process, but does not exclude the possibility of earlier degassing and the presence of such a volatile phase during the eruption. Angular clasts smaller than pebbles were likely formed by thermal quench granulation upon contact of magma and seawater. Larger pebbles, cobbles or small boulders often show a lobate outer texture that may be the result of a more viscous deformation as magma entered the water. The maximum clast size is similar to scoria cones on land, although these are usually much more vesicular.

The beds are often discontinuous on a lateral scale of meters and form lenses of different maximum clast sizes compared to the surrounding layer. Maximum clast size also varies frequently between whole beds and units show a considerable variation in radial thickness along the inner crater wall. This may be explained by a discontinuous eruptive process in which the direction of individual pulses changed frequently, analogous to debris jets on land.

Tambor shows considerable morphological differences compared to the neighboring volcanic edifices, primarily due to its large central crater. Lacking an appropriate underwater classification scheme, we apply the proportion criteria for fresh subaerial cones raised by Porter [1972] and Wood [1980], being diameter of the crater rim (W_{cr}), basal diameter of the cone (W_{co}) and height of the cone (H_{co}). Tambor cone (W_{cr} / W_{co} = 0.36, H_{co} / W_{co} = 0.1) lies slightly below the average ratios for cones on land (W_{cr} / W_{co} = 0.4, H_{co} / W_{co} = 0.14). Its average outward slope is 17°, which is less than the generally measured 25° - 28° of neighboring craterless cones, assumed to represent the angle of repose. On the other hand, the slopes at Tambor are considerably steeper than one would expect them for tuff ring like edifices that show a strong lateral transport on land.

Joints oriented along two different trends line the crater walls. A radial component may be associated with some degree of inflation during the eruption process. The joints of the second, tangential component are often oriented at an antithetic angle relative to the crater center. Although no measure for displacement could be determined, the comparison of the joint geometry to numerical simulations [*Holohan et al.*, 2011] suggests the collapse of a shallow magma reservoir under a thin roof of comparatively high strength. The assumption of subsidence of the crater floor is in agreement with the generally steep inner crater walls and the presence of a collapse scar and associated debris flow deposit on the eastern sector of the crater wall. The crater inward orientation of beds is not exclusively linked to, but supports the possibility of subsidence.

Concluding, Tambor carries many morphological characteristics of a cone of dense lava clasts that experienced some degree of subsidence, but lacks the vesicular clasts linking it to strombolian activity.

4.6.2 Construction of the Kolá Edifice

Considering the prevolcanic morphology dominated by Kolá A-C, the floor of the crater is dug deep into the country rock, eroding surrounding cones but constructing no pronounced positive relief. This also is a characteristic of maar craters on land [*Valentine et al.*, 2011; *White and Ross*, 2011]. The lavas at the foot of the crater wall likely constitute the country rock on which the Kolá cones were formed, as their stratigraphic position matches a morphological step marking the edge of this plateau (Figure 4-1).

Juvenile components are scarce in the Kolá deposits. Spheroidal lapilli contained in dredge samples 064-4, 064-8 and ROV sample 071-09 have a crystal-rich alkaline composition. Their concentric structure and quenched rims suggest that this magma was injected into a cooler liquid where spherules were formed in a process of highly fragmentative spray granulation. Most likely this liquid was ocean water, as no host medium remained attached to the spherules.

Lava fragments contained in these samples likely originate from the thick lava flows penetrated by the crater. The large suite of perfectly rounded blocks of gabbro found in all units indicates a deep root of eruptive activity. They may have experienced entrapment in the lower conduit where they entered a fluidized state during the eruption, explaining their high degree of rounding [*Ross et al.*, 2008]. Their large clast sizes, in con-

nection with their widespread occurrence also in high terrain suggest a highly energetic transport mechanism. Many layers containing such clasts (particularly Unit 4) have laterally highly variable thicknesses arguing for strong lateral transport. The thin bedded, discontinuous and mutually capping beds of Unit 1 and 2 on the western outcrops also indicate a highly energetic lateral transport.

The stepwise morphology and circular crater geometry argue for the development of ring faults resulting from subsidence of the crater flanks in large blocks. The orientation of antithetic crater-inward joints within the lavas suggests a strong inward stress associated with the subsidence of the vent. The lavas may have formed a high-strength, thin-roof element [*Holohan et al.*, 2011] similar to the basement at Tambor. Further upslope and away from the pit center, the normal faults found at outcrops 031 – 037 document that the surrounding cones Kola A – C were affected by such subsidence. Radial joints are interpreted as indicators for outward stress associated with the eruption. All of these features are suggestive of a development similar to a maar-diatreme type volcano.

4.6.3 Summary and Conclusions

The Tambor and Kolá craters of the CDVF are two end member products of highly fragmentative volcanism in the deep sea within close vicinity to each other.

Tambor features some morphology and depositional characteristics of a tuff ring whereas several aspects of its deposits, especially some layers with large clast sizes, show close resemblance of scoria cone deposits. Its dense clasts argue against strombolian eruption mechanisms, though. Kolá shows features of a maar-diatreme type edifice with the crater floor below the surrounding terrain, nested into a group of cones, and punctuating a lava plateau in the footwall. Its deposits are heterolithologic and dominated by crustal fragments whereas many layers indicate a large measure of lateral transport.

This study tested a number of innovative survey techniques on poorly understood volcanic edifices. The creation of digital outcrop models allowed the identification of tectonic lineaments and joints in loose gravel, which had been overlooked using the video footage alone. Statistical analysis of grain size distribution among units supported correlation of units lacking other distinguishing features.

Acknowledgements

The authors would like to thank the dedicated team of ROV Kiel 6000 and the M80/3 crew for their support, and the Senatskommission für Ozeanographie for granting ship time. This project was in part funded by the German Science Foundation (DFG) through an M80 coordination grant. Part of this work was carried out within the Jeddah Transect Project (www.jeddah-transect.org).

References

Allen, S. R., R. S. Fiske, and K. V. Cashman (2008), Quenching of steam-charged pumice: Implications for submarine pyroclastic volcanism, *Earth and Planetary Science Letters*, *274*, 40–49, doi:10.1016/j.epsl.2008.06.050.

Baker, E. T., G. J. Massoth, and R. A. Feely (1987), Cataclysmic hydrothermal venting on the Juan de Fuca Ridge, *Nature*, *329*(6135), 149–151, doi:10.1038/329149a0.

Baker, E. T., G. J. Massoth, C. E. J. de Ronde, J. Lupton, and B. I. A. McInnes (2002), Observations and sampling of an ongoing subsurface eruption of Kavachi volcano, Solomon Islands, May 2000, *Geology*, *30*(11), 975–978.

Barreyre, T., A. Soule, and R. A. Sohn (2011), Dispersal of volcaniclasts during deep-sea eruptions: Settling velocities and entrainment in buoyant seawater plumes, *J Volcanol Geoth Res*, *205*(3-4), 84–93, doi:10.1016/j.jvolgeores.2011.05.006.

Bischoff, J., and R. J. Rosenbauer (1985), An Empirical-Equation of State for Hydrothermal Seawater (3.2-Percent Nacl), *American Journal of Science*, *285*(8), 725–763.

Buettner, R., P. Dellino, H. Raue, I. Sonder, and B. Zimanowski (2006), Stress-induced brittle fragmentation of magmatic melts: Theory and experiments, *J Geophys Res-Sol Ea*, *111*, –, doi:10.1029/2005JB003958.

Busby-Spera, C. (2005), Possible distinguishing characteristics of very deepwater explosive and effusive silicic volcanism, *Geology*, *33*(11), 845–848, doi:10.1130/G21216.1.

Cann, J. R., and M. R. Strens (1989), Modeling Periodic Megaplume Emission by Black Smoker Systems, *J Geophys Res-Solid*, *94*(B9), 12227–12237, doi:10.1029/JB094iB09p12227.

Carey, S., and H. Sigurdsson (2007), Exploring Submarine Arc Volcanoes, *Oceanography*, *20*(4), 80–89.

Cashman, K. V., and R. S. Fiske (1991), Fallout of Pyroclastic Debris From Submarine Volcanic-Eruptions, *Science*, *253*(5017), 275–280.

Chadwick, W. W., K. V. Cashman, R. W. Embley, H. Matsumoto, R. P. Dziak, C. E. J. de Ronde, T. K. Lau, N. D. Deardorff, and S. G. Merle (2008), Direct video and hydrophone observations of submarine explosive eruptions at NW Rota-1 volcano, Mariana arc, *J Geophys Res-Sol Ea*, *113*(B8), B08S10, doi:10.1029/2007JB005215.

Clague, D. A. (2009), Accumulation rates of volcaniclastic deposits on Loihi Seamount, Hawaii, *B Volcanol*, *71*(6), 705–710, doi:10.1007/s00445-009-0281-y.

Clague, D. A., A. S. Davis, and J. E. Dixon (2003a), Submarine strombolian eruptions on the Gorda mid-ocean Ridge, *Geophysical monograph*, *140*, 111–128.

Clague, D. A., A. S. Davis, J. Bischoff, J. E. Dixon, and R. Geyer (2000), Lava bubble-wall fragments formed by submarine hydrovolcanic: explosions on Lo'ihi Seamount and Kilauea Volcano, *B Volcanol*, *61*(7), 437–449.

Clague, D. A., R. Batiza, J. W. Head III, and A. S. Davis (2003b), Pyroclastic and hydroclastic deposits on Loihi seamount, Hawaii, *Geophysical monograph*, *140*, 73–95.

Deardorff, N. D., K. V. Cashman, and W. W. Chadwick (2011), Observations of eruptive plume dynamics and pyroclastic deposits from submarine explosive eruptions at NW Rota-1, Mariana arc, *J Volcanol Geoth Res*, *202*(1-2), 47–59, doi:10.1016/j.jvolgeores.2011.01.003.

Fisher, R. (1984), Submarine volcaniclastic rocks, *Geological Society, London, Special Publications*, *16*(1), 5–27.

Fouquet, Y., J. P. Eissen, H. Ondreas, F. Barriga, R. Batiza, and L. Danyushevsky (1998), Extensive volcaniclastic deposits at the Mid-Atlantic Ridge axis: results of deep-water basaltic explosive volcanic activity? *Terra Nova-Oxford*, *10*(5), 280–286.

Grevemeyer, I., G. Helffrich, B. Faria, G. Booth Rea, M. Schnabel, and W. Weinrebe (2010), Seismic activity at Cadamosto seamount near Fogo Island, Cape Verdes—formation of a new ocean island? *Geophys J Int*, *180*(2), 552–558.

Head, J. W., III, and L. Wilson (2003), Deep submarine pyroclastic eruptions: theory and predicted landforms and deposits, *J Volcanol Geoth Res*, *121*(3-4), 155–193.

Hekinian, R., F. Pineau, S. Shilobreeva, D. Bideau, E. Gracia, and M. Javoy (2000), Deep sea explosive activity on the Mid-Atlantic Ridge near 34 degrees 50 ' N: Magma composition, vesicularity and volatile content, *J Volcanol Geoth Res*, *98*(1-4), 49–77.

Hekinian, R., R. Muehe, T. J. Worthington, and P. Stoffers (2008), Geology of a submarine volcanic caldera in the Tonga Arc: Dive results, *J Volcanol Geoth Res*, *176*(4), 571–582, doi:10.1016/j.jvolgeores.2008.05.007.

Helo, C., M. A. Longpré, N. Shimizu, D. A. Clague, and J. Stix (2011), Explosive eruptions at mid-ocean ridges driven by CO2-rich magmas, *Nature Geosci*, *4*(4), 260–263.

Holm, P. M., J. R. Wilson, B. P. Christensen, L. Hansen, S. L. Hansen, K. M. Hein, A. K. Mortensen, R. Pedersen, S. Plesner, and M. K. Runge (2006), Sampling the cape verde mantle plume: Evolution of melt compositions on Santo Antao, Cape Verde Islands, *J Petrol*, *47*(1), 145–189.

Holohan, E. P., M. P. J. Schopfer, and J. J. Walsh (2011), Mechanical and geometric controls on the structural evolution of pit crater and caldera subsidence, *J Geophys Res-Sol Ea*, *116*, B07202, doi:10.1029/2010JB008032.

Inman, D. L. (1952), Measures for describing the size distribution of sediments, *Journal of Sedimentary Research*, *22*(3), 125–145.

Kano, K. (2003), Subaqueous pumice eruptions and their products: A review, *Geophysical monograph*, *140*, 213–229.

Kwasnitschka, T., T. H. Hansteen, C. W. Devey, and S. Kutterolf (2012), Doing Fieldwork on the Seafloor: Photogrammetric Techniques to yield 3D Visual Models from ROV Video, *Computers and Geosciences*.

Lonsdale, P., and R. Batiza (1980), Hyaloclastite and Lava Flows on Young Seamounts Examined with a Submersible, *Geol Soc Am Bull*, *91*(9), 545–554.

Lorenz, V., B. Zimanowski, and R. Buettner (1999), Discussion on the formation of kimberlite pipes: the phreatomagmatic model, *Newsletter of the IAVCEI Commission on Explosive Volcanism, September, 1999; Flagstaff, Arizona, USA*, 11–17.

Lupton, J., E. T. Baker, R. W. Embley, R. Greene, and L. Evans (1999), Anomalous helium and heat signatures associated with the 1998 Axial Volcano Event, Juan de Fuca Ridge, *Geophys Res Lett*, *26*(23), 3449–3452.

Maicher, D., and J. D. L. White (2001), The formation of deep-sea Limu o Pele, *B Volcanol*, *63*(7), 482–496.

Maicher, D., J. D. L. White, and R. Batiza (2000), Sheet hyaloclastite: density-current deposits of quench and bubble-burst fragments from thin, glassy sheet lava flows, Seamount Six, Eastern Pacific Ocean, *Marine Geology*, *171*, 75–94.

Masson, D. G., T. P. Le Bas, I. Grevemeyer and W. Weinrebe (2008), Flank collapse and large-scale landsliding in the Cape Verde Islands, off West Africa, *Geochem Geophy Geosy*, *9*, Q07015, doi:10.1029/2008GC001983.

McNutt, M. (1988), Thermal and mechanical properties of the Cape Verde Rise, *Journal of Geophysical Research*, *93*(B4), 2784–2794.

Mueller, W., and J. D. L. White (1992), Felsic Fire-Fountaining beneath Archean Seas - pyroclastic deposits of the 2730-Ma Hunter-Mine-Group, Quebec, Canada, *J Volcanol Geoth Res*, *54*(1-2), 117–134.

Palmer, M. R., and G. Ernst (1998), Generation of hydrothermal megaplumes by cooling of pillow basalts at mid-ocean ridges, *Nature*, *393*(6686), 643–647.

Plesner, S., P. M. Holm, and J. R. Wilson (2003), 40Ar-39Ar geochronology of Santo Antão, Cape Verde Islands, *J Volcanol Geoth Res*, *120*(1-2), 103–121.

Pontbriand, C. W., A. Soule, R. A. Sohn, and S. E. Humphris (2008), Deep pyroclastic deposits and evidence for explosive volcanism on the ultraslow spreading Gakkel Ridge at 85E, *AGU Fall Meeting Abstracts*, *-1*, 2019.

Porter, S. C. (1972), Distribution, Morphology, and Size Frequency of Cinder Cones on Mauna Kea Volcano, Hawaii, *Geol Soc Am Bull*, *83*(12), 3607, doi:10.1130/0016-7606(1972)83[3607:DMASFO]2.0.CO;2.

Ross, P.-S., J. D. L. White, B. Zimanowski, and R. Büttner (2008), Rapid injection of particles and gas into non-fluidized granular material, and some volcanological implications, *B Volcanol*, *70*(10), 1151–1168, doi:10.1007/s00445-008-0230-1.

Schipper, C. I., J. D. L. White, B. F. Houghton, N. Shimizu, and R. B. Stewart (2010), Explosive submarine eruptions driven by volatile-coupled degassing at Loihi Seamount, Hawai'i, *Earth and Planetary Science Letters*, *295*(3-4), 497–510, doi:10.1016/j.epsl.2010.04.031.

Smith, T. L., and R. Batiza (1989), New Field and Laboratory Evidence for the Origin of Hyaloclastite Flows on Seamount Summits, *B Volcanol*, *51*(2), 96–114.

Sohn, R. A. et al. (2008), Explosive volcanism on the ultraslow-spreading Gakkel ridge, Arctic Ocean, *Nature*, *453*(7199), 1236–1238, doi:10.1038/nature07075.

Sonder, I., A. Schmid, R. Seegelken, B. Zimanowski, and R. Buettner (2011), Heat source or heat sink: What dominates behavior of non-explosive magma-water interaction? *J Geophys Res-Sol Ea*, *116*, B09203, doi:10.1029/2011JB008280.

Valentine, G. A., N. L. Shufelt, and A. R. L. Hintz (2011), Models of maar volcanoes, Lunar Crater (Nevada, USA), *B Volcanol*, *73*(6), 753–765, doi:10.1007/s00445-011-0451-6.

Van der Plas, L., and A. C. Tobi (1965), A chart for judging the reliability of point counting results, *American Journal of Science*.

Wentworth, C. K. (1922), A scale of grade and class terms for clastic sediments, *The Journal of Geology*, 377–392.

White, J. D. L., and P. S. Ross (2011), Maar-diatreme volcanoes: A review, *J Volcanol Geoth Res*, *201*(1-4), 1–29, doi:10.1016/j.jvolgeores.2011.01.010.

Wohletz, K. H. (1983), Mechanisms of hydrovolcanic pyroclast formation: grain-size, scanning electron microscopy, and experimental studies, *J Volcanol Geoth Res*, *17*(1-4), 31–63.

Wohletz, K. H. (2003), Water/magma interaction: physical considerations for the deep submarine environment, *GEOPHYSICAL MONOGRAPH-AMERICAN GEOPHYSICAL UNION*, *140*, 25–50.

Wood, C. A. (1980), Morphometric analysis of cinder cone degradation, *J Volcanol Geoth Res*, *8*(2), 137–160.

Wright, I. C., P. Stoffers, M. Hannington, C. E. J. de Ronde, P. Herzig, I. E. M. Smith, and P. Browne (2002), Towed-camera investigations of shallow-intermediate water-depth submarine stratovolcanoes of the southern Kermadec arc, New Zealand, *Marine Geology*, *185*(3-4), 207–218.

Zimanowski, B., G. Frohlich, and V. Lorenz (1995), Experiments on Steam Explosion by Interaction of Water with Silicate Melts, *Nucl Eng Des*, *155*, 335–343.

Zimanowski, B., R. Büttner, V. Lorenz, and H. G. Hafele (1997), Fragmentation of basaltic melt in the course of explosive volcanism, *J Geophys Res-Sol Ea*, *102*(B1), 803–814.

5 Conclusion and Outlook

The objective of this thesis was to study aspects of submarine volcanism in the Cape Verdes across a wide range of scales. It had previously been realized that the seamounts in the archipelago could potentially play an important role in the further understanding of its complex evolution known through research on the islands. Thus, at the beginning stood regional studies on the distribution and relative ages of the seamounts, many of which had not been previously mapped and described.

The volcanic history of the Cape Verdean Archipelago goes far beyond the development of the two island chains. At any time throughout its history, seamounts formed along the island chains that did not grow to break the surface or did so only for the shortest amount of time. This study demonstrates that seamounts in the Cape Verdes developed to any stage, and that, as volcanic activity migrates westward, the formation of new seamounts, and possibly new ocean islands, is still happening today.

The westward migration of volcanism defined by the age progression of the islands alone turns out to be discontinuous once the submarine edifices are taken into account. The Nola Seamounts, actually a cluster of two separate edifices, were previously thought to form the most recent expression of volcanic activity in the northwest. Yet they have erosional summit platforms indicating a substantial period of quiescence, whereas they are surrounded by morphologically young and recently active Sodade Seamount, CDVF and western Santo Antão. On the western tip of the Southern Chain, Brava and the Ilhéus Secos have entered a posterosional stage. Fogo to the east and Cadamosto Seamount to the southwest show recent volcanic activity, whereas Tavares Seamount to the west of Brava shows no signs of recent activity and is affected by tectonics.

The seamounts to the east of the Southern Chain are much older and in an advanced stage of erosion. Maio Seamount, solitary to the east of the island chain, never even completed the construction of a large volcanic shield. Later stages of seamount growth on the flanks of islands can be observed at Boavista Seamount and Maio Rise, where activity has long ago ceased and mass mass wasting dominates. Cabo Verde Seamount has long ago halted in a similar stage. In contrast, Senghor experienced a short subaerial phase during which its summit was capped to a small plateau. Senghor is the only seamount that shows clear signs of central subsidence and caldera formation, followed by a rejuvenated stage constructing a Somma-type volcano that now forms the summit plateau.

The wave cut plateaus of Nola East, Nola West and Senghor are attributed to glacial sea level low stands up to -122m during the last 0.64 Ma. Although the plateaus were mapped with great precision, no definitive correlations could be drawn among the seamounts or with respect to the large shallow shelf between Maio and Boavista, since no high resolution bathymetry is available for that area and the age of the seamount plateaus is unconstrained.

In order to further develop an age progression among Cape Verdean seamounts, sampling aiming at absolute age dates as well as the determination of trace element and isotopic signatures relative to the signatures of the islands is necessary. This involves the seamount summits in particular as the likely consist of the youngest deposits, addressing the question whether volcanic activity on seamounts spans a shorter period of time than on nearby islands. Due to technical limitations in dredging and the operation of the Kiel 6000 ROV, no samples have been collected from summit regions (apart from Cadamosto) as they are shallower than 600m. It should be realized that the highest elevation of Nola West is just 35m below sea level, a depth that can be reached with comparable ease by a number of inexpensive techniques.

The findings on a revised age progression in the Northern Chain inspired detailed studies of the processes connected to incipient volcanism at CDVF on the basis of data gathered by ROV. We chose to have a closer look at this system as it likely represents the earliest stage of submarine volcanic activity in the archipelago and offered a wide variety of morphologies. Since it is situated below 3000m depth, a prime focus was put on the eruption mechanisms at these great pressures. Such studies can only be carried out remotely but need great precision and accuracy, and thus they required the development of a unique remote sensing workflow.

Based on industrial software normally used in aerial photogrammetry, digital reconstructions of deep-sea outcrops were created from high definition video recordings made during the ROV surveys. The use of cameras beneath the sea requires underwater housings, and the air/glass/water interface of the window for the lens acts as an additional optical element. This introduces aberrations in the imagery for which to correct there is no commercial software solution available. One way to cope with this on the basis of commercially available tools is nonlinear distortion of the model according to known high resolution geometry of the ocean floor, data which is usually missing. Another compensation strategy is the incorporation of vehicle navigation data gathered independently from the images, in order to rectify the reconstructed terrain models based on acoustic techniques. Underwater navigation at great depth in turn is prone to inaccuracies due to the limitations of sound propagation. Therefore, the record of a differential velocity logger recording vehicle motion has to be merged with the acoustically triangulated position of the vehicle as determined from aboard the ship. Considerable advancements in terms of reconstruction quality, processing speed and coverage can be expected from improvements of the vehicle navigation sensors, data recording and processing of the records but mainly from the use of dedicated survey cameras recording continuously, matched by pilots mindful of the requirements in terms of slow, controlled vehicle motion.

The workflow yields georeferenced digital terrain models of underwater outcrops at a centimeter scale. The most significant advantage over acoustic mapping is, beyond increased resolution, the availability of a blended, full color image texture that may even surpass the model in resolution. Quantitative measurements of all visible geological features of the outcrops are possible, limited only by the resolution of the source imagery.

Orientation measurements are possible using a digital analogue to a geological compass that even surpasses classical terrestrial methods in cases of beds of loose clastic material where clearly defined surfaces on a scale of decimeters are absent. Measurements of grain size are possible through the manual identification of clasts following a point counting grid. It was discovered that this method still shows great shortcomings as the often limited quality of the source imagery a) limits the lower grain size detection limit to the centimeter range and b) causes the method to fail completely if the deposit is occluded by sediment cover or shadows due to improper lighting. Realistically, only the maximum grain sizes can reliably be determined but no significant advantages are gained over visual estimates when it comes to grain size distributions or sorting. Particularly grain size measurements may benefit from the above mentioned improvements on data acquisition in the field. Provided the outcrops are well lit and the resolution of cameras is increased, it may be possible to automate the grain size analysis via the power spectra of deposit images, eliminating the personal bias in point counting.

The photogrammetric reconstruction method was consequently applied to two cones at CDVF which show a unique morphology of large central depressions. The northern Tambor cone is a constructive edifice. It is composed of highly fragmented, yet dense volcaniclastic rock. Two different varieties of deposits of uniform lithology were discriminated based on their visible grain size distribution. Type A shows a maximum grain size in the range of pebbles, while type B is less well sorted and has maximum grain sizes in the range of blocks. These two deposit types alternate across four units, but correlation throughout the crater is difficult due to drastic lateral changes in deposit thickness. Antithetic tangential joints along the inner crater wall and a mass wasting scar and deposit on the eastern crater wall suggest subsidence of the central parts of Tambor following the main construction phase.

Kolá Crater, south of Tambor, is a destructive edifice that produced a negative relief amidst a group of small cones. A step-wise morphology of the inner crater walls and antithetic tangential joints similar to Tambor suggest an even larger amount of subsidence. The lower crater walls consist of thick lava flows producing vertical cliffs. Above, highly fragmented volcaniclastic deposits show a) heterogeneous lithologies of dense subspherical lava lapilli with concentric alignment of crystals and quenched rims mixed with country rock of lava fragments that likely originate from the underlying lavas, and b) coarse crystalline gabbro fragments up to block size that are very well rounded by abrasion. A sequence of four units with intercalated deposits of marine background sedimentation shows various signs of highly energetic lateral transport such as mutual capping and lateral thinning. Due to their characteristic lithology though, deposits could be correlated across the crater and their deposit thicknesses were quantitatively compared.

Both Tambor and Kolá show signs of effective fragmentation either by viscous deformation or thermal granulation. Lateral transport, particularly of block size clasts, was very effective. At the same time, nearby cones such as Koladera also consist of fragmented volcaniclastics but these are much more vesicular and are underlain by lava flows of the same lithology. Due to the limited amount of data gathered during the limited num-

ber of ROV dives each, and since the reconstruction workflow was developed a posteriori with no influence on specific aspects of data acquisition, a number of questions have to remain unanswered. This study could document volcanic deposits that were indeed unexpected at such great water depth in terms of their composition, emplacement and wide lateral distribution. Future studies at CDVF will have to focus on the eruption mechanisms creating such effective fragmentation as well as the lateral transport of large clasts over considerable distances in light of the great water depth. Tambor and Kolá are not the only submarine Cape Verdean volcanoes with a central depression. While Tambor- and Kolá-type morphologies were found on the upper slopes of the shields of Senghor and Nola East, there are also Tambor-type cones around Sodade Seamount, at depths comparable to those at CDVF. The prerequisite for any future work on this kind of volcanic activity is further high resolution mapping of the crater structures followed by detailed sampling of their complex stratigraphy, extending the scope of this study to even smaller scales.

Acknowledgements

My interest in volcanism on the Cape Verdes was sparked back in 2005. I am greatly indebted to Thor Hansteen for introducing me to this part of the world, for all the opportunities that arose for me through the M80/3 cruise, for his mentoring and support.

Colin Devey was confident enough to take me up as a PhD student based on my colourful yet highly speculative first digital reconstruction attempts and ever since has provided me with anything I could possibly need. I am sure that our greatest digital adventures are yet to come.

Steffen Kutterolf and Armin Freundt have supported me ever since my diploma thesis, helped me through an agonizing year of grant writing and joined me in the back seat of the ROV van as we tried to work out the deep sea landscape.

Fritz Abegg was there in the darkest chapters of my camera design studies, ensured the great success of our research cruise, but I received his greatest and most valued support afterwards back home.

Many friends in Kiel and at both ends of Geomar have learned about the deep sea as I did, and I owe a big thanks to all who stood by despite my absent staring at lunch, random outbursts of technical explanations and even my televised interpretation of submarine volcanic ash.

My family has always been my source of greatest strength, support and inspiration.

The greatest joy that my work on the Cape Verdes brought to me is my dear Maren. Thank you so much for all your love and support!

Curriculum Vitae

Tom Kwasnitschka

Address:	Zastrowstr. 18 24114 Kiel
Phone:	0431 / 66949538
Email:	tkwasnitschka@geomar.de
Date of birth:	05.04.1982
Place of birth:	Höxter
Nationality:	German

Academic Education

Since 09/2010	Doctorate student at the Magmatic and Hydrothermal Systems group of FB4, GEOMAR Helmholtz Center for Ocean Research Kiel
06/2009 – 02/2010	Coordination and research assistant for the cruise M80/3, IFM-GEOMAR Kiel
10/2002 – 05/2009	Diploma of Geology/Paleontology at the Christian-Albrechts-Universität zu Kiel; Undergraduate minor: Oceanography Graduate minor: Astrophysics

Appendix 1

Supplementary Map A1_059_Tambor.pdf
This map shows a stratigraphic correlation of outcrops along the southwestern flank of Tambor Crater. The images are orthographic renderings of the outcrop models at a decimeter resolution. The units in the geological map have been extrapolated based on the profiles above, where the four major units (colored bars) have been identified, honoring small local variations in grain size distribution, degree of compaction or sediment cover. Therefore, subunits have not been identified. Site 046 is included on top of site 047. All other study sites marked grey were omitted due to questionable georeferencing. Note that the erosional unconformity between units 1 and 2 can be readily correlated between sites 041 and 047. Superficial slumping structures were included in the geological map as black dashes, occurring on top of unit 4.

Supplementary Map A2_071_Kola.pdf
This map shows two profiles which position has been marked in Figure 4-3. The images are orthographic renderings of the outcrop models at decimeter resolution. Black (on profiles) and grey (on images) lines mark major sedimentary horizons. Red lines mark joints. The ROV track in immediate vicinity of the profiles was projected onto the profile plane to be visible. The crater profiles derived from bathymetry (dashed black) have been refined by a tentative local profile (thin black) based on the ROV track (red). A black arrow marks the approximate locations of outcrops as projected onto the profile planes.

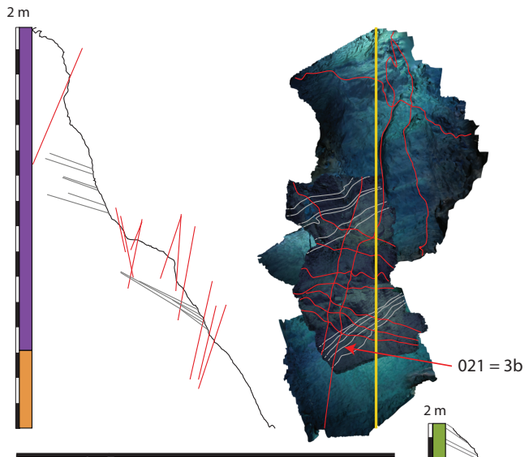

021

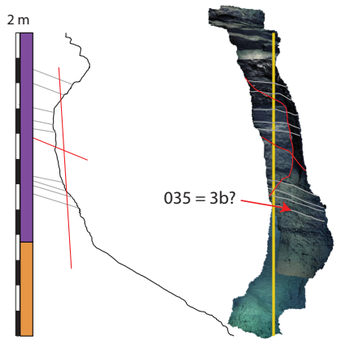

035

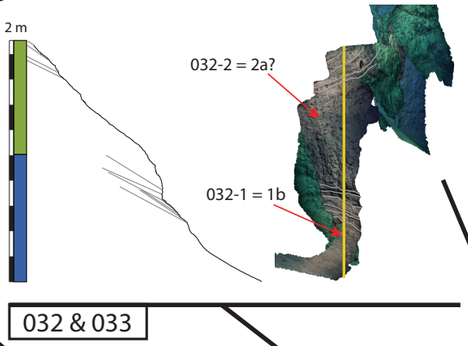

032 & 033

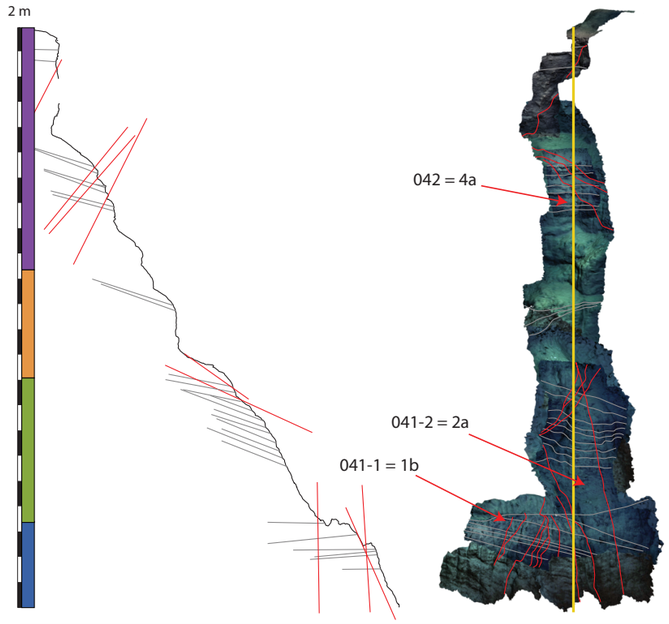

041

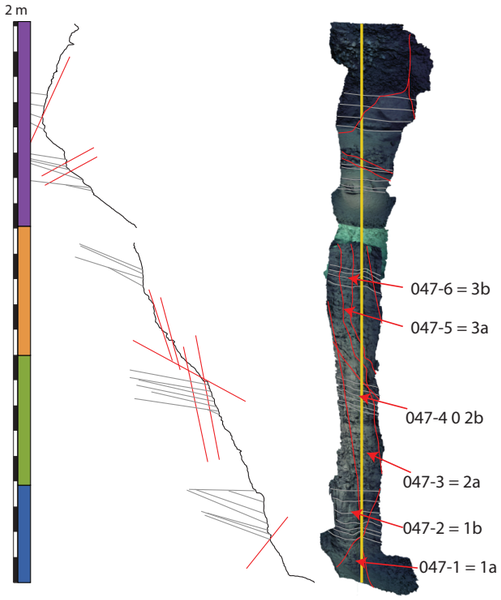

047

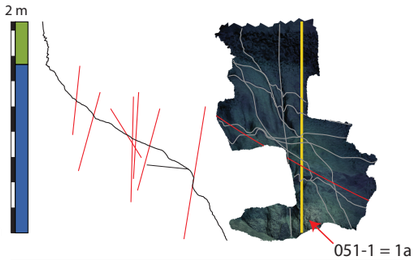

051

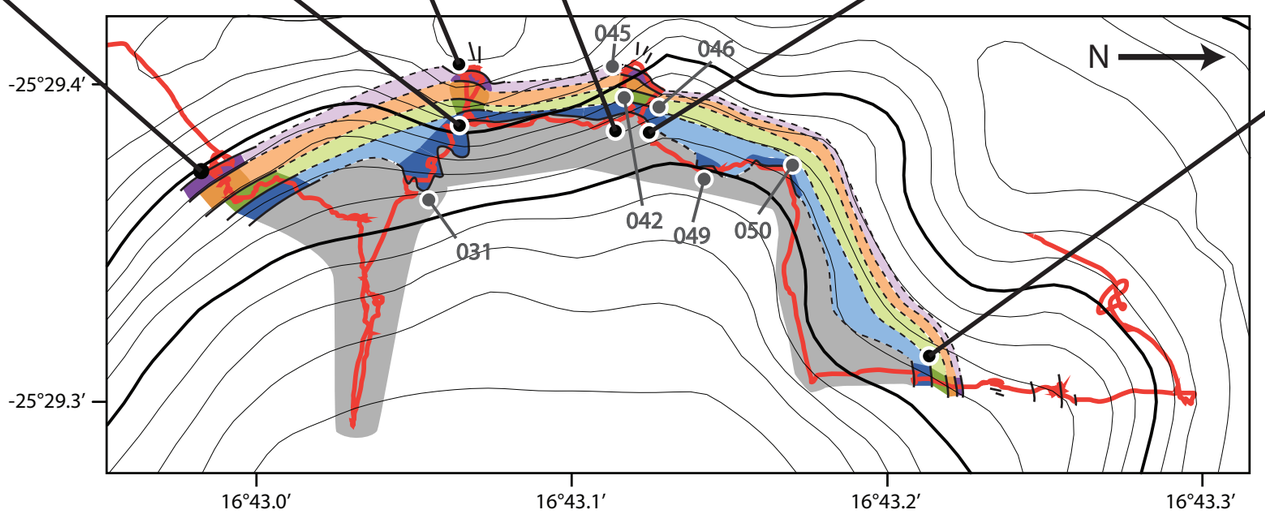

Talus
Unit 4
Unit 3
Unit 2
Unit 1

Tambor Crater
Stratigraphic Correlation of Four Major Units

Grain Size Sample = Unit
Joint
Bedding Plane
Section Plane
Superficial Slumping Structures

Kolá Crater, Charles Darwin Volcanic Field
Idealized Sections through the Crater with
Correlated Profiles of Selected Study Sites

Site 014
Site 013
Sites 018+019
071_023
Sites 021-022
Site 010
Site 009-3
Site 009-1
Site 024
Site 030
Site 031
2 m
P1
P2
-3500
-3600
-3700
Depth (m)
0
100
200
300
400
500
600
700
800
900
1000
1100
SW
Profile Length (m)
NE
Marine Sedimentation
Unit 4
Unit 3
Unit 2
Unit 1
Lava rock, basement
Joint
Bedding Plane

Appendix 2

This section contains the following raw data sets:

1. Orientation measurements for volcanotectonic joints and bedding planes as illustrated in Figure 4-6. The first measurement index corresponds to the study site, the second index describes coherent sets of measurements with comparable directions, or measurements of a single stratigraphic unit, and the last index is the number of the measurement within that set.
2. Grain size measurements of both dive (059) Tambor and 071 (Kolá). The data sets contain the measurements both expressed as clast diameter in meters (accurate within the millimeter range) and as phi scale measurements. Key statistical parameters for all data sets are provided at the top of the columns. The differences in data abundance result from varying image quality conditions and varying marine sediment cover on the deposits.

Site 059 - Tambor Cone					
Volcanotectonics			Bedding Orientations		
Measurement	Dip	Dip Direction	Measurement	Dip	Dip Direction
021_1_00	86.9	316.8	021_1_00	41.1	86.1
021_1_01	89.9	341.8	021_1_01	37.9	93.6
021_1_02	84.2	354.3	021_1_02	36.3	97.2
021_2_00	77.5	247.7	021_1_03	35.5	101.7
021_2_01	77.0	248.9	021_1_04	38.4	89.9
021_2_02	79.7	229.9	021_2_00	24.6	97.3
021_2_03	86.0	236.8	021_2_01	24.7	103.6
021_2_04	72.2	250.4	021_2_02	23.6	88.3
021_2_05	79.0	251.2	021_2_03	23.7	95.5
021_2_06	68.6	246.1	021_2_04	23.2	93.0
021_2_07	72.2	247.5	021_2_05	24.0	90.9
033_01	71.4	151.5	032_1_00	38.6	118.6
033_02	73.4	172.6	032_1_01	34.0	108.7
033_03	76.9	176.5	032_1_02	28.1	101.8
033_04	72.3	168.6	032_1_03	33.8	113.0
033_05	80.7	151.0	032_1_04	24.2	114.0
033_06	87.8	275.7	032_1_05	32.3	114.8
035_00	36.8	68.6	032_1_06	27.5	108.4
035_01	87.1	90.4	032_2_00	27.6	93.3
041_00	47.1	139.9	032_2_01	35.2	88.7
041_01	56.9	128.0	032_2_02	26.4	94.9
041_02	61.6	93.8	032_2_03	35.5	87.4
041_03	57.4	103.8	035_1_00	19.6	93.0
041_04	64.4	107.9	035_1_01	20.2	93.0
041_05	73.7	119.7	035_1_02	17.2	77.0
042_00	53.6	26.5	035_1_03	19.6	96.2
042_00	47.0	320.3	035_2_00	13.3	96.5
042_01	38.0	69.6	035_2_01	14.0	100.0
042_02	88.9	334.2	035_2_02	23.1	97.6
042_03	45.5	22.4	035_2_03	22.6	102.6
042_04	89.9	330.7	035_2_04	10.9	92.9
045_00	66.7	266.2	041_1_00	12.0	348.3
045_01	60.9	249.6	041_1_01	15.4	11.6
045_02	61.7	241.2	041_1_02	11.2	343.4
046_1_00	23.5	65.4	041_1_03	20.9	16.8
046_1_01	27.2	69.0	041_1_04	13.4	11.8
046_2_00	84.0	23.5	041_1_05	11.6	354.2
046_2_01	69.5	279.0	041_2_00	23.1	78.3
047_1_00	78.8	187.3	041_2_01	25.0	75.1
047_1_01	89.0	27.7	041_2_02	22.2	65.8
047_1_02	80.6	172.6	041_2_03	23.4	69.0
047_1_03	80.2	158.4	041_2_04	23.7	79.8
047_1_04	80.6	39.0	041_2_05	24.5	70.5
047_1_05	77.0	165.5	041_2_06	23.7	77.6
047_2_00	50.2	71.0	041_3_00	21.3	42.3
047_2_01	49.6	64.6	041_3_01	22.4	43.9
047_3_00	75.3	243.4	042_1_00	31.1	92.4
051_1_01	88.3	52.9	042_1_01	29.9	100.3

Site 059 - Tambor Cone					
Volcanotectonics			Bedding Orientations		
Measurement	Dip	Dip Direction	Measurement	Dip	Dip Direction
051_1_02	88.6	225.6	042_1_02	30.3	97.3
051_1_03	89.8	77.8	042_1_03	33.2	96.6
051_1_04	81.2	229.3	042_1_04	26.3	96.6
051_1_05	84.9	241.0	042_1_05	24.1	100.6
051_1_06	88.9	242.1	045_1_00	15.8	134.5
051_2_01	84.1	350.0	045_1_01	15.6	136.3
051_2_02	75.1	4.7	045_1_02	14.8	118.9
051_2_03	88.7	337.1	046_1_00	11.6	97.9
051_2_04	80.9	1.3	046_1_01	9.9	89.9
051_2_05	74.6	355.1	046_1_02	19.7	112.0
			046_1_03	27.1	118.4
			046_2_00	13.9	105.6
			046_2_01	8.9	92.3
			046_2_02	18.9	113.1
			046_2_03	14.5	108.6
			046_2_04	11.9	95.5
			047_1_00	24.6	94.0
			047_1_01	22.8	86.2
			047_1_02	24.7	91.0
			047_1_03	26.7	91.7
			047_1_04	28.4	94.5
			047_1_05	1.5	95.7
			047_1_06	22.4	95.2
			047_2_00	21.1	80.7
			047_2_01	20.5	78.1
			047_2_02	21.9	79.0
			047_2_03	20.0	71.8
			047_2_04	19.2	76.9
			047_2_05	18.1	71.5
			047_3_00	27.1	105.1
			047_3_01	26.6	99.4
			047_3_02	32.1	104.3
			047_3_03	21.0	99.4
			051_1_01	26.0	94.2
			051_1_02	20.7	133.8
			051_1_03	12.7	91.6
			051_1_04	16.6	111.7

Site 071 - Kolá Crater					
Volcanotectonics			Bedding Orientations		
Measurement	Dip	Dip Direction	Measurement	Dip	Dip Direction
014_1	81.1	49.5	010_1_01	9.6	92.6
018_019_1_01	58.7	109.0	010_1_02	5.3	104.3
018_019_1_02	63.5	118.6	010_2_01	19.7	87.1
018_019_1_03	71.1	124.7	010_2_02	20.9	94.9
018_019_1_04	66.7	114.7	010_2_03	25.1	103.5
018_019_1_05	45.3	122.8	010_2_04	26.3	104.6
018_019_1_06	46.0	111.2	010_2_05	26.8	105.2
018_019_1_07	46.3	113.5	010_2_06	26.9	96.5
018_019_1_08	62.7	88.8	010_2_07	27.6	98.7
018_019_1_09	80.4	108.8	010_2_08	23.6	92.0
018_019_1_10	51.5	116.5	010_2_09	23.7	96.1
018_019_1_11	38.4	97.5	010_2_10	23.7	92.4
018_019_1_12	44.1	88.8	010_2_11	25.5	101.2
018_019_2_01	75.1	10.9	010_2_12	19.9	93.8
018_019_2_02	59.0	10.1	010_2_13	17.8	96.4
018_019_2_03	79.2	348.6	013_1_01	12.7	270.2
018_019_2_04	82.3	5.2	013_1_02	12.4	261.8
018_019_3_01	23.2	75.0	013_1_03	14.4	255.6
018_019_3_02	31.0	62.5	013_1_04	13.7	252.2
018_019_3_03	15.5	70.5	013_1_05	5.6	186.1
018_019_3_04	47.9	58.4	013_1_06	8.4	201.7
018_019_3_05	50.4	235.8	013_1_07	6.2	220.7
018_019_3_06	47.9	229.0	014_1_01	31.2	237.9
018_019_3_07	34.2	87.3	014_1_02	29.8	233.4
018_019_3_08	22.2	193.8	021_022_1_01	21.2	198.7
024_01	72.9	148.8	021_022_1_02	11.2	219.7
024_02	62.5	149.9	021_022_1_03	8.0	232.3
024_03	71.2	143.1	021_022_2_01	36.3	207.9
024_04	77.8	146.0	021_022_2_02	45.4	201.7
024_05	69.6	130.8	021_022_3_01	33.6	200.2
030_01	36.7	62.5	021_022_3_02	28.5	201.7
030_02	54.3	63.3	021_022_4_01	21.4	212.7
030_03	68.1	79.7	021_022_4_02	23.0	209.6
030_04	50.9	83.8	021_022_4_03	54.0	195.5
030_05	71.3	89.7	023_01	29.6	175.3
030_06	60.7	68.2	023_02	45.5	179.4
030_07	49.0	57.8	023_03	44.2	166.4
			023_04	35.4	174.9
			023_05	29.5	173.1
			031_1_01	29.9	15.6
			031_1_02	23.1	1.3
			031_1_03	21.2	351.3
			031_1_04	21.1	351.3
			031_1_05	26.2	8.3
			031_1_06	26.4	9.7
			031_1_07	20.1	352.9
			031_2_01	32.5	303.2

Site 059 - Tambor Cone

Grain Size Diameter in Meters

	021	032-1	032-2	035	041-1	041-2	042	047-1	047-2	047-3	047-4	047-5	047-6	051-1
Average	0.019	0.017	0.024	0.022	0.015	0.024	0.012	0.026	0.016	0.028	0.016	0.027	0.019	0.022
Median	0.018	0.014	0.019	0.019	0.014	0.020	0.011	0.021	0.015	0.019	0.015	0.021	0.017	0.019
Min	0.009	0.007	0.009	0.006	0.009	0.011	0.007	0.010	0.006	0.008	0.007	0.010	0.010	0.009
Max	0.054	0.444	0.120	0.108	0.028	0.140	0.032	0.183	0.084	0.171	0.074	0.244	0.101	0.066
Count	198	270	272	296	218	233	252	245	329	287	289	249	275	321
StDev	**0.006**	**0.027**	**0.018**	**0.013**	**0.003**	**0.015**	**0.003**	**0.019**	**0.006**	**0.025**	**0.006**	**0.022**	**0.009**	**0.009**
	0.019	0.031	0.019	0.022	0.011	0.029	0.011	0.034	0.015	0.017	0.017	0.029	0.023	0.037
	0.018	0.020	0.022	0.010	0.011	0.023	0.017	0.024	0.017	0.042	0.018	0.038	0.015	0.031
	0.028	0.016	0.015	0.019	0.013	0.025	0.024	0.034	0.014	0.013	0.021	0.056	0.014	0.015
	0.028	0.020	0.017	0.017	0.012	0.029	0.019	0.022	0.021	0.020	0.019	0.020	0.015	0.018
	0.018	0.025	0.014	0.019	0.012	0.057	0.032	0.022	0.020	0.018	0.014	0.019	0.013	0.031
	0.017	0.018	0.023	0.013	0.016	0.016	0.015	0.046	0.025	0.021	0.017	0.025	0.018	0.015
	0.025	0.019	0.014	0.018	0.016	0.027	0.011	0.028	0.021	0.016	0.016	0.021	0.018	0.030
	0.027	0.013	0.022	0.020	0.015	0.024	0.015	0.034	0.014	0.027	0.016	0.019	0.018	0.029
	0.017	0.018	0.014	0.019	0.010	0.027	0.014	0.035	0.018	0.017	0.041	0.022	0.015	0.012
	0.025	0.017	0.035	0.019	0.012	0.019	0.016	0.025	0.016	0.013	0.012	0.020	0.019	0.016
	0.022	0.027	0.021	0.010	0.015	0.014	0.016	0.015	0.017	0.020	0.015	0.034	0.016	0.020
	0.018	0.014	0.026	0.018	0.015	0.055	0.018	0.015	0.019	0.050	0.020	0.018	0.015	0.016
	0.018	0.023	0.021	0.011	0.009	0.016	0.013	0.021	0.017	0.029	0.015	0.043	0.018	0.022
	0.017	0.008	0.020	0.007	0.018	0.021	0.015	0.036	0.016	0.016	0.016	0.017	0.021	0.022
	0.014	0.018	0.016	0.015	0.013	0.015	0.014	0.029	0.013	0.023	0.014	0.017	0.017	0.028
	0.019	0.015	0.030	0.020	0.023	0.019	0.009	0.028	0.014	0.016	0.021	0.024	0.020	0.023
	0.018	0.015	0.063	0.010	0.012	0.016	0.012	0.026	0.015	0.086	0.018	0.017	0.014	0.021
	0.054	0.020	0.013	0.017	0.016	0.026	0.013	0.027	0.014	0.019	0.013	0.021	0.023	0.022
	0.022	0.017	0.030	0.017	0.021	0.016	0.012	0.066	0.017	0.015	0.018	0.026	0.014	0.029
	0.021	0.013	0.014	0.013	0.014	0.021	0.010	0.022	0.011	0.023	0.013	0.021	0.017	0.019
	0.018	0.011	0.014	0.013	0.018	0.027	0.009	0.032	0.015	0.016	0.015	0.062	0.018	0.021
	0.020	0.019	0.019	0.036	0.019	0.019	0.014	0.024	0.018	0.017	0.019	0.043	0.014	0.015
	0.012	0.010	0.019	0.022	0.015	0.013	0.015	0.030	0.015	0.018	0.018	0.027	0.013	0.030
	0.019	0.017	0.120	0.030	0.012	0.025	0.015	0.037	0.014	0.017	0.013	0.023	0.018	0.015
	0.011	0.015	0.012	0.014	0.013	0.019	0.013	0.024	0.021	0.041	0.014	0.017	0.016	0.016
	0.016	0.011	0.028	0.014	0.020	0.027	0.009	0.013	0.017	0.011	0.016	0.032	0.018	0.019
	0.017	0.008	0.108	0.013	0.020	0.023	0.010	0.016	0.017	0.032	0.013	0.013	0.017	0.024
	0.013	0.018	0.101	0.026	0.013	0.023	0.012	0.013	0.014	0.020	0.013	0.037	0.023	0.028
	0.025	0.015	0.028	0.020	0.013	0.028	0.012	0.021	0.012	0.052	0.014	0.013	0.085	0.015
	0.016	0.009	0.012	0.037	0.014	0.024	0.013	0.034	0.016	0.043	0.010	0.044	0.013	0.009
	0.015	0.015	0.029	0.014	0.014	0.020	0.012	0.015	0.017	0.018	0.015	0.023	0.017	0.031
	0.019	0.010	0.014	0.020	0.017	0.019	0.010	0.021	0.018	0.060	0.015	0.028	0.023	0.050
	0.018	0.011	0.028	0.027	0.013	0.017	0.010	0.017	0.019	0.019	0.016	0.011	0.017	0.030
	0.016	0.020	0.015	0.017	0.014	0.033	0.012	0.014	0.023	0.023	0.016	0.054	0.014	0.030
	0.013	0.019	0.032	0.014	0.013	0.049	0.012	0.019	0.022	0.013	0.016	0.026	0.024	0.016
	0.021	0.014	0.026	0.059	0.013	0.017	0.013	0.023	0.017	0.095	0.020	0.063	0.015	0.015
	0.033	0.018	0.043	0.026	0.023	0.021	0.014	0.031	0.012	0.017	0.014	0.045	0.022	0.030
	0.022	0.014	0.048	0.013	0.018	0.049	0.013	0.035	0.020	0.017	0.020	0.019	0.016	0.042
	0.021	0.009	0.018	0.021	0.012	0.018	0.011	0.023	0.014	0.024	0.019	0.020	0.020	0.022
	0.024	0.016	0.018	0.015	0.009	0.092	0.013	0.030	0.015	0.011	0.016	0.028	0.014	0.015
	0.017	0.017	0.013	0.023	0.012	0.028	0.015	0.040	0.017	0.152	0.009	0.030	0.015	0.012
	0.022	0.014	0.037	0.014	0.012	0.023	0.014	0.031	0.022	0.017	0.017	0.019	0.020	0.035
	0.016	0.020	0.013	0.009	0.012	0.038	0.020	0.032	0.018	0.020	0.016	0.026	0.015	0.015
	0.054	0.016	0.013	0.045	0.012	0.017	0.013	0.029	0.018	0.032	0.015	0.047	0.016	0.012
	0.011	0.010	0.029	0.012	0.015	0.022	0.016	0.028	0.011	0.019	0.013	0.027	0.015	0.018
	0.017	0.014	0.010	0.024	0.018	0.030	0.013	0.029	0.016	0.016	0.011	0.014	0.018	0.013
	0.013	0.013	0.021	0.020	0.012	0.015	0.020	0.023	0.031	0.029	0.012	0.038	0.015	0.016
	0.012	0.016	0.019	0.013	0.021	0.016	0.019	0.019	0.013	0.022	0.013	0.020	0.016	0.018
	0.011	0.016	0.029	0.018	0.012	0.036	0.013	0.027	0.015	0.022	0.017	0.019	0.010	0.044
	0.015	0.012	0.019	0.022	0.019	0.043	0.011	0.020	0.020	0.012	0.019	0.023	0.012	0.028
	0.015	0.019	0.017	0.013	0.016	0.018	0.013	0.022	0.017	0.027	0.014	0.038	0.015	0.021
	0.015	0.013	0.020	0.018	0.016	0.034	0.015	0.020	0.014	0.028	0.013	0.015	0.022	0.039
	0.018	0.017	0.014	0.020	0.012	0.022	0.016	0.025	0.020	0.013	0.009	0.025	0.017	0.023
	0.014	0.017	0.018	0.025	0.018	0.028	0.015	0.017	0.016	0.020	0.010	0.069	0.015	0.037
	0.016	0.019	0.012	0.085	0.018	0.019	0.016	0.020	0.011	0.016	0.018	0.021	0.017	0.015
	0.014	0.015	0.023	0.014	0.015	0.020	0.013	0.066	0.015	0.030	0.012	0.022	0.013	0.033
	0.021	0.019	0.013	0.011	0.017	0.023	0.012	0.045	0.020	0.020	0.017	0.015	0.022	0.024
	0.015	0.030	0.014	0.025	0.018	0.018	0.012	0.038	0.012	0.017	0.013	0.026	0.017	0.027
	0.016	0.017	0.016	0.012	0.022	0.021	0.009	0.036	0.013	0.035	0.010	0.025	0.015	0.022
	0.024	0.013	0.023	0.016	0.020	0.020	0.010	0.022	0.019	0.080	0.017	0.080	0.016	0.016
	0.016	0.013	0.017	0.043	0.014	0.029	0.011	0.022	0.014	0.068	0.012	0.017	0.018	0.023
	0.018	0.009	0.009	0.013	0.015	0.020	0.011	0.024	0.015	0.025	0.010	0.019	0.018	0.016
	0.019	0.019	0.023	0.020	0.016	0.025	0.007	0.023	0.018	0.044	0.009	0.039	0.018	0.017
	0.016	0.016	0.015	0.025	0.011	0.018	0.010	0.021	0.015	0.064	0.010	0.032	0.062	0.019
	0.023	0.017	0.016	0.015	0.012	0.015	0.011	0.014	0.015	0.083	0.020	0.024	0.017	0.019
	0.013	0.013	0.017	0.024	0.016	0.014	0.011	0.028	0.025	0.055	0.022	0.020	0.017	0.015
	0.013	0.014	0.011	0.024	0.016	0.017	0.012	0.018	0.016	0.128	0.015	0.013	0.020	0.016
	0.015	0.018	0.024	0.018	0.018	0.018	0.014	0.040	0.010	0.020	0.018	0.016	0.020	0.015
	0.026	0.013	0.068	0.011	0.013	0.017	0.014	0.018	0.011	0.014	0.028	0.017	0.010	0.017
	0.014	0.011	0.014	0.020	0.015	0.011	0.012	0.020	0.020	0.013	0.017	0.017	0.015	0.021
	0.021	0.027	0.012	0.021	0.015	0.026	0.012	0.030	0.015	0.018	0.017	0.020	0.021	0.015
	0.025	0.013	0.023	0.018	0.014	0.011	0.013	0.032	0.015	0.016	0.015	0.025	0.016	0.015
	0.014	0.031	0.019	0.019	0.011	0.021	0.014	0.020	0.011	0.011	0.013	0.020	0.015	0.012
	0.018	0.009	0.065	0.012	0.012	0.028	0.011	0.028	0.014	0.047	0.018	0.059	0.018	0.012
	0.019	0.015	0.015	0.010	0.014	0.034	0.013	0.035	0.032	0.012	0.014	0.068	0.020	0.019
	0.013	0.025	0.064	0.011	0.012	0.022	0.017	0.027	0.018	0.033	0.009	0.019	0.029	0.024
	0.012	0.015	0.022	0.036	0.015	0.021	0.014	0.023	0.025	0.020	0.017	0.018	0.015	0.013
	0.018	0.019	0.032	0.023	0.015	0.016	0.014	0.027	0.020	0.019	0.017	0.019	0.019	0.021
	0.013	0.009	0.012	0.011	0.017	0.029	0.011	0.046	0.017	0.034	0.012	0.012	0.015	0.019
	0.018	0.015	0.038	0.023	0.014	0.015	0.012	0.042	0.018	0.025	0.017	0.026	0.023	0.015
	0.014	0.021	0.025	0.015	0.012	0.024	0.012	0.068	0.021	0.028	0.013	0.017	0.019	0.018

021	032-1	032-2	035	041-1	041-2	042	047-1	047-2	047-3	047-4	047-5	047-6	051-1
0.014	0.039	0.032	0.027	0.013	0.050	0.014	0.031	0.016	0.015	0.040	0.022	0.015	0.023
0.018	0.012	0.014	0.035	0.013	0.024	0.010	0.040	0.017	0.116	0.016	0.041	0.029	0.018
0.015	0.011	0.015	0.009	0.011	0.047	0.013	0.064	0.018	0.035	0.012	0.015	0.019	0.018
0.025	0.012	0.023	0.024	0.011	0.013	0.016	0.024	0.011	0.031	0.014	0.020	0.024	0.025
0.023	0.012	0.024	0.021	0.012	0.023	0.010	0.040	0.020	0.019	0.014	0.015	0.018	0.021
0.016	0.009	0.027	0.016	0.012	0.013	0.013	0.027	0.020	0.017	0.012	0.018	0.019	0.014
0.022	0.020	0.015	0.012	0.012	0.025	0.011	0.030	0.016	0.024	0.024	0.016	0.015	0.015
0.016	0.012	0.101	0.049	0.011	0.081	0.009	0.019	0.027	0.015	0.014	0.012	0.020	0.015
0.019	0.013	0.020	0.024	0.017	0.019	0.009	0.023	0.016	0.019	0.013	0.244	0.026	0.018
0.014	0.014	0.013	0.014	0.011	0.018	0.011	0.022	0.019	0.107	0.012	0.028	0.023	0.024
0.017	0.022	0.011	0.020	0.014	0.027	0.011	0.026	0.011	0.024	0.014	0.034	0.016	0.021
0.016	0.008	0.010	0.082	0.014	0.014	0.013	0.025	0.024	0.015	0.013	0.016	0.016	0.021
0.021	0.017	0.019	0.017	0.022	0.022	0.010	0.024	0.015	0.018	0.014	0.018	0.023	0.022
0.022	0.012	0.075	0.020	0.011	0.023	0.011	0.022	0.017	0.020	0.012	0.020	0.019	0.025
0.019	0.016	0.012	0.016	0.013	0.022	0.013	0.010	0.018	0.026	0.014	0.016	0.015	0.019
0.021	0.013	0.010	0.039	0.010	0.025	0.011	0.079	0.016	0.012	0.015	0.028	0.017	0.019
0.020	0.013	0.031	0.022	0.013	0.024	0.010	0.034	0.025	0.028	0.032	0.016	0.023	0.015
0.020	0.019	0.021	0.021	0.017	0.018	0.013	0.057	0.014	0.171	0.015	0.024	0.013	0.016
0.016	0.015	0.026	0.021	0.010	0.017	0.010	0.025	0.039	0.025	0.013	0.024	0.019	0.023
0.024	0.018	0.010	0.015	0.011	0.017	0.012	0.021	0.015	0.018	0.010	0.070	0.039	0.033
0.020	0.015	0.015	0.018	0.012	0.019	0.010	0.126	0.012	0.018	0.013	0.014	0.023	0.031
0.020	0.012	0.025	0.083	0.017	0.014	0.013	0.183	0.017	0.017	0.012	0.051	0.016	0.032
0.022	0.016	0.013	0.015	0.017	0.020	0.009	0.017	0.019	0.095	0.014	0.014	0.025	0.024
0.013	0.038	0.021	0.025	0.014	0.022	0.010	0.019	0.011	0.021	0.013	0.098	0.017	0.016
0.016	0.023	0.011	0.061	0.014	0.025	0.011	0.019	0.013	0.018	0.015	0.014	0.016	0.058
0.037	0.027	0.012	0.016	0.017	0.019	0.009	0.111	0.014	0.020	0.021	0.012	0.020	0.019
0.040	0.021	0.016	0.033	0.013	0.023	0.009	0.154	0.016	0.091	0.009	0.014	0.019	0.016
0.022	0.011	0.016	0.010	0.014	0.013	0.010	0.016	0.014	0.025	0.016	0.019	0.015	0.024
0.018	0.024	0.035	0.020	0.017	0.018	0.009	0.016	0.012	0.025	0.016	0.017	0.015	0.061
0.025	0.012	0.021	0.025	0.012	0.018	0.011	0.053	0.016	0.026	0.018	0.018	0.018	0.024
0.016	0.016	0.016	0.021	0.017	0.023	0.012	0.011	0.014	0.019	0.010	0.017	0.015	0.024
0.022	0.024	0.020	0.008	0.017	0.020	0.013	0.024	0.010	0.096	0.010	0.022	0.015	0.037
0.014	0.019	0.017	0.013	0.016	0.022	0.009	0.022	0.013	0.022	0.017	0.025	0.022	0.021
0.022	0.014	0.020	0.031	0.013	0.014	0.012	0.012	0.021	0.017	0.032	0.034	0.016	0.024
0.025	0.027	0.029	0.025	0.017	0.022	0.010	0.016	0.014	0.154	0.029	0.012	0.014	0.016
0.025	0.014	0.018	0.023	0.015	0.018	0.014	0.016	0.013	0.052	0.013	0.021	0.014	0.013
0.014	0.023	0.018	0.029	0.017	0.020	0.010	0.028	0.018	0.032	0.016	0.021	0.015	0.024
0.016	0.018	0.028	0.018	0.010	0.020	0.011	0.028	0.017	0.021	0.016	0.030	0.016	0.018
0.019	0.020	0.022	0.015	0.019	0.014	0.011	0.023	0.021	0.025	0.016	0.012	0.018	0.016
0.019	0.008	0.013	0.035	0.016	0.017	0.011	0.022	0.011	0.027	0.019	0.069	0.023	0.015
0.018	0.012	0.012	0.026	0.016	0.049	0.011	0.012	0.025	0.079	0.011	0.038	0.018	0.018
0.023	0.021	0.034	0.012	0.015	0.020	0.012	0.016	0.012	0.035	0.013	0.019	0.016	0.012
0.015	0.013	0.033	0.015	0.013	0.027	0.010	0.020	0.014	0.026	0.012	0.073	0.018	0.012
0.021	0.013	0.028	0.013	0.019	0.023	0.011	0.017	0.017	0.012	0.013	0.020	0.017	0.019
0.027	0.013	0.022	0.028	0.014	0.016	0.016	0.016	0.011	0.066	0.014	0.024	0.023	0.012
0.029	0.011	0.017	0.042	0.011	0.018	0.015	0.015	0.018	0.076	0.010	0.032	0.025	0.042
0.020	0.007	0.020	0.022	0.018	0.021	0.010	0.025	0.025	0.079	0.015	0.039	0.019	0.026
0.016	0.011	0.023	0.012	0.015	0.047	0.010	0.021	0.019	0.016	0.013	0.013	0.021	0.019
0.017	0.009	0.020	0.021	0.014	0.030	0.012	0.037	0.019	0.016	0.011	0.086	0.055	0.013
0.018	0.012	0.046	0.017	0.020	0.032	0.010	0.024	0.084	0.018	0.016	0.021	0.017	0.018
0.016	0.009	0.060	0.024	0.015	0.016	0.016	0.019	0.013	0.016	0.010	0.031	0.019	0.024
0.019	0.013	0.011	0.011	0.013	0.015	0.010	0.024	0.014	0.015	0.016	0.011	0.017	0.024
0.018	0.015	0.017	0.012	0.016	0.021	0.016	0.014	0.020	0.015	0.010	0.016	0.020	0.034
0.016	0.012	0.016	0.006	0.012	0.016	0.013	0.017	0.012	0.027	0.020	0.015	0.020	0.013
0.013	0.015	0.088	0.012	0.019	0.019	0.008	0.024	0.016	0.036	0.010	0.019	0.015	0.019
0.021	0.015	0.037	0.015	0.013	0.018	0.011	0.020	0.015	0.010	0.015	0.018	0.017	0.023
0.014	0.009	0.034	0.015	0.021	0.013	0.011	0.020	0.014	0.025	0.016	0.015	0.018	0.035
0.009	0.014	0.040	0.012	0.014	0.024	0.010	0.015	0.014	0.015	0.020	0.021	0.026	0.015
0.014	0.012	0.021	0.019	0.022	0.019	0.010	0.015	0.015	0.030	0.023	0.026	0.025	0.012
0.021	0.011	0.015	0.027	0.016	0.017	0.010	0.019	0.020	0.019	0.020	0.031	0.015	0.018
0.028	0.017	0.020	0.021	0.020	0.022	0.008	0.033	0.011	0.109	0.016	0.030	0.017	0.015
0.018	0.012	0.042	0.019	0.021	0.017	0.013	0.020	0.014	0.023	0.021	0.036	0.026	0.048
0.011	0.014	0.062	0.011	0.028	0.018	0.014	0.026	0.019	0.104	0.022	0.015	0.016	0.018
0.018	0.014	0.031	0.013	0.021	0.140	0.010	0.025	0.015	0.027	0.018	0.024	0.015	0.026
0.017	0.012	0.036	0.017	0.013	0.015	0.010	0.024	0.017	0.016	0.012	0.022	0.025	0.048
0.030	0.014	0.012	0.012	0.021	0.065	0.010	0.032	0.016	0.042	0.016	0.026	0.015	0.023
0.014	0.012	0.037	0.017	0.013	0.016	0.007	0.018	0.019	0.017	0.019	0.015	0.019	0.024
0.015	0.011	0.033	0.019	0.017	0.069	0.014	0.017	0.021	0.024	0.013	0.012	0.022	0.016
0.022	0.017	0.029	0.021	0.014	0.025	0.010	0.014	0.014	0.018	0.017	0.030	0.020	0.026
0.016	0.016	0.011	0.019	0.023	0.017	0.012	0.023	0.016	0.046	0.016	0.030	0.019	0.044
0.015	0.011	0.014	0.022	0.016	0.018	0.012	0.018	0.012	0.017	0.019	0.015	0.030	0.015
0.021	0.011	0.031	0.021	0.014	0.023	0.010	0.013	0.021	0.025	0.012	0.019	0.021	0.027
0.017	0.011	0.025	0.026	0.016	0.017	0.014	0.027	0.019	0.017	0.012	0.016	0.015	0.015
0.019	0.012	0.026	0.016	0.017	0.020	0.009	0.021	0.014	0.017	0.014	0.020	0.017	0.021
0.019	0.015	0.018	0.057	0.012	0.036	0.007	0.049	0.014	0.041	0.018	0.067	0.024	0.066
0.017	0.013	0.022	0.023	0.013	0.011	0.009	0.038	0.015	0.021	0.020	0.023	0.016	0.013
0.015	0.010	0.012	0.018	0.017	0.013	0.009	0.015	0.017	0.020	0.018	0.022	0.020	0.049
0.018	0.009	0.015	0.028	0.017	0.037	0.009	0.010	0.012	0.074	0.016	0.017	0.021	0.039
0.020	0.014	0.021	0.023	0.010	0.019	0.009	0.015	0.015	0.086	0.011	0.018	0.021	0.012
0.010	0.012	0.020	0.018	0.013	0.025	0.011	0.047	0.008	0.018	0.014	0.019	0.028	0.025
0.018	0.016	0.016	0.013	0.019	0.031	0.013	0.022	0.012	0.019	0.028	0.122	0.014	0.025
0.017	0.016	0.013	0.025	0.018	0.015	0.012	0.012	0.018	0.020	0.016	0.030	0.019	0.018
0.028	0.017	0.022	0.035	0.017	0.025	0.009	0.017	0.017	0.035	0.013	0.055	0.020	0.015
0.032	0.017	0.033	0.013	0.014	0.026	0.011	0.015	0.015	0.018	0.011	0.016	0.019	0.025
0.020	0.012	0.040	0.012	0.016	0.017	0.013	0.019	0.017	0.013	0.016	0.021	0.017	0.017
0.017	0.018	0.035	0.024	0.015	0.034	0.010	0.014	0.012	0.046	0.012	0.024	0.016	0.019
0.017	0.013	0.014	0.012	0.017	0.130	0.010	0.015	0.022	0.016	0.010	0.027	0.023	0.021
0.016	0.013	0.057	0.012	0.015	0.041	0.008	0.018	0.029	0.016	0.017	0.020	0.020	0.018
0.019	0.015	0.025	0.022	0.014	0.038	0.012	0.015	0.013	0.018	0.013	0.035	0.016	0.011
0.022	0.018	0.021	0.010	0.017	0.020	0.010	0.018	0.022	0.049	0.011	0.018	0.016	0.019
0.020	0.010	0.027	0.018	0.014	0.025	0.010	0.017	0.009	0.019	0.017	0.018	0.018	0.013

021	032-1	032-2	035	041-1	041-2	042	047-1	047-2	047-3	047-4	047-5	047-6	051-1
0.015	0.016	0.064	0.014	0.018	0.022	0.009	0.019	0.019	0.013	0.016	0.012	0.017	0.028
0.019	0.013	0.084	0.015	0.017	0.027	0.009	0.018	0.017	0.112	0.011	0.018	0.014	0.018
0.021	0.010	0.028	0.024	0.015	0.063	0.017	0.013	0.013	0.013	0.015	0.017	0.058	0.021
0.028	0.019	0.015	0.020	0.014	0.023	0.007	0.016	0.022	0.012	0.014	0.018	0.016	0.017
0.014	0.014	0.014	0.017	0.010	0.017	0.008	0.023	0.013	0.096	0.013	0.021	0.017	0.012
0.019	0.011	0.031	0.016	0.012	0.017	0.010	0.017	0.018	0.029	0.021	0.020	0.018	0.024
0.016	0.010	0.020	0.012	0.014	0.019	0.011	0.025	0.015	0.043	0.017	0.010	0.012	0.015
0.018	0.012	0.021	0.012	0.015	0.025	0.010	0.021	0.016	0.013	0.012	0.039	0.017	0.021
0.016	0.012	0.014	0.008	0.012	0.020	0.008	0.019	0.013	0.027	0.024	0.015	0.013	0.039
0.015	0.011	0.020	0.014	0.014	0.017	0.009	0.019	0.015	0.021	0.012	0.021	0.020	0.020
0.018	0.014	0.014	0.015	0.010	0.018	0.011	0.014	0.021	0.017	0.010	0.016	0.023	0.045
0.020	0.015	0.045	0.020	0.021	0.013	0.017	0.016	0.014	0.016	0.015	0.016	0.016	0.024
0.029	0.013	0.023	0.014	0.018	0.018	0.011	0.016	0.016	0.010	0.010	0.017	0.014	0.019
0.015	0.012	0.024	0.019	0.013	0.012	0.009	0.017	0.012	0.013	0.014	0.025	0.025	0.019
0.019	0.010	0.012	0.010	0.010	0.013	0.012	0.016	0.009	0.043	0.011	0.023	0.013	0.035
0.022	0.010	0.017	0.019	0.013	0.012	0.017	0.020	0.014	0.028	0.015	0.017	0.014	0.012
0.027	0.008	0.026	0.022	0.012	0.020	0.013	0.018	0.016	0.022	0.017	0.022	0.016	0.027
0.018	0.017	0.010	0.014	0.011	0.023	0.017	0.020	0.009	0.019	0.015	0.021	0.022	0.019
0.018	0.017	0.014	0.010	0.013	0.012	0.015	0.021	0.020	0.021	0.012	0.025	0.014	0.015
0.014	0.011	0.014	0.010	0.010	0.018	0.010	0.025	0.013	0.047	0.022	0.075	0.021	0.030
0.017	0.015	0.046	0.018	0.016	0.016	0.014	0.019	0.020	0.014	0.020	0.020	0.014	0.021
0.025	0.021	0.070	0.017	0.011	0.021	0.015	0.017	0.010	0.015	0.014	0.102	0.014	0.016
0.019	0.013	0.027	0.020	0.010	0.020	0.013	0.016	0.018	0.033	0.015	0.025	0.012	0.016
0.019	0.030	0.025	0.027	0.011	0.029	0.011	0.019	0.013	0.019	0.011	0.025	0.015	0.018
0.015	0.024	0.009	0.054	0.015	0.018	0.014	0.018	0.009	0.086	0.020	0.021	0.016	0.022
0.016	0.011	0.023	0.016	0.013	0.025	0.009	0.028	0.013	0.020	0.022	0.020	0.017	0.042
	0.010	0.025	0.024	0.018	0.018	0.011	0.030	0.012	0.011	0.008	0.052	0.017	0.028
	0.012	0.021	0.028	0.013	0.035	0.011	0.021	0.012	0.047	0.012	0.022	0.018	0.029
	0.016	0.012	0.027	0.013	0.018	0.011	0.020	0.014	0.012	0.017	0.021	0.015	0.032
	0.011	0.019	0.018	0.020	0.031	0.013	0.034	0.015	0.015	0.015	0.017	0.016	0.019
	0.017	0.026	0.030	0.011	0.018	0.007	0.016	0.013	0.032	0.021	0.019	0.018	0.039
	0.016	0.030	0.016	0.014	0.020	0.011	0.020	0.012	0.013	0.010	0.024	0.014	0.019
	0.015	0.023	0.011	0.017	0.026	0.009	0.029	0.017	0.016	0.012	0.047	0.014	0.035
	0.012	0.013	0.012	0.016	0.019	0.012	0.016	0.014	0.013	0.012	0.025	0.015	0.025
	0.014	0.036	0.015	0.014	0.025	0.017	0.018	0.015	0.010	0.012	0.023	0.028	0.024
	0.012	0.020	0.024	0.012	0.034	0.009	0.014	0.010	0.010	0.019	0.024	0.012	0.033
	0.014	0.017	0.025	0.017	0.012	0.011	0.015	0.016	0.013	0.016	0.038	0.014	0.029
	0.021	0.015	0.028	0.015	0.016	0.013	0.019	0.010	0.019	0.015	0.015	0.012	0.022
	0.015	0.012	0.012	0.013	0.025	0.011	0.014	0.014	0.019	0.012	0.051	0.019	0.012
	0.017	0.015	0.023	0.012	0.011	0.016	0.017	0.010	0.014	0.013	0.017	0.016	0.044
	0.016	0.029	0.032	0.013	0.015	0.014	0.022	0.011	0.014	0.019	0.013	0.014	0.018
	0.011	0.022	0.022	0.011	0.023	0.009	0.013	0.011	0.014	0.017	0.087	0.015	0.013
	0.014	0.009	0.012	0.013	0.033	0.010	0.015	0.011	0.023	0.020	0.017	0.018	0.030
	0.009	0.015	0.014	0.012	0.015	0.010	0.013	0.013	0.018	0.013	0.018	0.018	0.023
	0.010	0.011	0.014	0.011	0.013	0.013	0.017	0.017	0.013	0.013	0.020	0.016	0.024
	0.015	0.013	0.014	0.017	0.013	0.010	0.021	0.014	0.008	0.012	0.011	0.011	0.017
	0.012	0.013	0.016		0.036	0.009	0.016	0.015	0.010	0.012	0.015	0.015	0.024
	0.014	0.010	0.057		0.018	0.012	0.020	0.010	0.014	0.011	0.017	0.011	0.021
	0.444	0.025	0.012		0.020	0.011	0.015	0.012	0.011	0.019	0.022	0.014	0.018
	0.011	0.019	0.018		0.021	0.010	0.015	0.011	0.015	0.014	0.020	0.016	0.015
	0.012	0.014	0.041		0.021	0.012	0.016	0.014	0.018	0.019	0.015	0.016	0.021
	0.014	0.009	0.019		0.023	0.016	0.015	0.007	0.015	0.025	0.021	0.013	0.015
	0.009	0.012	0.016		0.017	0.012	0.015	0.013	0.017	0.014	0.019	0.014	0.018
	0.010	0.043	0.022		0.019	0.013	0.014	0.012	0.013	0.014	0.027	0.010	0.025
	0.013	0.026	0.014		0.019	0.011	0.015	0.015	0.014	0.015	0.029	0.014	0.021
	0.016	0.015	0.020		0.012	0.009	0.019	0.014	0.014	0.015	0.011	0.017	0.015
	0.007	0.015	0.011		0.047	0.011	0.031	0.010	0.014	0.018	0.018	0.020	0.032
	0.019	0.041	0.012		0.034	0.011	0.020	0.021	0.014	0.013	0.013	0.021	0.015
	0.011	0.031	0.009		0.027	0.011	0.020	0.013	0.009	0.017	0.012	0.013	0.015
	0.013	0.012	0.010		0.030	0.010	0.018	0.011	0.014	0.021	0.054	0.022	0.018
	0.015	0.018	0.021		0.015	0.015	0.020	0.011	0.015	0.020	0.014	0.014	0.016
	0.013	0.022	0.023			0.015	0.023	0.022	0.020	0.027	0.019	0.013	0.028
	0.012	0.033	0.023			0.008	0.015	0.016	0.013	0.013	0.021	0.018	0.017
	0.012	0.059	0.024			0.011	0.026	0.016	0.015	0.013	0.022	0.015	0.019
	0.012	0.015	0.037			0.011	0.014	0.016	0.015	0.012	0.016	0.011	0.013
	0.013	0.014	0.016			0.008	0.023	0.016	0.012	0.013	0.016	0.015	0.019
	0.015	0.012	0.051			0.009	0.085	0.011	0.016	0.016	0.014	0.012	0.031
	0.020	0.014	0.012			0.008	0.017	0.015	0.015	0.015	0.039	0.014	0.015
	0.015	0.023	0.012			0.012	0.015	0.012	0.009	0.048	0.022	0.012	0.024
	0.015	0.036	0.014			0.007	0.014	0.015	0.022	0.074	0.012	0.032	0.013
	0.015	0.010	0.020			0.014	0.022	0.015	0.016	0.019	0.070	0.016	0.030
	0.009	0.047	0.030			0.008	0.014	0.013	0.015	0.017	0.026	0.017	0.024
	0.013	0.012	0.028			0.023	0.025	0.017	0.036	0.013	0.016	0.060	0.021
	0.012	0.010	0.025			0.012		0.009	0.037	0.021	0.015	0.010	0.024
	0.020	0.045	0.018			0.011		0.014	0.029	0.014	0.021	0.010	0.015
	0.014	0.013	0.012			0.010		0.011	0.032	0.014	0.021	0.016	0.015
	0.017	0.013	0.061			0.010		0.009	0.017	0.022	0.022	0.011	0.021
	0.023	0.012	0.015			0.012		0.013	0.017	0.016		0.013	0.017
	0.011	0.014	0.012			0.011		0.015	0.017	0.013		0.011	0.027
	0.014	0.014	0.015			0.011		0.012	0.034	0.014		0.012	0.019
	0.011	0.009	0.108					0.013	0.014	0.018		0.017	0.015
	0.013	0.020	0.024					0.010	0.036	0.014		0.015	0.021
	0.014	0.009	0.011					0.018	0.014	0.021		0.018	0.020
	0.014	0.009	0.021					0.010	0.017	0.012		0.021	0.041
	0.012	0.106	0.010					0.016	0.016	0.015		0.013	0.015
	0.029	0.012	0.024					0.024	0.021	0.013		0.017	0.030
	0.016	0.017	0.011					0.011	0.022	0.022		0.020	0.015
	0.010	0.011	0.019					0.012	0.029	0.013		0.015	0.018
	0.012	0.015	0.026					0.014	0.010	0.014		0.022	0.024
	0.016	0.016	0.026					0.011	0.019	0.015		0.018	0.018
	0.015	0.012	0.071					0.011	0.014	0.017		0.018	0.025

021	032-1	032-2	035	041-1	041-2	042	047-1	047-2	047-3	047-4	047-5	047-6	051-1
	0.012	0.013	0.020					0.021	0.026	0.012		0.019	0.015
	0.021	0.013	0.026					0.020	0.013	0.023		0.012	0.033
	0.015	0.015	0.019					0.012	0.016	0.021		0.020	0.026
	0.014	0.013	0.034					0.018	0.014	0.009		0.015	0.046
	0.017	0.013	0.015					0.008	0.015	0.017		0.013	0.025
	0.019	0.016	0.016					0.010	0.026	0.011		0.011	0.016
	0.039	0.012	0.012					0.017	0.016	0.017		0.022	0.042
		0.016	0.020					0.014	0.013	0.011		0.017	0.022
		0.042	0.019					0.011	0.017	0.014		0.015	0.011
			0.017					0.013	0.018	0.023		0.101	0.016
			0.029					0.012	0.013	0.014		0.014	0.028
			0.023					0.010	0.021	0.018		0.017	0.019
			0.012					0.016	0.020	0.015			0.016
			0.034					0.013	0.015	0.010			0.024
			0.024					0.016	0.015	0.017			0.015
			0.044					0.013	0.029	0.012			0.028
			0.026					0.011	0.025	0.010			0.021
			0.019					0.012	0.024	0.014			0.027
			0.018					0.014	0.014	0.010			0.021
			0.066					0.011	0.017	0.015			0.024
			0.018					0.022	0.014	0.007			0.021
			0.025					0.015	0.014	0.015			0.021
			0.024					0.013	0.019	0.012			0.020
			0.033					0.009	0.012	0.010			0.019
			0.029					0.013		0.012			0.013
			0.020					0.011		0.013			0.018
			0.050					0.020					0.020
			0.021					0.008					0.017
			0.042					0.008					0.013
			0.026					0.017					0.013
			0.029					0.030					0.012
			0.012					0.011					0.013
			0.021					0.012					0.012
								0.013					0.009
								0.020					0.015
								0.046					0.012
								0.015					0.009
								0.019					0.012
								0.015					0.012
								0.015					0.014
								0.012					0.010
								0.013					0.010
								0.013					0.017
								0.013					0.014
								0.013					0.013
								0.014					0.037
								0.014					0.021
								0.021					0.020
								0.017					0.028
								0.018					0.021
								0.017					0.011
								0.016					0.012
								0.014					0.016
								0.010					0.021
								0.021					0.017
								0.015					0.017
								0.011					0.024
								0.022					0.013
								0.015					
								0.008					
								0.011					
								0.006					
								0.007					
								0.011					
								0.010					
								0.009					

Site 059 - Tambor Cone

Grain Size Diameter in PHI Scale

	021	032-1	032-2	035	041-1	041-2	042	047-1	047-2	047-3	047-4	047-5	047-6	051-1
Average	-4.2	-3.9	-4.4	-4.3	-3.9	-4.5	-3.5	-4.5	-3.9	-4.5	-3.9	-4.6	-4.1	-4.3
Median	-4.2	-3.8	-4.3	-4.2	-3.8	-4.3	-3.5	-4.4	-3.9	-4.2	-3.9	-4.4	-4.1	-4.3
Min	-5.8	-8.8	-6.9	-6.8	-4.8	-7.1	-5.0	-7.5	-6.4	-7.4	-6.2	-7.9	-6.7	-6.0
Max	-3.2	-2.9	-3.1	-2.6	-3.2	-3.4	-2.8	-3.4	-2.6	-3.0	-2.9	-3.4	-3.2	-3.1
Count	198	270	272	296	218	233	252	245	329	287	289	249	275	321
StDev	**0.4**	**0.5**	**0.8**	**0.7**	**0.3**	**0.6**	**0.3**	**0.6**	**0.4**	**0.9**	**0.4**	**0.7**	**0.4**	**0.5**
	-4.3	-5.0	-4.2	-4.4	-3.5	-4.8	-3.4	-5.1	-3.9	-4.1	-4.1	-4.9	-4.5	-5.2
	-4.1	-4.3	-4.4	-3.3	-3.5	-4.5	-4.1	-4.6	-4.1	-5.4	-4.2	-5.2	-4.0	-4.9
	-4.8	-4.0	-3.9	-4.2	-3.7	-4.6	-4.6	-5.1	-3.8	-3.7	-4.4	-5.8	-3.8	-3.9
	-4.8	-4.3	-4.1	-4.1	-3.5	-4.8	-4.2	-4.5	-4.4	-4.3	-4.2	-4.3	-3.9	-4.2
	-4.2	-4.6	-3.8	-4.3	-3.6	-5.8	-5.0	-4.5	-4.3	-4.1	-3.8	-4.3	-3.7	-4.9
	-4.1	-4.2	-4.5	-3.7	-4.0	-4.0	-3.9	-5.5	-4.6	-4.4	-4.1	-4.6	-4.2	-3.9
	-4.6	-4.3	-3.8	-4.2	-4.0	-4.7	-3.4	-4.8	-4.4	-4.0	-4.0	-4.4	-4.2	-4.9
	-4.7	-3.7	-4.4	-4.3	-3.9	-4.6	-3.9	-5.1	-3.9	-4.7	-4.0	-4.3	-4.2	-4.8
	-4.1	-4.2	-3.8	-4.2	-3.3	-4.8	-3.8	-5.1	-4.2	-4.1	-5.4	-4.5	-3.9	-3.6
	-4.6	-4.1	-5.1	-4.3	-3.5	-4.3	-4.0	-4.7	-4.0	-3.7	-3.5	-4.3	-4.2	-4.0
	-4.5	-4.8	-4.4	-3.3	-3.9	-3.8	-4.0	-3.9	-4.1	-4.3	-3.9	-5.1	-4.0	-4.3
	-4.1	-3.8	-4.7	-4.1	-3.9	-5.8	-4.2	-3.9	-4.3	-5.6	-4.3	-4.2	-3.9	-4.0
	-4.1	-4.5	-4.4	-3.4	-3.2	-4.0	-3.7	-4.4	-4.1	-4.9	-3.9	-5.4	-4.2	-4.5
	-4.1	-2.9	-4.3	-2.7	-4.1	-4.4	-3.9	-5.2	-4.0	-4.0	-4.0	-4.1	-4.4	-4.5
	-3.8	-4.2	-4.0	-4.0	-3.7	-3.9	-3.8	-4.9	-3.7	-4.5	-3.8	-4.1	-4.1	-4.8
	-4.3	-3.9	-4.9	-4.3	-4.5	-4.3	-3.1	-4.8	-3.8	-4.0	-4.4	-4.6	-4.3	-4.5
	-4.2	-3.9	-6.0	-3.4	-3.6	-4.0	-3.6	-4.7	-3.9	-6.4	-4.2	-4.1	-3.8	-4.4
	-5.8	-4.3	-3.7	-4.1	-4.0	-4.7	-3.8	-4.8	-3.8	-4.2	-3.7	-4.4	-4.5	-4.4
	-4.4	-4.1	-4.9	-4.1	-4.4	-4.0	-3.6	-6.0	-4.1	-3.9	-4.2	-4.7	-3.9	-4.8
	-4.4	-3.7	-3.9	-3.7	-3.8	-4.4	-3.3	-4.5	-3.5	-4.5	-3.7	-4.4	-4.1	-4.2
	-4.2	-3.4	-3.9	-3.7	-4.1	-4.8	-3.1	-5.0	-4.0	-4.0	-3.9	-6.0	-4.2	-4.4
	-4.4	-4.2	-4.3	-5.2	-4.3	-4.2	-3.8	-4.6	-4.2	-4.1	-4.2	-5.4	-3.8	-3.9
	-3.6	-3.3	-4.2	-4.4	-3.9	-3.7	-3.9	-4.9	-3.9	-4.2	-4.1	-4.7	-3.7	-4.9
	-4.2	-4.1	-6.9	-4.9	-3.6	-4.6	-4.0	-5.2	-3.8	-4.1	-3.7	-4.5	-4.2	-3.9
	-3.5	-3.9	-3.5	-3.8	-3.7	-4.3	-3.6	-4.6	-4.4	-5.4	-3.8	-4.1	-4.0	-4.0
	-4.0	-3.5	-4.8	-3.8	-4.3	-4.8	-3.2	-3.7	-4.1	-3.5	-4.0	-5.0	-4.2	-4.3
	-4.1	-3.1	-6.8	-3.7	-4.3	-4.5	-3.3	-4.0	-4.1	-5.0	-3.7	-3.7	-4.1	-4.6
	-3.7	-4.2	-6.7	-4.7	-3.7	-4.5	-3.6	-3.7	-3.8	-4.3	-3.7	-5.2	-4.5	-4.8
	-4.6	-3.9	-4.8	-4.3	-3.7	-4.8	-3.5	-4.4	-3.6	-5.7	-3.9	-3.7	-6.4	-3.9
	-4.0	-3.2	-3.6	-5.2	-3.8	-4.6	-3.6	-5.1	-4.0	-5.4	-3.3	-5.4	-3.7	-3.1
	-3.9	-3.9	-4.8	-3.8	-3.8	-4.3	-3.5	-3.9	-4.1	-4.2	-3.9	-4.5	-4.1	-5.0
	-4.2	-3.3	-3.8	-4.4	-4.1	-4.2	-3.3	-4.4	-4.2	-5.9	-3.9	-4.8	-4.5	-5.6
	-4.2	-3.5	-4.8	-4.8	-3.7	-4.1	-3.3	-4.1	-4.2	-4.2	-4.0	-3.5	-4.1	-4.9
	-4.0	-4.3	-3.9	-4.1	-3.8	-5.0	-3.5	-3.9	-4.5	-4.6	-4.0	-5.7	-3.8	-4.9
	-3.7	-4.3	-5.0	-3.8	-3.7	-5.6	-3.6	-4.3	-4.5	-3.7	-4.0	-4.7	-4.6	-4.0
	-4.4	-3.8	-4.7	-5.9	-3.7	-4.1	-3.7	-4.5	-4.1	-6.6	-4.3	-6.0	-3.9	-3.9
	-5.0	-4.1	-5.4	-4.7	-4.5	-4.4	-3.8	-4.9	-3.6	-4.1	-3.8	-5.5	-4.4	-4.9
	-4.4	-3.8	-5.6	-3.7	-4.2	-5.6	-3.7	-5.1	-4.3	-4.1	-4.3	-4.3	-4.0	-5.4
	-4.4	-3.1	-4.1	-4.4	-3.6	-4.1	-3.5	-4.5	-3.8	-4.6	-4.2	-4.3	-4.3	-4.5
	-4.6	-4.0	-4.2	-3.9	-3.2	-6.5	-3.7	-4.9	-4.0	-3.5	-4.0	-4.8	-3.8	-3.9
	-4.1	-4.1	-3.7	-4.5	-3.6	-4.8	-3.9	-5.3	-4.1	-7.2	-3.2	-4.9	-3.9	-3.6
	-4.5	-3.8	-5.2	-3.8	-3.5	-4.5	-3.8	-4.9	-4.5	-4.1	-4.1	-4.3	-4.3	-5.1
	-4.0	-4.3	-3.7	-3.2	-3.5	-5.3	-4.3	-5.0	-4.1	-4.3	-4.0	-4.7	-3.9	-3.9
	-5.8	-4.0	-3.7	-5.5	-3.6	-4.1	-3.7	-4.9	-4.1	-5.0	-3.9	-5.6	-4.0	-3.6
	-3.4	-3.4	-4.9	-3.6	-3.9	-4.5	-4.0	-4.8	-3.5	-4.3	-3.7	-4.8	-3.9	-4.2
	-4.1	-3.8	-3.3	-4.6	-4.2	-4.9	-3.7	-4.9	-4.0	-4.0	-3.4	-3.8	-4.2	-3.7
	-3.7	-3.8	-4.4	-4.3	-3.6	-3.9	-4.3	-4.5	-4.9	-4.9	-3.6	-5.2	-3.9	-4.0
	-3.6	-4.0	-4.2	-3.7	-4.4	-4.0	-4.2	-4.3	-3.7	-4.4	-3.7	-4.3	-4.0	-4.2
	-3.5	-4.0	-4.8	-4.2	-3.6	-5.2	-3.7	-4.7	-3.9	-4.5	-4.1	-4.3	-3.2	-5.5
	-3.9	-3.6	-4.2	-4.5	-4.3	-5.4	-3.5	-4.3	-4.3	-3.6	-4.2	-4.5	-3.5	-4.8
	-3.9	-4.2	-4.1	-3.6	-4.0	-4.2	-3.7	-4.5	-4.1	-4.8	-3.8	-5.2	-3.9	-4.4
	-3.9	-3.7	-4.4	-4.2	-4.0	-5.1	-3.9	-4.3	-3.8	-4.8	-3.7	-3.9	-4.4	-5.3
	-4.2	-4.1	-3.8	-4.3	-3.6	-4.4	-4.0	-4.6	-4.3	-3.7	-3.2	-4.7	-4.1	-4.5
	-3.8	-4.1	-4.2	-4.6	-4.1	-4.8	-3.9	-4.1	-4.0	-4.3	-3.4	-6.1	-3.9	-5.2
	-4.0	-4.3	-3.6	-6.4	-4.2	-4.2	-4.0	-4.3	-3.4	-4.0	-4.2	-4.4	-4.1	-3.9
	-3.8	-3.9	-4.5	-3.8	-3.9	-4.3	-3.7	-6.0	-3.9	-4.9	-3.6	-4.4	-3.7	-5.1
	-4.4	-4.2	-3.7	-3.5	-4.1	-4.5	-3.6	-5.5	-4.3	-4.3	-4.1	-4.0	-4.4	-4.6
	-3.9	-4.9	-3.8	-4.6	-4.2	-4.2	-3.6	-5.3	-3.6	-4.1	-3.7	-4.7	-4.1	-4.8
	-4.0	-4.1	-4.0	-3.5	-4.5	-4.4	-3.1	-5.2	-3.7	-5.1	-3.4	-4.6	-3.9	-4.5
	-4.6	-3.7	-4.5	-4.0	-4.3	-4.3	-3.3	-4.5	-4.2	-6.3	-4.1	-6.3	-4.0	-4.0
	-4.0	-3.7	-4.1	-5.4	-3.8	-4.9	-3.5	-4.5	-3.8	-6.1	-3.6	-4.1	-4.2	-4.5
	-4.2	-3.1	-3.2	-3.7	-3.9	-4.3	-3.4	-4.6	-3.9	-4.7	-3.3	-4.2	-4.2	-4.0
	-4.2	-4.3	-4.5	-4.4	-4.0	-4.6	-2.8	-4.5	-4.1	-5.5	-3.2	-5.3	-4.2	-4.1
	-4.0	-4.0	-3.9	-4.6	-3.5	-4.1	-3.3	-4.4	-3.9	-6.0	-3.3	-5.0	-5.9	-4.3
	-4.6	-4.1	-4.0	-3.9	-3.6	-3.9	-3.4	-3.8	-3.9	-6.4	-4.4	-4.6	-4.1	-4.2
	-3.7	-3.7	-4.1	-4.6	-4.0	-3.8	-3.5	-4.8	-4.6	-5.8	-4.4	-4.3	-4.1	-3.9
	-3.7	-3.8	-3.4	-4.6	-4.0	-4.1	-3.5	-4.1	-4.0	-7.0	-3.9	-3.7	-4.3	-4.0
	-3.9	-4.2	-4.6	-4.2	-4.2	-4.2	-3.8	-5.3	-3.3	-4.3	-4.2	-4.0	-4.3	-3.9
	-4.7	-3.7	-6.1	-3.4	-3.7	-4.1	-3.8	-4.2	-3.4	-3.8	-4.8	-4.1	-3.3	-4.1
	-3.8	-3.5	-3.8	-4.3	-3.9	-3.5	-3.6	-4.4	-4.3	-3.7	-4.1	-4.1	-3.9	-4.4
	-4.4	-4.8	-3.6	-4.4	-3.9	-4.7	-3.6	-4.9	-3.9	-4.2	-4.1	-4.3	-4.4	-3.9
	-4.6	-3.7	-4.5	-4.2	-3.9	-3.5	-3.7	-5.0	-3.9	-4.0	-3.9	-4.6	-4.0	-3.9
	-3.8	-5.0	-4.2	-4.2	-3.4	-4.4	-3.8	-4.3	-3.5	-3.5	-3.7	-4.3	-3.9	-3.6
	-4.2	-3.1	-6.0	-3.6	-3.5	-4.8	-3.4	-4.8	-3.8	-5.5	-4.1	-5.9	-4.1	-3.6
	-4.3	-3.9	-3.9	-3.3	-3.9	-5.1	-3.7	-5.1	-5.0	-3.6	-3.8	-6.1	-4.3	-4.3
	-3.7	-4.7	-6.0	-3.4	-3.6	-4.5	-4.1	-4.8	-4.2	-5.0	-3.2	-4.3	-4.9	-4.6
	-3.6	-3.9	-4.5	-5.2	-3.9	-4.4	-3.8	-4.5	-4.6	-4.3	-4.0	-4.2	-3.9	-3.7
	-4.1	-4.2	-5.0	-4.5	-3.9	-4.0	-3.8	-4.8	-4.3	-4.3	-4.1	-4.3	-4.3	-4.4
	-3.7	-3.2	-3.6	-3.4	-4.1	-4.9	-3.4	-5.5	-4.1	-5.1	-3.6	-3.6	-3.9	-4.3
	-4.1	-3.9	-5.2	-4.5	-3.8	-3.9	-3.5	-5.4	-4.1	-4.6	-4.1	-4.7	-4.5	-3.9
	-3.8	-4.4	-4.7	-3.9	-3.6	-4.6	-3.6	-6.1	-4.4	-4.8	-3.7	-4.1	-4.2	-4.2

021	032-1	032-2	035	041-1	041-2	042	047-1	047-2	047-3	047-4	047-5	047-6	051-1
-3.8	-5.3	-5.0	-4.8	-3.7	-5.6	-3.8	-5.0	-4.0	-3.9	-5.3	-4.5	-3.9	-4.5
-4.2	-3.5	-3.8	-5.1	-3.7	-4.6	-3.3	-5.3	-4.1	-6.9	-4.0	-5.4	-4.9	-4.2
-3.9	-3.4	-3.9	-3.1	-3.5	-5.6	-3.7	-6.0	-4.2	-5.1	-3.6	-3.9	-4.2	-4.2
-4.6	-3.6	-4.5	-4.6	-3.4	-3.7	-4.0	-4.6	-3.5	-5.0	-3.8	-4.4	-4.6	-4.6
-4.5	-3.6	-4.6	-4.4	-3.5	-4.5	-3.4	-5.3	-4.3	-4.3	-3.8	-3.9	-4.1	-4.4
-4.0	-3.2	-4.8	-4.0	-3.6	-3.7	-3.7	-4.7	-4.3	-4.1	-3.6	-4.2	-4.3	-3.8
-4.5	-4.3	-3.9	-3.6	-3.6	-4.6	-3.4	-4.9	-4.0	-4.6	-4.6	-4.0	-3.9	-3.9
-4.0	-3.6	-6.7	-5.6	-3.4	-6.3	-3.2	-4.3	-4.7	-3.9	-3.8	-3.6	-4.3	-3.9
-4.3	-3.6	-4.3	-4.6	-4.1	-4.3	-3.1	-4.5	-4.0	-4.3	-3.7	-7.9	-4.7	-4.2
-3.8	-3.8	-3.7	-3.8	-3.5	-4.1	-3.5	-4.5	-4.3	-6.7	-3.6	-4.8	-4.6	-4.6
-4.1	-4.4	-3.5	-4.3	-3.8	-4.8	-3.4	-4.7	-3.4	-4.6	-3.8	-5.1	-4.0	-4.4
-4.0	-3.1	-3.3	-6.4	-3.8	-3.8	-3.7	-4.7	-4.6	-3.9	-3.7	-4.0	-4.0	-4.4
-4.4	-4.1	-4.2	-4.1	-4.4	-4.4	-3.4	-4.6	-3.9	-4.1	-3.8	-4.2	-4.5	-4.4
-4.5	-3.6	-6.2	-4.3	-3.5	-4.5	-3.5	-4.4	-4.1	-4.3	-3.6	-4.4	-4.3	-4.7
-4.3	-4.0	-3.6	-4.0	-3.7	-4.4	-3.7	-3.4	-4.2	-4.7	-3.8	-4.0	-3.9	-4.2
-4.4	-3.7	-3.3	-5.3	-3.3	-4.6	-3.5	-6.3	-4.0	-3.6	-3.9	-4.8	-4.1	-4.3
-4.3	-3.7	-5.0	-4.5	-3.7	-4.6	-3.4	-5.1	-4.7	-4.8	-5.0	-4.0	-4.5	-3.9
-4.3	-4.2	-4.4	-4.4	-4.1	-4.1	-3.6	-5.8	-3.8	-7.4	-3.9	-4.6	-3.6	-4.0
-4.0	-3.9	-4.7	-4.4	-3.4	-4.1	-3.3	-4.7	-5.3	-4.7	-3.7	-4.6	-4.2	-4.5
-4.6	-4.2	-3.3	-4.0	-3.5	-4.0	-3.6	-4.4	-3.9	-4.2	-3.3	-6.1	-5.3	-5.0
-4.3	-3.9	-3.9	-4.1	-3.6	-4.3	-3.3	-7.0	-3.5	-4.2	-3.7	-3.8	-4.5	-5.0
-4.4	-3.6	-4.6	-6.4	-4.1	-3.8	-3.7	-7.5	-4.1	-4.0	-3.6	-5.7	-4.0	-5.0
-4.5	-4.0	-3.7	-3.9	-4.1	-4.3	-3.1	-4.1	-4.2	-6.6	-3.8	-3.8	-4.6	-4.6
-3.7	-5.3	-4.4	-4.6	-3.8	-4.5	-3.4	-4.2	-3.4	-4.4	-3.7	-6.6	-4.1	-4.0
-4.0	-4.5	-3.4	-5.9	-3.9	-4.7	-3.5	-4.2	-3.7	-4.1	-3.9	-3.9	-4.0	-5.9
-5.2	-4.7	-3.6	-4.0	-4.1	-4.3	-3.1	-6.8	-3.8	-4.3	-4.4	-3.6	-4.3	-4.2
-5.3	-4.4	-4.0	-5.1	-3.7	-4.5	-3.1	-7.3	-4.0	-6.5	-3.2	-3.8	-4.2	-4.0
-4.5	-3.4	-4.0	-3.3	-3.9	-3.7	-3.3	-4.0	-3.8	-4.6	-4.0	-4.3	-3.9	-4.6
-4.2	-4.6	-5.1	-4.3	-4.1	-4.2	-3.2	-4.0	-3.6	-4.6	-4.0	-4.1	-3.9	-5.9
-4.7	-3.6	-4.4	-4.6	-3.6	-4.2	-3.5	-5.7	-4.0	-4.7	-4.1	-4.2	-4.2	-4.6
-4.0	-4.0	-4.0	-4.4	-4.1	-4.5	-3.5	-3.5	-3.8	-4.2	-3.4	-4.1	-3.9	-4.6
-4.5	-4.6	-4.4	-3.1	-4.1	-4.3	-3.7	-4.6	-3.3	-6.6	-3.4	-4.4	-3.9	-5.2
-3.8	-4.2	-4.1	-3.7	-4.0	-4.5	-3.1	-4.5	-3.7	-4.4	-4.1	-4.6	-4.4	-4.4
-4.4	-3.8	-4.3	-4.9	-3.7	-3.8	-3.6	-3.6	-4.4	-4.1	-5.0	-5.1	-4.0	-4.6
-4.7	-4.8	-4.8	-4.7	-4.1	-4.5	-3.3	-4.0	-3.8	-7.3	-4.9	-3.6	-3.8	-4.0
-4.6	-3.8	-4.2	-4.5	-3.9	-4.2	-3.8	-4.0	-3.7	-5.7	-3.7	-4.4	-3.8	-3.7
-3.8	-4.5	-4.2	-4.8	-4.1	-4.3	-3.3	-4.8	-4.2	-5.0	-4.0	-4.4	-3.9	-4.6
-4.0	-4.2	-4.8	-4.2	-3.4	-4.3	-3.4	-4.8	-4.1	-4.4	-4.0	-4.9	-4.0	-4.2
-4.3	-4.3	-4.4	-3.9	-4.3	-3.8	-3.4	-4.5	-4.4	-4.7	-4.0	-3.6	-4.2	-4.0
-4.2	-3.0	-3.7	-5.1	-4.0	-4.1	-3.5	-4.5	-3.4	-4.7	-4.2	-6.1	-4.5	-3.9
-4.2	-3.6	-3.6	-4.7	-4.0	-5.6	-3.4	-3.6	-4.6	-6.3	-3.5	-5.3	-4.2	-4.1
-4.5	-4.4	-5.1	-3.6	-3.9	-4.3	-3.6	-4.0	-3.6	-5.1	-3.7	-4.2	-4.0	-3.6
-3.9	-3.7	-5.0	-3.9	-3.7	-4.8	-3.3	-4.3	-3.8	-4.7	-3.6	-6.2	-4.2	-3.6
-4.4	-3.7	-4.8	-3.7	-4.3	-4.5	-3.4	-4.1	-4.1	-3.6	-3.7	-4.3	-4.1	-4.2
-4.7	-3.7	-4.5	-4.8	-3.8	-4.0	-4.0	-4.0	-3.5	-6.0	-3.8	-4.6	-4.5	-3.6
-4.9	-3.5	-4.1	-5.4	-3.5	-4.2	-3.9	-3.9	-4.2	-6.3	-3.3	-5.0	-4.6	-5.4
-4.3	-2.9	-4.4	-4.4	-4.2	-4.4	-3.3	-4.6	-4.7	-6.3	-3.9	-5.3	-4.2	-4.7
-4.0	-3.4	-4.5	-3.6	-3.9	-5.6	-3.3	-4.4	-4.3	-4.0	-3.7	-3.7	-4.4	-4.2
-4.1	-3.2	-4.3	-4.4	-3.8	-4.9	-3.6	-5.2	-4.2	-4.0	-3.5	-6.4	-5.8	-3.7
-4.2	-3.5	-5.5	-4.1	-4.3	-5.0	-3.3	-4.6	-6.4	-4.2	-4.0	-4.4	-4.1	-4.2
-4.0	-3.2	-5.9	-4.6	-4.0	-4.0	-4.0	-4.3	-3.7	-4.0	-3.4	-5.0	-4.3	-4.6
-4.3	-3.7	-3.4	-3.5	-3.6	-3.9	-3.3	-4.6	-3.8	-3.9	-4.0	-3.5	-4.1	-4.6
-4.2	-3.9	-4.1	-3.6	-4.0	-4.4	-4.0	-3.8	-4.3	-3.9	-3.3	-4.0	-4.3	-5.1
-4.0	-3.6	-4.0	-2.6	-3.6	-4.0	-3.6	-4.1	-3.6	-4.8	-4.3	-3.9	-4.4	-3.7
-3.7	-3.9	-6.5	-3.6	-4.2	-4.3	-3.0	-4.6	-4.0	-5.2	-3.4	-4.2	-3.9	-4.2
-4.4	-3.9	-5.2	-3.9	-3.7	-4.2	-3.4	-4.3	-3.9	-3.3	-3.9	-4.2	-4.1	-4.5
-3.8	-3.2	-5.1	-3.9	-4.4	-3.7	-3.5	-4.3	-3.8	-4.7	-4.0	-3.9	-4.2	-5.1
-3.2	-3.8	-5.3	-3.5	-3.8	-4.6	-3.3	-3.9	-3.8	-3.9	-4.3	-4.4	-4.7	-3.9
-3.8	-3.6	-4.4	-4.3	-4.5	-4.2	-3.3	-3.9	-3.9	-4.9	-4.5	-4.7	-4.6	-3.6
-4.4	-3.4	-3.9	-4.8	-4.0	-4.1	-3.3	-4.2	-4.3	-4.3	-4.3	-5.0	-3.9	-4.2
-4.8	-4.1	-4.3	-4.4	-4.3	-4.5	-3.1	-5.0	-3.4	-6.8	-4.0	-4.9	-4.1	-3.9
-4.2	-3.6	-5.4	-4.3	-4.4	-4.1	-3.7	-4.3	-3.8	-4.5	-4.4	-5.2	-4.7	-5.6
-3.5	-3.8	-5.9	-3.5	-4.8	-4.1	-3.8	-4.7	-4.3	-6.7	-4.5	-3.9	-4.0	-4.2
-4.1	-3.8	-5.0	-3.8	-4.4	-7.1	-3.4	-4.6	-3.9	-4.8	-4.2	-4.6	-3.9	-4.7
-4.1	-3.6	-5.2	-4.1	-3.7	-3.9	-3.3	-4.6	-4.1	-4.0	-3.6	-4.5	-4.6	-5.6
-4.9	-3.8	-3.6	-3.6	-4.4	-6.0	-3.3	-5.0	-4.0	-5.4	-4.0	-4.7	-3.9	-4.5
-3.8	-3.6	-5.2	-4.1	-3.7	-4.0	-2.8	-4.2	-4.2	-4.1	-4.2	-3.9	-4.2	-4.6
-3.9	-3.4	-5.1	-4.2	-4.1	-6.1	-3.8	-4.1	-4.4	-4.6	-3.7	-3.6	-4.4	-4.0
-4.5	-4.1	-4.8	-4.4	-3.8	-4.7	-3.4	-3.8	-3.8	-4.2	-4.1	-4.9	-4.3	-4.7
-4.0	-4.0	-3.4	-4.2	-4.5	-4.1	-3.6	-4.5	-4.0	-5.5	-4.0	-4.9	-4.3	-5.5
-3.9	-3.5	-3.8	-4.4	-4.0	-4.2	-3.6	-4.2	-3.6	-4.1	-4.3	-3.9	-4.9	-3.9
-4.4	-3.5	-5.0	-4.4	-3.8	-4.5	-3.4	-3.7	-4.4	-4.6	-3.5	-4.2	-4.4	-4.7
-4.1	-3.4	-4.7	-4.7	-4.0	-4.1	-3.8	-4.8	-4.3	-4.1	-3.6	-4.0	-3.9	-3.9
-4.3	-3.6	-4.7	-4.0	-4.0	-4.3	-3.2	-4.4	-3.8	-4.1	-3.9	-4.3	-4.1	-4.4
-4.2	-3.9	-4.2	-5.8	-3.5	-5.2	-2.9	-5.6	-3.8	-5.4	-4.2	-6.1	-4.6	-6.0
-4.1	-3.6	-4.4	-4.5	-3.7	-3.5	-3.1	-5.2	-3.9	-4.4	-4.3	-4.5	-4.0	-3.7
-3.9	-3.3	-3.6	-4.1	-4.1	-3.7	-3.1	-3.9	-4.1	-4.3	-4.1	-4.5	-4.3	-5.6
-4.1	-3.1	-3.9	-4.8	-4.1	-5.2	-3.2	-3.4	-3.6	-6.2	-4.0	-4.1	-4.4	-5.3
-4.3	-3.8	-4.4	-4.5	-3.4	-4.2	-3.1	-3.9	-3.9	-6.4	-3.4	-4.2	-4.4	-3.6
-3.3	-3.6	-4.3	-4.2	-3.7	-4.7	-3.4	-5.5	-3.0	-4.2	-3.8	-4.3	-4.8	-4.6
-4.1	-4.0	-4.0	-3.7	-4.2	-4.9	-3.7	-4.4	-3.6	-4.2	-4.8	-6.9	-3.8	-4.6
-4.1	-4.0	-3.7	-4.7	-4.1	-3.9	-3.6	-3.6	-4.2	-4.3	-4.0	-4.9	-4.3	-4.1
-4.8	-4.1	-4.5	-5.1	-4.1	-4.6	-3.1	-4.0	-4.1	-5.1	-3.7	-5.8	-4.3	-3.9
-5.0	-4.1	-5.0	-3.7	-3.8	-4.7	-3.4	-3.9	-3.9	-4.2	-3.4	-4.0	-4.3	-4.6
-4.3	-3.6	-5.3	-3.6	-4.0	-4.1	-3.7	-4.2	-4.1	-3.7	-4.0	-4.4	-4.1	-4.1
-4.1	-4.2	-5.1	-4.6	-3.9	-5.1	-3.3	-3.8	-3.6	-5.5	-3.6	-4.6	-4.0	-4.2
-4.1	-3.6	-3.8	-3.6	-4.1	-7.0	-3.4	-3.9	-4.5	-4.0	-3.4	-4.8	-4.5	-4.4
-4.0	-3.7	-5.8	-3.6	-3.9	-5.4	-3.1	-4.2	-4.9	-4.0	-4.1	-4.3	-4.3	-4.2
-4.2	-4.0	-4.6	-4.5	-3.8	-5.3	-3.6	-3.9	-3.7	-4.2	-3.7	-5.1	-4.0	-3.4
-4.5	-4.2	-4.4	-3.3	-4.1	-4.3	-3.3	-4.2	-4.5	-5.6	-3.5	-4.1	-4.0	-4.2
-4.4	-3.4	-4.7	-4.1	-3.8	-4.7	-3.4	-4.1	-3.2	-4.2	-4.1	-4.1	-4.2	-3.7

021	032-1	032-2	035	041-1	041-2	042	047-1	047-2	047-3	047-4	047-5	047-6	051-1
-3.9	-4.0	-6.0	-3.9	-4.2	-4.5	-3.1	-4.2	-4.2	-3.7	-4.0	-3.6	-4.1	-4.8
-4.2	-3.7	-6.4	-3.9	-4.1	-4.7	-3.2	-4.2	-4.1	-6.8	-3.4	-4.1	-3.8	-4.2
-4.4	-3.4	-4.8	-4.6	-3.9	-6.0	-4.1	-3.7	-3.7	-3.7	-3.9	-4.1	-5.9	-4.4
-4.8	-4.2	-3.9	-4.3	-3.8	-4.5	-2.8	-4.0	-4.4	-3.5	-3.8	-4.2	-4.0	-4.1
-3.8	-3.8	-3.8	-4.1	-3.4	-4.1	-3.1	-4.5	-3.7	-6.6	-3.7	-4.4	-4.0	-3.6
-4.2	-3.5	-4.9	-4.0	-3.5	-4.1	-3.4	-4.1	-4.2	-4.9	-4.4	-4.3	-4.2	-4.6
-4.0	-3.4	-4.3	-3.6	-3.8	-4.3	-3.5	-4.6	-3.9	-5.4	-4.0	-3.4	-3.6	-3.9
-4.2	-3.6	-4.4	-3.6	-3.9	-4.6	-3.3	-4.4	-4.0	-3.7	-3.6	-5.3	-4.1	-4.4
-4.0	-3.6	-3.9	-2.9	-3.6	-4.3	-3.1	-4.3	-3.7	-4.8	-4.6	-3.9	-3.7	-5.3
-3.9	-3.5	-4.3	-3.8	-3.8	-4.1	-3.1	-4.3	-3.9	-4.4	-3.5	-4.4	-4.3	-4.3
-4.1	-3.8	-3.8	-3.9	-3.3	-4.2	-3.5	-3.8	-4.4	-4.1	-3.3	-4.0	-4.5	-5.5
-4.3	-3.9	-5.5	-4.3	-4.4	-3.8	-4.1	-4.0	-3.8	-4.0	-3.9	-4.0	-4.0	-4.6
-4.9	-3.7	-4.5	-3.8	-4.2	-4.1	-3.5	-4.0	-4.0	-3.4	-3.4	-4.1	-3.8	-4.2
-3.9	-3.6	-4.6	-4.3	-3.7	-3.6	-3.2	-4.1	-3.6	-3.7	-3.8	-4.7	-4.6	-4.2
-4.3	-3.4	-3.6	-3.3	-3.4	-3.6	-3.6	-4.0	-3.2	-5.4	-3.5	-4.5	-3.7	-5.1
-4.5	-3.3	-4.1	-4.2	-3.7	-3.6	-4.1	-4.4	-3.8	-4.8	-3.9	-4.1	-3.8	-3.6
-4.7	-3.0	-4.7	-4.4	-3.5	-4.3	-3.7	-4.2	-4.0	-4.4	-4.0	-4.5	-4.0	-4.7
-4.2	-4.1	-3.3	-3.8	-3.5	-4.5	-4.1	-4.4	-3.2	-4.2	-3.9	-4.4	-4.5	-4.2
-4.2	-4.1	-3.8	-3.3	-3.7	-3.6	-3.9	-4.4	-4.3	-4.4	-3.6	-4.6	-3.8	-3.9
-3.8	-3.5	-3.8	-3.3	-3.3	-4.2	-3.3	-4.6	-3.7	-5.6	-4.5	-6.2	-4.4	-4.9
-4.1	-3.9	-5.5	-4.1	-4.0	-4.0	-3.8	-4.2	-4.3	-3.8	-4.3	-4.4	-3.8	-4.4
-4.7	-4.4	-6.1	-4.1	-3.4	-4.4	-3.9	-4.1	-3.4	-3.9	-3.8	-6.7	-3.8	-4.0
-4.2	-3.7	-4.7	-4.3	-3.3	-4.3	-3.7	-4.0	-4.1	-5.0	-3.9	-4.6	-3.5	-4.0
-4.2	-4.9	-4.6	-4.8	-3.4	-4.8	-3.5	-4.3	-3.7	-4.3	-3.4	-4.6	-3.9	-4.2
-3.9	-4.6	-3.2	-5.8	-3.9	-4.2	-3.8	-4.1	-3.2	-6.4	-4.3	-4.4	-4.0	-4.4
-4.0	-3.5	-4.5	-4.0	-3.7	-4.7	-3.2	-4.8	-3.7	-4.3	-4.5	-4.3	-4.1	-5.4
	-3.3	-4.7	-4.6	-4.2	-4.1	-3.5	-4.9	-3.5	-3.5	-3.0	-5.7	-4.0	-4.8
	-3.6	-4.4	-4.8	-3.7	-5.1	-3.4	-4.4	-3.6	-5.6	-3.6	-4.5	-4.2	-4.8
	-4.0	-3.6	-4.8	-3.7	-4.2	-3.4	-4.3	-3.8	-3.5	-4.1	-4.4	-3.9	-5.0
	-3.4	-4.3	-4.2	-4.3	-5.0	-3.7	-5.1	-3.9	-3.9	-3.9	-4.1	-4.0	-4.2
	-4.1	-4.7	-4.9	-3.5	-4.2	-2.8	-4.0	-3.7	-5.0	-4.4	-4.3	-4.1	-5.3
	-4.0	-4.9	-4.0	-3.8	-4.3	-3.5	-4.3	-3.5	-3.7	-3.3	-4.6	-3.8	-4.2
	-3.9	-4.5	-3.5	-4.1	-4.7	-3.2	-4.9	-4.1	-4.0	-3.5	-5.6	-3.9	-5.1
	-3.6	-3.7	-3.6	-4.0	-4.3	-3.6	-4.0	-3.8	-3.7	-3.6	-4.6	-4.0	-4.6
	-3.8	-5.2	-3.9	-3.8	-4.6	-4.1	-4.2	-3.9	-3.4	-3.6	-4.5	-4.8	-4.6
	-3.6	-4.3	-4.6	-3.6	-5.1	-3.2	-3.8	-3.3	-3.3	-4.3	-4.6	-3.6	-5.0
	-3.8	-4.1	-4.6	-4.1	-3.6	-3.5	-3.9	-4.0	-3.7	-4.0	-5.3	-3.8	-4.9
	-4.4	-3.9	-4.8	-3.9	-4.0	-3.7	-4.3	-3.3	-4.3	-3.9	-3.9	-3.6	-4.4
	-3.9	-3.6	-3.6	-3.8	-4.6	-3.5	-3.8	-3.8	-4.2	-3.6	-5.7	-4.3	-3.6
	-4.1	-3.9	-4.5	-3.6	-3.4	-4.0	-4.1	-3.4	-3.8	-3.7	-4.1	-4.0	-5.4
	-4.0	-4.9	-5.0	-3.8	-3.9	-3.8	-4.5	-3.5	-3.8	-4.2	-3.7	-3.8	-4.2
	-3.5	-4.5	-4.5	-3.4	-4.5	-3.2	-3.7	-3.5	-3.8	-4.0	-6.5	-3.9	-3.7
	-3.8	-3.2	-3.6	-3.7	-5.0	-3.3	-3.9	-3.4	-4.5	-4.3	-4.1	-4.1	-4.9
	-3.2	-3.9	-3.8	-3.6	-3.9	-3.3	-3.7	-3.7	-4.2	-3.7	-4.2	-4.2	-4.5
	-3.3	-3.4	-3.8	-3.4	-3.7	-3.7	-4.1	-4.0	-3.7	-3.7	-4.3	-4.0	-4.6
	-4.0	-3.7	-3.9	-4.1	-3.7	-3.3	-4.4	-3.8	-3.0	-3.5	-3.5	-3.5	-4.1
	-3.6	-3.7	-4.0		-5.2	-3.2	-4.0	-3.9	-3.3	-3.6	-3.9	-3.9	-4.6
	-3.8	-3.3	-5.8		-4.2	-3.5	-4.3	-3.3	-3.8	-3.5	-4.0	-3.5	-4.4
	-8.8	-4.7	-3.6		-4.3	-3.5	-3.9	-3.6	-3.5	-4.3	-4.5	-3.8	-4.2
	-3.4	-4.3	-4.2		-4.4	-3.4	-3.9	-3.5	-3.9	-3.8	-4.3	-4.0	-3.9
	-3.5	-3.8	-5.4		-4.4	-3.5	-4.0	-3.8	-4.2	-4.2	-3.9	-4.0	-4.4
	-3.8	-3.2	-4.3		-4.5	-4.0	-3.9	-2.8	-3.9	-4.6	-4.4	-3.7	-3.9
	-3.2	-3.6	-4.0		-4.0	-3.6	-3.9	-3.7	-4.1	-3.8	-4.3	-3.8	-4.1
	-3.4	-5.4	-4.4		-4.3	-3.7	-3.8	-3.6	-3.7	-3.8	-4.8	-3.3	-4.6
	-3.7	-4.7	-3.8		-4.3	-3.4	-3.9	-3.9	-3.9	-3.9	-4.9	-3.8	-4.4
	-4.0	-3.9	-4.3		-3.6	-3.2	-4.2	-3.8	-3.8	-3.9	-3.5	-4.1	-3.9
	-2.9	-3.9	-3.4		-5.6	-3.5	-5.0	-3.3	-3.8	-4.1	-4.2	-4.3	-5.0
	-4.3	-5.4	-3.6		-5.1	-3.4	-4.3	-4.4	-3.8	-3.7	-3.7	-4.4	-3.9
	-3.5	-5.0	-3.2		-4.8	-3.5	-4.4	-3.7	-3.1	-4.1	-3.6	-3.6	-3.9
	-3.7	-3.6	-3.4		-4.9	-3.4	-4.2	-3.4	-3.8	-4.4	-5.8	-4.5	-4.2
	-3.9	-4.2	-4.4		-3.9	-3.9	-4.3	-3.5	-3.9	-4.3	-3.9	-3.8	-4.0
	-3.7	-4.5	-4.5			-3.9	-4.5	-4.5	-4.3	-4.8	-4.2	-3.7	-4.8
	-3.6	-5.0	-4.5			-3.0	-3.9	-4.0	-3.7	-3.7	-4.4	-4.2	-4.1
	-3.5	-5.9	-4.6			-3.4	-4.7	-4.0	-3.9	-3.7	-4.5	-3.9	-4.2
	-3.6	-3.9	-5.2			-3.4	-3.8	-4.0	-3.9	-3.6	-4.0	-3.4	-3.7
	-3.7	-3.8	-4.0			-3.1	-4.5	-4.0	-3.6	-3.7	-4.0	-3.9	-4.2
	-3.9	-3.6	-5.7			-3.1	-6.4	-3.5	-4.0	-4.0	-3.8	-3.6	-4.9
	-4.3	-3.8	-3.6			-3.1	-4.1	-4.0	-3.9	-3.9	-5.3	-3.8	-3.9
	-3.9	-4.5	-3.6			-3.5	-3.9	-3.6	-3.1	-5.6	-4.5	-3.5	-4.6
	-3.9	-5.2	-3.8			-2.9	-3.8	-3.9	-4.4	-6.2	-3.6	-5.0	-3.7
	-3.9	-3.4	-4.3			-3.8	-4.5	-3.9	-4.0	-4.2	-6.1	-4.0	-4.9
	-3.2	-5.5	-4.9			-3.0	-3.8	-3.8	-3.9	-4.1	-4.7	-4.1	-4.6
	-3.7	-3.6	-4.8			-4.5	-4.6	-4.1	-5.2	-3.7	-4.0	-5.9	-4.4
	-3.6	-3.4	-4.6			-3.5		-3.2	-5.2	-4.4	-3.9	-3.3	-4.6
	-4.3	-5.5	-4.2			-3.4		-3.8	-4.9	-3.8	-4.4	-3.4	-3.9
	-3.8	-3.7	-3.6			-3.3		-3.4	-5.0	-3.8	-4.4	-4.0	-3.9
	-4.1	-3.7	-5.9			-3.4		-3.1	-4.1	-4.4	-4.5	-3.4	-4.4
	-4.5	-3.6	-3.9			-3.6		-3.7	-4.1	-4.0		-3.7	-4.1
	-3.4	-3.9	-3.6			-3.4		-3.9	-4.1	-3.7		-3.5	-4.8
	-3.8	-3.9	-3.9			-3.5		-3.6	-5.1	-3.8		-3.6	-4.3
	-3.4	-3.1	-6.8					-3.7	-3.8	-4.2		-4.1	-4.0
	-3.6	-4.3	-4.6					-3.3	-5.2	-3.8		-3.9	-4.4
	-3.8	-3.2	-3.4					-4.2	-3.8	-4.4		-4.1	-4.4
	-3.8	-3.2	-4.4					-3.3	-4.1	-3.6		-4.4	-5.4
	-3.6	-6.7	-3.3					-4.0	-4.0	-3.9		-3.7	-3.9
	-4.9	-3.6	-4.6					-4.6	-4.4	-3.7		-4.1	-4.9
	-4.0	-4.1	-3.5					-3.4	-4.5	-4.5		-4.3	-3.9
	-3.4	-3.5	-4.2					-3.6	-4.9	-3.6		-3.9	-4.2
	-3.6	-3.9	-4.7					-3.8	-3.3	-3.8		-4.5	-4.6
	-4.0	-4.0	-4.7					-3.5	-4.2	-3.9		-4.1	-4.2
	-3.9	-3.6	-6.2					-3.5	-3.8	-4.1		-4.2	-4.6

021	032-1	032-2	035	041-1	041-2	042	047-1	047-2	047-3	047-4	047-5	047-6	051-1
	-3.6	-3.7	-4.3					-4.4	-4.7	-3.6		-4.3	-3.9
	-4.4	-3.7	-4.7					-4.3	-3.6	-4.5		-3.6	-5.0
	-3.9	-3.9	-4.3					-3.5	-4.0	-4.4		-4.3	-4.7
	-3.8	-3.7	-5.1					-4.2	-3.8	-3.1		-3.9	-5.5
	-4.1	-3.7	-3.9					-3.0	-3.9	-4.1		-3.7	-4.6
	-4.3	-4.0	-4.0					-3.4	-4.7	-3.4		-3.5	-4.0
	-5.3	-3.6	-3.6					-4.1	-4.0	-4.1		-4.5	-5.4
		-4.0	-4.3					-3.8	-3.6	-3.5		-4.1	-4.5
		-5.4	-4.2					-3.4	-4.0	-3.8		-3.9	-3.4
			-4.1					-3.7	-4.2	-4.5		-6.7	-4.0
			-4.9					-3.6	-3.7	-3.8		-3.8	-4.8
			-4.5					-3.4	-4.4	-4.2		-4.1	-4.2
			-3.6					-4.0	-4.3	-3.9			-4.0
			-5.1					-3.7	-3.9	-3.3			-4.6
			-4.6					-4.0	-3.9	-4.1			-3.9
			-5.5					-3.7	-4.9	-3.6			-4.8
			-4.7					-3.5	-4.6	-3.3			-4.4
			-4.2					-3.5	-4.6	-3.8			-4.7
			-4.2					-3.9	-3.9	-3.3			-4.4
			-6.0					-3.5	-4.1	-3.9			-4.6
			-4.2					-4.5	-3.8	-2.9			-4.4
			-4.7					-3.9	-3.8	-3.9			-4.4
			-4.6					-3.7	-4.2	-3.6			-4.3
			-5.0					-3.1	-3.5	-3.4			-4.2
			-4.9					-3.7		-3.6			-3.7
			-4.3					-3.4		-3.7			-4.2
			-5.7					-4.3					-4.3
			-4.4					-3.1					-4.1
			-5.4					-3.0					-3.7
			-4.7					-4.1					-3.6
			-4.8					-4.9					-3.6
			-3.6					-3.5					-3.7
			-4.4					-3.6					-3.6
								-3.7					-3.2
								-4.3					-3.9
								-5.5					-3.6
								-3.9					-3.2
								-4.3					-3.6
								-3.9					-3.6
								-3.9					-3.8
								-3.6					-3.3
								-3.7					-3.3
								-3.7					-4.1
								-3.7					-3.8
								-3.6					-3.7
								-3.8					-5.2
								-3.8					-4.4
								-4.4					-4.3
								-4.1					-4.8
								-4.2					-4.4
								-4.1					-3.4
								-4.0					-3.6
								-3.8					-4.0
								-3.4					-4.4
								-4.4					-4.1
								-3.9					-4.1
								-3.4					-4.6
								-4.4					-3.7
								-3.9					
								-3.0					
								-3.5					
								-2.6					
								-2.8					
								-3.5					
								-3.3					
								-3.2					

Site 071 - Kolá Crater

Grain Size Diameter in Meters

	071-09	071-10	071-14	071-21-1	071-21-2	071-21-3
Average	0.024	0.030	0.031	0.016	0.026	0.022
St Dev	0.011	0.017	0.022	0.007	0.015	0.009
Median	0.021	0.024	0.023	0.015	0.021	0.019
Min	0.014	0.010	0.010	0.008	0.011	0.011
Max	0.089	0.119	0.118	0.084	0.123	0.070
Count	216	132	157	238	188	183
	0.022	0.021	0.031	0.012	0.034	0.022
	0.022	0.043	0.036	0.012	0.032	0.014
	0.023	0.058	0.021	0.012	0.044	0.015
	0.016	0.031	0.021	0.012	0.015	0.021
	0.021	0.064	0.064	0.016	0.064	0.017
	0.024	0.045	0.021	0.015	0.017	0.026
	0.018	0.034	0.020	0.014	0.040	0.022
	0.019	0.036	0.030	0.012	0.041	0.019
	0.017	0.017	0.027	0.016	0.079	0.013
	0.021	0.024	0.100	0.013	0.049	0.037
	0.029	0.038	0.022	0.013	0.021	0.030
	0.019	0.030	0.105	0.014	0.019	0.025
	0.023	0.067	0.106	0.015	0.015	0.011
	0.017	0.045	0.025	0.013	0.026	0.023
	0.016	0.034	0.067	0.014	0.015	0.041
	0.019	0.016	0.025	0.018	0.019	0.029
	0.022	0.015	0.013	0.023	0.041	0.023
	0.016	0.035	0.015	0.043	0.016	0.017
	0.022	0.024	0.016	0.011	0.022	0.023
	0.023	0.048	0.031	0.013	0.047	0.070
	0.022	0.054	0.034	0.013	0.023	0.016
	0.020	0.023	0.017	0.013	0.021	0.020
	0.021	0.119	0.030	0.015	0.013	0.014
	0.016	0.019	0.032	0.015	0.033	0.018
	0.016	0.017	0.043	0.012	0.015	0.028
	0.016	0.067	0.091	0.017	0.017	0.016
	0.020	0.017	0.026	0.016	0.023	0.012
	0.020	0.018	0.019	0.027	0.011	0.028
	0.015	0.022	0.118	0.018	0.026	0.018
	0.017	0.017	0.033	0.014	0.014	0.026
	0.019	0.071	0.025	0.014	0.028	0.022
	0.023	0.051	0.032	0.042	0.014	0.014
	0.021	0.049	0.039	0.015	0.034	0.022
	0.023	0.011	0.030	0.010	0.015	0.023
	0.014	0.028	0.035	0.015	0.018	0.013
	0.023	0.081	0.025	0.016	0.061	0.033
	0.022	0.020	0.020	0.013	0.021	0.014
	0.020	0.014	0.018	0.025	0.023	0.023
	0.016	0.021	0.067	0.013	0.043	0.028
	0.021	0.017	0.018	0.011	0.041	0.029
	0.018	0.029	0.021	0.014	0.040	0.028
	0.030	0.028	0.016	0.018	0.039	0.022
	0.020	0.027	0.014	0.018	0.024	0.017
	0.023	0.024	0.021	0.014	0.023	0.026
	0.020	0.019	0.044	0.018	0.020	0.020
	0.016	0.039	0.023	0.015	0.038	0.034
	0.020	0.028	0.023	0.013	0.018	0.016
	0.016	0.060	0.023	0.017	0.019	0.012
	0.026	0.015	0.039	0.021	0.038	0.045
	0.019	0.020	0.026	0.013	0.012	0.017
	0.021	0.031	0.015	0.019	0.072	0.026
	0.019	0.045	0.032	0.031	0.017	0.019
	0.017	0.016	0.024	0.016	0.015	0.031
	0.020	0.024	0.035	0.014	0.022	0.026
	0.016	0.047	0.046	0.022	0.020	0.015
	0.020	0.038	0.047	0.021	0.044	0.014
	0.023	0.041	0.018	0.021	0.025	0.021
	0.021	0.045	0.028	0.021	0.034	0.022
	0.025	0.052	0.020	0.017	0.020	0.022
	0.016	0.020	0.020	0.018	0.027	0.016
	0.020	0.021	0.027	0.023	0.020	0.019
	0.019	0.016	0.010	0.017	0.027	0.016
	0.019	0.024	0.013	0.022	0.059	0.021
	0.032	0.032	0.014	0.019	0.019	0.017
	0.042	0.033	0.023	0.018	0.022	0.035
	0.026	0.023	0.028	0.015	0.027	0.017
	0.016	0.014	0.022	0.022	0.021	0.020
	0.016	0.012	0.016	0.018	0.029	0.014
	0.017	0.020	0.015	0.018	0.025	0.032
	0.016	0.042	0.046	0.011	0.014	0.015
	0.017	0.024	0.012	0.084	0.039	0.017
	0.021	0.022	0.017	0.020	0.014	0.012
	0.022	0.015	0.034	0.016	0.037	0.022
	0.019	0.068	0.031	0.054	0.032	0.014
	0.017	0.024	0.024	0.015	0.018	0.036
	0.017	0.023	0.053	0.018	0.017	0.024
	0.016	0.014	0.023	0.021	0.020	0.029
	0.017	0.017	0.039	0.015	0.021	0.028
	0.023	0.017	0.037	0.020	0.017	0.025
	0.022	0.052	0.016	0.024	0.053	0.013
	0.019	0.018	0.015	0.014	0.021	0.017
	0.020	0.064	0.052	0.016	0.022	0.028
	0.019	0.021	0.017	0.019	0.123	0.020

Grain Size Diameter in PHI Scale

	071-09	071-10	071-14	071-21-1	071-21-2	071-21-3
Average	-4.5	-4.7	-4.7	-3.9	-4.5	-4.3
St Dev	0.5	0.7	0.8	0.4	0.7	0.5
Median	-4.4	-4.6	-4.5	-3.9	-4.4	-4.3
Min	-6.5	-6.9	-6.9	-6.4	-6.9	-6.1
Max	-3.8	-3.4	-3.3	-3.0	-3.4	-3.5
Count	216	132	157	238	188	183
	-4.5	-4.4	-5.0	-3.6	-5.1	-4.4
	-4.4	-5.4	-5.2	-3.6	-5.0	-3.8
	-4.5	-5.9	-4.4	-3.6	-5.4	-4.0
	-4.0	-4.9	-4.4	-3.6	-3.9	-4.4
	-4.4	-6.0	-6.0	-4.0	-6.0	-4.1
	-4.6	-5.5	-4.4	-3.9	-4.1	-4.7
	-4.2	-5.1	-4.3	-3.8	-5.3	-4.4
	-4.3	-5.1	-4.9	-3.5	-5.4	-4.3
	-4.1	-4.0	-4.8	-4.0	-6.3	-3.7
	-4.4	-4.6	-6.6	-3.7	-5.6	-5.2
	-4.9	-5.2	-4.5	-3.7	-4.4	-4.9
	-4.2	-4.9	-6.7	-3.8	-4.3	-4.6
	-4.6	-6.1	-6.7	-3.9	-3.9	-3.5
	-4.1	-5.5	-4.6	-3.7	-4.7	-4.5
	-4.0	-5.1	-6.1	-3.8	-3.9	-5.3
	-4.2	-4.0	-4.6	-4.1	-4.3	-4.8
	-4.5	-3.9	-3.7	-4.5	-5.3	-4.5
	-4.0	-5.1	-3.9	-5.4	-4.0	-4.1
	-4.5	-4.6	-4.0	-3.4	-4.4	-4.5
	-4.5	-5.6	-5.0	-3.7	-5.6	-6.1
	-4.5	-5.8	-5.1	-3.7	-4.5	-4.0
	-4.3	-4.5	-4.1	-3.7	-4.4	-4.4
	-4.4	-6.9	-4.9	-3.9	-3.7	-3.9
	-4.0	-4.3	-5.0	-3.9	-5.0	-4.2
	-4.0	-4.1	-5.4	-3.6	-3.9	-4.8
	-4.0	-6.1	-6.5	-4.1	-4.1	-4.0
	-4.3	-4.1	-4.7	-4.0	-4.5	-3.6
	-4.3	-4.1	-4.3	-4.7	-3.5	-4.8
	-3.9	-4.5	-6.9	-4.2	-4.7	-4.2
	-4.1	-4.1	-5.0	-3.8	-3.8	-4.7
	-4.2	-6.1	-4.6	-3.8	-4.8	-4.4
	-4.5	-5.7	-5.0	-5.4	-3.8	-3.8
	-4.4	-5.6	-5.3	-3.9	-5.1	-4.5
	-4.5	-3.5	-4.9	-3.3	-3.9	-4.5
	-3.9	-4.8	-5.1	-3.9	-4.2	-3.6
	-4.5	-6.3	-4.7	-4.0	-5.9	-5.0
	-4.5	-4.3	-4.3	-3.7	-4.4	-3.8
	-4.3	-3.8	-4.2	-4.7	-4.5	-4.5
	-4.0	-4.4	-6.1	-3.7	-5.4	-4.8
	-4.4	-4.1	-4.2	-3.5	-5.3	-4.9
	-4.2	-4.9	-4.4	-3.8	-5.3	-4.8
	-4.9	-4.8	-4.0	-4.1	-5.3	-4.4
	-4.3	-4.8	-3.8	-4.1	-4.6	-4.1
	-4.5	-4.6	-4.4	-3.8	-4.5	-4.7
	-4.3	-4.2	-5.5	-4.2	-4.3	-4.4
	-4.0	-5.3	-4.5	-3.9	-5.3	-5.1
	-4.3	-4.8	-4.5	-3.7	-4.2	-4.0
	-4.0	-5.9	-4.5	-4.1	-4.2	-3.6
	-4.7	-3.9	-5.3	-4.4	-5.2	-5.5
	-4.3	-4.3	-4.7	-3.7	-3.5	-4.1
	-4.4	-5.0	-3.9	-4.3	-6.2	-4.7
	-4.2	-5.5	-5.0	-4.9	-4.1	-4.3
	-4.1	-4.0	-4.6	-4.0	-3.9	-4.9
	-4.3	-4.6	-5.1	-3.8	-4.5	-4.7
	-4.0	-5.5	-5.5	-4.5	-4.3	-3.9
	-4.3	-5.3	-5.6	-4.4	-5.5	-3.8
	-4.5	-5.4	-4.1	-4.4	-4.6	-4.4
	-4.4	-5.5	-4.8	-4.4	-5.1	-4.5
	-4.6	-5.7	-4.3	-4.1	-4.3	-4.5
	-4.0	-4.3	-4.3	-4.2	-4.8	-4.0
	-4.3	-4.4	-4.8	-4.5	-4.3	-4.3
	-4.2	-4.0	-3.4	-4.1	-4.7	-4.0
	-4.3	-4.6	-3.7	-4.5	-5.9	-4.4
	-5.0	-5.0	-3.8	-4.3	-4.2	-4.1
	-5.4	-5.0	-4.5	-4.2	-4.5	-5.1
	-4.7	-4.5	-4.8	-3.9	-4.7	-4.1
	-4.0	-3.8	-4.4	-4.5	-4.4	-4.3
	-4.0	-3.6	-4.0	-4.1	-4.8	-3.8
	-4.1	-4.3	-3.9	-4.2	-4.6	-5.0
	-4.0	-5.4	-5.5	-3.5	-3.8	-3.9
	-4.1	-4.6	-3.6	-6.4	-5.3	-4.1
	-4.4	-4.4	-4.1	-4.4	-3.8	-3.6
	-4.5	-3.9	-5.1	-4.0	-5.2	-4.5
	-4.2	-6.1	-5.0	-5.7	-5.0	-3.8
	-4.1	-4.6	-4.6	-3.9	-4.1	-5.2
	-4.1	-4.5	-5.7	-4.2	-4.1	-4.6
	-4.0	-3.8	-4.5	-4.4	-4.4	-4.8
	-4.1	-4.1	-5.3	-3.9	-4.4	-4.8
	-4.5	-4.1	-5.2	-4.3	-4.1	-4.6
	-4.5	-5.7	-4.0	-4.6	-5.7	-3.7
	-4.3	-4.2	-3.9	-3.8	-4.4	-4.1
	-4.3	-6.0	-5.7	-4.0	-4.5	-4.8
	-4.2	-4.4	-4.1	-4.2	-6.9	-4.3

071-09	071-10	071-14	071-21-1	071-21-2	071-21-3
0.029	0.051	0.021	0.015	0.024	0.019
0.017	0.033	0.028	0.018	0.023	0.044
0.017	0.033	0.026	0.015	0.014	0.017
0.018	0.020	0.010	0.019	0.015	0.016
0.017	0.023	0.025	0.019	0.018	0.020
0.023	0.035	0.012	0.016	0.026	0.048
0.016	0.044	0.015	0.021	0.038	0.027
0.023	0.023	0.029	0.017	0.047	0.018
0.022	0.032	0.020	0.020	0.047	0.017
0.036	0.034	0.016	0.015	0.034	0.025
0.016	0.024	0.013	0.015	0.029	0.049
0.038	0.024	0.014	0.013	0.017	0.022
0.021	0.015	0.014	0.013	0.035	0.019
0.037	0.018	0.015	0.015	0.021	0.017
0.020	0.024	0.016	0.016	0.038	0.025
0.016	0.018	0.015	0.014	0.019	0.017
0.046	0.022	0.016	0.014	0.026	0.021
0.022	0.018	0.072	0.014	0.015	0.014
0.020	0.022	0.021	0.018	0.024	0.025
0.019	0.015	0.018	0.020	0.023	0.022
0.022	0.019	0.085	0.017	0.018	0.022
0.029	0.019	0.023	0.014	0.016	0.033
0.027	0.024	0.039	0.016	0.019	0.021
0.020	0.021	0.014	0.014	0.019	0.040
0.017	0.030	0.015	0.014	0.018	0.024
0.016	0.041	0.038	0.016	0.038	0.014
0.016	0.042	0.012	0.016	0.015	0.026
0.016	0.063	0.017	0.015	0.022	0.014
0.017	0.025	0.028	0.016	0.012	0.017
0.025	0.027	0.011	0.016	0.015	0.018
0.017	0.056	0.014	0.016	0.018	0.017
0.023	0.019	0.017	0.017	0.017	0.020
0.024	0.018	0.016	0.011	0.023	0.017
0.032	0.019	0.013	0.015	0.024	0.018
0.017	0.025	0.020	0.015	0.019	0.021
0.020	0.019	0.012	0.016	0.033	0.016
0.033	0.032	0.044	0.016	0.027	0.016
0.022	0.031	0.023	0.016	0.040	0.018
0.020	0.013	0.011	0.017	0.038	0.016
0.032	0.017	0.011	0.017	0.019	0.017
0.024	0.014	0.014	0.015	0.015	0.019
0.019	0.017	0.012	0.016	0.018	0.016
0.017	0.010	0.020	0.012	0.013	0.017
0.022	0.010	0.015	0.016	0.016	0.015
0.021	0.028	0.093	0.014	0.020	0.024
0.020	0.038	0.078	0.016	0.018	0.014
0.024	0.046	0.013	0.013	0.037	0.021
0.017	0.011	0.031	0.013	0.026	0.013
0.020	0.015	0.019	0.013	0.015	0.043
0.023		0.019	0.018	0.014	0.014
0.022		0.058	0.013	0.081	0.014
0.024		0.022	0.016	0.028	0.034
0.017		0.024	0.014	0.015	0.016
0.019		0.069	0.016	0.012	0.016
0.021		0.013	0.011	0.019	0.012
0.019		0.054	0.013	0.012	0.023
0.021		0.022	0.014	0.016	0.014
0.020		0.013	0.016	0.027	0.036
0.026		0.019	0.014	0.019	0.015
0.034		0.047	0.013	0.012	0.027
0.016		0.053	0.014	0.018	0.022
0.020		0.084	0.011	0.036	0.019
0.019		0.018	0.013	0.016	0.015
0.014		0.033	0.011	0.019	0.016
0.021		0.014	0.013	0.025	0.014
0.020		0.098	0.011	0.021	0.022
0.031		0.033	0.020	0.019	0.015
0.019		0.031	0.011	0.032	0.021
0.020		0.030	0.013	0.014	0.018
0.021		0.024	0.014	0.014	0.015
0.020		0.072	0.017	0.015	0.014
0.020		0.018	0.014	0.017	0.021
0.019		0.044	0.011	0.011	0.015
0.025		0.090	0.011	0.014	0.025
0.024			0.017	0.019	0.040
0.023			0.013	0.015	0.021
0.016			0.016	0.015	0.013
0.016			0.022	0.017	0.017
0.017			0.015	0.021	0.028
0.026			0.011	0.012	0.025
0.019			0.013	0.017	0.015
0.018			0.010	0.034	0.036
0.021			0.015	0.026	0.034
0.022			0.010	0.012	0.017
0.017			0.023	0.020	0.012
0.024			0.014	0.043	0.022
0.020			0.014	0.022	0.013
0.021			0.011	0.051	0.013
0.024			0.017	0.029	0.018
0.081			0.011	0.018	0.014
0.037			0.013	0.045	0.017
0.049			0.014	0.027	0.032

071-09	071-10	071-14	071-21-1	071-21-2	071-21-3
-4.9	-5.7	-4.4	-3.9	-4.6	-4.3
-4.1	-5.1	-4.8	-4.2	-4.5	-5.5
-4.1	-5.1	-4.7	-3.9	-3.9	-4.1
-4.1	-4.3	-3.3	-4.2	-3.9	-4.0
-4.1	-4.5	-4.6	-4.2	-4.2	-4.4
-4.5	-5.1	-3.6	-4.0	-4.7	-5.6
-4.0	-5.5	-3.9	-4.4	-5.3	-4.8
-4.5	-4.5	-4.9	-4.1	-5.6	-4.2
-4.5	-5.0	-4.3	-4.3	-5.6	-4.1
-5.2	-5.1	-4.0	-3.9	-5.1	-4.6
-4.0	-4.6	-3.7	-3.9	-4.8	-5.6
-5.2	-4.6	-3.8	-3.7	-4.1	-4.4
-4.4	-3.9	-3.8	-3.7	-5.1	-4.3
-5.2	-4.2	-3.9	-3.9	-4.4	-4.1
-4.3	-4.6	-4.0	-4.0	-5.2	-4.6
-4.0	-4.2	-3.9	-3.8	-4.2	-4.1
-5.5	-4.5	-4.0	-3.8	-4.7	-4.4
-4.5	-4.2	-6.2	-3.8	-3.9	-3.8
-4.4	-4.4	-4.4	-4.2	-4.6	-4.6
-4.2	-3.9	-4.2	-4.3	-4.5	-4.5
-4.4	-4.3	-6.4	-4.1	-4.2	-4.5
-4.9	-4.3	-4.5	-3.8	-4.0	-5.0
-4.8	-4.6	-5.3	-4.0	-4.3	-4.4
-4.4	-4.4	-3.8	-3.8	-4.3	-5.3
-4.1	-4.9	-3.9	-3.8	-4.2	-4.6
-4.0	-5.3	-5.2	-4.0	-5.2	-3.8
-4.0	-5.4	-3.6	-4.0	-3.9	-4.7
-4.0	-6.0	-4.1	-3.9	-4.4	-3.8
-4.1	-4.6	-4.8	-4.0	-3.5	-4.1
-4.6	-4.8	-3.5	-4.0	-3.9	-4.2
-4.1	-5.8	-3.8	-4.0	-4.2	-4.1
-4.5	-4.2	-4.1	-4.1	-4.1	-4.3
-4.6	-4.1	-4.0	-3.5	-4.5	-4.1
-5.0	-4.3	-3.7	-3.9	-4.6	-4.2
-4.1	-4.7	-4.3	-3.9	-4.3	-4.4
-4.3	-4.2	-3.6	-4.0	-5.1	-4.0
-5.1	-5.0	-5.5	-4.0	-4.7	-4.0
-4.5	-4.9	-4.6	-4.0	-5.3	-4.2
-4.3	-3.6	-3.5	-4.1	-5.3	-4.0
-5.0	-4.1	-3.5	-4.1	-4.2	-4.1
-4.6	-3.8	-3.8	-3.9	-3.9	-4.3
-4.3	-4.1	-3.6	-4.0	-4.1	-4.0
-4.1	-3.4	-4.3	-3.6	-3.7	-4.0
-4.5	-3.4	-3.9	-4.0	-4.0	-3.9
-4.4	-4.8	-6.5	-3.8	-4.3	-4.6
-4.3	-5.2	-6.3	-4.0	-4.2	-3.8
-4.6	-5.5	-3.7	-3.7	-5.2	-4.4
-4.1	-3.4	-5.0	-3.7	-4.7	-3.7
-4.3	-3.9	-4.2	-3.7	-3.9	-5.4
-4.6		-4.3	-4.2	-3.8	-3.8
-4.4		-5.9	-3.7	-6.3	-3.8
-4.6		-4.5	-4.0	-4.8	-5.1
-4.1		-4.6	-3.8	-3.9	-4.0
-4.2		-6.1	-4.0	-3.6	-4.0
-4.4		-3.7	-3.5	-4.3	-3.6
-4.2		-5.8	-3.7	-3.6	-4.5
-4.4		-4.5	-3.8	-4.0	-3.8
-4.3		-3.7	-4.0	-4.8	-5.2
-4.7		-4.3	-3.8	-4.2	-3.9
-5.1		-5.6	-3.7	-3.6	-4.8
-4.0		-5.7	-3.8	-4.1	-4.4
-4.3		-6.4	-3.5	-5.2	-4.3
-4.3		-4.2	-3.7	-4.0	-3.9
-3.8		-5.1	-3.5	-4.3	-4.0
-4.4		-3.8	-3.7	-4.7	-3.8
-4.3		-6.6	-3.5	-4.4	-4.5
-4.9		-5.0	-4.3	-4.3	-3.9
-4.3		-5.0	-3.5	-5.0	-4.4
-4.3		-4.9	-3.7	-3.8	-4.2
-4.4		-4.6	-3.8	-3.8	-3.9
-4.3		-6.2	-4.1	-3.9	-3.8
-4.3		-4.2	-3.8	-4.1	-4.4
-4.2		-5.5	-3.5	-3.4	-4.0
-4.6		-6.5	-3.5	-3.8	-4.6
-4.6			-4.1	-4.3	-5.3
-4.5			-3.7	-3.9	-4.4
-4.0			-4.0	-3.9	-3.7
-4.0			-4.5	-4.1	-4.1
-4.0			-3.9	-4.4	-4.8
-4.7			-3.5	-3.6	-4.6
-4.2			-3.8	-4.1	-3.9
-4.2			-3.3	-5.1	-5.2
-4.4			-4.0	-4.7	-5.1
-4.4			-3.3	-3.6	-4.1
-4.1			-4.6	-4.3	-3.6
-4.6			-3.8	-5.4	-4.4
-4.3			-3.8	-4.5	-3.7
-4.4			-3.5	-5.7	-3.7
-4.6			-4.1	-4.9	-4.2
-6.3			-3.5	-4.2	-3.8
-5.2			-3.7	-5.5	-4.1
-5.6			-3.8	-4.8	-5.0